INVESTIGATION OF CONTINUOUS WET GRANULATION PROCESSES VIA IMPLEMENTATION OF PHARMACEUTICAL QUALITY BY DESIGN PRINCIPLES

By

WEI MENG

A dissertation submitted to the

School of Graduate Studies

Rutgers, The State University of New Jersey

In partial fulfillment of the requirements

For the degree of

Doctor of Philosophy

Graduate Program in Pharmaceutical Science

Written under the direction of

Dr. Fernando J. Muzzio

And approved by

_____

_____

_____

_____

New Brunswick, New Jersey

MAY, 2018

ABSTRACT OF THE DISSERTATION

Investigation of continuous wet granulation processes via implementation of pharmaceutical quality by design principles

by WEI MENG

Dissertation Director:

Dr. Fernando J. Muzzio

Wet granulation is a widely used downstream unit operation for size enlargement in the manufacturing of solid oral dosage forms. It has also been considered as a particle design technique to improve powder flow properties, reduce ingredient segregation and modulate compatibility of particulates as well as drug release kinetics. In recent years, continuous manufacturing has been drawing considerable attention due to its intrinsic advantages over conventional batch processing such as improved manufacturing efficiency and enhanced product quality.

The main focus of this dissertation is to understand diverse continuous wet granulation systems by employing pharmaceutical quality by design principles. The performance of different commercial twin-screw and high-shear granulators were compared and their design space was explored by leveraging statistical design of experiments. Critical process parameters (e.g., rotation speed, liquid to solid ratio, throughput and barrel temperature), design elements (e.g., screw configuration and injection location of liquid constituents) and formulation variables (e.g., drug hydrophobicity, primary particle size, binder delivery methods and granulation liquid viscosity and surface tension) were

comprehensively studied to examine the influence on critical attributes of granules (e.g., size distribution, porosity, bulk density, tapped density, flowability, strength, drug segregation and particle shape) and tablets (tensile strength, porosity, friability, disintegration time, drug agglomerate size distribution and release kinetics).

Furthermore, process understanding was enhanced by unraveling the granulation mechanisms with fundamental regime maps regarding wetting and nucleation as well as consolidation and coalescence. Dissolution mechanisms of tablets produced at different processing conditions were elucidated by delving into the discrepancy in their physical and chemical microstructures. In addition, several complementary process analytical technologies such as Eyecon^{TM}, near-infrared and Raman spectroscopy were implemented in a twin-screw granulation process to enable real-time release testing of granule physical properties and drug content uniformity.

ACKNOWLEDGEMENT

As approaching the finish line of this long journey in pursuing my doctoral degree, I want to acknowledge all the exceptional individuals who have helped me reach this far. First and foremost, I would like to express my sincere gratitude to my advisor Dr. Fernando Muzzio for his continuous support, mentorship and encouragement. His perspicacity, enthusiasm and ambition have always inspired me to explore the unknown and emboldened me to confront with the challenges in research. This has benefited me throughout my entire graduate studies and will certainly make a significant difference in my future career.

I also want to extend my sincere appreciation to my committee members, Dr. Bozena Michniak-Kohn, Dr. Tamara Minko and Dr. Benoit Igne, for their time, support and insightful critical review and feedback on this dissertation.

This dissertation is more than a compilation of my research work. It is also a cumulation of years of efforts and contribution from many industrial and academic collaborators. It has been my privilege of working with so many kind and talented colleagues in our Engineering Research Center for Structured Organic Particulate Systems (C-SOPS): Dr. Xue Liu, Dr. Yijie Gao, Dr. Eric Jayjock, Dr. Sara Koynov, Dr. Bill Engisch, Dr. Juan Osorio, Dr. Sarang Oka, Dr. Jun Zhang, Dr. Pallavi Pawar, Dr. Savitha Panikar, Dr. Yifan Wang, Dr. Douglas Hausner, Dr. James Scicolone, Dr. Gerardo Callegari, Dr. Andrés Román, Dr. Sonia Razavi, Zhanjie Liu, Tianyi Li, Hao Chen, Golshid Keyvan and Thamer Omer. I also would like to acknowledge my fellow graduate students: Lalith Kotamarthy, Ravish Kumar and Kallakuri Suparna Rao who had spent many hours assisting me in the experiments.

I particularly want to thank my parents, Xianpo Meng and Ling Tao, who have provided unconditional support for so many years, encouraged me to rise to the occasion and always being there for me. Finally, a most heartfelt thank you to my wife, Yingyue Zhang, who has been a tremendous source of love, patience and support.

DEDICATION

To Yingyue, and my parents

TABLE OF CONTENTS

LIST OF TABLES

LIST OF ILLUSTRATIONS

Chapter 1

Introduction

1.1 Continuous manufacturing of solid oral dosage forms

For decades, most commercial manufacturing processes were carried out by batch-wise operation, largely due to the high profit margins, stringent regulatory framework and limited material throughput (Vervaet and Remon, 2005). In recent years, largely due to the increasing demand for solid oral dosage forms and expiring patents of drug molecules, it is imperative to accelerate and de-risk process and product development. Although batch manufacturing still predominates in pharmaceutical industry, continuous processing in such a context has been drawing considerable attention and advancing in leaps and bounds. In fact, this approach has been adopted in many other industries, such as food, polymers, consumer products, dairy, etc. by virtue of its intrinsic advantages (Tężyk et al., 2016). It enables the prospect of curtailing capital investment with smaller equipment footprint and elimination of intermediate storage and facilitating process design and understanding. Typically, continuous processes can reach a new controlled state in a matter of minutes, and as a result, processes and products can be developed rapidly and using a small amount of materials even when developed in manufacturing-scale equipment. Process scale-up can be achieved simply by running the operation for a longer time instead of requiring larger equipment (Lee et al., 2015).

In addition, regulatory authorities, such as the U.S. Food and Drug Administration (FDA) and European Medicines Agency, also encourage and incentivize pharmaceutical industry to adopt such a paradigm transformation from batch to continuous processing. In compliance with the concept of Quality by Design (QbD), continuous manufacturing has

inherent advantages to improve production efficiency by mitigating scale-up issues and achieving automated real-time quality monitoring and control by implementing Process Analytical Technologies (PATs), thus facilitating process understanding and technical transfer associated with manageable variability and enhanced product quality (Maniruzzaman et al., 2017). Recently, FDA has approved the first new drug, Orkambi™ (lumacaftor/ivacaftor), manufactured by continuous technology as well as the first new drug, Prezista™ (darunavir), manufactured by shifting an existent process from batch to continuous.

The technology transfer from batch to continuous processing is hitherto perceived as a challenge primarily due to the deficiency in profound understanding and control of manufacturing processes, which entails uncompromising the product quality and safety when exploiting the benefits of process continuity (Beer et al., 2014; Zhang et al., 2016b). This comes in accordance with the pharmaceutical QbD paradigm framed by the International Conference of Harmonisation (ICH) Q8, Q9 and Q10 guidelines describing a systematic, scientific, risk-based, holistic and proactive approach towards better controlled development and manufacturing practices (Yu et al., 2014). The initiative accentuates the necessity of identifying, monitoring and controlling all critical sources of variability influential in a pharmaceutical process. Therefore, by complying with QbD principles, the ultimate goal should be accomplished, namely developing a flexible and robust process where predefined quality attributes can be persistently delivered and building quality into the end product (Yu, 2008).

1.2 Wet granulation in secondary pharmaceutical manufacturing

Wet granulation is a particle design process where formulation design (primary

particles and liquid properties) and process design (granulator type and operation condition) are combined to produce granulated materials with desirable attributes (Meng et al., 2016). While granulation is traditionally considered as a size enlargement process, other particle properties such as porosity, flowability, compressibility and shape can be modified simultaneously to meet specific use requirements. This in turn is driven by the rates of several macroscopic granulation mechanisms: wetting and nucleation, consolidation and coalescence, breakage and attrition (Iveson et al., 2001). In secondary pharmaceuticals manufacturing, wet granulation has been widely carried out to modulate the attributes of in-process intermediates (granules), enabling exquisite control of finished drug product quality. In the past decades, however, most commercial granulation processes such as high-shear wet granulation or fluidized-bed granulation are still executed in batch-wise mode (Saleh et al., 2005).

In particular, during the high-shear granulation process, the interaction between binder liquid and powder bed usually generates inter-particle bonds, thus resulting in granule growth. As defined by Iveson et al. (1996), granule nucleation and binder distribution are the first steps of any wet granulation process (Iveson et al., 1996). The size distribution of initial loose agglomerates and subsequent granule growth behavior are highly dependent on the processes occurring in the spray zone. Hapgood et al. (2003) developed the nucleation regime map based on drop penetration kinetics and flux of drops onto the bed surface (Hapgood et al., 2003). The former is determined by formulation properties, while the later depends on process parameters. Two dimensionless numbers used in the regime map were defined as:

$$\tau_p = \frac{t_p}{t_c} \tag{1.1}$$

$$\Psi_a = \frac{3\dot{V}}{2\dot{A}d_d} \tag{1.2}$$

where t_p is drop penetration time; t_c is the time internal that a packet of powder circulates back to the spray zone; $\dot{V}$ is liquid spray flux; $\dot{A}$ is the flux that powder surface traversing the spray zone; d_d is droplet diameter.

The single drop behavior (dimensionless penetration time, τ_p), together with the interaction between liquid and powder surface (dimensionless spray flux, Ψ_a), defines three potential regimes within this map. In the drop-controlled regime, the binder is well dispersed and quickly penetrates into the powder bed. One drop forms one nucleus and the drop-footprint overlapping is minimum. The second, intermediate regime, is reached when spraying increases and shear force dispersion is large. This is a regime where nuclei formation is more susceptible to the variations in the nucleation zone and is difficult to control. Finally, at the largest τ_p or Ψ_a, mechanical dispersion dominates the process. This regime is characterized by substantial drop coalescence, leading to powder surface caking or liquid pooling. In this regime, intense mechanical mixing and agitation is needed to disperse the binder and break the lumps to form nuclei (Litster et al., 2001).

1.3 Continuous wet granulation techniques

One of the most examined continuous wet granulation techniques is the so-called "extrusion granulation", typically implemented using twin-screws rotating inside a barrel (Keleb et al., 2002). As currently implemented, this method does not use a die and it is not a true form of extrusion, but the equipment otherwise resembles an extruder. Twin-screw granulation (TSG) was first introduced for pharmaceutical applications in the late 1980s when Gamlen at al. (1986) conducted some initial work to evaluate the feasibility

of employing twin-screw extruder for wet granulation purposes (Gamlen and Eardley, 1986). Nowadays it is emerging as a continuous granulation technique amenable to various pharma-oriented applications and over the last decade, considerable attention has been drawn to this extrusion-based granulation process.

As more extruders or granulators tailored for pharmaceutical processes are commissioned, the inherent flexibility of these equipment associated with their modular nature provides multitudinous configurable variables in terms of screw design and arrangement, barrel layout and the placement of auxiliary units like powder feeding and liquid binder addition systems (El Hagrasy et al., 2013b). Therefore, TSG enables regime-separated granulation rate processes along the length of granulator conferring different functionalities to specific barrel compartments. The interplay between process parameters, equipment settings and formulation variables dictate mechanical energy input, liquid-solid dispersive and distributive mixing, materials channel fill level and residence time distribution, which subsequently resulting in distinct granule attributes and yields (Seem et al., 2015). While enabling optimum throughput with limited materials loss for pharmaceutical manufacturing, TSG has also demonstrated its robustness towards variation in process and raw materials properties, and consequently maintains consistent product quality against unexpected changes (Fonteyne et al., 2015a).

Currently, extensive research activities have been undertaken to unravel the relationships between critical materials attributes (CMAs) or critical process parameters (CPPs) and the critical quality attributes (CQAs) of granules and tablets. Geometry and configuration of screw elements are identified as one of the most momentous factors with respect to granulation mechanisms, liquid distribution and subsequent granule properties.

In particular, increasing the number of energy-intensive mixing elements, kneading and comb, resulted in more densified and oversized agglomerates. Liquid to solid (L/S) ratio is demonstrated to be another very influential variable dominating the extent of liquid saturation essential for granule consolidation and growth (El Hagrasy and Litster, 2013). With high L/S ratio and wet binder addition method, size distribution of granules was characterized as narrow and monomodal due to enhanced liquid distribution, despite the fact that it may beyond the usable size range for direct tableting (Sayin et al., 2015a). In addition, more deformable and spherical granules were obtained as liquid addition increased, leading to decreased porosity and smoother granule morphology. Other parameters such as screw speed and powder feed rate were reported to determine the barrel fill level, which further affected materials residence time and the degree of compaction and densification inside (Dhenge et al., 2011; Djuric and Kleinebudde, 2010). Regime maps were also explored to gather insights into the working principles underlying granulation process (Dhenge et al., 2012).

Despite the aforementioned advantages, it is notable that granule size distribution (GSD) from the TSG is highly sensitive to its screw configuration and certain configurations can give rise to broad and multimodal GSD (Li et al., 2014). This is quite undesirable from an industrial perspective in virtue of its serious implication on uniformity of drying process and potential powder segregation in the ensuing processing. Although narrower GSD could be attained at high liquid content, the resultant median diameter (D_{50}) is typically above 1 mm, rendering it less usable in the downstream tableting (Djuric et al., 2009). Findings by Dhenge et. al (2010) showed that low shear conditions with conveying screws failed to effectively disperse the liquid binder,

especially with direct injection delivery method, which eventually resulted in a multitude of un-granulated fines and lumps (Dhenge et al., 2010). Studies undertaken by EI Hagrasy et. al (2013) reported several configurations of kneading elements that could improve liquid distribution, yet the intensive shear force also induced breakage of granules, leading to the production of smaller granules and bimodal distributions (El Hagrasy and Litster, 2013). Studies from Sayin et al. (2015) and and Vercruysse et al. (2015) demonstrated that incorporation of comb mixing elements could allow intimate liquid-powder mixing and optimize granulator performance (Sayin et al., 2015a; Vercruysse, 2015). As with current implemented TSG, however, it seems challenging to have relatively monomodal GSD and favorable liquid homogeneity without compromising other essential properties like shape and porosity.

Ever since equipment manufacturers were mindful of the specific requirements in pharmaceutical industry, small and versatile continuous granulators designed for the production at low throughput have been emerging (Järvinen et al., 2015; Meng et al., 2016; Meng et al., 2017). Aside from the twin-screw granulator, there are also several other continuous granulation techniques that have been on market for years. For instance, the companies Lödige and Glatt offered their respective horizonal high-shear mixer granulators: CoriMix® CM5 and GCG-70 for continuously granulating the incoming raw materials. However, there are very few scientific reports so far on the aforementioned two pieces of equipment.

1.4 PAT strategies for continuous wet granulation processes

Implementation of process analytical technologies (PATs) is consistent with the overarching QbD paradigm. It involves a complicated system combining interdisciplinary

and multivariate (chemical, physical, microbiological, mathematical and risk analysis) methodologies for mechanistic understanding of material and process influence in a timely fashion (Laske et al., 2017). According to the regulatory framework launched by FDA in 2004, enhanced product quality and process efficiency with mitigated risks can be achieved through integration of PATs for automated real-time quality monitoring and feed-forward control rather than the conventional sampling and time-consuming off-line analysis. As such, it has been playing a pivotal role in real time release testing (RTRT) and reduction of cycle times by means of in-, on- or at-line measurements and is accounted one of the pillars of designing, analyzing and controlling the manufacturing process (Fonteyne et al., 2015b).

In terms of wet granulation, however, some PATs investigated so far are primarily for batch processes, such as power consumption, capacitance measurement, stress and vibration sensing, acoustic emissions, etc. (Hansuld and Briens, 2014). Since last decade, implementation of near-infrared (NIR) and Raman spectroscopy for RTRT has increased considerably during pharmaceutical production (De Beer et al., 2011). These more promising spectroscopic techniques not only enable rapid non-invasive and non-destructive measurements in the absence of sample preparation but supply versatile qualitative and quantitative physical and chemical information regarding critical process and product attributes (Luypaert et al., 2007). More importantly, aside from the extensive studies of their employment on batch wet granulation, NIR and Raman spectroscopy can be easily interfaced with continuous process streams for in-line acquisition of multivariate data. Fonteyne et al. (2013) demonstrated the feasibility of using NIR and Raman for at-line measurements of anhydrous/monohydrate solid-state transformation of

theophylline during TSG (Fonteyne et al., 2013). Although both techniques were capable of detecting the nuance of solid-state changes, Raman spectra were more definite compared to the NIR spectra in drug polymorph discrimination. Chablani et al. (2011) employed NIR for in-line real-time measurement of residual moisture content of dried granules in a commercial production scale of continuous TSG-fluidized bed drying-milling process (Chablani et al., 2011). Moisture predicted by NIR showed satisfactory statistical correlation with the conventional reference methods of loss-on-drying and Karl Fischer. Fonteyne et al. (2012) combined NIR with Raman as complementary tools for at-line analysis of drug solid-state, granule moisture content, flowability, bulk and tapped densities at different TSG and drying conditions. Partial least squares (PLS) models were successfully constructed to predict the CQAs of granules (Fonteyne et al., 2012).

Furthermore, several other PATs implemented for TSG exclusively focused on assessing granule size or morphology. EI Hagrasy et al. (2013) and Sayin et al. (2015) explored the potential of a 3D high-speed imaging camera (Eyecon^{TM}) for in-line monitoring of particle size and count and its applicability in real-time process control (El Hagrasy et al., 2013a; Sayin et al., 2015c). The results exhibited adequate sensitivity to intentional process perturbations and the concomitant variations in granule characteristics. Fonteyne et al. (2013) integrated a spatial filter velocimetry for in-line particle size analysis as well as materials flowing velocities as they crossed the laser beam casting shadows on a detector array of optical fibers (Fonteyne et al., 2013). The recurrent problem nevertheless was the fouling of optical surfaces. Besides, a similar technique implemented by Kumar et al. (2013) was called focused beam reflective measurements. It analyzed the chord length of milled granules based on the mechanism

that rotating laser light were reflected and propagated back into the probe once in contact with moving particles (Kumar et al., 2013). A meaningful relationship was established between this technique and sieve analysis enabling the creation of real-time feedback control loops. In addition, Fonteyne et al. (2012) used photometric stereo imaging for at-line evaluation of size, roughness and shape of granules produced by TSG. It was found that PLS model developed on the basis of imaging data showed the best prediction performance for granule flowability (Fonteyne et al., 2012).

1.5 Outline of the dissertation

In this dissertation, the overall research was geared towards better design, understanding and control of continuous wet granulation process. Pharmaceutical QbD methodologies, such as design of experiments (DoE), multivariate data analysis and PATs, were employed to enhance the process capability and product quality without compromising the development and manufacturing efficiencies. Comprehensive studies were conducted to delve into the complex correlation between CMAs, CPPs and CQAs, which after optimization assisted in establishing the design space for the end-product.

1.5.1 Specific Aim I: influence of process and design parameters on critical granule attributes

This aim explored the design space of different commercial continuous twin-screw and high-shear granulators with different scales by leveraging DoE and statisticaly analysis. The key process (rotation speed, liquid to solid ratio and throughput) and design (screw/blade configuration) variables were correlated to the critical granule attributes (size distribution, morphology, porosity, bulk density, tapped density, flowability, friability and liquid distribution) and granulator performance (residence time distribution,

materials hold-up and equipment torque). Fundamental regime maps were also leveraged to unveil the underlying granulation mechanisms in several case studies. Aim I was discussed in Chapter 2, 3 and 6.

1.5.2 Specific Aim II: effect of process parameters on tablet properties

This aim investigated the effect of CPPs on critical quality attributes including hardness, disintegration time, friability, porosity, content uniformity and *in-vitro* dissolution kinetics. In particular, processing conditions were demonstrated to be able to modulate granule physical microstructure and drug agglomerate size distribution, which will further influence the tablet performance after compression. Such a relationship was elucidated by utilizing diverse imaging techniques. Aim II was discussed in Chapter 4.

1.5.3 Specific Aim III: influence of material properties and binder delivery on critical granule and tablet attributes

This aim focused on the effect of different formulations on in-process intermediates and final drug product properties. Varying drug loadings, primary particle size and hydrophobicity were investigated on granule size, porosity, flowability and tablet hardness and drug agglomerate size distribution. The influence of binder delivery methods (dry or wet), solution viscosity and surface tension were also examined by analyzing the droplet penetration behavior into the powder bed. Aim III was discussed in Chapter 5.

1.5.4 Specific Aim IV: implementation of complementary PATs in TSG

This aim explored the feability of deploying complementary in-line analytical tools to eable real-time release testing (RTRT). Eyecon^{TM} direct imaging was integrated for real-time granule size and shape assessment. Near-infrared (NIR) spectroscopy was

implemented to predict granule physical attributes (size, porosity, bulk density, tapped density and flowability). Raman spectroscopy was used for in-line evaluation of granule drug content uniformity. Aim IV was discussed in Chapter 7.

Chapter 2

Mechanistic understanding of the effects of process and design parameters on granule size distribution in a continuous high shear granulation process

2.1 Objectives

This study examined a commercially available continuous high shear mixer granulator that has received much less attention - a tubular mixer equipped with an axially placed shaft. The process resembles a batch high shear granulation in terms of processing steps, namely, dry powder mixing, binder addition and wet massing. The effect of process and design variables on GSD were investigated based on the drop penetration tests, nucleation regime map and aided by statistical tools. The objectives of this work are: (1) to promote a fundamental understanding of the influence of process and design parameters on GSD and provide more mechanistic insights into granule formation and growth in continuous high shear granulation systems; (2) to explore the design space using QbD methodologies and (3) to relate granulation mechanisms to the critical attributes of in-process intermediates.

2.2 Materials and methods

2.2.1 Materials

A placebo formulation used in this work contains 70% (w/w) α-lactose monohydrate 200M (Foremost Farms USA, Baraboo, WI, USA) and 30% (w/w) microcrystalline cellulose (MCC, Avicel® PH101, FMC Biopolymer, Philadelphia, PA, USA). The median diameter (D_{50}) of lactose is 78.35 μm while that of MCC is 58.72 μm. Purified water was used as granulation liquid.

2.2.2 Experimental set-up

Photographs and schematics of the experimental set-up are shown in Figure 2.1. The feeding system consists of two loss-in-weight feeders, operated in gravimetric mode. The feeders were fitted with fine concave screws and had no screen at the outlet. A K-Tron KT35 twin-screw LIW feeder was used for dosing α-lactose monohydrate 200M and a K-Tron KT20 was used to feed microcrystalline cellulose (Avicel® PH101). All experiments were performed at a constant total powder feed rate of 10 kg/h. A Quadro conical screen mill (Comil, Model #197S, Quadro Engineering, Ontario, Canada) was integrated into the experimental set-up upstream of the granulator to de-lump agglomerates from the incoming powder streams and enhance micro-mixing. The mill was operated at 1400 rpm and was fitted with a 800 μm round-holed screen. Granulation was then carried out in a continuous high shear granulator, the Glatt GCG 70 shown in Fig. 2.1 (a). The granulator consisted of a horizontal tube, 68.3 cm in length, with a diameter of 8.8 cm. Fitted along the axial length of the tube was a central rotating shaft with 24 evenly spaced blades. Three kinds of blades (60°, 90° and 120°) are available and can be mounted in any chosen combination (see Fig. 2.1 (c)). The material entered the unit through the granulator inlet, and was conveyed and sheared by the impeller blades until exiting the granulator. Convection transports the material along the vessel axis (from the entrance to the discharge) during which it undergoes dry mixing, wetting and consolidation.

The blade configurations (forward/backward and forward/straight) for the first nozzle position are illustrated in Fig. 2.2. The transition from forward/straight configuration to forward/backward configuration can be obtained by adjusting the blade angles with the shaft. As powder enters the granulator, blades convey raw materials forward and, to a

lesser extent, backwards, promoting net convective flow, dispersive axial mixing and convective cross-sectional mixing.

Wetting occurs immediately once the mixture reaches the nozzle location. Granulating liquid is delivered through Tygon® tubing with a peristaltic pump (Masterflex LS, Model 7518-12) in dripping mode. Powder mixing coupled with several granulation mechanisms (nucleation, coalescence, consolidation and attrition or breakage) continues along the granulator axis until the output point is reached. After exiting the granulator, granules pass through a #5 mesh size sieve (4 mm in hole diameter) to remove lumps and then are dried to a loss-on-drying value of not more than 3.0% in a hot-air convection oven.

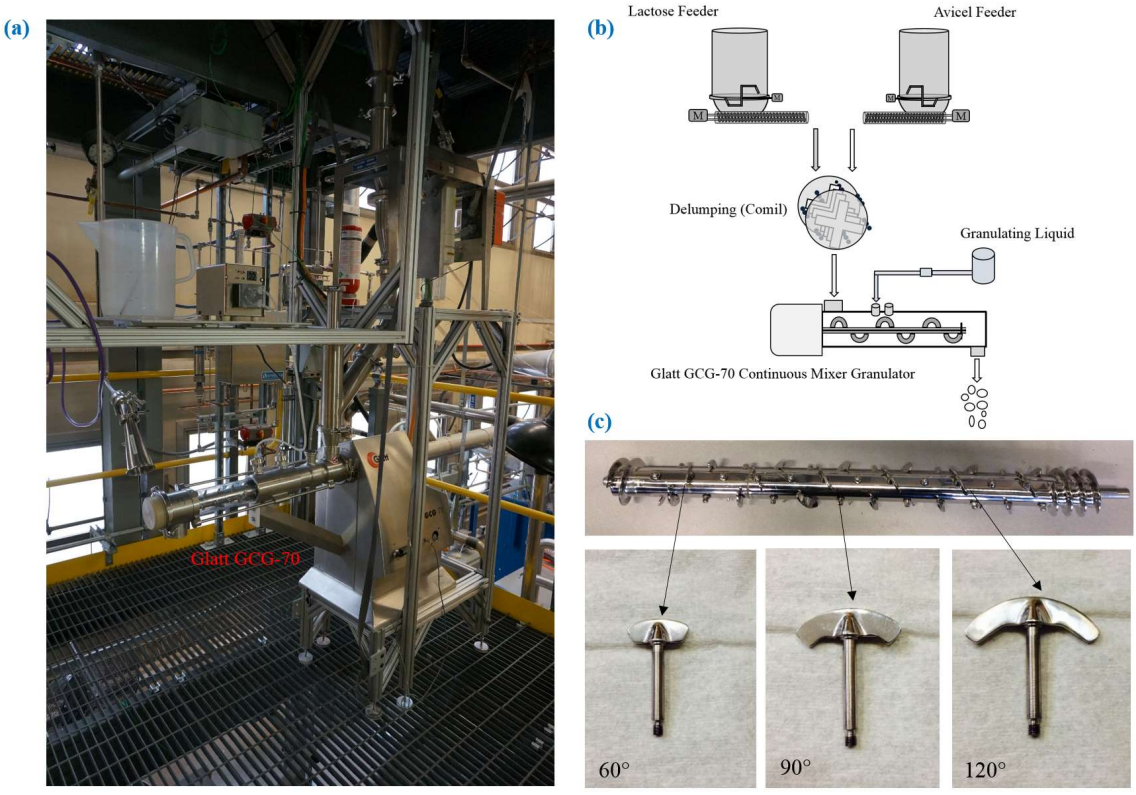

Fig. 2.1. (a) Glatt GCG 70 in the continuous granulation rig. (b) Schematic of the experimental setup. (c) Granulation shaft and blade designs.

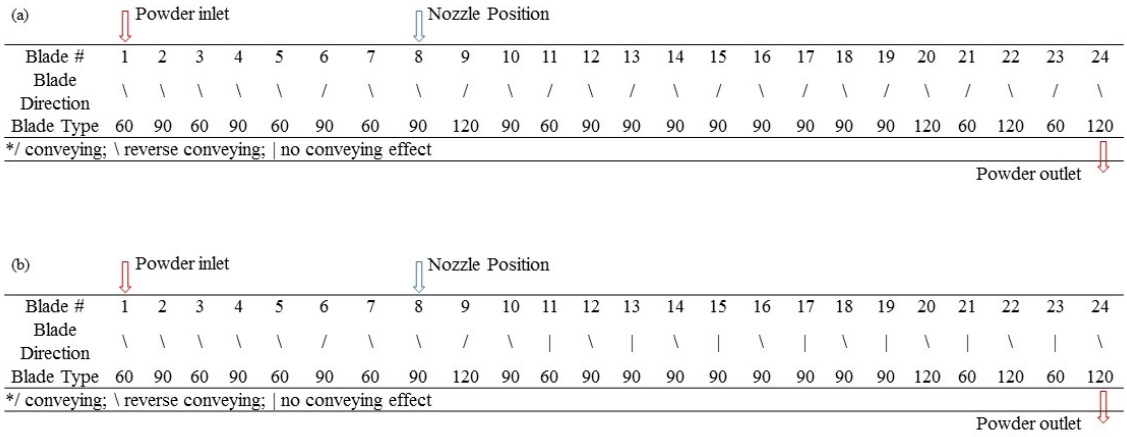

Fig. 2.2. Blade arrangement with a (a) forward/backward and (b) forward/straight alternate configurations.

2.2.3 Experimental design

Table 2.1 specifies the process and equipment design parameters involved in the Design of Experiments. An I-optimal design including 38 batches (see Table 2.2) was generated by JMP® statistical software (SAS Institute Inc., Cary, NC, USA).

Table 2.1 Experimental conditions employed during granulation

Process Parameters	
Flow Rate (kg/h)	10
Rotation Rate (RPM)	133, 275, 415, 538, 660
L/S Ratio	0.1, 0.2, 0.3
Granulator Design Parameters	
Blade Configuration: blade direction, inclination angle (angle with the shaft)	1. F/S-Alternate blades directing in forward and straight, inclined angle-45°/90° 2. F/B-Alternate blades directing in forward and Backward, inclined angle-45°/135°
Nozzle Positions	Position 1 (above the 12th blade from granulator inlet, 24 blades in total) Position 2 (above the 8th blade from granulator inlet, 24 blades in total)

Table 2.2 The I-optimal design used to explore the effect of process and design parameters on granule quality attributes

Batch #	Rotation Speed(RPM)	L/S Ratio	Blade Configuration	Nozzle Position	Flow rate(kg/h)
1	415	0.2	FB	P1	10
2	415	0.2	FB	P1	10
3	415	0.2	FB	P1	10
4	275	0.3	FB	P2	10
5	133	0.1	FB	P1	10
6	538	0.3	FB	P1	10
7	275	0.3	FB	P1	10
8	133	0.2	FB	P1	10
9	660	0.1	FB	P1	10
10	660	0.3	FB	P1	10
11	133	0.1	FB	P2	10
12	415	0.1	FB	P2	10
13	415	0.3	FB	P2	10
14	660	0.3	FB	P2	10
15	660	0.2	FB	P2	10
16	538	0.2	FB	P2	10
17	275	0.2	FB	P2	10
18	133	0.2	FS	P2	10
19	133	0.1	FS	P2	10
20	660	0.1	FS	P2	10
21	660	0.3	FS	P2	10
22	415	0.3	FS	P2	10
23	660	0.1	FB	P2	10
24	415	0.2	FB	P2	10
25	415	0.2	FS	P2	10
26	415	0.2	FS	P2	10
27	415	0.2	FS	P2	10
28	275	0.3	FS	P2	10
29	133	0.3	FS	P1	10
30	415	0.3	FS	P1	10
31	660	0.3	FS	P1	10
32	660	0.1	FS	P1	10
33	275	0.1	FS	P1	10
34	660	0.2	FS	P1	10
35	538	0.2	FS	P1	10
36	415	0.1	FS	P1	10
37	133	0.1	FS	P1	10
38	133	0.2	FS	P1	10

2.2.4 Physical characterization

2.2.4.1 Granule size distribution

The particle size distribution of the dry mixture of 70% (w/w) α-lactose monohydrate and 30% (w/w) MCC was measured by sieve analysis using a $\sqrt{2}$ series of sieves from 37 μm to 4 mm. GSD of the dried granules was measured both by sieve analysis and by Eyecon^{TM} 3D high speed imaging camera (Innopharma Laboratories, Dublin, Ireland), which is a direct imaging system for in-line and benchtop characterization of particle size, shape and surface morphology. The camera is equipped with 3-color LED illumination that allows the capture of 3D features of particles and distinction between their boundaries.

Fig. 2.3 demonstrates its performance in benchtop measurement mode and compares it with sieve analysis of batch # 28. A very good correlation was obtained ($R^2 = 0.98$). Fig. 2.4 presents the particle shape and surface information of granules from batch #28. The granules size from 37 to 1410 μm and had an irregular shape. Similar results were observed for other batches (not shown). Results were examined using statistical analysis. D_{50} and percentage of fines (%fines) were selected as the two responses examined. Particles smaller than 64 μm were defined as fines, while those above 1 mm were designated as “coarse”.

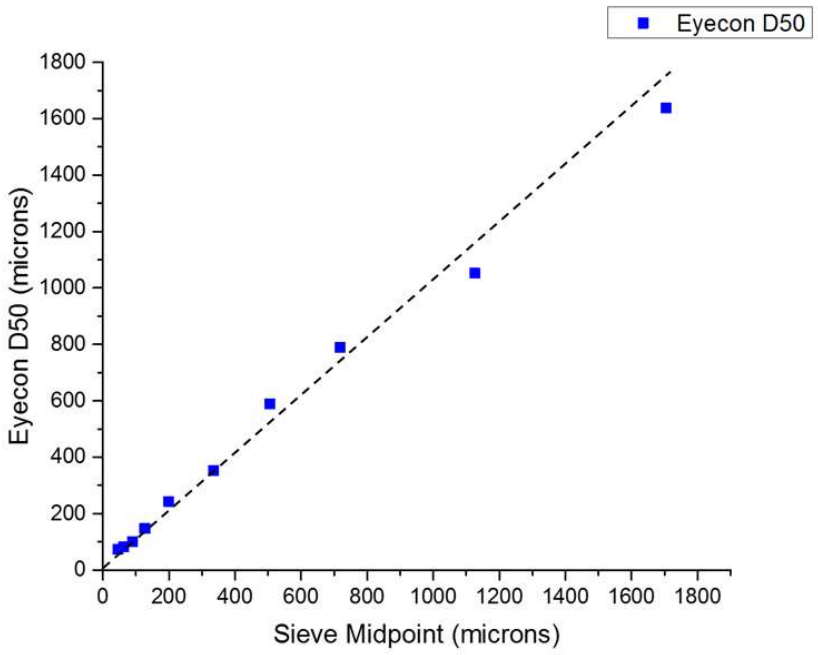

Fig. 2.3. Correlation between median particle size values obtained from Eyecon^{TM} camera measurements and sieve analysis ($R^2 = 0.98$).

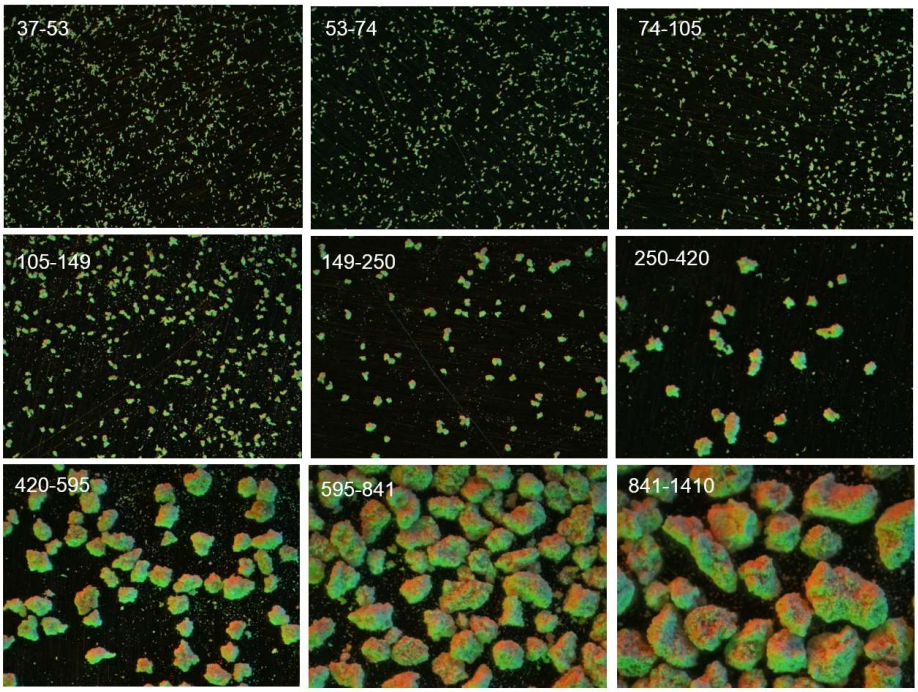

Fig. 2.4. Granules from different size fractions of batch # 28 under Eyecon^{TM} camera.

2.2.4.2 Drop Penetration Time

To investigate the wetting behavior of the material, drop penetration tests were performed on a static powder bed of the starting material. A dry blends containing 70% (w/w) α-lactose monohydrate and 30% (w/w) MCC was prepared and conditioned in the FT4 Powder Rheometer (Freeman Technology Inc., Medford, NJ, USA), to generate reproducible powder bed conditions. A vessel with a diameter of 50 mm was split into an upper 85 mL vessel and a bottom 160 mL vessel. Material in the vessel was above the split line before conditioning. A rotating blade moved up and down several times through the powder bed to remove the trapped air and erase the pre-consolidation history. The conditioned powder bed was then split to generate a level surface for the droplet penetration test. A high-speed camera (GimaGO, NET USA Inc., Highland, IN, USA) was set up and recorded the penetrating process until there was no significant change in light reflection on the powder bed surface, at which point drop penetration was deemed to be complete. The penetration time was determined by analyzing the video in Adobe Photoshop CC (Adobe Systems Inc., San Jose, CA, USA). A single droplet was released onto the powder bed from a syringe with #22 gauge needle and its size was determined after averaging the weight of 10 droplets. Under constant drawing area assumptions, the relationship given in Eq. 2.1 can be expected from the penetration time equation defined by Hapgood et al (2002). provided that all other conditions are equal.

$$\frac{t_{p,1}}{t_{p,2}} = \frac{d_{d,1}^2}{d_{d,2}^2} \tag{2.1}$$

where t_p is the penetration time and d_d is the diameter of a droplet (Hapgood et al., 2002).

2.3 Results and discussion

2.3.1 The effect of process and design parameters on GSD

In this study, sieve analysis gave a median particle size of 75.88 μm for the dry un-granulated blends. The GSD of dried granules was measured both by the sieve method and by direct imaging approach and both methods yielded similar results.

Fig. 2.5 and 2.7 showed the analysis of variance (ANOVA) results for D_{50} and %fines from Eyecon^{TM} 3D high speed imaging camera. The bar chart presents the t-ratios with blue lines marking a critical value at $p<0.05$ significance. Since the first five bars crossed the blue line, these factors were statistically significant, i.e., the p values of the first five factors were less than 0.05. It was clear that the two process variables, rotation speed and L/S ratio, had a statistically significant impact on the responses, whereas the design parameters (blade configuration and nozzle position) were less consequential factors. The interaction effect between L/S ratio and blade configuration was also significant. The *p* value of the quadratic term, L/S Ratio*L/S Ratio, was also less than 0.05, indicating a curvature (non-linearity) in the response surface. The terms highlighted in red were quite close to the significance threshold, but their statistical significance could not be established due to the insufficient data in the I-optimal design. Terms highlighted in blue were less important.

The contour plot displayed in Fig. 2.6 shows that increasing the L/S ratio and simultaneously decreasing the rotation speed leads to increased granule growth. However, wet powder clogged the granulator at the highest L/S ratio (0.3) and lowest rotation speed (133 RPM) because of the presence of a substantial amount of over-wetted material, causing the granulation vessel to choke. Under these conditions, the granulator

cylinder over-heated and finally the shaft stopped rotating due to motor overload. Based on Fig. 2.5 and Fig. 2.6, the L/S ratio was more influential than the rotation speed. For cases where the L/S ratio was smaller than 0.25, the effect of rotation speed on D_{50} was found to be negligible. The %fines correlated inversely to D50, as shown in Fig. 2.6 and 2.8. An increase in D_{50} was accompanied by a decrease in %fines, and vice versa.

Term	Estimate	Std Error	t Ratio	Prob>|t|
L/S Ratio(0.1,0.3)	34.642445	3.490502	9.92	<.0001*
Rotation Speed*L/S Ratio	-16.24226	4.444146	-3.65	0.0012*
Rotation Speed(133,660)	-11.78926	3.727268	-3.16	0.0041*
L/S Ratio*L/S Ratio	17.073444	5.441668	3.14	0.0043*
L/S Ratio*Blade Configuration[FS]	-7.486961	3.4031	-2.20	0.0373*
Blade Configuration[FS]	-4.734646	2.614487	-1.81	0.0822
Rotation Speed*Rotation Speed	11.102382	6.252867	1.78	0.0880
Rotation Speed*Nozzle Position[P1]	-3.024796	3.671298	-0.82	0.4178
Nozzle Position[P1]	1.6851909	2.611985	0.65	0.5247
L/S Ratio*Nozzle Position[P1]	2.009352	3.403388	0.59	0.5602
Rotation Speed*Blade Configuration[FS]	1.6961055	3.649314	0.46	0.6461
Blade Configuration[FS]*Nozzle Position[P1]	0.8338561	2.597912	0.32	0.7509

Fig. 2.5. ANOVA results showing effect of process of process and design parameters on the D50. Process parameters were found to be more significant than design parameters. Terms highlighted by red are close to statistical significance while those highlighted by blue not significant.

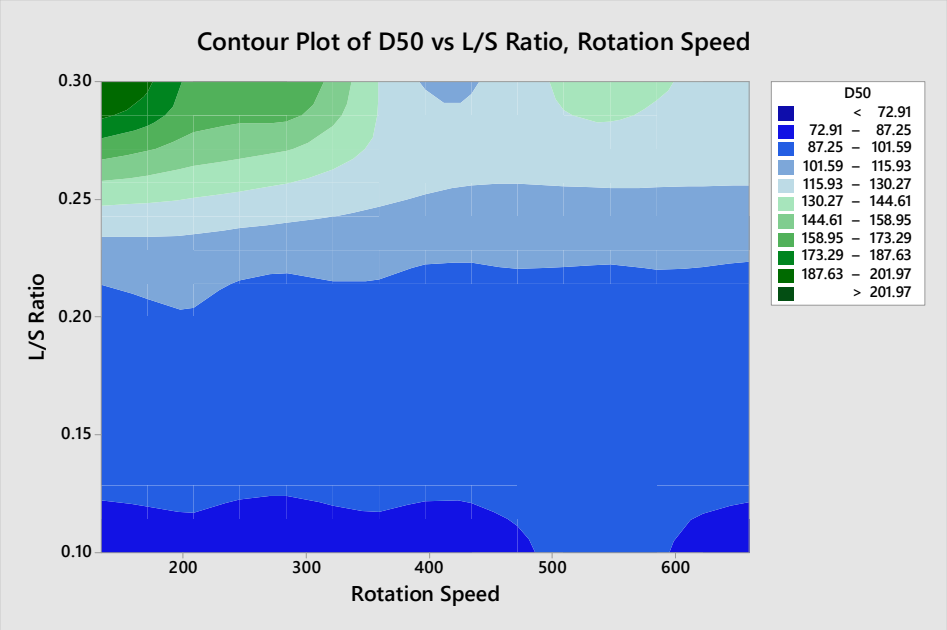

Fig. 2.6. Contour plot showing main and interaction effects of L/S ratio and rotation speed on D50; granule size decreases as color gradually varies from dark green to blue.

Term	Estimate	Std Error	t Ratio	Prob>|t|
L/S Ratio(0.1,0.3)	-0.097602	0.008007	-12.19	<.0001*
Rotation Speed*L/S Ratio	0.0280438	0.010194	2.75	0.0109*
Rotation Speed(133,660)	0.0233107	0.00855	2.73	0.0115*
L/S Ratio*Blade Configuration[FS]	0.0172846	0.007806	2.21	0.0362*
Rotation Speed*Nozzle Position[P1]	0.0165809	0.008421	1.97	0.0601
Nozzle Position[P1]	-0.009971	0.005991	-1.66	0.1086
Rotation Speed*Rotation Speed	-0.020248	0.014343	-1.41	0.1704
Blade Configuration[FS]	0.0084	0.005997	1.40	0.1736
L/S Ratio*L/S Ratio	0.0132589	0.012482	1.06	0.2983
Blade Configuration[FS]*Nozzle Position[P1]	-0.005085	0.005959	-0.85	0.4016
L/S Ratio*Nozzle Position[P1]	-0.002529	0.007807	-0.32	0.7486
Rotation Speed*Blade Configuration[FS]	0.0003697	0.008371	0.04	0.9651

Fig. 2.7. ANOVA for % fines indicating more significant influence of process variables over design parameters; terms highlighted by red are close to statistical significance while those highlighted by blue are not shown to be significant.

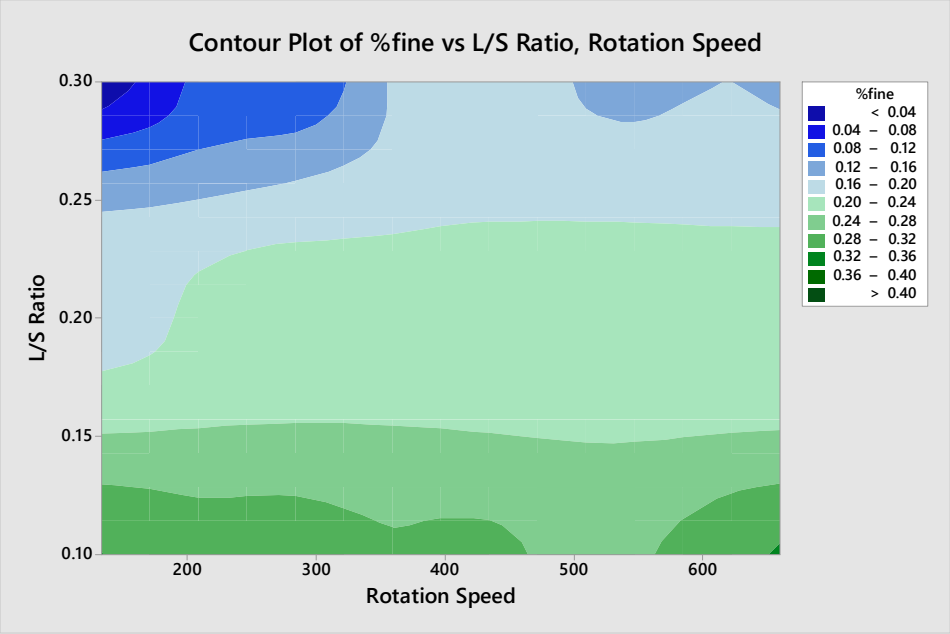

Fig. 2.8. Contour plot showing main and interaction effects of L/S ratio and rotation speed on %fines; %fines increases as color gradually varies from dark blue to green.

Fig. 2.9 (a), (b) and (c) showed the effect of L/S ratio on the cumulative GSD under different rotation speeds and Fig. 2.9 (d) compares the D_{50} at different rotation speeds with a constant L/S ratio, 30%. All the results in Fig. 2.9 are from sieve analysis. The green dot arrow in Fig. 2.9 (a) represents an increase in D_{50}, which increases with an increase in the L/S ratio. Better granulation performance could be obtained at a rotation speed of 275 RPM or 660 RPM. At the rotation speed of 415 RPM, however, the effect of the L/S ratio on the size enlargement was much smaller. In Fig. 2.9 (d), D_{50} first decreased and then increased as the rotation speed increased. A bimodal GSD could also be observed from the experiments, including a peak around 150 µm and another peak above 1000 µm. Therefore, these operation conditions generated granules with broad GSD containing large amount of big agglomerates/lumps. Similar conclusions can be elicited from the direct imaging approach. A quadratic response surface model for the D_{50}

was obtained and is presented in Eq. 2.2. The R-Square for the response surface model was found to be 0.89.

$$D50(um) = 95.47 - 11.13 \times \left(\frac{(RPM - 396.5)}{263.5} \right) + 32.84 \times \left(\frac{(L/S - 0.2)}{0.1} \right) + \left(\frac{(L/S - 0.2)}{0.1} \right) \times \left(\left(\frac{(L/S - 0.2)}{0.1} \right) \times 19.66 \right) + Match(Blade\_Conf) \{ ("FS" \Rightarrow -4.51) or ("FB" \Rightarrow 4.51) \} - \ldots$$

$$\left(\frac{(RPM - 396.5)}{263.5} \right) \times \left(\left(\frac{(L/S - 0.2)}{0.1} \right) \times 14.96 \right) + \left(\frac{(L/S - 0.2)}{0.1} \right) * Match(Blade\_Conf) \{ ("FS" \Rightarrow -6.59) or ("FB" \Rightarrow 6.59) \}$$

(2.2)

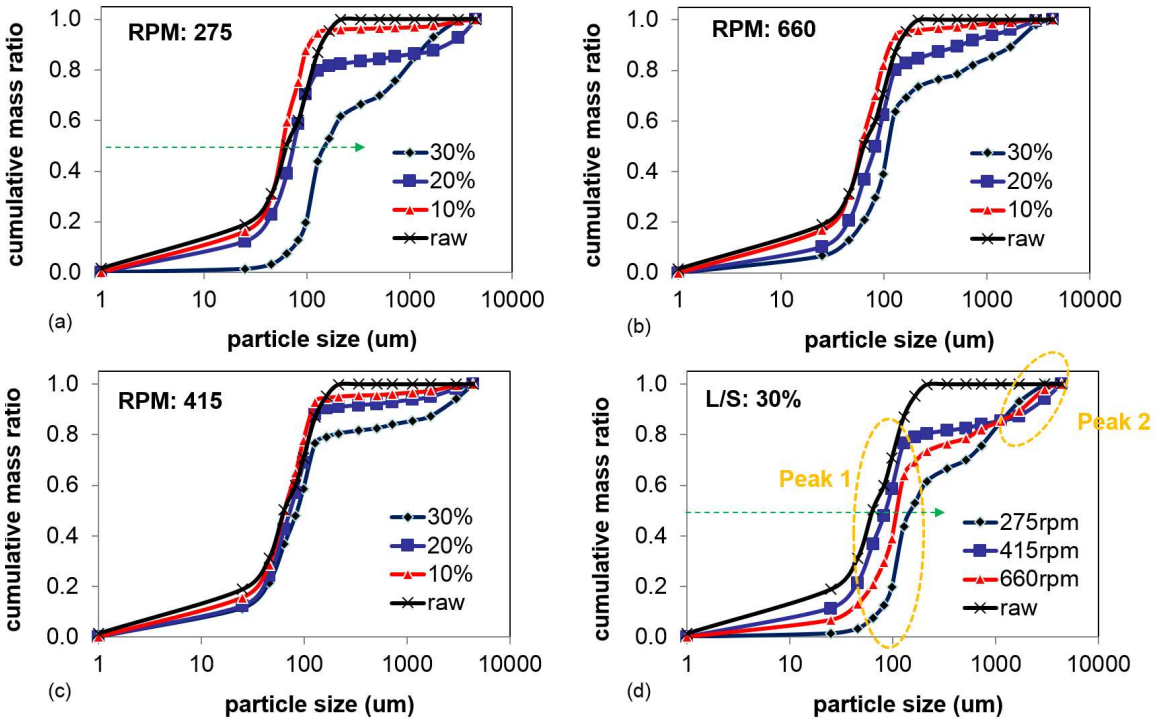

Fig. 2.9. Effect of L/S ratio on the cumulative GSD at (a) 275 rpm, (b) 415 rpm and c) 660 rpm showing less significant influence of moisture content at 415 rpm. (d) Effect of rotation speed on the cumulative GSD at 30% L/S ratio. The distribution exhibited a distinct bimodal nature.

As illustrated in Fig. 2.5 and 2.7, liquid to solid ratio was the most influential factor for granule growth. This is in agreement with the results obtained for batch high shear granulation in other studies (Badawy et al., 2012; Pandey et al., 2013). It is well known that water content can greatly affect the degree of liquid saturation and further determine

granule coalescence (Iveson and Litster, 1998c). For sub-saturated and deformable granules, the degree of liquid saturation was high and free liquid could be easily squeezed onto granule surfaces or contact zones during a fast consolidating process, thereby reducing the induction period and promoting steady growth (Ritala et al., 1988). When water content was very low, particles may remain as dry powders or just form nuclei due to van de Waals interactions, but little granule coalescence can be induced.

The interaction effect between rotation speed and L/S ratio was statistically significant as shown in Fig. 2.5. The effect of rotation speed was more pronounced at high L/S ratios due to the variability in the mechanical properties of granules at different levels of the L/S ratio-i.e., granules may break or deform when the dynamic yield stress is exceeded (Iveson et al., 2001). At low L/S ratios and thus, low degree of liquid saturation, the capillary forces dominated the granule yield behavior, leading to dry-powder-like brittle behavior. Under such conditions, granules were less resistant to the breaking force exerted by the mechanical tools (blades and shaft) (Iveson and Neil, 2004). As a result, at low L/S and high strain rate conditions, granules exhibited a tendency to break instead of coalescence and growth. Tardos et al. (1997) first proposed the dimensionless Stokes deformation number, defined as the ratio of externally applied kinetic energy to the internal energy required for breakage (Tardos et al., 1997).

$$St_{def} = \frac{m_g U^2}{2V_g \tau_y} \tag{2.3}$$

where m_g and V_g are the granules mass and volume, respectively; U is the relative velocity between colliding particles; τ_y is the dynamic yield strength. Brittle granules possess low yield strength leading to high St_{def} . Based on the growth regime map

developed by Iveson et al. (2001), when St_{def} >0.2, granules growth ceased while crumbling behavior occurred (Iveson and Litster, 1998c). Under this scenario, Tardos et al. (1997) reported the maximum stable granule size d_{cr} by taking $U \approx d\dot{\gamma}$, namely

$$d_{cr} = \frac{(2\tau_y St^*_{def} / \rho_g)^{1/2}}{\dot{\gamma}} \tag{2.4}$$

where St^*_{def} is the critical deformation number above which breakage will happen, ρ_g is granule's density, d is a characteristic particle size defined by the sizes of two colliding particles and $\dot{\gamma}$ is the average shear rate in granulators (Tardos et al., 1997). Since $\dot{\gamma}$ was determined by the rotation speed, Eq. 2.4 indicated that d_{cr} was inversely dependent on the rotation speed. In the present study, however, this relationship is not captured at low L/S ratios (see Fig. 2.6 and 2.8).

In contrast, at high L/S ratios, the viscous force started to dominate the yield behavior, causing liquid-like plastic flow. At their yield stress, the plastic granules (high yield strength) were more likely to deform than to break due to a high critical Stokes number. For this scenario, the effect of rotation speed on the granules coalescence and growth became significant. When the impeller speed was relatively low (less than 415 RPM), droplets from the dripping nozzle were broken up and dispersed more uniformly with an increase in shear rates, reducing the localized over-wetting and preventing the formation of oversized lumps. In addition, in this continuous granulator, higher rotation speed decreased the bulk residence time and thus the wet massing time available for sufficient granule formation and growth (Ohno et al., 2007; Pathare et al., 2011; Wang et al., 2008; Zhang et al., 2017). Therefore, the granule median diameter decreased with an increase in the rotation speed if the impeller speed was less than 415 RPM (see Fig. 2.6). When the

impeller speed was relatively high (larger than 415 RPM), granules were densified (or consolidated) because of the normal stresses at high agitation intensity and hence the maximum pore saturation increased, indicating more available liquid present on the granules surface.

Since St_{def} increased with the rotation speed (see Eq. 2.3), the growth behavior, with reasonable nucleation and binder distribution, should shift from the induction region towards the steady growth or the rapid growth regions on the regime map (Iveson and Litster, 1998c). Liu et al. reported that at low impact velocities, the relative granule velocity may decrease to zero due to the viscous force from surface binder and hence no surface contact and permanent deformation occur on granules (Liu et al., 2000). Higher rotation speed increased the collision frequency, deformation of contact area and finally probability of granule coalescence. However, when the impeller speed was further increased (larger than 660RPM), for granules with high yield strength, the deformation area just increased slowly, but the viscous force was not strong enough to avoid the particle separation during rebound. Besides, increasing the agitation intensity to a critical value (higher St_{def}) may shift the granule growth from the steady growth region to the crumbling region. As such, the D50 decreased again after 660 RPM as shown in Fig. 2.6.

2.3.2 Exploration of granulation mechanisms via wetting and nucleation regime map

Fig. 2.9 (d) displayed a broad GSD and a large amount of lumps at high L/S ratios. In order to gain more insight into the underlying nucleation mechanism, drop penetration tests were performed. In this work, instead of testing the droplet distribution in the granulator, a static powder bed was used and thus the drop penetration process was

observed directly. Following the procedure described in section 2.2.4.2, the drop released from the syringe took around 3.92 ± 0.76s to infiltrate into the bed surface completely driven by capillary pressure (Fig. 2.10). The syringe drop size was estimated to be $5.62 \pm$ 0.11mm. When scaled to a nozzle drop size of 11.68 ± 1.05mm, the drop penetration time t_p was estimated to be 16.94s according to Eq. 2.1. As a result of the large drop size compared with the particle, smaller particles were layering on the drops to form nuclei.

As mentioned in Chapter 1.2, dimensionless penetration time τ_p is defined by the ratio of drop penetration time t_p and powder circulation time t_c. Configuration of this granulator, however, results in an inability to directly measure the t_c and thus, it was estimated through powder surface velocity and granulator geometry. As a general rule, surface velocities are approximately one order of magnitude smaller than the corresponding blade tip speed (Kayrak-Talay et al., 2013; Kayrak-Talay and Litster, 2011; Plank et al., 2003). In addition, Litster et al. (2001) and Chan et al. (2012) reported that bed surface velocity also depended heavily on the granulation flow behavior (Chan et al., 2012; Litster et al., 2001). As impeller speed increased, they described a similar flow patterns transition compared to that observed from 133 to 660 RPM in this study, despite the configuration difference in batch and continuous mixer granulators. At 133 RPM, there was little vertical turn over and powder bed surface remained almost horizontal as the blades move up and down, known as “bumping” regime.

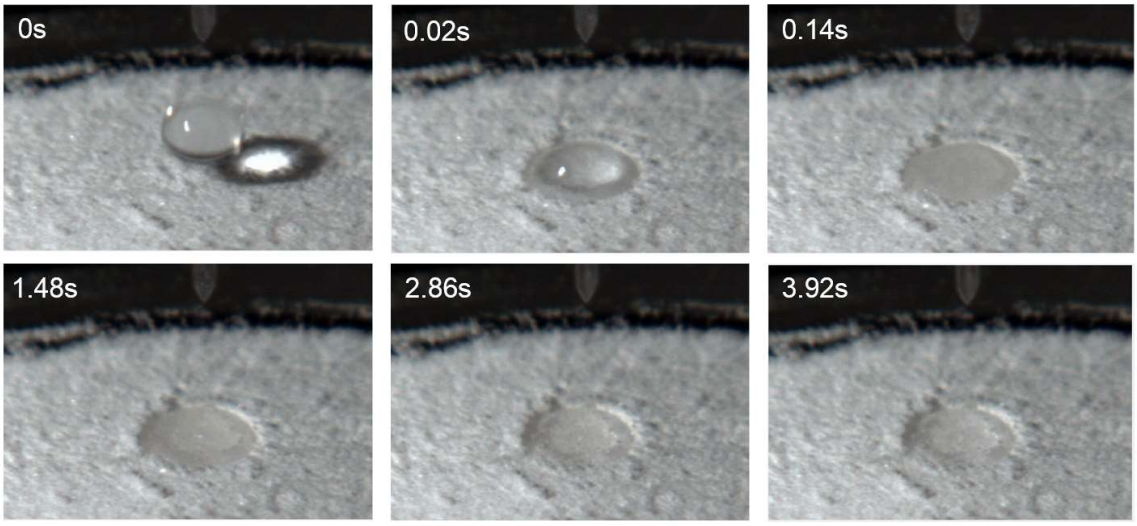

Fig. 2.10. Syringe droplet penetration tests showing the droplet being imbibed into the powder bed, forming granule nuclei.

At higher rotational rate (415 RPM), granules were continuously forced up along the granulator wall, owing to the swift movements of mixing tools beneath, and then tumbled down the bed free surface towards the center. Fluidization of the powder bed eventually took place at 660 RPM where the Froude number exceeded 1 (see Table 2.3) and materials increasingly adhered to the granulator walls to form an annular flow. However, the surface velocity, as indicated in Litster et al. (2002), did not increase consistently with the rotational speed, with less pronounced increase being observed in the fluidized state (Litster et al., 2002). It was believed that bed surface was more sensitive to the mixing blades in "bumping" regime and started to stabilize at very high RPM. Therefore, based on other researchers' work (Chan et al., 2012; Kayrak-Talay et al., 2013), we hypothesize that surface velocity v_{surf} is 15%, 25%, 20%, 20% and 10% of the blade tip speed v_{tip}, corresponding to 133, 275, 415, 538 and 660 RPMs, respectively (see Table

2.3). Subsequently, circulation time t_c was calculated by v_{surf} and cross-sectional circumference of the granulator.

The dimensionless spray flux quantified the binder dispersion as a function of primary operating parameters. It indicated the binder density on the powder surface or mixing quality between the granulating liquid and powder bed, which played a pivotal role in the size and shape of granules size distribution. In the present case, Eq. 2.5 was used to determine $\dot{A}$ by taking the droplet diameter as the spray width because the binder addition method was dripping (Litster et al., 2001). The calculated Ψ_a were shown in Table 2.3.

$$\dot{A} = v \cdot D \tag{2.5}$$

where v is the powder surface velocity passing the spray zone and D is the drop diameter.

Fig. 2.11 located different experimental conditions on the nucleation regime map. Due to the high penetration time and low spray flux, all the operations were in the upper-left corner of the mechanical dispersion regime, indicating good dispersion of the granulating liquids but severe drop overlapping. In case “c”, the liquid dispersion was relatively less effective ($\Psi_a > 0.1$) due to the low rotation speed and high L/S ratio, eventually leading to the granulator choking. In practice, the circulation time was extremely short and imbibition of drops into capillary pores was not as instantaneous as expected because of the drop’s large size. This caused liquid pooling, formation of undesirably large agglomerates and broad granule size distribution. The negative impact of droplet size on penetration time had also been reported by Ax et al. (2008) (Ax et al., 2008). In contrast to the thin surface caking that occurred at high spray flux and fast penetration time

(lower-right corner), the breakage of sticky lumps was more difficult to realize under mechanical mixing and agitation.

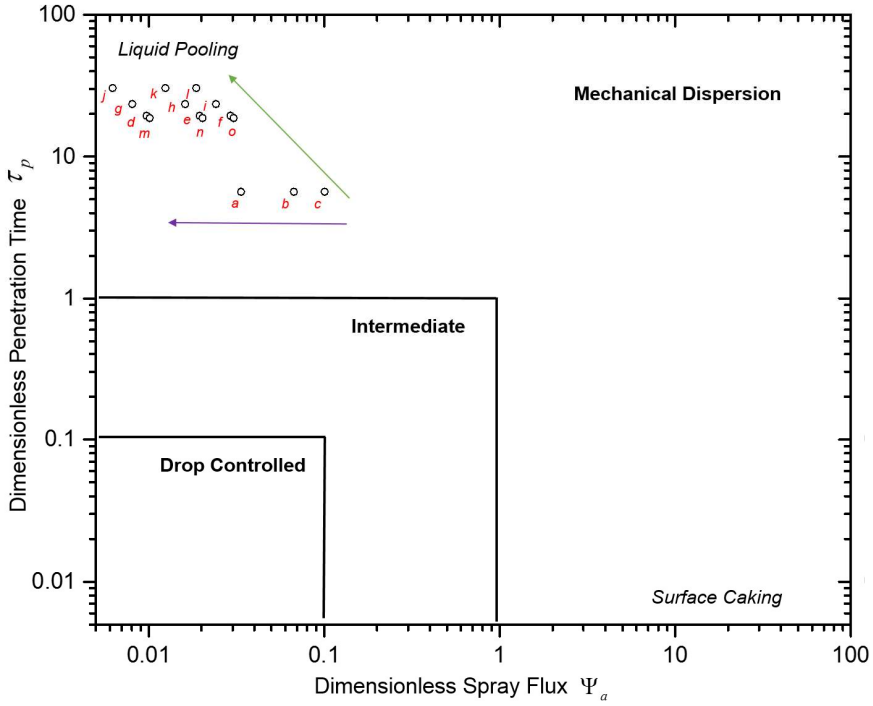

Fig. 2.11. Experimental runs plotted on the nucleation regime map. (adapted from Hapgood et al.).

Hapgood et al. (2003) demonstrated that in batch processes, decreasing spray flux has little influence on the nuclei size distribution at high penetration time due to an increased probability of drop coalescence (Hapgood et al., 2003). In the present work, however, we found that this conclusion could not be extended directly from batch granulators to continuous granulators. For instance, from "c" to "l" (green arrow, constant L/S ratio but decreasing rotation speed) in Fig. 2.11, decreasing Ψ_a had no clear effect on GSD, which remained broad with a large span ranging from 14.6 to 24.4. This is consistent with Hapgood's results. Nevertheless, remarkable decrease in granule size span can be observed if Ψ_a moves from "c" to "a" (purple arrow, constant rotation speed but

decreasing L/S ratio). This phenomenon actually could be ascribed to the change of water content. In a batch granulator the liquid content is determined by the spray rate and the spay time, whereas in a continuous granulator the L/S ratio is determined by the liquid spray rate and the powder flow rate.

Table 2.3 Parameters for the nucleation regime map calculations and flow behavior quantified by the Froude number

Label	Impeller Speed (RPM)	Liquid Flowrate (kg/hr)	Tip Speed(m/s)	Surface Velocity (m/s)	Powder Areaflux (m^2/s)*10^3	Penetration Time(s)	Circulation Time(s)*	Dimensionless Penetration Time	Dimensionless Spray Flux	Froude Number
a	133	1.01	0.61	0.092	1.07	16.94	3.01	5.63	0.034	0.044
b	133	2.02	0.61	0.092	1.07	16.94	3.01	5.63	0.067	0.044
c	133	3.03	0.61	0.092	1.07	16.94	3.01	5.63	0.101	0.044
d	275	1.01	1.27	0.317	3.70	16.94	0.87	19.41	0.010	0.189
e	275	2.02	1.27	0.317	3.70	16.94	0.87	19.41	0.020	0.189
f	275	3.03	1.27	0.317	3.70	16.94	0.87	19.41	0.029	0.189
g	415	1.01	1.91	0.382	4.47	16.94	0.72	23.43	0.008	0.430
h	415	2.02	1.91	0.382	4.47	16.94	0.72	23.43	0.016	0.430
i	415	3.03	1.91	0.382	4.47	16.94	0.72	23.43	0.024	0.430
j	538	1.01	2.48	0.496	5.79	16.94	0.56	30.38	0.006	0.722
k	538	2.02	2.48	0.496	5.79	16.94	0.56	30.38	0.012	0.722
l	538	3.03	2.48	0.496	5.79	16.94	0.56	30.38	0.019	0.722
m	660	1.01	3.04	0.304	3.55	16.94	0.91	18.63	0.010	1.087
n	660	2.02	3.04	0.304	3.55	16.94	0.91	18.63	0.020	1.087
o	660	3.03	3.04	0.304	3.55	16.94	0.91	18.63	0.030	1.087

*The granulator diameter is 8.8 cm giving a cross-sectional circumference of 0.276 m

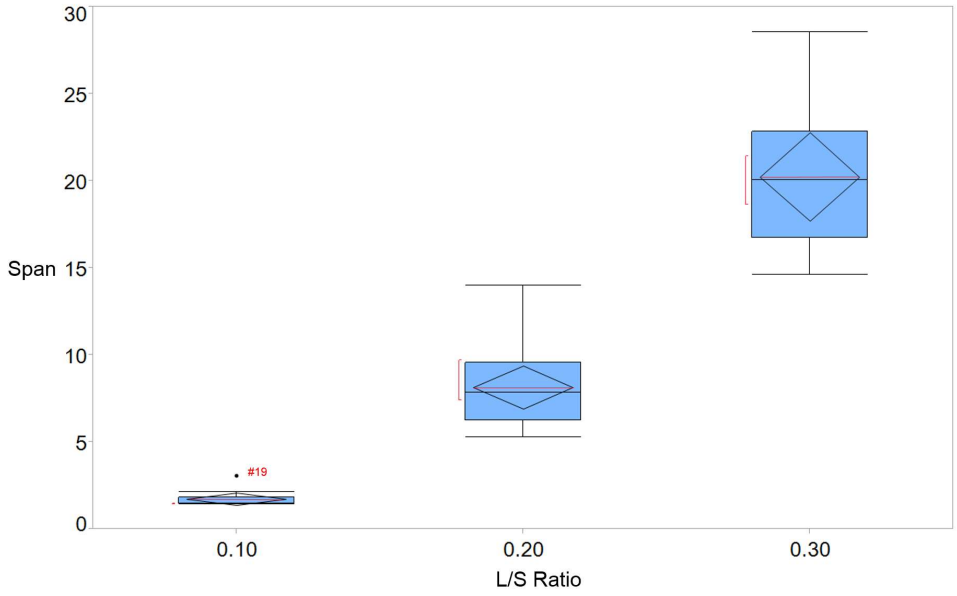

Fig. 2.12. Box plot indicating the increasing span of the GSD with more liquid addition.

As shown in Fig. 2.12, the box plot illustrated the relation between span and L/S ratio. A red line through the 95% confidence diamond represented the mean and a red bracket outside the box identified the shortest half, i.e. the densest 50% of the observations. Batch #19 was beyond the box whiskers and thus viewed as an outlier. Notably the span increased with an increase of L/S ratio. At low L/S ratio, the nucleation process dominated product size distribution and little granule growth was induced. Since the particle bonds were weak in this case, there also existed an increased probability of agglomerates breakage, as a result of intensive collision or shear forces (Abdelhamid et al., 2015). This expectation was confirmed by experimental observations where a reduced proportion of lumps was formed. The increased water content led to more liquid pooling on the powder surface and simultaneously, more saturated granules grew faster, thereby resulting in broader GSD. Schaafsma et al. (2000) proved that larger agglomerates were formed from overlapping of multiple drops in the spray zone (Schaafsma et al., 2000). A multi-peak distribution was observed in which the first peak in the size distribution

consisted of the nuclei formed by a single drop while subsequent peaks correspond to the granules formed from coalesced drops. Eq. 2.6 gives the relation between number of coalesced drops and the agglomerate volume where a peak occurs:

$$V_g = KV_d N_d \tag{2.6}$$

where V_g is the granule volume at a peak; V_d is the droplet volume; N_d is the number of merged droplets to form nuclei; K is the nucleation ratio, a constant for specific formulation, binder fluid and drop size. This linear relationship corroborated that agglomerate size was proportional to the number of coalesced drops or total binder liquid volume. These underlying wetting and nucleation mechanisms explained the bimodal distribution shown in Fig. 2.9 (d).

2.4 Conclusions

This paper explored the design space of a continuous high-shear granulator enhancing process understanding and facilitating the transfer from conventional batch manufacturing processes to more advantageous continuous processes. It was observed the critical granule attribute of size distribution can be controlled by manipulating process variables, with the most desirable median diameter (200-300 μm) obtained at L/S ratio 0.3 and rotation speed either 275 or 660 RPM. Design parameters, in contrast, showed less considerable impact. However, a broad GSDs and ungranulated fines were observed even for the optimum operation conditions.

The existence of large agglomerates was elucidated through fundamental wetting experiments and a subsequent nucleation regime map analysis, indicating the necessity of more effective binder delivery approach. It is recommended that the binder solution be sprayed through an atomization nozzle to reduce the droplet size and decrease the

penetration time. The granulation process is thus expected to migrate to the drop-controlled regime, with a low dimensionless penetration time, subsequently leading to efficient nucleation and a narrower GSD. Mixing tools with sharper blades may also be beneficial. Sharper mixing tools enhance the level of input shear and may prove to be effective in eliminating coarse granules.

Chapter 3

Statistical analysis and comparison of a continuous high-shear granulator with a twin-screw granulator: effect of process parameters on critical granule attributes and granulation mechanisms

3.1 Objectives

In this study, both TSG and a continuous high-shear mixer granulator, Lödige CoriMix® CM5, were comprehensively characterized with paracetamol formulations. The objectives of the present work were: (1) to bridge the knowledge gap between important process parameters and critical granule attributes using QbD methodologies; (2) to investigate the interplay among different granule properties and identify the granulator design space based desirable specifications; (3) to elucidate the discrepancies in granule properties from different granulators and unveil the underlying granulation mechanisms for better process control in the future.

3.2 Material and methods

3.2.1 Materials

The formulation of low-dose drugs was tested on both granulators. It was composed of 8% (w/w) semi-fine acetaminophen (APAP, Mallinckrodt Inc, Raleigh, NC, USA), 44.75% (w/w) α-lactose monohydrate 200M (Foremost Farms USA, Baraboo, WI, USA) and 44.75% (w/w) microcrystalline cellulose (MCC, Avicel® PH101, FMC Biopolymer, Philadelphia, PA, USA). 2.5% (w/w) binder, Polyvinylpyrrolidone (PVP K29-32, Fisher Scientific, Pittsburgh, PA, USA), was added as dry powders in the blend and distilled water was used as granulation liquid. A high-dose formulation comprising 80% (w/w) semi-fine acetaminophen, 8.75% (w/w) α-lactose monohydrate 200M, 8.75% (w/w)

microcrystalline cellulose and 2.5% (w/w) Polyvinylpyrrolidone K29-32 was further tested on the continuous HSG process. The particle size specifications of each formulation component were shown in Table 3.1.

Table 3.1 Specifications and physical properties of input formulation

Component	D10 (μm)	D50 (μm)	D90 (μm)	Bulk Density (g/ml)	Tapped Density (g/ml)	Hausner Ratio
APAP	5.5	29.8	116.4	-	-	-
MCC	19.1	58.7	132.5	-	-	-
Lactose	13.7	78.4	159.5	-	-	-
Low dose premix	14.3	69.8	140.3	0.476	0.629	1.32
High dose premix	9.4	42.6	123.2	0.361	0.586	1.63

3.2.2 Experimental set-up

3.2.2.1 Powder mixing

All the excipient ingredients were firstly premixed in a Glatt tumble tote blender (Model TAM 40, Glatt GmbH, Binzen, Germany) for 30 minutes at 25 RPM, and then transferred into a K-Tron loss-in-weight (LIW) feeder (K-CL-KT 35, K-Tron Soder, Niederlenz, Switzerland). Another K-Tron LIW feeder (K-CL-KT 20) was used for dosing APAP gravimetrically. The drug and excipients were then mixed in a Glatt convective continuous mixer (Model GCG70) under 260 RPM with a total powder feeding rate of 30 kg/h. A Quadro conical screen mill (Comil, Model #197S, Quadro Engineering, Ontario, Canada) was integrated into the experimental set-up upstream of the mixer to de-lump agglomerates from incoming powder stream and enhance the micro-mixing behavior with high shear input. The mill was operated at 1420 rpm and fitted with a 800 μm round-holed screen.

3.2.2.2 Continuous high-shear mixer granulator

The continuous high-shear mixer granulator (Lödige CoriMix® CM5, Gebrüder Lödige Maschinenbau GmbH, Paderborn, Germany) consisted of a horizontal chamber (38 cm in length and 12 cm in diameter) with a rotary shaft, along which different blades were mounted to provide different functionalities: speedup/preblending, granulation, and shaping of granules, as shown in Fig. 3.1 (a) and (b). The high rotation speed (up to 4000 RPM) ensured a large Froude number (above 9) where centrifugal force predominated the bulk flow over gravity, eventually provoking a concentric annular flow in the granulator and retained materials on the vessel wall to form a ring layer (refer to Fig. 3.1 (c)). Instead of spraying, the liquid constituents were pumped (Masterflex LS Peristaltic Pump, Model 7518-12, Cole Parmer, Vermon Hills, IL, USA) tangentially from the top into the ring layer through a single phase nozzle in dripping mode. The profile of annular layer featured an intimate intermixing of liquid and powders inside the granulation unit, and instant formation of granules was enabled by the high differential speed between rotating mixing elements and static chamber wall. Product was moved through the mixing vessel in a plug-like flow, with the residence time distribution (RTD) controlled by processing conditions. The granulator throughput ranges from 10 to 80 kg/h, making it suitable for the practical use in pharmaceutical industry. A K-Tron LIW feeder (K-CL-KT 20) was used to feed both low-dose and high-dose premix.

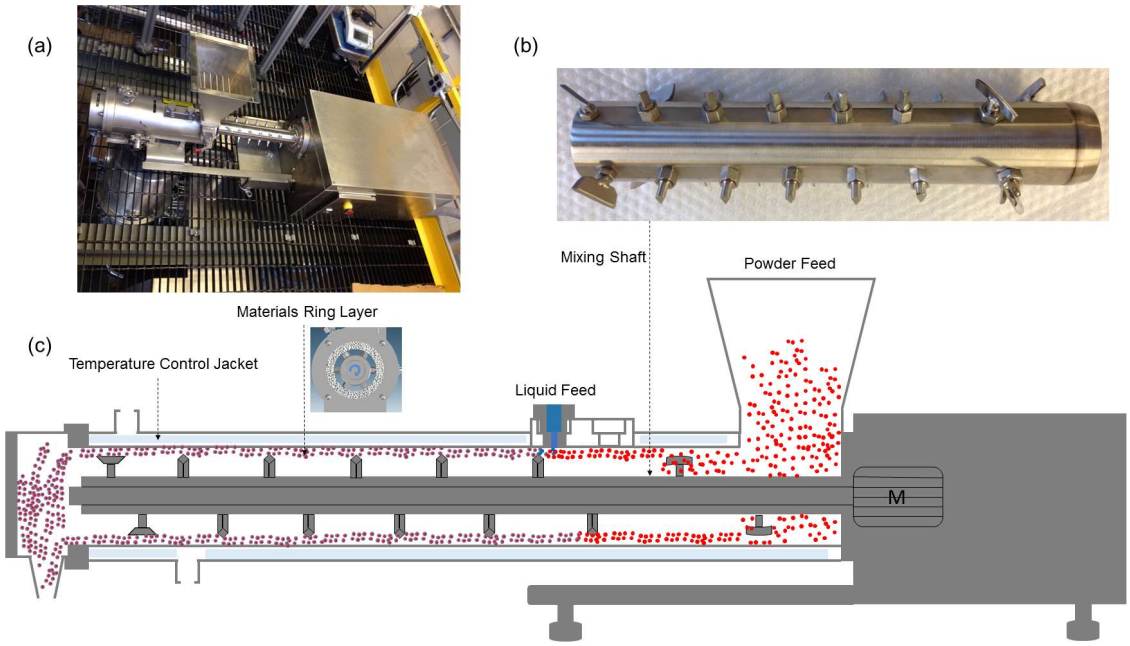

Fig. 3.1. (a) Lödige CoriMix® CM5 continuous high shear mixer granulator; (b) configuration of mixing shaft; (c) schematics of granulator functioning principles.

3.2.2.3 Twin-screw granulator

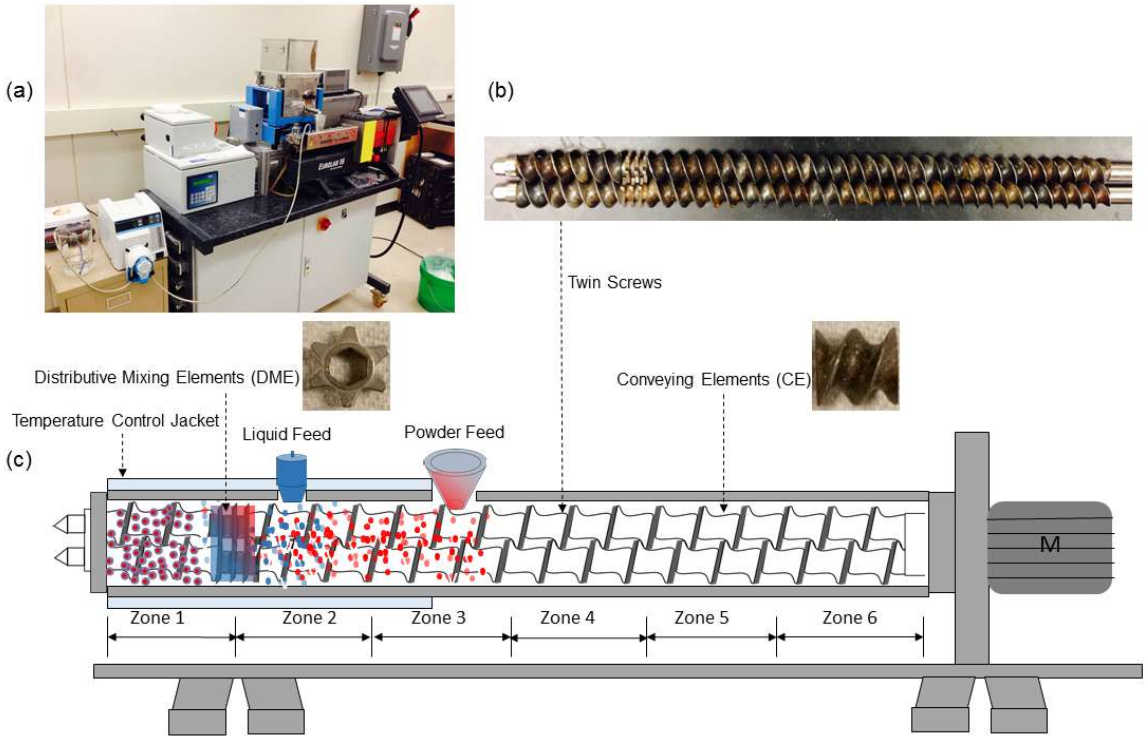

Fig. 3.2. (a) Thermo Scientific™ EuroLab 16mm TSG; (b) configuration of screws; (c) schematics of granulator functioning principles.

The EuroLab 16mm co-rotating intermeshing TSG, 25:1 L/D (Thermo Fisher Scientific, Karlsruhe, Germany) used in the present study (refer to Fig. 3.2 (a)) had a production rate from 1 to 10 kg/h. The screw configuration consisted of 18 pairs of 1-D conveying elements (CE) and 3 pairs of distributive mixing elements (DME), also known as comb mixing elements. A detailed description of the DME can be found in (Sayin et al., 2015b). In general, each element comprises six evenly spaced angularly-cut blades to allow the passage of in-flowing materials, and an annular portion (ring) being perpendicular to the upstream or downstream screw elements. The DMEs acted to distribute and recombine powders and liquid binder in an intermediate shear environment, which are higher than CE but typically lower than kneading blocks (Djuric and Kleinebudde, 2008). The upstream flow can be either facilitated or retarded depending on the orientation of cutting angle (forwarding or reversing), thus applying different compressive forces on the incoming materials. Fig. 3.2 (b) presented that 3 pairs of adjacent DME were arranged in the reverse cutting direction and placed between 3 pairs of CE downstream and 15 pairs of CE upstream, abbreviated as 3CE-3DME-15CE. As depicted in Fig. 3.2 (c), liquid and powder blends were introduced into the granulator through the second and third barrel zones, respectively, and DMEs were positioned immediately after the liquid inlet port. Prior to TSG studies, low-dose formulation components were premixed in the same Glatt continuous blender, but fed by a different gravimetric feeder (Brabender Flexwall® Feeder, Brabender-Technologie, Germany). Temperature of the barrel jacket was maintained at 25 °C throughout the experiments.

3.2.3 Experimental design

In this study, a face-centered cubic design augmented with 3 center points was leveraged to investigate the influence of process variables: rotation speed, liquid to solid (L/S) ratio and throughput, on critical granules attributes. Table 3.2 specified the levels of each variable involved in the Design of Experiments (DoE). Those in parentheses indicated the operation conditions at center points. A total of 17 randomized experiments (see Table 3.3) were generated and analyzed by JMP® statistical software (SAS Institute Inc., Cary, NC, USA).

Table 3.2 Variable levels in DoE

Input variables	Lödige CM5						TSG		
	Low dose			High dose			Low dose		
Rotation Speed (RPM)	1000	(2000)	3000	1500	(2250)	3000	200	(500)	800
Throughput (kg/h)	10	(15)	20	8	(12)	16	4	(6)	8
L/S Ratio	0.35	(0.45)	0.55	0.1	(0.2)	0.3	0.36	(0.51)	0.66

Table 3.3 The 17-run face-centered cubic design

Run #	Lödige CM5								TSG			
	Low dose				High dose				Low dose			
	Pattern	Rotation speed (RPM)	Through put (kg/h)	L/S Ratio	Pattern	Rotation speed (RPM)	Through put (kg/h)	L/S Ratio	Pattern	Rotation speed (RPM)	Through put (kg/h)	L/S ratio
1	000	2000	15	0.45	000	2250	12	0.2	000	500	6	0.51
2	00A	2000	15	0.55	+−−	3000	8	0.1	00A	500	8	0.51
3	0a0	2000	10	0.45	−−+	1500	8	0.3	−−−	200	4	0.36
4	0A0	2000	20	0.45	++−	3000	16	0.1	A00	800	6	0.51
5	000	2000	15	0.45	+++	3000	16	0.3	++−	800	4	0.66
6	a00	1000	15	0.45	A00	3000	12	0.2	0a0	500	6	0.36
7	000	2000	15	0.45	0A0	2250	16	0.2	000	500	6	0.51
8	++−	3000	20	0.35	000	2250	12	0.2	+−+	800	8	0.36
9	−−−	1000	10	0.35	−++	1500	16	0.3	a00	200	6	0.51
10	+−+	3000	10	0.55	a00	1500	12	0.2	0A0	500	6	0.66
11	−−+	1000	10	0.55	00A	2250	12	0.3	−−+	200	8	0.36
12	+−−	3000	10	0.35	−−−	1500	8	0.1	−++	200	8	0.66
13	−+−	1000	20	0.35	000	2250	12	0.2	−+−	200	4	0.66
14	00a	2000	15	0.35	00a	2250	12	0.1	00a	500	4	0.51
15	−++	1000	20	0.55	0a0	2250	8	0.2	+++	800	8	0.66
16	A00	3000	15	0.45	+−+	3000	8	0.3	+−−	800	4	0.36
17	+++	3000	20	0.55	−+−	1500	16	0.1	000	500	6	0.51

3.2.4 Granule characterization

Granules collected after each experiment were immediately spread out in thin layers on an aluminum tray and air-dried at ambient conditions until the moisture content was less than 3%, as determined by loss-on-drying in a moisture analyzer (MJ33, Mettler Toledo™, Greifensee, Switzerland). The dried samples were then split using a spinning riffler (Gilson Company, Inc., Lewis Center, OH, USA) to ensure unbiased sampling for different granule characterizations. With respect to the Lödige high-dose granules, only the GSD and porosity were characterized.

3.2.4.1 Granule size distribution

The size distribution of granules was measured by sieve analysis using the following sieves: 38, 63, 90, 125, 250, 355, 500, 710, 850, 1000, 1400, 2000, 2380, 4000 μm. The

particle size of un-granulated powder blends listed in Table 1 was measured by laser diffraction size analyzer (Beckman-Coulter LS 13 320 Series Tornado Dry Powder System, Pasadena, CA, USA). All granule size distributions were plotted as the normalized mass frequency shown in Eq. 3.1 versus the midpoint of each size interval on logarithmic scale (Allen, 2003),

$$f_{mi}(\ln x) = \frac{y_i}{\ln(\overline{x_i} / \overline{x_{i-1}})} \tag{3.1}$$

where y_i is the mass fraction in size interval i and $\overline{x_i}$ is the midpoint of size interval i.

3.2.4.2 Porosity, internal structure and strength

The true density of granules was first measured by a helium pycnometer (AccuPyc II 1340, Micromeritics, Norcross, GA, USA), followed by the envelope density tests using Geopyc 1360 (Micromeritics, Norcross, GA, USA) where a dry solid medium (DryFlow®) comprising small and rigid spheres with high flowability displaced the void space and closely enveloped the particle surface. Granules with a size classification 1.0-1.4 mm were placed in a desiccator overnight prior to any densities measurements. The granule porosity (ε_g) was then calculated by the equation as follows,

$$\varepsilon_g = 1 - \frac{\rho_e}{\rho_t} \tag{3.2}$$

where ρ_e and ρ_t are the envelope and true density of granules, respectively.

Visualization of the granules internal structure was performed by Bruker microCT (SkyScan 1172, Billerica, MA, USA). X-ray tomographic images were reconstructed to display the granules cross-sectional porous structure, and a three-dimensional (3D) digital representation of individual granule was created to visually inspect the closed and open pores. Shadow images with the pixel size of 4.89 μm were acquired with an optimized X-

ray source at 40 kV (250μA) and scanned in the 0-180° interval using a 0.40° rotation step.

The strength of granules between 250 to 710 μm was estimated by a uniaxial confined compression test in Gamlen tablet press GTP-1 (Gamlen Tableting Limited, Nottingham, Nottinghamshire, UK). 100 mg of dry granules were compressed at a low strain rate of 5 mm/min with the 6 mm diameter die and punch set to a maximum load limit of 250 kg. The fracture strength was then calculated using the following equation (Adams et al., 1994),

$$\ln P = \ln(\frac{\tau}{\alpha}) + \alpha\varepsilon_n + \ln(1 - e^{-\alpha\varepsilon_n}) \tag{3.3}$$

where P is the applied pressure, τ is average agglomerate fracture strength, α is a constant related to Mohr-Coulomb failure criterion and ε_n is the natural strain. τ and α were obtained by fitting Eq. 3.3 to plot natural logarithms of the applied pressure versus natural strain.

3.2.4.3 Bulk and tapped densities

The bulk densities of granules and premixed formulation blends were measured by FT4 powder rheometer (Freeman Technology, Tewkesbury, Gloucestershire, UK). After conditioning the powder bed, bulk density was determined by splitting a 25 mm/10 ml vessel and then recording its weight and volume. Tapped density was measured via an automated tapped density analyzer (Quantachrome Instruments, Boynton Beach, FL, USA) associated with a 250 ml graduated cylinder (readable to 2 ml). Consecutive 10, 500 and 1250 taps were carried out on the same pre-weighted samples and the corresponding volumes V_{10}, V_{500} and V_{1250} were recorded. If the volume difference between V_{500} and V_{1250} is less than or equal to 2 ml, V_{1250} was recorded as the final

volume and then divided by samples weight to obtain the tapped density. If not, repeats with an increment of 1250 taps were performed until the maximum settled density was achieved. The Hausner ratio (HR), a descriptor of the flowability of granular materials, was calculated by the following equation,

$$\mathrm{HR} = \frac{\rho_T}{\rho_B} \tag{3.4}$$

where ρ_B is the bulk density; ρ_T is the tapped density. In general, a Hausner ratio larger than 1.25 is deemed to be an indication of poor flowability.

3.2.4.4 Liquid distribution and RTD

To examine the liquid distribution, a water-soluble nigrosin stain (Sigma Aldrich Corp., St. Louis, MO) was dissolved in distilled water at the concentration of 1 g/L before granulation experiments. After sieving the colored granules, 450 mg sub-sample of granules across different size fractions were weighted and mixed with 10 ml distilled water. The suspension was then sonicated for 2 h to ensure dyes were completely released from granules and the absorbance of extracted supernatant was measured by UV/Vis spectroscopy (Cary 60 UV-Vis Spectrophotometer, Agilent Technologies, Santa Clara, CA, USA) at the wavelength of 578 nm. Dye concentration at each size class was determined on the basis of a pre-developed calibration model (R^2 = 0.9967) in the range from 0.000625 to 0.16 g/L. The hypothesis underlying this approach is that dye distribution is in conformity with liquid distribution. Similar methods have also been reported by Smirani-Khayati et al. (Smirani-Khayati et al., 2009) and EI Hagrasy et al. (El Hagrasy and Litster, 2013).

RTD tests were conducted with the same nigrosin stain as a pulse of tracer (40 mg), which was directly injected into the feedstream at $t = 0$. Granule samples were collected every 3 s up to 90 s and then dissolved in 10 ml distilled water. Same UV/Vis spectroscopic method was performed as the liquid distribution to quantify the dye concentration in samples at different time points. The RTD function, $E(t)$, is calculated as

$$E(t) = \frac{c(t)}{\int_0^\infty c(t)dt} \tag{3.5}$$

where $c(t)\,\mathrm{dt}$ is the dye concentration (g/L) between time t and Δt. The mean residence time τ and variance σ^2 was obtained by the first and second moment of RTD function, respectively:

$$\tau = \int_0^\infty tE(t)dt \tag{3.6}$$

$$\sigma^2 = \int_0^\infty (t-\tau)^2 E(t)dt \tag{3.7}$$

Due to different granulator sizes in this study, a normalized RTD function, $E(\Theta)$, is plotted as a function of dimensionless time Θ to directly compare their flow performance, where

$$\Theta = \frac{t}{\tau} \tag{3.8}$$

$$E(\Theta) = \tau E(t) \tag{3.9}$$

The dimensionless variance σ_Θ^2 was used to characterize the spread of the RTD curves:

$$\sigma_\Theta^2 = \frac{\sigma^2}{\tau^2} \tag{3.10}$$

In addition, degree of axial mixing in each granulator was quantified by the Péclet number (Pe_r), representing the ratio of transport by convection and transport by dispersion or diffusion:

$$Pe_r = \frac{Ul}{D_a} \tag{3.11}$$

where D_a is the diffusion coefficient; U is the superficial velocity and l is the granulator length. Regarding the cases studied here, tracer was introduced into the granulator from its inlet port and collected from the outlet. Therefore, closed-closed vessel boundary condition was applied to solve for Pe_r, indicating no dispersion or radial variation in concentration to the immediate left of entrance (upstream) and to the immediate right of exit (downstream). Pe_r was calculated by the following numerical solution:

$$\frac{\sigma^2}{\tau^2} = \frac{2}{Pe_r} - \frac{2}{Pe_r^2}(1 - e^{-Pe_r}) \tag{3.12}$$

3.2.4.5 Granule morphology

Particle shape of dried granules was quantified by the aspect ratio (AR) through Eyecon^{TM} 3D high speed imaging camera (Innopharma Laboratories, Dublin, Ireland) in the benchtop characterization mode. A charge-coupled device (CCD) camera was encircled by RGB (Red, Green, Blue) light-emitting diode (LED) illumination arranged according to the principle of photometric stereo, which allowed 3D surface mapping of the granules after data integration. Topological information of particles was derived based on the color distribution, enabling the detection of particle edges, especially those overlapped granules. The size of fully identified particle was estimated from 3D-projected image where an iterative optimization was employed to determine the

equivalent diameter of the best fitting ellipse (El Hagrasy et al., 2013a). AR values were then calculated by the ratio of maximum and minimum diameter.

Granule morphology was observed under the SIGMA Series of Field Emission Scanning Electron Microscopes (FE-SEM, Carl Zeiss Microscopy, Jena, Germany) operating at an accelerating voltage of 5 kV and high vacuum mode. Samples were stored in a vacuum desiccator overnight and then sputter-coated with 5 nm gold layer prior to tests.

3.3 Results and discussion

3.3.1 Granule size distribution

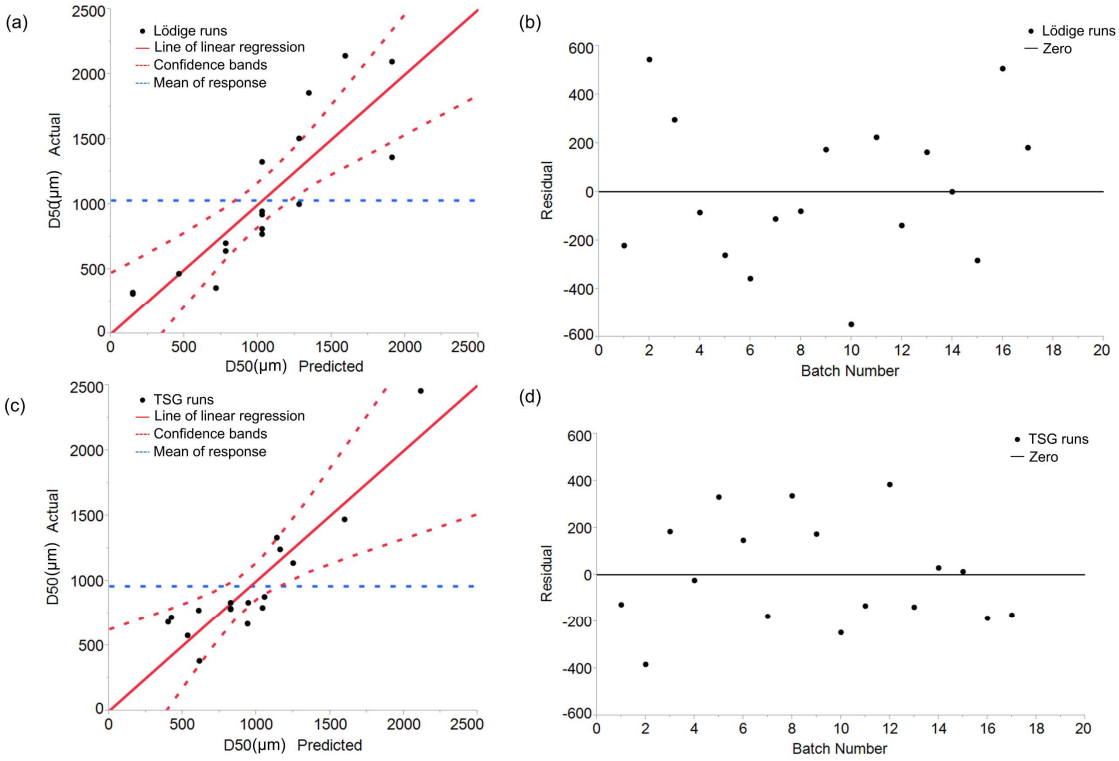

Fig. 3.3. Actual by predicted D_{50} plot of (a) Lödige and (c) TSG low-dose granules. Residuals in time sequence of low-dose (b) Lödige and (d) TSG experiments.

The initial multi-factor analysis of variance (ANOVA) model included main effects, interaction effects and quadratic effects for the low-dose D_{50} from both Lödige granulator and TSG. The results, however, revealed that only main effects were statistically significant ($p < 0.05$), namely L/S ratio ($p = 0.0033$) and rotation speed ($p = 0.0454$) for Lödige and L/S ratio ($p = 0.0023$) and throughput ($p = 0.0493$) for TSG. Therefore, reduced regression models with exclusion of several nonsignificant terms were developed to generate D_{50} surface plots. Fig. 3.3 (a) and (c) illustrated the goodness of model fit for Lödige (R^2_{adj} = 0.7062) and TSG (R^2_{adj} = 0.7250) while (b) and (d) showed the model adequacy checking by examination of residuals versus time sequence. The structureless residuals contained no outliers and random scattered patterns around zero implied that underlying assumption of independent errors were validated. Other graphical analysis such as normal probability and residuals versus predicted values also did not discover any abnormalities (not shown).

Fig. 3.4 presented low-dose D_{50} response surface with the corresponding significant main effects of each granulator. In the case of continuous HSG (Fig. 3.4 (a)), increasing L/S ratio and rotation speed could effectively facilitate the granule growth, associated with median diameter increasing from 311.28 to 2141.94 μm throughout the DoE. Granule growth in TSG (Fig. 3.4(b)), by contrast, followed a similar trend by increasing the throughput along with L/S ratio. In particular, influence of throughput on D_{50} was more pronounced at higher L/S ratio and became less detectable when liquid content was below 0.35, though the interaction effect of these two terms was not statistically significant. D_{50} of granule samples in the TSG DoE ranged from 381.04 to 2453.07 μm. As shown in Fig. 3.5, size distribution of raw blends was compared to the selected

granules from each granulator using one-factor-at-a-time approach. The two significant main effects of each granulator were varied individually and successively over its scope with all other operation parameters held constant at the midpoints. It was apparent that Lödige granules from higher rotation speed and liquid content displayed a more monomodal size distribution in contrast to those produced by TSG where broader multimodal distributions were observed. One intriguing phenomenon is that as the incremental agglomeration of fines took place, the mode of Lödige distributions underwent evident left-to-right shifts as opposed to the TSG up-to-down mode shifts in which the height of first peak diminished gradually accompanied by the enhancement of subsequent two peaks. These distinct trends can be mainly attributed to the different functioning principles during granulation processes.

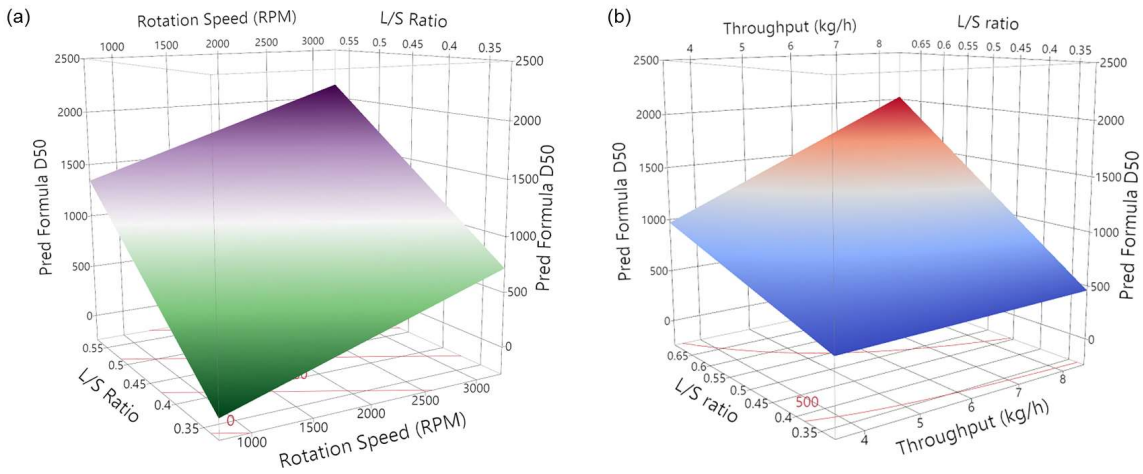

Fig. 3.4. Low-dose granules D_{50} response surface of (a) Lödige and (b) TSG.

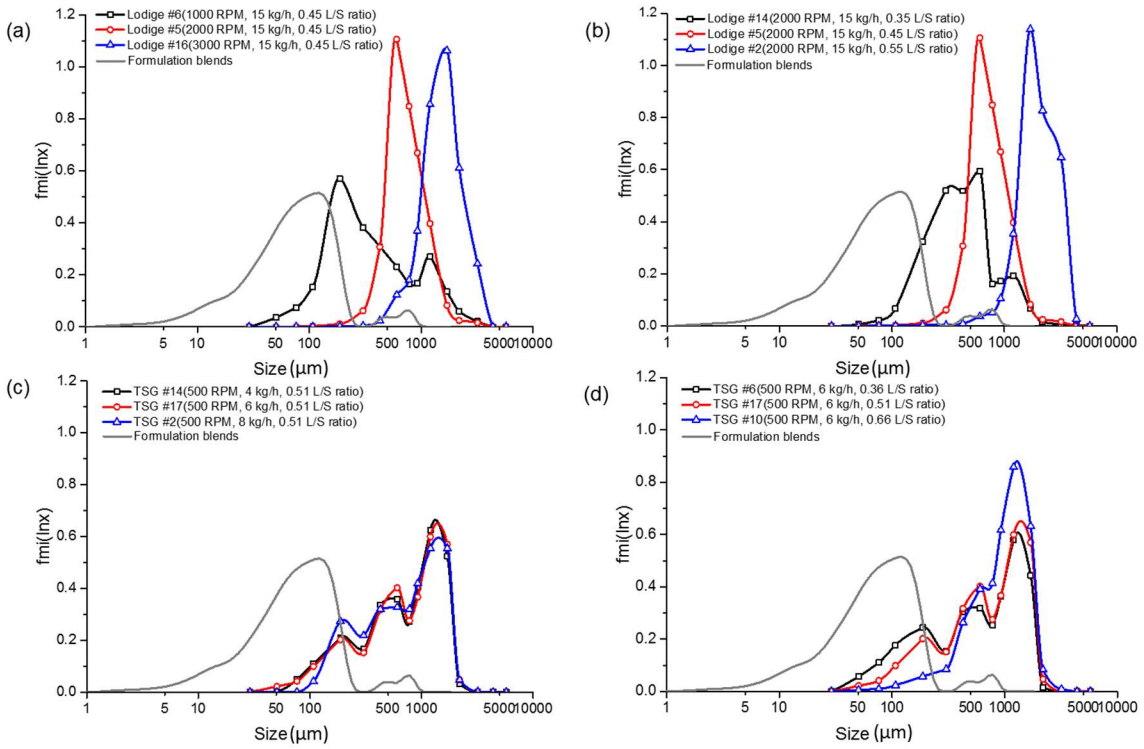

Fig. 3.5. Size distribution of low-dose formulation blends and granules from selected runs of Lödige with varying (a) rotation speed and (b) L/S ratio, selected runs of TSG with varying (c) throughput and (d) L/S ratio.

In the present study, water content was shown to be an influential factor for both granulation processes, with substantial amount of fines obtained when L/S ratio decreased to a certain level. It is well known that water amount can alter degree of liquid saturation and further determine granule coalescence. For sub-saturated and deformable granules, the degree of liquid saturation was high and more free liquid could be easily squeezed to granule surfaces or contact zones during a fast consolidating process, thereby reducing the induction period and promoting steady growth. When L/S ratio was very low, particles may remain as dry powders or just form nuclei on account of van de Waals interactions, and little granule coalescence can be induced. From examination of Fig. 3.5

(c) and (d), it was seen that only the GSD at the highest L/S ratio (0.66) approximated to a monomodal distribution.

Increasing the rotation speed of Lödige granulator from 1000 to 3000 RPM consistently enhanced the granule coalescence, largely due to the more frequent inter-particle collisions at higher agitation intensity. Granules, as a result, tended to be densified or consolidated, leading to increased maximum pore saturation with more available liquid present on the contact area during deformation. In addition, low viscosity of distilled water and relatively hydrophilic formulation enabled that once injected, droplets could promptly penetrate into the ring layer by capillary action and then homogeneously redistributed via mechanical mixing. It could be inferred that the ensuing intimate liquid-powder mixing owing to intensive shear force thus minimized the localized over-wetting and formation of large undesirable lumps, as aptly illustrated by the narrower distribution of run #5 (2000 RPM) compared to #6 (1000 RPM) in Fig. 3.5 (a). The granulation rate processes in the DME section of TSG were believed to be the breakage of granulated materials followed by layering of surrounding dry fines (Sayin et al., 2015b). Hence the chopping and shearing motions of DMEs breaking apart large agglomerates into smaller fragments should account for the multimodal distributions in Fig. 3.5 (c) and (d). Besides, the water absorption of 44.75% MCC in the formulation necessitated fairly high water level to ensure sufficient liquid saturation, rendering it more challenging to uniformly redistribute the liquid with limited wet massing time and relatively low shear input compared with Lödige.

Finally, throughput range in the Lödige low-dose DoE (10-20 kg/h) was close to the lowest threshold of granulator operational range (10-80 kg/h), so it was possible that the

materials hold up inside the granulator was not significantly altered. However, throughput in the TSG (4-8 kg/h) spanned almost the entire permissible operation range (1-10 kg/h). The materials fill level in this case was considerably changed during different operation conditions.

For Lödige high-dose granules, L/S ratio was the only significant variable positively influencing granule size and size distribution (not shown). Most GSD curves showed relatively monomodal distribution but broader with more fines observed. This is believed that water as a low viscosity binder induced lower strength of interparticle bonds and hence wet binder addition method is expected to generate stronger granules. The median diameter of granules ranged from 98.4 (run #14) to 1479.9 μm (run #9) with close values obtained at the same L/S ratios. The D_{50} first slightly decreased and then increased along with the increasing impeller speed from 1500 to 3000 RPM, inferring the transition from granules breakage to permanent coalescence as collision frequency and impact energy changes.

3.3.2 Porosity and internal structure

The ANOVA results of porosity indicated that both main effects, L/S ratio ($p = 0.0134$) and rotation speed ($p = 0.0006$), and quadratic effect, rotation speed*rotation speed ($p = 0.0317$), were significantly impacting on the continuous HSG process whilst in regard to TSG the interaction effect of L/S ratio*rotation speed ($p = 0.0181$) obscured the main effects and became the only significant term. The reduced regression model for Lödige showed good fitting and predictive ability: R^2_{adj} = 0.8228, and the residuals were normally distributed without any potential outliers. A large proportion of observed

variance nevertheless remained unexplained by the TSG model: $R^2_{adj} = 0.4728$ in that only subtle nuance of porosity could be detected among the majority of TSG runs.

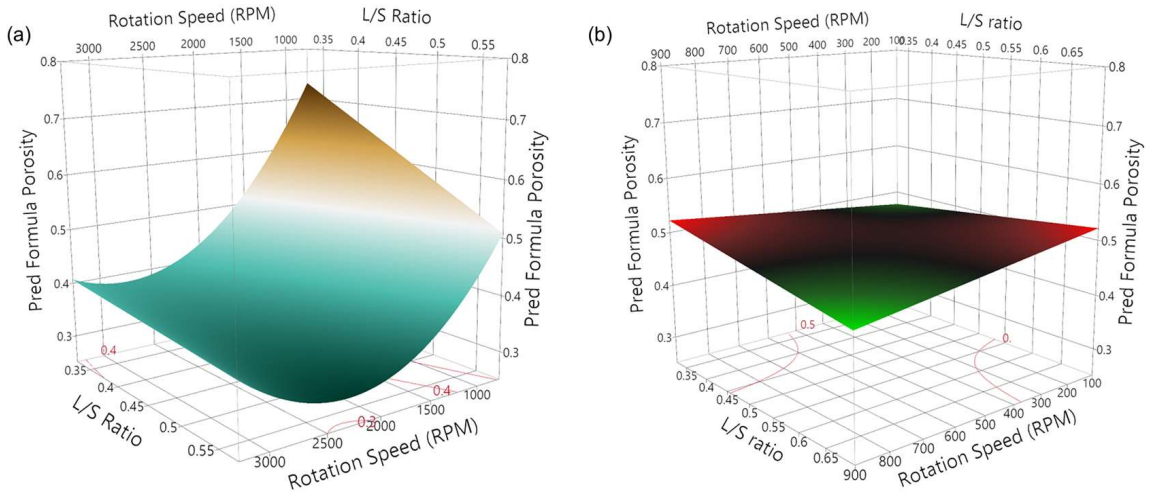

Fig. 3.6. Low-dose granules porosity response surface of (a) Lödige and (b) TSG.

The quadratic curvature effect caused by impeller speed appeared as in Fig. 3.6 (a), illustrating the operation condition generating a minimum response, i.e. the most densified granules, in Lödige granulator. The most porous granules could be obtained with the lowest rotation speed and L/S ratio. When rotation speed was high, its implication on porosity predominated over that of L/S ratio. In contrast, at low rotation speed, granule porosity was more susceptible to and adversely correlated to the increase of liquid content. In this scenario, low-viscosity liquid binder (water) reduced inter-particle frictions due to lubrication and thus aid consolidation (Iveson and Litster, 1998a). The decreased dynamic strength and enhanced deformability thereof also increased the extent of compaction. Granules experiencing more densification inside the granulator with increasing rotation speed were ended up with smaller porosity, in which case higher impact frequency and energy during inter-particle collisions and granule consolidation

with vessel wall had played a pivotal role. The mixing pins also exerted shear and compressive forces on the wetted powder mass to reduce granules voids.

Fig. 3.6 (b) showed that the significant interaction effect twisted the plane slightly and created a saddle point. The granule voidage was quite robust to the variation of L/S ratio and rotation speed at different levels, and their influence were hardly discernable in TSG. According to the findings by Iveson et al. (Iveson and Litster, 1998a), granules could either dilate or compact during impacts, depending on the competition among three forces: inter-particle friction, capillary and viscous. It can be postulated that high water levels in the TSG DoE made granules close to saturation, rendering capillary force less changeable, and approximate to the minimum porosity with a dynamic balance between the rest of two forces. Particularly, the trend with L/S ratio at low rotation speed contradicted the results of EI Hagrasy et al. (El Hagrasy et al., 2013c) and Sayin et al. (Sayin et al., 2015b) who found considerable decrease in porosity with increasing L/S ratio. Presumably this was a feature specific to the formulation and screw configuration in the present study and is worthy of further investigation. Besides, as reported by other researchers (Dhenge et al., 2011), powder feed rate altered the degrees of barrel filling and torque, which affected the extent of materials compaction and intragranular porosity, yet this effect was also not captured here. In this comparison work, porosity values from Lödige and TSG were in the range of 0.295 to 0.619 and 0.461 to 0.536, respectively, which were much higher than expected from a typical batch HSG process. The more porous granules obtained from these continuous granulators can be largely ascribed to the short residence time or wet massing time, which in turn limited the extent of consolidation.

The X-ray tomographic images in Fig. 3.7 manifested the change in voids inside the granules produced from two extremes of operation conditions of each granulator. The black color in Fig. 3.7 (a-d) embodied air or void and the white represented granulated powder mass. It was obvious that difference in granules internal structure by TSG was much less perceptible as opposed to that in Lödige granulator. The more granules were consolidated; the more entrapped air/liquid were squeezed out with more generated closed pores (refer to Fig. 3.7 (a1-d1)).

Granule strength and internal structure are typically interrelated. Similar to the porosity, L/S ratio and agitation intensity significantly influenced the strength of Lödige low-dose granules with the most fragile granules produced at the lowest water content and rotation speed. Fig. 3.8 (a) showed a strong linear inverse correlation between granule fracture strength and porosity (R^2 = 0.82). As porosity increased from 0.342 to 0.601, granule strength decreased from 12.72 to 1.28 MPa. For TSG granules, however, a poor linear correlation was identified (R^2 = 0.08) in Fig. 3.8 (b). Since granule strength was measured on a powder bed rather than the crushing strength of individual granules, the irregular particle shape in this case may interfere during the compaction tests and obscure the relationship with porosity. Furthermore, L/S ratio showed a significant positive effect on granule strength with decreasing values from 8.84 to 2.92 MPa when moisture content reduced from 0.66 to 0.36 (not shown). When comparing the Lödige and TSG strength results, a similarity can still be revealed as the comparison of porosity results, namely that strength of Lödige granules showed a wider range covering the values obtained from TSG.

The porosity of Lödige high-dose granules, as expected, decreased from 0.658 (run #14) to 0.334 (run #16) with increasing L/S ratio from 0.1 to 0.3 and rotation speed from 1500 to 3000 RPM (not shown). In contrast to Lödige low-dose granules, the influence of L/S ratio outweighed rotation speed and became the only significant parameter.

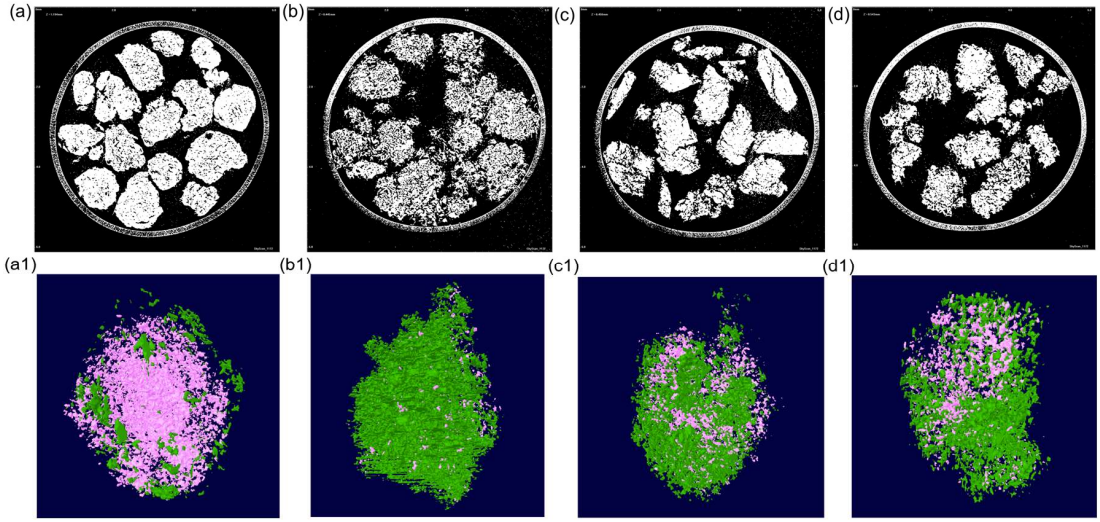

Fig. 3.7. X-ray tomographic images of low-dose granules from Lödige run #1 (a, porosity = 0.342) and #6 (b, porosity = 0.601); TSG run #3 (c, porosity = 0.461) and #16 (d, porosity = 0.536). 3D visualization of closed (pink) and open (green) pores distribution of individual granule from corresponding above runs (a1-d1).

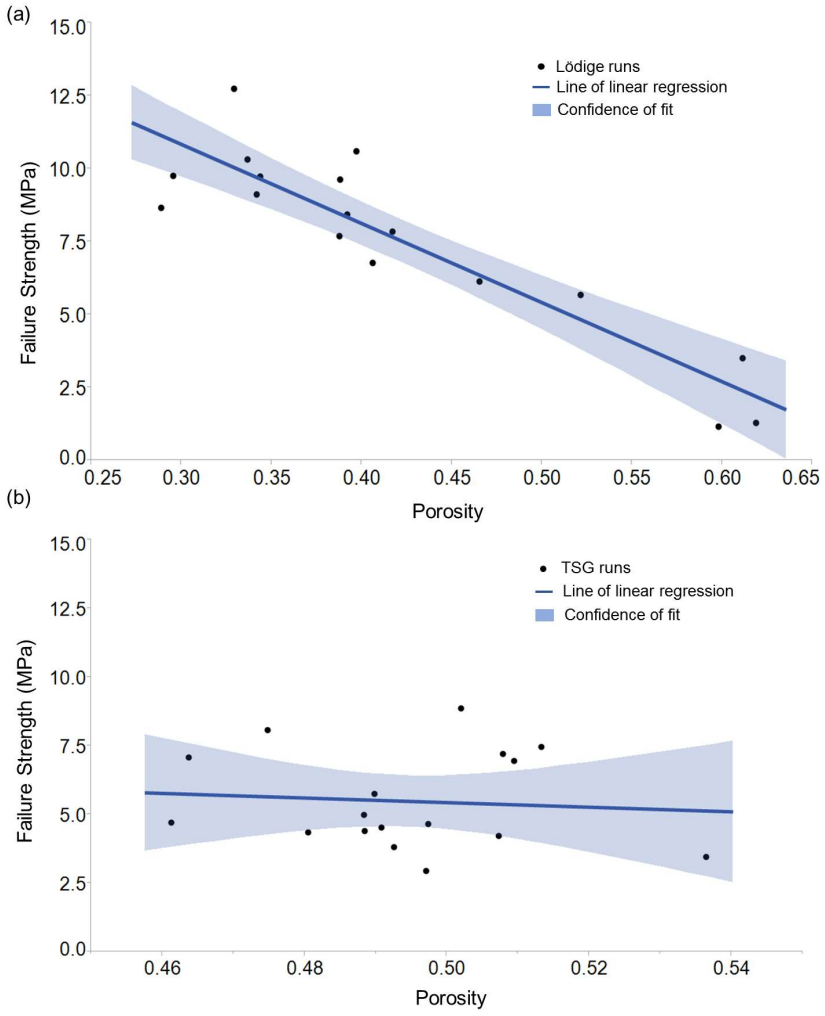

Fig. 3.8. Relationship between low-dose granule porosity and failure strength: (a) Lödige and (b) TSG.

3.3.3 Bulk and tapped densities

Fig. 3.9 showed the variation of material densities and flowability along the observation (time) sequence. Properties of formulation blends were also listed as a control group. The bulk and tapped densities exhibited limited degree of increase after both granulation processes or, conversely, some runs even had decreased densities because of their extremely high granule voidage, as illustrated by batch L6, L9 and L13 corresponding to the porosity of 0.601, 0.598 and 0.619, respectively. On the contrary,

Hausner ratio of all the experimental runs were smaller than that of raw blends, indicating ameliorated powder flow properties. By examining Fig. 3.9, it could also be found that analogous to porosity, the densities and flowability of TSG granules were again less sensitive to the alteration of process parameters. Furthermore, the majority of Lödige granules evidenced superior flow properties and efficiency of particle packing, i.e., smaller Hausner ratio, when compared with TSG granules, despite that almost all the Hausner ratios were below the fair flow level 1.25.

Bulk and tapped densities are strong functions of particle size, shape and porosity, which further determines bulk solid storage and handling requirements. As discussed in the following section, granules produced in continuous HSG process were more spherical, leading to excellent flowability. The irregularly shaped particles from TSG increased the interparticulate frictions, surface contact and interlocked with each other eventually retarding powder flow. Also, GSD of Lödige granules was narrower and contained less fine particles. Minimum air in this case was entrapped in the bulk and powder bed was thus less compressible with volume change more resistant to the normal stress. Given larger proportions of fines in the TSG powder bed, the number of particle contact points in a certain volume increased substantially. Those contact points could be associated with cohesive forces and adversely influence the degree of powder flowability.

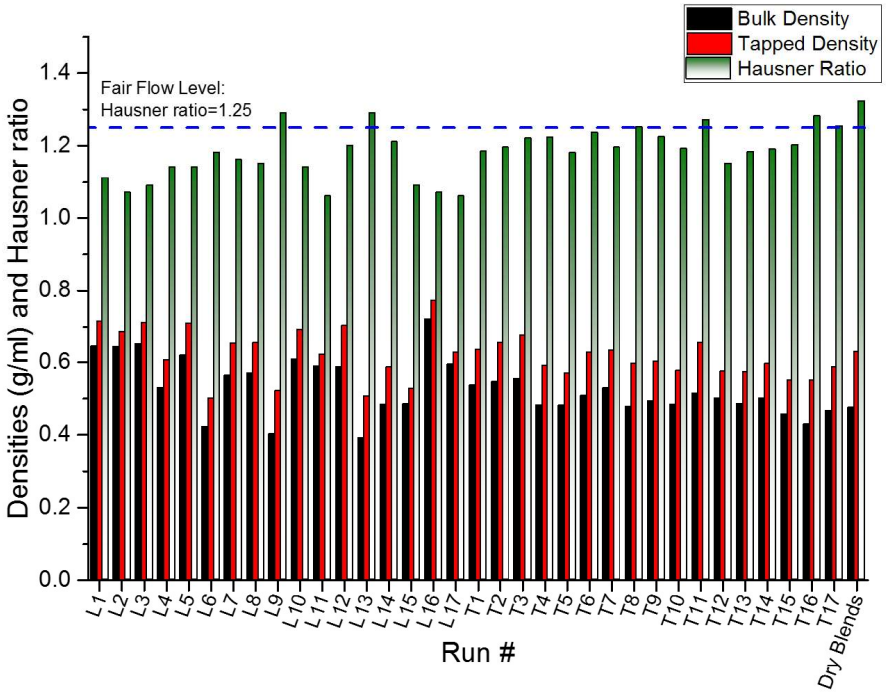

Fig. 3.9. Densities and flowability of Lödige low-dose run #1-17 (L1-L17) and TSG run #1-17 (T1-T17) granules exhibited in observation sequence.

3.3.4 Liquid distribution and RTD

Table 3.4 Characteristics of the Lödige and TSG RTD

Granulator	Run #	τ (s)	σ_Θ^2	Pe_r
Lödige	12	11.07	0.37	4.08
	14	9.74	0.21	8.75
TSG	3	7.46	0.058	33.43
	14	3.88	0.44	3.16

The liquid distribution quantified by the amount of nigrosine dye across different low-dose granule size fractions was leveraged to reveal the performance of solid-liquid mixing. Fig. 3.10 presented the characterization results of two batches yielding the D_{50} relatively closer to 500 μm for each granulator. In contrast to the marginal dependence on granule size shown by L12 and L14, the dye concentration of T3 and T14 maintained an incremental change with increasing granule size. Since a horizontal line implies

perfectly homogeneous liquid distribution, the selected operation conditions of TSG were deemed to demonstrate slightly inferior efficiency of liquid-powder mixing. Virtually T14 displayed considerable improvement when compared to T3 in light of the more dramatic increase in the latter, albeit less concentrated dyes in smaller particles for both cases. The implications of liquid distribution uniformity on granulation performance were reflected by the broadness of GSD, i.e., the spans of L12 and L14 (1.25 and 1.69) were smaller than that of T3 and T14 (3.25 and 2.39).

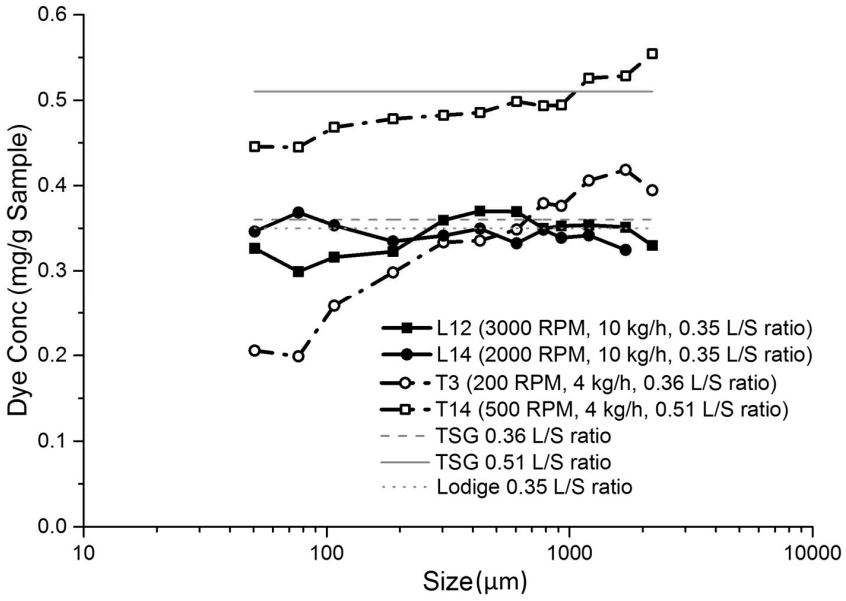

Fig. 3.10. Liquid distribution in granule size fractions of Lödige low-dose run #12 (L12, D_{50} = 641.34 μm) and #14 (L14, D_{50} = 463.38 μm); TSG run #3 (T3, D_{50} = 573.53 μm) and #14 (T14, D_{50} = 771.25 μm).

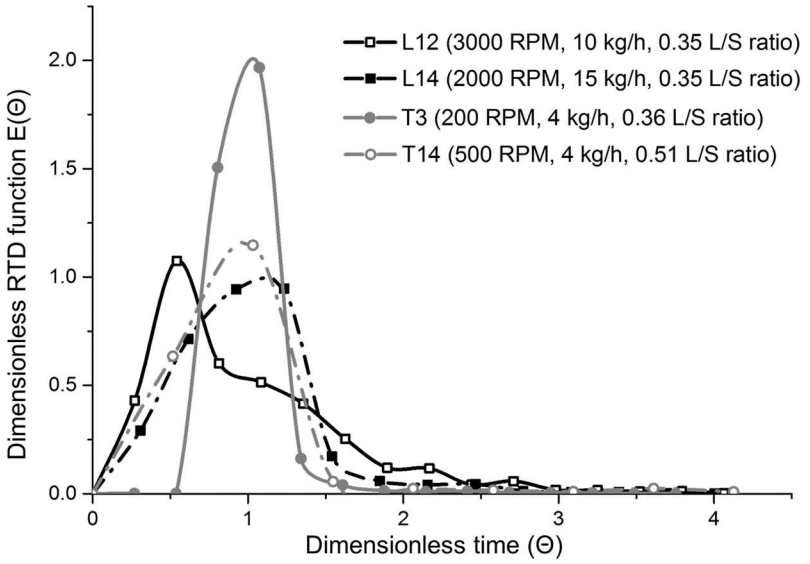

Fig. 3.11. Normalized RTD plot of Lödige low-dose run #12 (L12) and #14 (L14); TSG run #3 (T3) and #14 (T14).

Previous studies (El Hagrasy et al., 2013c; Kumar et al., 2015; Sayin et al., 2015b) reported that the mean residence time in TSG was typically between 2 to 40 s dictated by the functional role of screw configuration and process parameters. This is much shorter than the granulation time available in a batch high shear granulator, which is in the order of minutes. Hence RTD studies were carried out on low-dose formulation to gain more insights into the axial mixing characteristics in these two granulators and further link the findings with aforementioned liquid distribution outcomes. The normalized RTD curves illustrated in Fig. 3.11 corresponded to the same runs as those in Fig. 3.10 and were characterized by three quantified factors: MRT (τ), normalized variance (σ_θ^2) and Péclet number (Pe_r). As summarized in Table 3.4, the granulation time in Lödige granulator was around 10 s while that in TSG was even shorter. Specifically, τ increased slightly from L14 to L12 with elevated impeller speed but less materials feeding rate. Conversely, increasing the rotation speed and L/S ratio in TSG gave rise to a noticeable decrease in

MRT from 7.46 to 3.88 s. The extent of axial mixing and the relative dominance between convection and superimposed axial dispersion were identified by the breadth of distribution (σ_θ^2) and Pe_r , respectively. All selected runs turned out to have large amount of backward mixing except for T3 where the smallest σ_θ^2 and largest Pe_r were indicative of more plug-like flow behavior.

Typically processing conditions and design parameters should be manipulated to avoid plug flow regime and achieve sufficient powder-liquid mixing within such a short duration time. In this study, L12, L14 and T14 showed broader RTD with more desired mixing efficiency, relatively homogeneous liquid distribution and narrower GSD (smaller span values). Notice that in continuous HSG process, the distribution mode of L12 shifted to the left compared to L14 (refer to Fig. 3.11), but the former still demonstrated longer MRT mainly because the distribution profile was wider and accordingly more back mixing occurred, as confirmed by its larger σ_θ^2 and smaller Pe_r in Table 3.4. According to the results discussed earlier, throughput was of minimum magnitude to most granules quality attributes (e.g. GSD and porosity), so the reduction of τ from L12 to L14 can be primarily ascribed to the rise in rotation speed. Apparently the intensive shear motions and smearing against vessel wall played an essential role in distributing different constituents, and as a result of escalating centrifugal force, materials lingered longer in the ring layer associated with more axial mixing.

In terms of TSG, Kumar et al. (Kumar et al., 2015) and Vercruysse et al. (Vercruysse et al., 2014) reported that only marginal change of MRT and curve variance were observed when varying moisture content, despite that more sluggish powder with enhanced flow restriction can be induced at higher L/S ratio, potentially raising the residence time.

However, both studies revealed the vital importance of screw speed in determining the RTD and axial mixing. Therefore, from T3 to T14, it was believed that influence of rotation speed outweighed the L/S ratio and largely accounted for the variation of RTD and flow behavior. In contrary to Lödige granulator, increasing the RPM of TSG resulted in higher conveying capacity, which dragged materials out of the granulator more quickly (both real and perceived) and thus reduced the powder fill level and residence time. Analogous to Lödige granulator, nevertheless, increasing the screw speed led to an increase in σ_θ^2 and higher degree of axial dispersion. In fact, this trend stemmed from the significant change of powder fill degree at different RPMs where a low fill ratio accompanied by an increase in the wall slippage can exert less throughput force on the materials, thereby decreasing the compaction and inducing more axial mixing. Similar outcomes were also obtained by other researchers (Kumar et al., 2015; Kumar et al., 2014).

It is worth noting that solid-liquid mixing in the bulk mixture is usually driven by both axial and convective mixing. Although L/S ratio may have less impact on RTD profiles and axial mixing, bulk mixing always necessitates proper amount of liquid addition to achieve desirable homogeneity of the two phases. Aside from better axial mixing, the higher L/S ratio of T14 also contributed to its improved liquid distribution when compared with T3. This was also accentuated by the fact that TSG run #10 (0.66 L/S ratio) with the same RPM and even higher barrel filling level produced more monomodal GSD than T14 (see Fig. 3.5 (c) and (d)).

3.3.5 Granule morphology

The ANOVA F test revealed that particle shape of Lödige granules were significantly influenced by L/S ratio and rotation speed. As shown by the contours of constant aspect ratios in Fig. 3.12, granule sphericity increased dramatically with the initial rise of these two factors followed by more gradual improvement when they reached higher levels. A minimum response could be located around 2000 RPM and 0.55 L/S ratio with reasonable precision, which indicated the inclusion of curvature effect in the regression model. Besides, Eyecon^{TM} images of representative samples were integrated in Fig. 3.12 along the diagonal of contour plot, illustrating the evolution of particle morphology at different operation conditions. Apparently, Lödige granules exhibited superb uniformity and sphericity when rotation speed and L/S ratio were above moderate level. With respect to TSG, L/S ratio was found to be the only significant parameter in this case. Box plot in Fig. 3.13 reflected that the aspect ratio of TSG granules diminished steadily with the increase of liquid addition. With more liquid available for bonding primary particles, granules were getting less fragile, more deformable and thus easier to be shaped. By analogy, typical Eyecon^{TM} images were selected for each L/S ratio level, which demonstrated slight advances in granule size homogeneity yet irregularly or needle shaped particles. SEM images in Fig. 3.14 depicted the appearance of surface morphology regarding the same most porous and densest granules as in Fig. 3.7 (a-d) and served as complementary characterization together with those X-ray tomographic images. The two outcomes, as expected, were in agreement with each other, illustrating the spherical Lödige granules with disparate smoothness and surface texture in contrast to the elongated and angular TSG granules featured with more morphological resemblance.

Particle shape, as discussed previously, influenced critical powder properties such as flowability and compressibility. Irregularly shaped particles having more interparticulate contact points and bonding were inclined to interlock with each other and lead to poor flow and bridging. The granule edges and corners were subject to higher extent of deformation in virtue of the existence of lattice defects and primarily dislocations, thereby allowing more volume change during compression. Virtually the remarkable discrepancies of particle shape between Lödige and TSG granules were the inevitable corollary of different granulator functioning mechanisms. Granules produced from Lödige showed to be highly spherical, irrespective of the particle morphology (refer to Fig. 3.7 (a-b) and Fig. 3.14 (a-b)). In continuous HSG process, the sharp mixing elements rotating at extremely high RPM shaved granules off the ring layer and ensuing frequent collisions rounded any irregular particles at the expense of fragmenting to a limited degree. This inference can be particularly corroborated by Fig. 3.14 (a) where particles coalesced and then any protuberant parts got rounded off leaving the “wrinkles” on the granule surface. Granules shaped in the TSG was heavily predicated on the screw configuration that was also dominant over the changes in formulation or binder concentration (Seem et al., 2015). In this work, as powder materials went through DMEs, smaller pieces were chopped off from large agglomerates and granules with irregular polyhedron shape were formed by the angularly-cut blades. The surface cut on granules can be easily identified from Fig. 3.14 (c-d).

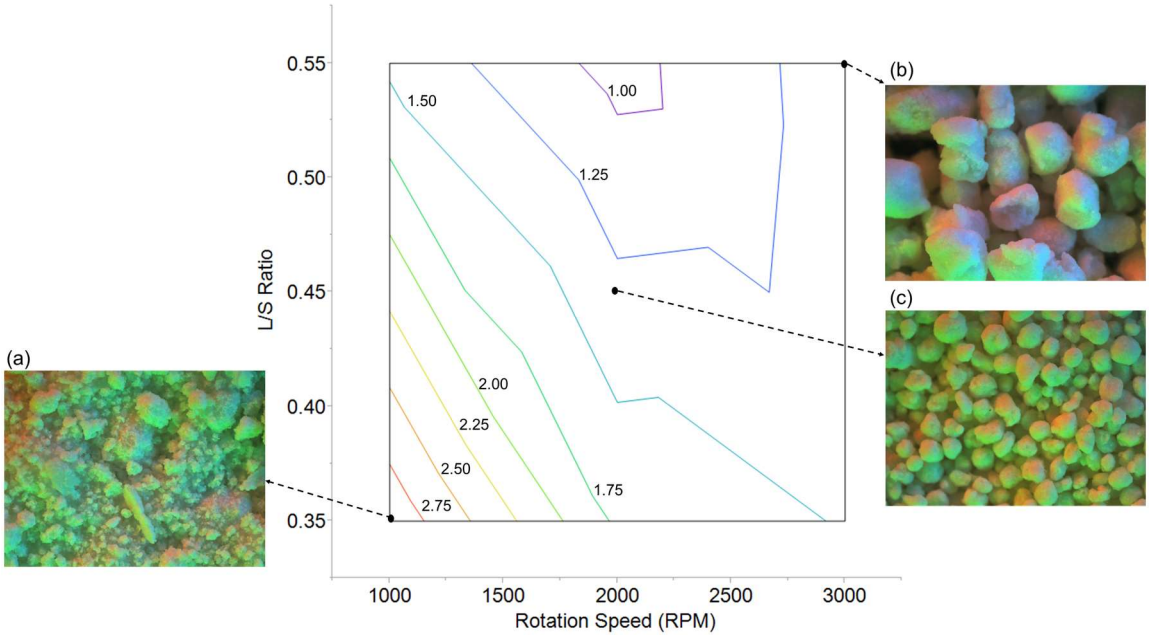

Fig. 3.12. Contour plot of Lödige low-dose granules aspect ratio complemented with Eyecon^{TM} images of run (a) #13, (b) #10 and (c) #5.

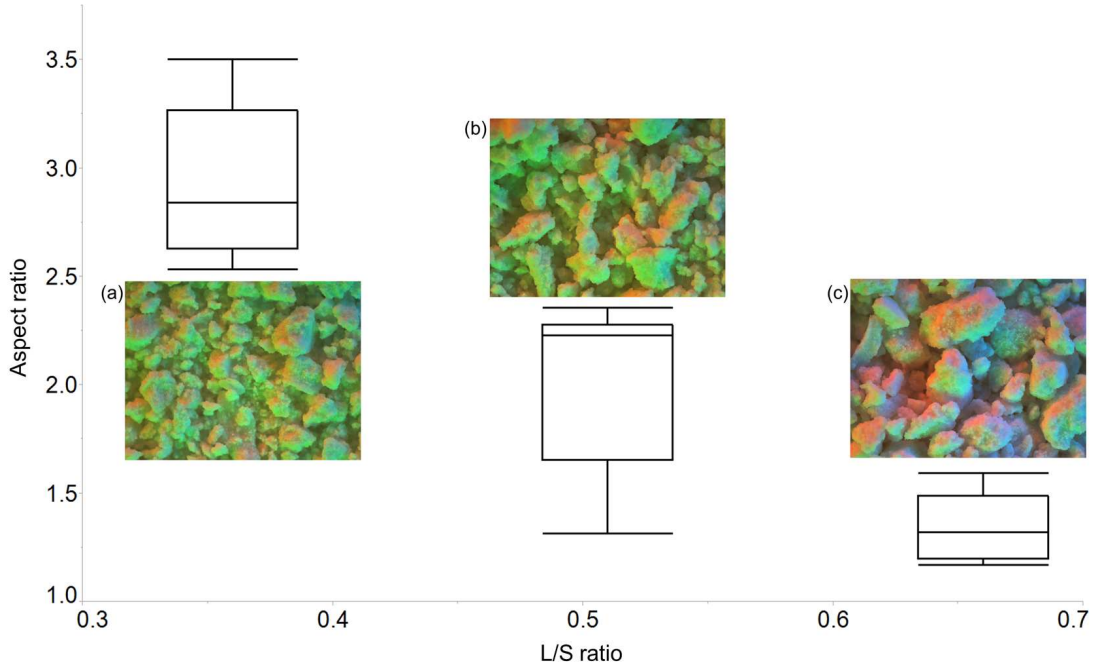

Fig. 3.13. Box plot of TSG granules aspect ratio complemented with Eyecon^{TM} images of run (a) #6, (b) #17 and (c) #10.

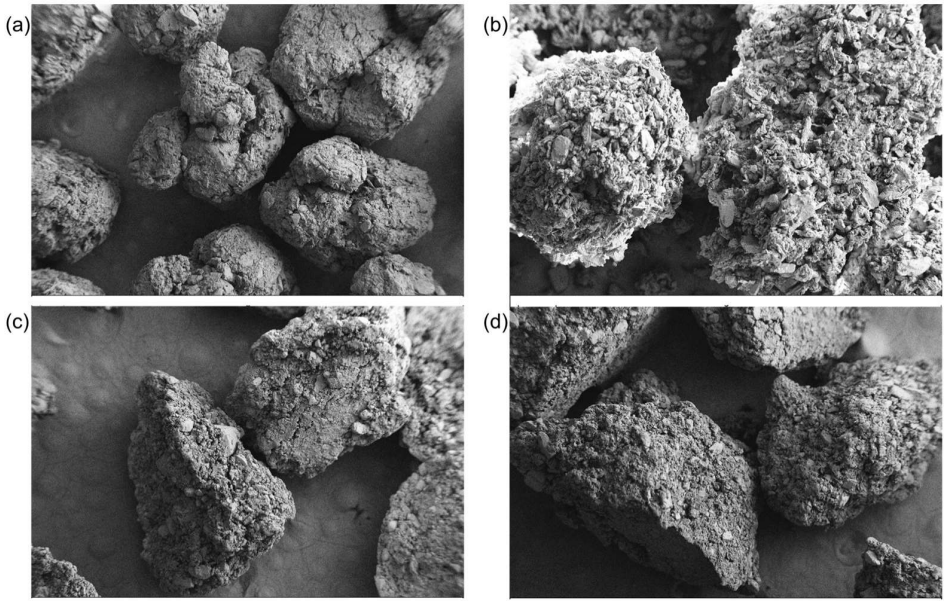

Fig. 3.14. SEM images of granules from Lödige low-dose run (a) #1 and (b) #6; TSG run (c) #3 and (d) #16.

3.3.6 Data overview and design space

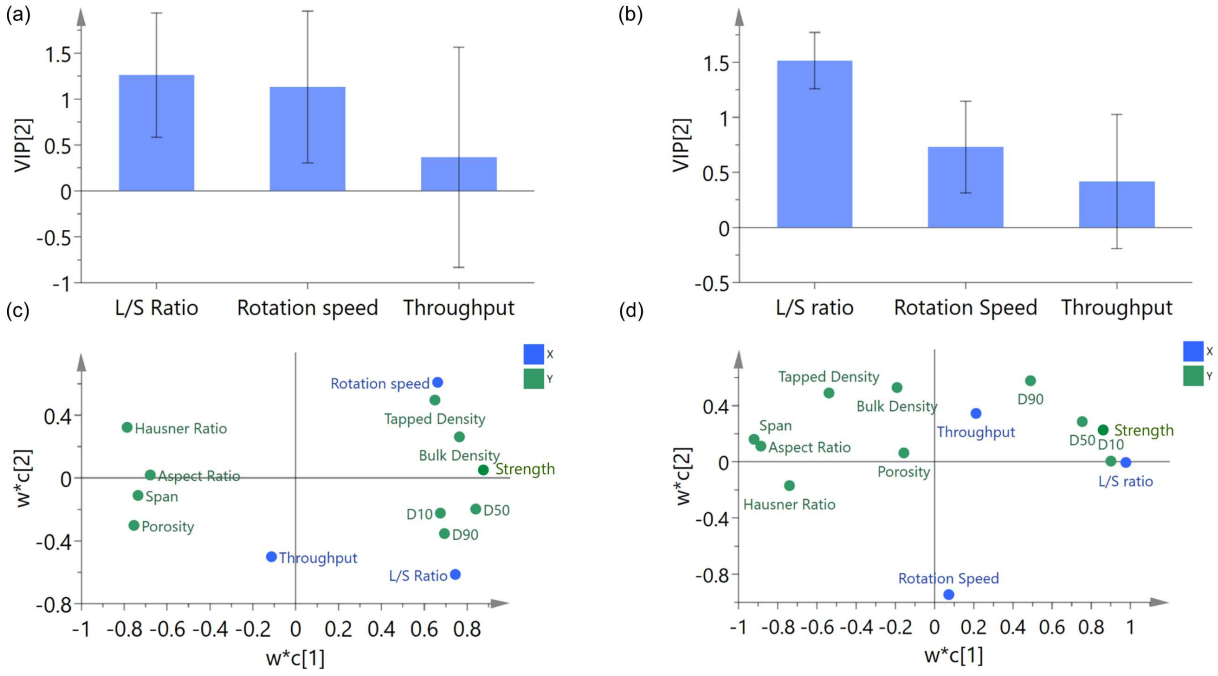

Fig. 3.15. Lödige low-dose (a) VIP and (c) PLS weight plots; TSG (b) VIP and (d) PLS weight plots.

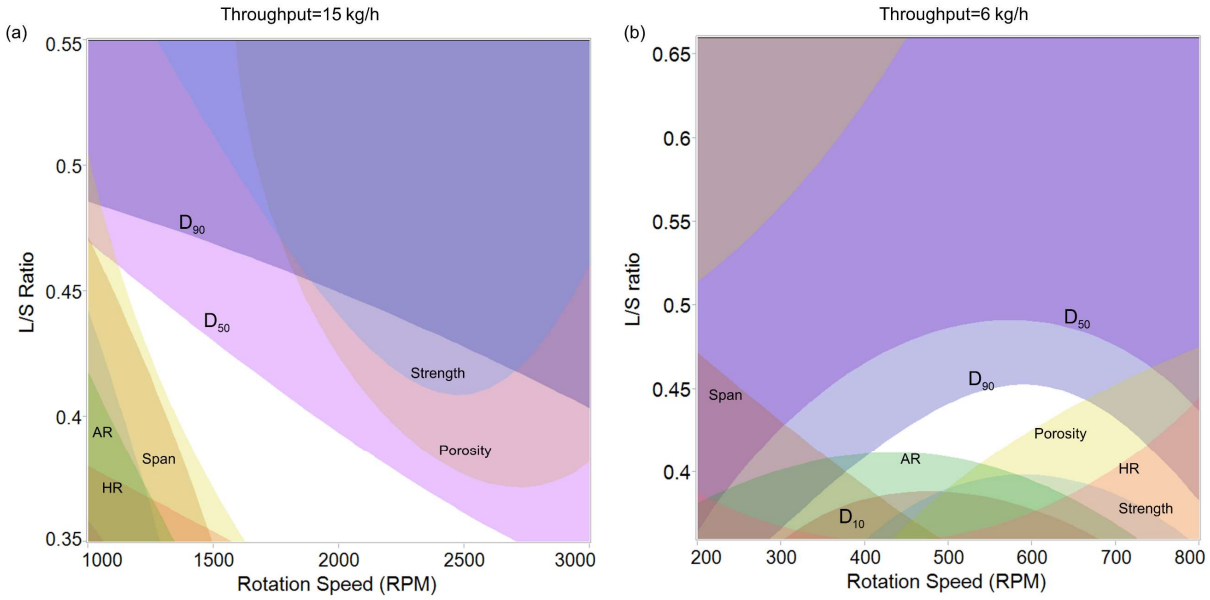

Fig. 3.16. Design space of (a) Lödige low-dose and (b) TSG based on the overlay of CQAs contours.

Table 3.5 Contour boundaries of multiple responses for design space

Granulator	Limit	D10(μm)	D50(μm)	D90(μm)	Span	Porosity	Aspect Ratio	Hausner Ratio	Strength (MPa)
Lödige &TSG	Lo	120	250	-	-	0.38	-	-	3.5
	Hi	-	750	2000	2.8	0.5	2.6	1.25	9

VIP (Variable Importance for the Projection) plots in Fig. 3.15 (a) and (b) summarized the overall contribution of each process parameter in modulating ten critical granule attributes displayed in Fig. 3.15 (c) and (d). The VIP values larger than 1 normally indicated “important” variables whereas values lower than 0.5 suggest “unimportant” ones. The interval between 1 and 0.5 is a gray area, the importance level depends on the size of the data set (Zhang et al., 2015). Consequently, in this study, L/S ratio and rotation speed predominated over throughput for both granulation processes and, by implication, the paramount roles of proper liquid amount and interaction between these two phases. However, the effect of powder feed rate in Lödige granulator is worthy of

more investigation since all its levels covered in this DoE were approximate to the lowest threshold. It was reasonable to expect more remarkable magnitude of throughput if the granulator fill level was substantially altered. When examining the TSG performance, other researchers (Dhenge et al., 2011; Kumar et al., 2015; Vercruysse et al., 2014) reported that throughput was a crucial factor in modification of barrel filling degree and further affect the extent of compaction, mixing mechanisms and granule properties. The minimum overall importance of throughput in the present study may be specific to such a screw configuration. In contrast to kneading elements, DMEs associated with more free volumes exerted less restrictive force on upstream powders, and accordingly, very limited densification of powder bed could be induced. Since the filling level was governed three factors: screw and barrel geometry, screw speed and material feed rate, it was essential to investigate the effect of throughput coupled with diverse screw configurations in the future. The PLS weight plots in Fig. 3.15 (c) and (d) displayed how the process variables affected various responses. For Lödige granulator, rotation speed and L/S ratio exhibited synergistic effect on granule size and strength, i.e., the higher level it was, the narrower distribution (smaller span) and stronger granules were acquired. Granule size and strength in TSG were proportional to L/S ratio but reversely correlated to rotation speed. It can be inferred that in both granulators, granule strength and size were positively interrelated. Bulk and tapped densities showed exactly opposite results when changing rotation speed and moisture content in the two granulators, which may be due to the more densified granules generated in most Lödige runs. Porosity of Lödige granules was located opposite to the projection positions of water content and agitation intensity and thus was negatively related to the two variables. As consistent with the surface plot, porosity of

TSG granules was situated near the plot origin and hardly influenced by any parameters. In addition, increasing L/S ratio significantly improved flowability and particle sphericity in both granulation processes. Throughput demonstrated limited impact on most of the properties, as aptly illustrated by its position relatively closer to the plot origin (0, 0).

Based on the desirable low and high limits for each critical granule attribute (refer to Table 3.5), Fig. 3.16 presented the optimum region for each granulator found by overlaying the contours of corresponding responses. The unshaded portion (white area) was considered as design space where we can arbitrarily adjust the L/S ratio and rotation speed while simultaneously satisfying the predetermined boundaries of CQAs. Apparently, within the identical limits, Lödige showed larger design space, implying that it was more sensitive to the process variation and amenable to tighter specifications. In fact, this area will in all likelihood extend beyond the lowest DoE L/S ratio 0.35 since its bottom has not been sealed by any contours. In other words, the effect reducing liquid content with all its concomitant effects on granule properties can be counteracted to a certain extent by increasing the rotation speed. The strong influence of rotation speed and L/S ratio on Lödige offered potential for a capable control loop to make real time adjustments through manipulating process parameters. While TSG illustrated narrower design space, it demonstrated robustness towards process variation, which was critical for maintaining product quality against unexpected changes or noise factors during the manufacturing process. Unlike Lödige, screw configuration is an essential ingredient of TSG and should be taken into account during process optimization. To expand the “sweet spot” of TSG, it necessitated the inclusion of different screw configurations and characterizing the performance by combining both process and design parameters.

3.3.7 Granulation mechanisms

To gain a sound scientific understanding of the underlying phenomena and have a better process control in the future, granulation rate processes in the two granulators were further explored based on the nucleation regime map and growth regime map for liquid-bound granules. A detailed description of these regime maps can be found in (Hapgood et al., 2003; Iveson and Litster, 1998b).

Wetting and nucleation is the first stage of any wet granulation processes. The nucleation regime map was developed by combining single drop penetration kinetics: dimensionless penetration time τ_p, and flux of drops onto the bed surface: dimensionless spray flux Ψ_a.

$$\tau_p = \frac{t_p}{t_c} \tag{3.13}$$

$$\Psi_a = \frac{3\dot{V}}{2\dot{A}d_d} \tag{3.14}$$

where t_p is drop penetration time; t_c is the time internal that a packet of powder circulate back to the spray zone; $\dot{V}$ is liquid spray flux; $\dot{A}$ is the flux that powder surface traversing the spray zone; d_d is droplet diameter. In the drop-controlled regime, binder was well dispersed and quickly penetrated into the powder bed. One drop formed one nucleus and the drop-footprint overlapping was at a minimum as shown in Fig. 3.17. The intermediate regime was reached with more significant penetration dynamics and shear force dispersion. This is a region where nuclei formation was more susceptible to the variations in the nucleation zone and was difficult to control. The final mechanical dispersion regime begins to dominate the process when severe drop coalescence occurred, leading to

powder surface caking or liquid pooling. Intense mechanical mixing and agitation are needed here to disperse the binder and break large agglomerates to form nuclei.

For the low-dose feed formulation used in this study, t_p was estimated to be less than 1 s by the definition:

$$t_p = 1.35 \frac{V_o^{2/3}}{\varepsilon_{eff}^2 R_{eff}} \frac{\mu}{\gamma_{LV} \cos\theta_d} \tag{3.15}$$

where V_o is the droplet volume, ε_{eff} is the effective porosity of powder bed, R_{eff} is the effective pore radius, μ is the liquid viscosity, θ_d is dynamic solid-liquid contact angle, and γ_{LV} is the liquid-vapor surface tension (Hapgood et al., 2002). Unlike batch systems, the pre-mixed materials in this work were continuously added to the processes and granules were continuously removed at the same rate with a constant materials hold-up in the two granulators. Therefore, we postulate that once a packet of powder goes through the wetting zone, it will keep moving forward and never circulate back to this area, namely that the t_c tends to infinity, making τ_p tended to zero. As a result, Ψ_a determines the regime where different granulation conditions will be situated. The powder surface velocity was estimated to be an order of magnitude lower than the corresponding tip speed (15% in this case) in Lödige granulator (Litster et al., 2002) while it was set as 45% of TSG screw tip speed based on the literature (Dhenge et al., 2013b).

The calculated Ψ_a for all Lödige runs were less than 1 and some were even less than 0.1, revealing that the granulation processes were either in the drop controlled regime or intermediate regime (refer to Fig. 3.17). A small Ψ_a is expected to generate a narrow GSD (smaller span), which is actually in accordance with the experimental results. For

instance, run #9, #14 and #12 with an increasing rotation speed showed a decreasing Ψ_a from 0.15 to 0.11 and finally to 0.05 and an identical trend was observed when examining their respective span value: 4.10, 1.70 and 1.25. The Ψ_a for almost all TSG processes fell between 0.1 and 1 leaving them in the intermediate regime, except for run #12 of which Ψ_a was 1.2 indicating that the granulation was in mechanical dispersion regime. TSG in this condition was carried out with 200 RPM rotation speed, 8 kg/h throughput and 0.66 L/S ratio. The lowest rotation speed and highest throughput engendered a low powder surface velocity and the highest level of L/S ratio 0.66 merged dripping droplets into a single stream of liquid. Hence when powders moved slowly from the translational area to the intermeshing area, high spray flux created local patches of high moisture content and preferential growth as illustrated in Fig. 3.17, eventually resulting in broader nuclei size distribution and large amount of oversized agglomerates. Although nuclei were subsequently subject to collisions and shear forces, the process still retained a memory of the nucleation stage, as confirmed by a larger and wider GSD of run #12 (D_{50} = 2453.07 μm; D_{90} = 4094.79 μm) compared to that of run #15 (D_{50} = 1471.54 μm; D_{90} = 2304.42 μm) with the same throughput and L/S ratio but higher rotation speed 800 RPM (larger surface velocity and smaller Ψ_a). Note that for batch granulators, the liquid content can still be a constant with varying spray rate and time whereas in a continuous granulator, L/S ratio usually changes along with different liquid flowrates and powder feeding rates. Therefore, when comparing Ψ_a at different operation conditions, it was important to ensure these batches having the same level of L/S ratio and throughput.

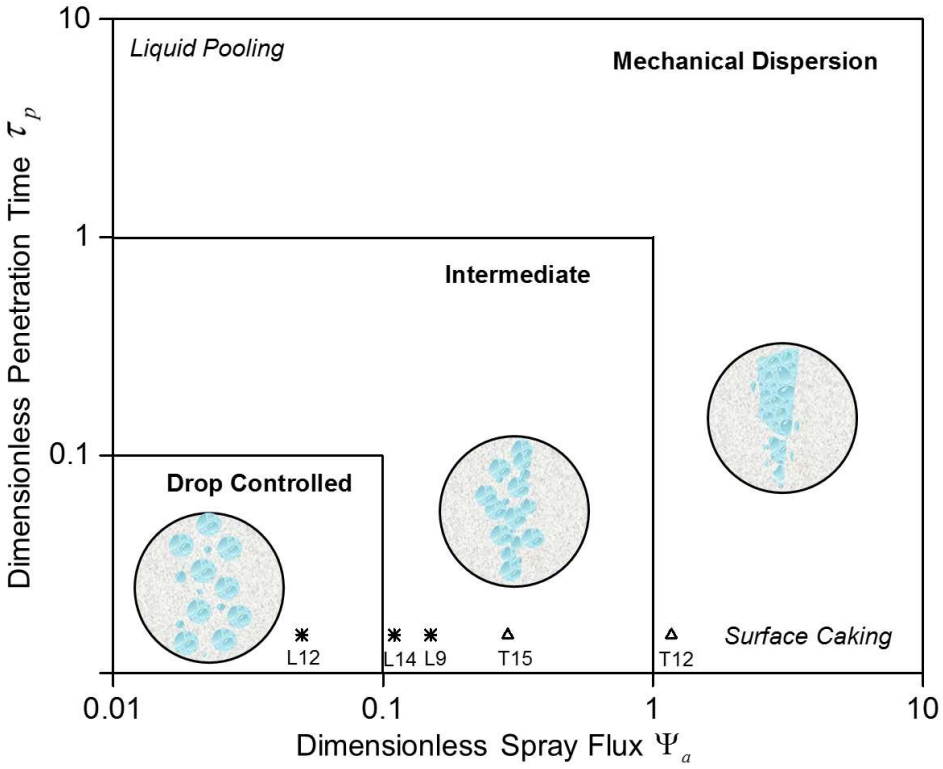

Fig. 3.17. Nucleation regime map proposed by Hapgood et. al (Hapgood et al., 2003).

The second phenomenon following wetting and nucleation was considered to be consolidation and coalescence where nuclei were agitated and collided with each other to trigger potential growth. Based on our findings for the first rate process, it was assumed that liquid binder was already distributed evenly through the powder mass. Iveson and Litster (Iveson and Litster, 1998b) reported that granule growth behavior was a function of system's liquid content and impact deformation during granulation. As illustrated in Fig. 3.18, they proposed several generic types of growth behavior demarcated by the values of maximum granule pore saturation, $s_{\max}$:

$$s_{\max} = \frac{w\rho_s(1-\varepsilon_{\min})}{\rho_l \varepsilon_{\min}} \tag{3.16}$$

where w is the mass ratio of liquid to solid, ρ_s is the true density of solid particles, ρ_l is the liquid density, $\varepsilon_{\min}$ is the minimum porosity the formulation reached for that particular set of operation condition, and Stokes deformation number, St_{def} :

$$St_{def} = \frac{\rho_g U_c^2}{2Y_g} \tag{3.17}$$

where U_c is the representative collision velocity in the granulator, ρ_g and Y_g are the granule density and dynamic yield stress, respectively. At very low liquid content (low $s_{\max}$), particles will either remain as a dry, free-flowing powder, or just form nuclei due to van de Waals interactions and cease growing any further (Zhang et al., 2016a). At slightly higher liquid contents, either only nuclei are formed without further growth, or if the system is extremely fragile ($St_{def} > 0.2$), granules will fail to withstand the breakage forces, thereby producing nongranular "crumb" materials. At intermediate levels of liquid content, granulations usually exhibit steady growth and are likely to be more robust to process and material modifications, provided that granules are deformable and consolidated quickly (medium St_{def}), otherwise induction-time behavior can be observed at low-deformation, slowly-consolidating systems ($St_{def} < 0.001$). At high liquid content, both fast and slow consolidating systems will grow rapidly. If liquid content continues increasing, eventually a slurry or over-wetted mass will be formed.

To calculate $s_{\max}$ in our study, measured granule porosity was considered as the minimum porosity $\varepsilon_{\min}$ that can be reached after a certain amount of residence time in continuous processes. When calculating St_{def} , impeller tip speed and screw tip speed were used to estimate the particle collision velocities U_c for Lödige and TSG granulators,

respectively. The dynamic yield stress Y_g was based on the stress vs. strain relationship obtained from the compression tests described in section 3.2.4.2.

A plot of St_{def} vs. $s_{\max}$ for the Lödige granulation experiments was illustrated in Fig. 3.18, the data of which fit the growth regime map reasonably well. All St_{def} of the 17 runs (L1-L17) ranged from 0.002 to 0.03 and lay below the steady-crumb regime boundary 0.2 measured by Tardos et al. (Tardos et al., 1997), making the transition across different regimes largely dependent on the $s_{\max}$ values. In this study, other regime map boundaries were arbitrarily defined according to the particle size before and after granulation. The initial addition of water was believed to be absorbed and held by MCC, which typically acts as a "molecular sponge". When $s_{\max} < 0.3$, granule size distribution was close to the raw materials blends and mainly in the "dry" free-flowing powder region. It suggested that nucleation occurred at $0.3 < s_{\max} < 0.6$ with relatively broad GSD but small D_{10} and D_{50}, implying the inability to promote the growth of all primary particles with insufficient liquid binder for redistribution. The formation of some large nuclei basically reflected the large droplet size in dripping mode. Regime of steady growth was demarcated with $0.6 < s_{\max} < 1$ where GSD was narrow and D_{50} was between 500-1000 μm. The rapid growth was assumed to take place when a narrow GSD with the D_{50} above 1 mm was obtained ($1< s_{\max} < 1.7$). If $s_{\max} > 1.8$, the median diameter of granules would be larger than 2.5 mm and eventually, slurry/paste was observed when conducting the trials. As seen in Fig. 3.18, operation conditions in Lödige DoE triggered granulation processes in nucleation, steady growth and rapid growth regimes. Specifically, increasing agitation intensity (L6, L7 and L16) shifted the system's behavior towards the

top-right of the regime map largely due to increased typical impact velocity U_c and decreased minimum granule porosity $\varepsilon_{\min}$. Increasing liquid content (L14, L7 and L2) shifted the system's behavior towards the bottom-right of the regime map on account of increased granule dynamic yield stress Y_g and mass ratio of liquid to solid w. As mentioned earlier, the effect of decreasing L/S ratio can be compensated to a certain extent by increasing the rotation speed (from L6 to L14). Moreover, the behavior of induction followed by rapid growth became unlikely to be observed at such a short residence time in continuous granulator. It will always appear to be nucleation if the granulation process ceased before the induction time is reached.

The calculated St_{def} for all the TSG experiments were less than 10^{-5} and thus not shown in Fig. 3.18. Since the granules Y_g were in the same order of magnitude as Lödige granules, this should be attributed to the underestimation of particle collision velocities. The $s_{\max}$, however, showed much more reasonable values from 0.48 to 1.12. According to the experimental results, granulation processes in TSG DoE were expected to have similar growth behaviors as those in Lödige granulator.

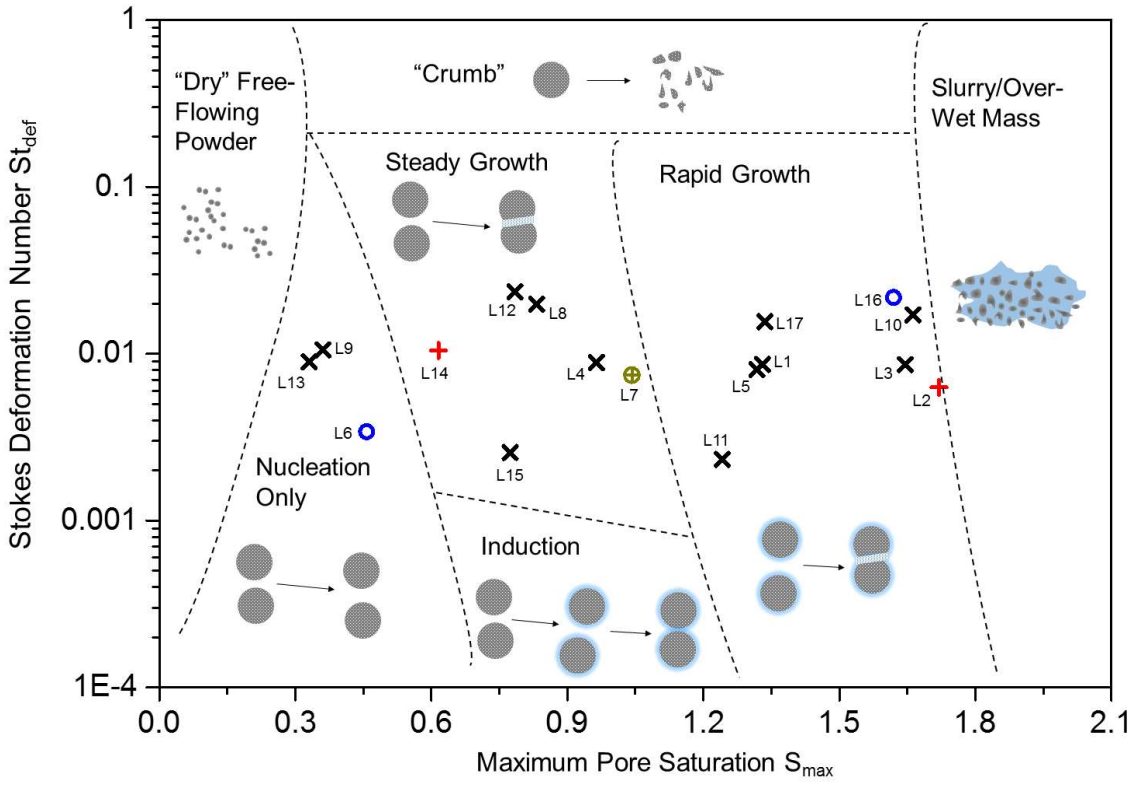

Fig. 3.18. Growth regime map proposed by Iveson et. al (Iveson and Litster, 1998b).

3.4 Conclusions

As continuous granulators, both Lödige and TSG generated granules with controllable attributes within a very short residence time. Despite the constraints of altering design elements like blade angle or type, Lödige showed high dependence on process variables. It produced a smaller size variance and finer granule structure after the "real" high shear granulation process, leading to a wider design space and higher flexibility in terms of tight specifications. Overall, Lödige demonstrated to be an effective continuous granulator to produce granules with controllable attributes and an excellent alternative to conventional batch high shear granulators. TSG with such a particular screw configuration provided a granulation environment with intermediate shear level. Granules exhibited multimodal distributions, especially at low liquid addition level, and subtler

internal structure difference. The ungranulated materials were always present, suggesting the suboptimal liquid dispersion and micro-mixing efficiency of liquid and powder. Instead of spreading the binder, dripping addition method rendered it more challenging to uniformly distribute binder within confined space and limited wet massing time. However, the authors understand the necessity of further investigations of TSG by including screw configuration as well. Different screw configurations are capable of producing granules with very different attributes, therefore any particular one can be chosen according to the requirements. The modular characteristics of TSG can be taken advantage of to accommodate more diverse production needs. The flexibility of screw configuration and locations of powder and liquid feeding ports should be fully leveraged to achieve different residence times and granule properties. Future work will focus on the tableting characteristics of produced granules and correlating the properties of intermediates to the performance of final drug product.

Chapter 4

Continuous high-shear granulation: in-depth understanding of the influence of process parameters on critical quality attributes of tablets via elucidating the internal physical and chemical microstructure

4.1 Objectives

The present study focused on the continuous high-shear mixer granulator, Lödige CoriMix® CM5. Effect of key process parameters on tablet performance were comprehensively investigated with paracetamol formulations. The objectives were to: (1) unravel the relationship among input process parameters, intermediate granule properties and final drug product tablet attributes; (2) to elucidate the underlying dissolution mechanisms accompanied by distinct tablet physical microstructures; (3) to gain insight into the influence of tablet drug agglomerate size distribution (chemical microstructure) on release kinetics.

4.2 Materials and methods

4.2.1 Materials

The low-dose formulation comprised 8% (w/w) semi-fine acetaminophen (APAP, Mallinckrodt Inc, Raleigh, NC), 44.75% (w/w) α-lactose monohydrate 200M (Foremost Farms USA, Baraboo, WI, USA), 44.75% (w/w) microcrystalline cellulose (MCC, Avicel® PH101, FMC Biopolymer, Philadelphia, PA) and 2.5% (w/w) polyvinylpyrrolidone (PVP K29-32, Fisher Scientific, Pittsburgh, PA). The dry binder addition method was adopted, i.e., PVP was premixed with other ingredients as dry powders. Distilled water as granulation liquid was pumped into the system in dripping

mode. Several crucial physical specifications of each formulation component were listed in Table 4.1.

Table 4.1 Key physical specifications of formulation ingredients and premix

Component	D10 (μm)	D50 (μm)	D90 (μm)	Bulk Density (g/ml)	Tapped Density (g/ml)	Hausner Ratio
APAP	5.5	29.8	116.4	-	-	-
MCC	19.1	58.7	132.5	-	-	-
Lactose	13.7	78.4	159.5	-	-	-
Premix	14.3	69.8	140.3	0.476	0.629	1.32

4.2.2 Production of granules

4.2.2.1 Continuous mixing (CM) of raw materials

With respect to the 17-run face-centered cubic design (refer to section 4.2.3), all the excipients were firstly premixed in a Glatt tumble tote blender (Model TAM 40, Glatt GmbH, Binzen, Germany) for 30 minutes at 25 RPM, and then transferred into a K-Tron loss-in-weight (LIW) feeder (KT 35, K-Tron Soder, Niederlenz, Switzerland). Another K-Tron LIW feeder (KT 20) was used for dosing APAP gravimetrically (see Fig. 4.1 (a)). The drug and excipients were then mixed in a Glatt convective continuous mixer (Model GCG-70) under 260 RPM with a total powder feeding rate of 30 kg/h. A Quadro conical screen mill (Comil®, Model #197S, Quadro Engineering, Ontario, Canada) was integrated into the experimental set-up upstream of the mixer to de-lump agglomerates from incoming powder stream and enhance the micro-mixing behavior with high shear input. The mill equipped with a 800 μm round-holed screen was operated at 1420 rpm.

4.2.2.2 Batch mixing (BM) of raw materials

A separate experiment was designed to examine the effect of drug agglomerate size distribution on tablet dissolution performance. In this study, raw materials were premixed

by two different approaches. The first method was continuous mixing (section 4.2.2.1) whereas the second avenue was batch mixing where all ingredients were subjected to the gravity-driven low-shear batch mixing in the Glatt tumble tote blender (see Fig. 4.1 (b)). The premixed raw materials were then transferred into a K-Tron LIW feeder (KT 20) was for continuous granulation processing (see Fig. 4.1 (c)). The purpose was to modulate or manipulate the drug agglomerate size distribution only by distinct mixing methods while keeping the variables of downstream unit operations constant, i.e., identical granulation, tableting and dissolution conditions. Consequently, if tablets demonstrated substantial difference in drug release profiles, the cause can be traced back to the powder mixing approaches, namely the discrepancy in drug agglomerate size in mixture (de Villiers, 1996).

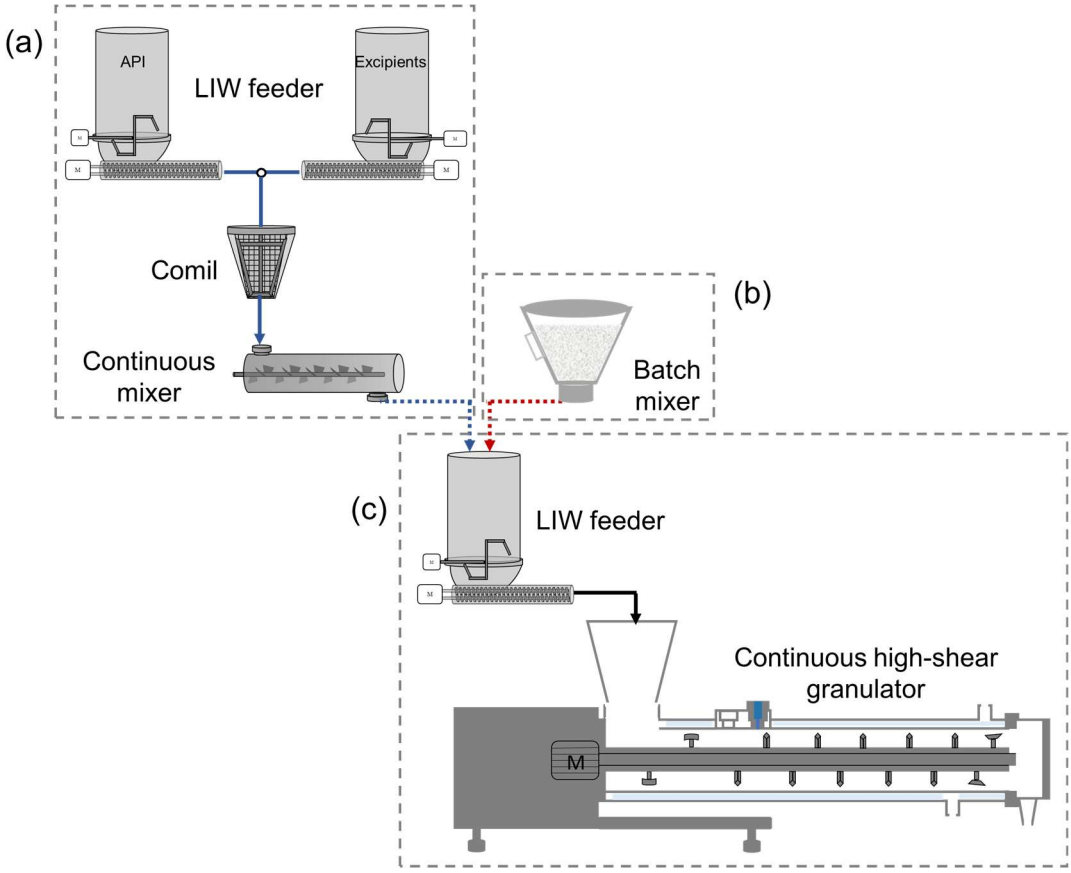

Fig. 4.1. Experimental set-up for granules production. (a) Continuous mixing of raw materials prior to granulation. (b) Batch mixing of raw materials prior to granulation. (c) Continuous high-shear granulation.

4.2.2.3 Continuous high-shear granulation

The premixed materials underwent continuous high-shear granulation in the Lödige CoriMix® CM5 granulator (Gebrüder Lödige Maschinenbau GmbH, Paderborn, Germany). It included a horizontal chamber inside which a rotary shaft was mounted with plough-shaped blades to enable different shear intensities: speeding up, granulation, and shaping of granules (Fig. 4.1 (c)). The high rotation speed and concomitant large centrifugal force dominated the bulk flow over gravity, which formed a concentric annular layer of materials on the vessel wall moving through the chamber in a plug-like flow with the retension time dictated by processing parameters. The liquid components were introduced tangentially from the top into the product layer through a single phase nozzle in dripping mode, thereby ensuring a homogeneous distribution within the mixture and avoiding wetting of the mixing wall and shaft.

4.2.3 Granulation experimental design and multivariate data analysis

In the current study, a face-centered cubic design augmented with three center points was employed to investigate the influence of three critical process parameters (X variables): rotation speed (x_1), L/S ratio (x_2) and throughput (x_3), on critical quality attributes of tablets (Y variables). Table 4.2 specified the levels of each investigated parameter as well as the characterized properties involved in the DoE. A total of 17 randomized experiments (see Table 4.3) were generated by JMP® statistical software (SAS Institute Inc., Cary, NC). Note that any “run #” mentioned in the following sections

referred to the granulation run # in Table 4.3. In addition, a partial least squares (PLS) model was constructed by the SIMCA 14.1 software (Umetrics AB, Umeå, Sweden). Since the DoE was identical as the one used in Chapter 3, granule properties and mean residence time (MRT) were also incorporated in the model to delve into the interrelation between CPPs, intermediates and final drug product properties.

Table 4.2 Independent variables and responses in the face-centered cubic design

X variables	Level			Y variables	
	Low	Intermediate	High	Granules	Tablets
Rotation speed (rpm)	1000	2000	3000	Granules size distribution; Shape; Porosity; Bulk density; Tapped density; Flowability; Strength	Tensile strength; Porosity; Friability; Disintegration time; in vitro dissolution
L/S ratio	0.35	0.45	0.55		
Throughput (kg/h)	10	15	20		

Table 4.3 The 17-run face-centered cubic design for wet granulation

Run#	Pattern	Rotation speed (rpm)	Throughput (kg/h)	L/S Ratio
1	000	2000	15	0.45
2	00A	2000	15	0.55
3	0a0	2000	10	0.45
4	0A0	2000	20	0.45
5	000	2000	15	0.45
6	a00	1000	15	0.45
7	000	2000	15	0.45
8	++−	3000	20	0.35
9	−−−	1000	10	0.35
10	+−+	3000	10	0.55
11	−−+	1000	10	0.55
12	+−−	3000	10	0.35
13	−+−	1000	20	0.35
14	00a	2000	15	0.35
15	−++	1000	20	0.55
16	A00	3000	15	0.45
17	+++	3000	20	0.55

4.2.4 Tablet compression

Granules from each experiment were air-dried at ambient conditions until the loss-on-drying moisture content was less than 3%. The dried granules were then sieved and the

fractions between 250 to 710 μm were compacted into tablets by a tablet press emulator (Presster™, Metropolitan Computing Corporation, East Hanover, NJ) with an upper compaction force of 8 and 24 kN. It emulated the Fette Compacting 1200i tablet press (24 station). A round flat-faced punch was used to obtain cylindrical tablets with 10 mm diameter. Powder dosing weight was controlled around 350 mg for each tablet.

4.2.5 Tablet characterization

4.2.5.1 Tensile strength

Tablet thickness was measured by a digimatic digital caliper (Mitutoyo America, Aurora, IL) and radial fracture force was determined in a hardness tester (MultiTest 50, SOTAX, Westborough, MA). Tablet tensile strength was then calculated by the following equation (Fell and Newton, 1970),

$$\sigma_t = \frac{2F}{\pi dh} \tag{4.1}$$

where σ_t was the tablet tensile strength (MPa), F was tablet fracture force (N), d and h were the tablet diameter (mm) and thickness (mm), respectively.

4.2.5.2 Porosity

The apparent density ρ_o of tablet was calculated by weight and volume. True density ρ_t was measured by a helium pycnometer (AccuPyc II 1340, Micromeritics, Norcross, GA). The tablet porosity ε_t can be obtained with Eq. 4.2.

$$\varepsilon_t = 1 - \frac{\rho_o}{\rho_t} \tag{4.2}$$

4.2.5.3 Friability

The unit mass of tablets was around 350 mg which is less than 650 mg, so eighteen tablets approximately corresponding to 6.5 g from each run were used for tests. Tablets were carefully dedusted and weighed (w_1) prior to being placed in a dual drum friability tester (PTF 20E, Pharma Test, Hainburg, Germany). The drum rotated 100 revolutions with the speed of 25 rpm for 4 minutes. After testing, samples were accurately weighed (w_2) again following the removal of any accumulated dust on the surface. The friability (FR) was expressed as the percentage weight loss in Eq. 4.3.

$$\mathrm{FR} = \frac{w_1 - w_2}{w_1} \tag{4.3}$$

4.2.5.4 Disintegration time

Six tablets from each DoE condition were evaluated for the disintegration time (T_d) in the Agilent 100 Automated disintegration apparatus (Agilent Technologies, Santa Clara, CA). The temperature and volume of distilled water in each beaker were 37.3 °C and 1000 ml, respectively. The end of each test was determined visually when no residue of the tablet was left on the basket mesh wire.

4.2.5.5 In vitro dissolution

Six tablets from each selected batch were dissolved in 900 ml phosphate buffer solution at pH 5.8 and 37.3 °C (USP <711>). The dissolution apparatus (708-DS, Agilent Technologies, Santa Clara, CA) coupled with a UV/Vis spectrophotometer were utilized to measure acetaminophen absorbance at the wavelength of 248 nm every 3 minutes. The rotation speed of paddle was 50 RPM. Drug concentration at each time point was then

derived from a standard UV calibration curve with the linear correlation (R^2 = 0.9996) from 4.9*10^{-5} to 0.05 g/L.

Parameters $t_{3\,\mathrm{min}}$, $t_{90\%}$ and dissolution efficiency ($DE_{10\ \mathrm{min}}$) were used to characterize and compare the drug release profiles. $t_{3\,\mathrm{min}}$ and $t_{90\%}$ correspond to the percentage of drug dissolved after 3 min and the time necessary to release 90% of the drug, respectively. $DE_{10\,\mathrm{min}}$ defined in Eq. 4.4 is the area under the dissolution curve up to 10 min dissolution as a percentage of the area of the rectangle described 100% dissolution at the same time (Costa and Sousa Lobo, 2001).

$$\mathrm{DE}_{10\,\mathrm{min}}\,(\%) = \frac{\int_0^t k \cdot dt}{k_{100} \cdot t} \cdot 100 \tag{4.4}$$

where k is the drug percent dissolved at time t.

4.2.5.6 Content uniformity

To evaluate the consistency of dosage units, 10 tablets were randomly selected from each batch and dissolved individually in a glass vial with 10 ml pure methanol before being placed in an incubator shaker (New Brunswick™ Excella® E25/E25R, Eppendorf, Hamburg, Germany) at 37.3 °C for 24 hours. 5 ml samples were then withdrawn from the supernatant and diluted to the concentration range of calibration model from 0.0008 to 0.0128 g/L (R^2 = 0.9999). Same UV/Vis spectrophotometer was used to assay the drug content in each tablet based on its absorbance at 248 nm. An acceptance value (AV) was computed in Eq. and compared to the passing criteria depicted in USP <905> uniformity of dosage units.

$$\mathrm{AV} = \left|M - \bar{X}\right| + k \times s \tag{4.5}$$

where $\overline{X}$ depicted the mean of individual contents, expressed as a percentage of the lable claim (350mg, 8% API in this case); k was the acceptability constant that equals to 2.4 when sample size is 10; s represented the sample standard deviation; M referred to the reference value (98.5% or 101.5%). The maximum allowed AV for sample size of 10 was 15.

4.2.6 Morphology and physical microstructure studies

4.2.6.1 Scanning electron microscopy (SEM)

The morphology of tablet surface was observed under the SIGMA Series of Field Emission Scanning Electron Microscopes (FE-SEM, Carl Zeiss Microscopy, Jena, Germany) operating at an accelerating voltage of 5 kV and high vacuum mode. Samples were stored in a vacuum desiccator overnight and then sputter-coated with 5 nm gold layer prior to tests.

4.2.6.2 X-ray micro-computed tomography (micro-CT)

Examination of the tablet internal structure was performed by Bruker microCT (SkyScan 1172, Billerica, MA). X-ray tomographic images were reconstructed to display the granules cross-sectional porous structure, and a three-dimensional (3D) digital representation of individual granule was created to visually inspect the closed and open pores. The region of interest for each tablet selected in this study was a cycle on the surface with 4 mm in diameter. Shadow images with the pixel size of 4.89 μm were acquired with an optimized X-ray source at 40 kV (250μA) and scanned in the 0-180° interval using a 0.40° rotation step.

4.2.6.3 Magnetic resonance imaging (MRI)

MRI analysis enabled the observation of tablet disintegration process in 3D space. The elementary disintegration processes such as water ingress, leaching, erosion, break-up and potential structural changes could be revealed assisting in understanding the underlying disintegration mechanisms of tablet with distinct internal sturctures (Punčochová et al., 2015).

The Bruker MRI desktop system (ICON^{TM}, Billerica, MA) was used in conjunction with a custom-built flow cell where the tablet was placed. The analysis was on the basis of multi-slice multi-echo (MSME) sequence of pulses measuring the concentration of mobile hydrogen protons. The echo time was 20 ms and repetition time was 1200 ms. The image presented in this work was the middle slice and its resolution included a matrix size of 128×128 pixels and field of view 1.8×1.8 cm. During testing, the flow cell was fixed by a holder with minimum contact area with tablet, thus preventing its movement in the dissolution medium.

4.2.6.4 Laser diffraction particle size distribution analysis

Following the disintegration time test, particle size of disintegrated tablets from different compression forces or granulation conditions were further measured by the laser diffraction analyzer (LA-950V2, HORIBA Scientific, Edison, NJ). The goal was to examine the integrity of granule internal structure after undergoing different tableting compression forces and illuminate the effect of physical microstructure on tablet disintegration and dissolution kinetics.

4.2.7 Drug agglomerate distribution and chemical microstructure studies

The 3D distribution of drug agglomerates in the tablets was investigated by a Raman imaging system (mPAT LAB-Pillerator, H2Optx, San Jose, CA). The device integrated Raman spectroscopy, microscopy, high-resolution optical imaging with automated X-Y-Z surface scanning. By interfacing the Pillerator sampling accessory with mPAT LAB, it enabled automatic sectioning of tablets with layer by layer hyperspectral imaging. After finishing the scan of multipe layers, a 3D chemical map and structural analysis of the tablet were established.

In the present study, the layer thickness was defined as 40 microns and in total 20 layers of each tablet were scanned. The field of view was 4×4 mm. The image scan settings were 50 Z steps with 2 microns for each step. The Raman scan settings included a XY resolution of 10×10 microns and laser current of 160 mA with a exposure time of 10 ms.

4.3 Results and discussion

4.3.1 Parametric analysis of continuous high-shear granulation process

4.3.1.1 Effect of process parameters on tablet properties

Based on stepwise regression, Table 4.4 summarized the independent variables in different response surface reduced quadratic models concerning tablet attributes. The regression statistics (Adj R-Sq and Pred R-Sq) of most models are indicative of satisfactory performance. However, it was noticeable that the figures of merit for tablet porosity model were very low implying more residual variability remained unexplained in the current experiment. L/S ratio was deemed to be the most critical factor as it was included in the reduced models for all tablet attributes. The contour plots (not shown)

indicated that t_{3min} and DE_{10min} decreased while $t_{90\%}$ increased as the L/S ratio or impeller rotation speed elevated to higher levels, irrespective of the throughput settings. The curvature and interaction effects in the friability model were significant. Consequently, the influence of L/S ratio on tablet friability substantially contingent on the levels of rotation speed. Tablets exhibited the largest amount of weight loss when both L/S ratio and rotation speed were at their intermediate levels. In contrast, one factor demonstrated marginal implication if the other parameter was set to low or high conditions. Besides, disintegration time was negatively related to the shear intensity when throughput was held constant at low level. However, it was primarily dictated by water addition amount at intermediate level of throughput where prolonged disintegration process was acquired at L/S ratio increased. This response was determined by both parameter as powder feeding rate eventually rose to the high level. In terms of tensile strength, it consistently declined in conjunction with L/S ratio, especially when throughout was relatively low. Additionally, all acceptance values were less than 2, indicating excellent tablet content uniformity (not shown). Given that only granules from 250 to 710 μm were selected for tableting, the small AVs also implied limited degree of drug segregation across different granule size fractions.

Table 4.4 t-statistic of independent variables and regression statistics of response surface reduced quadratic model

Regressor	t-statistic of independent variables for each response						
	t_{3min}	$t_{90\%}$	DE_{10min}	Tablet porosity	Friability	Disintegration time	Tensile strength
x_1	-4.51	5.78	-4.98		-1.81	1.39	
x_2	-4.32	4.45	-4.21	-1.76	-0.75	4.54	3.34
x_3					0.42	0.27	-3.80
x_1*x_2		3.37					
x_1*x_3					-5.26	7.04	
x_2*x_3						3.83	-6.87
x_1^2					-2.94	3.78	
x_2^2					-3.60		
x_3^2							
Regression Statistics							
Adj R-Sq	0.70	0.80	0.72	0.12	0.82	0.86	0.81
Pred R-Sq	0.63	0.72	0.66	-	0.66	0.44	0.72

4.3.1.2 Overview of the correlation betweet CPPs, intermediates and final drug product

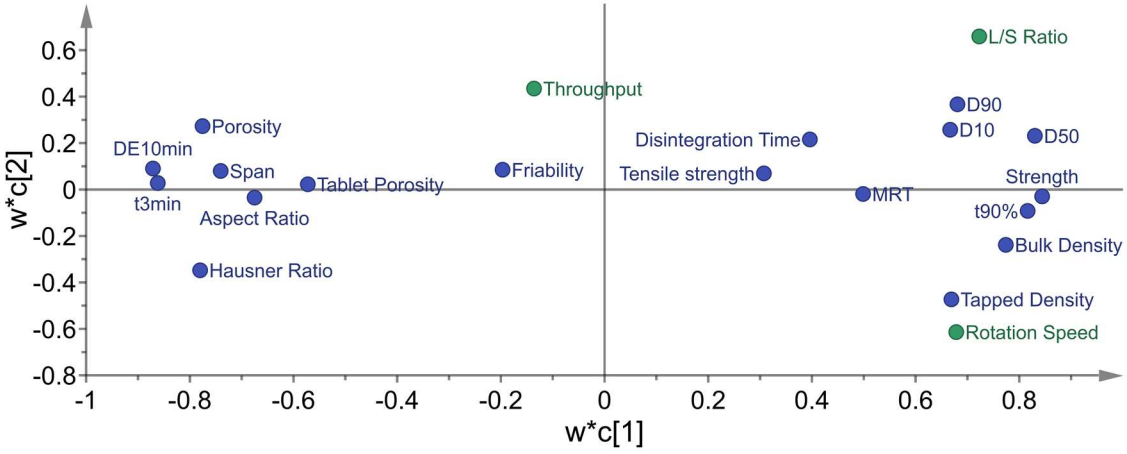

Fig. 4.2. Superimposition of the loading weights of X-variables (w*) and Y-variables (c) for the first and second PLS components.

With respect to partial least squares regression, cross-validation suggested two PLS factor in modeling the responses with 66.7% variation explained in the X-data and 52.3% in the Y-data. The PLS loading weights plot in Fig. 4.2 simultaneously displayed the overall relationship between critical process parameters, granule and tablet attributes. The X-variables with substantial impact were situated far away from the origin and highly correlated with Y-variables. To interpret this plot, a base line can be drawn through the origin and one certain response. With all X-variables and other responses projected orthogonally onto this line, those opposite to each other were negatively correlated and positively related if clustered together. For instance, as shown in Fig. 4.2, $t_{90\%}$ was positively correlated to the granule strength and negatively correlated to the granule porosity. When granules were more porous, they demonstrated lower strength accompanied by faster disintegration and smaller tensile strength once compacted into tablets. The drug dissolution rate was accordingly more rapid, namely that less time was necessitated achieving 90% of released drug. Analogously, t_{3min} and DE_{10min} were located near granule porosity and thus more APAP was release within the first 3 minutes, reflecting higher dissolution efficiency in the first 10 minutes.

In addition, it can seen that the longer residence time of materials underwent inside the granulator, the following concomitant results were obtain: larger particle size, smaller porosity, better flowability, more spherical particles, higher tablet tensile strength and slower drug release kinetics. Overall, this plot implied that degree of liquid saturation (L/S ratio) and shear intensity (rotation speed) possessed higher leverage as opposed to materials filling degree (throughput) towards modulating all granule and tablet attributes and hence should be controlled carefully during manfuacturing processes.

4.3.2 Influence of tablet internal structure on dissolution performance

4.3.2.1 Morphology and physical microstructure

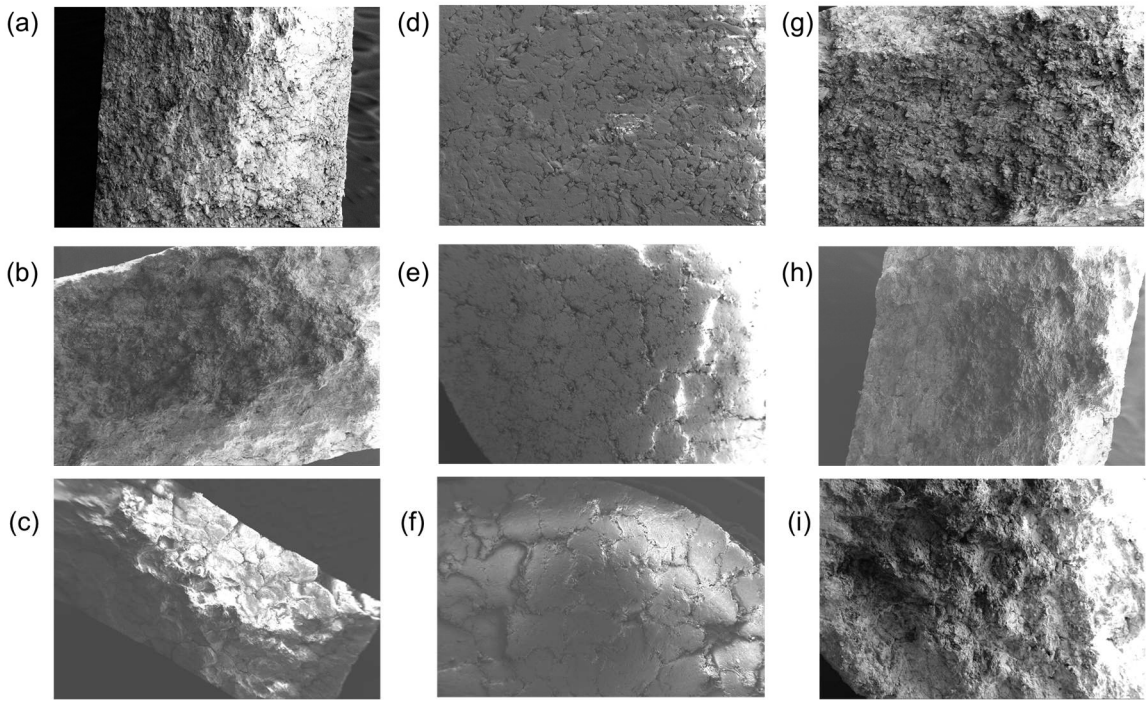

Fig. 4.3. SEM images of tablets. Run #13: (a), (d) and (g); Run #7: (b), (e) and (h); Run #10: (c), (f) and (i). Cross section of tablets with compression force at 10 kN: (a), (b) and (c); Cross section of tablets with compression force at 24 kN: (g), (h) and (i); Surface of tablets with compression force at 10 kN: (d), (e) and (f).

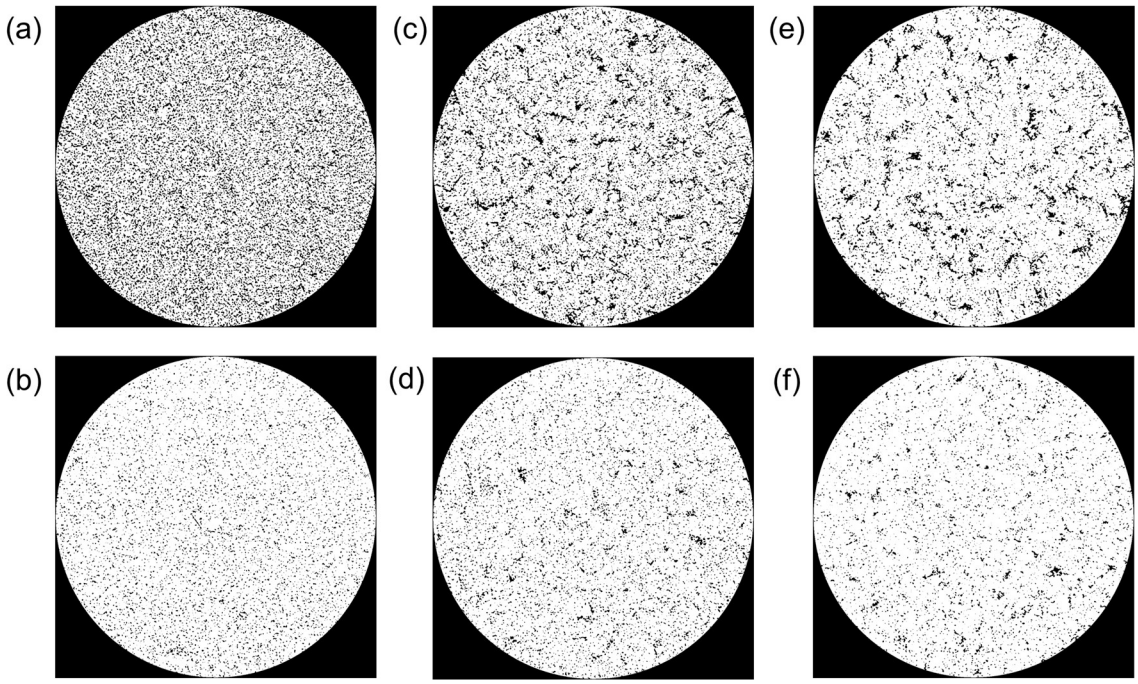

Fig. 4.4. Tablet physical microstructure within region of interest by 2D binary micro-CT images. Run #13: (a) and (b); Run #7: (c) and (d); Run #10: (e) and (f). Tablets with compression force at 10 kN: (a), (c) and (e); Tablets with compression force at 24 kN: (b), (d) and (f). Groups of white and black pixels represented the solids (object) and pores (background), respectively.

Table 4.5 Pore volume information within the volume of interest extracted on the basis of 3D analysis

Run#	Compression force (kN)	Volume percentage		
		Open pore	Closed pore	Total
13	10	18.40	0.601	18.90
	24	0.767	4.66	5.39
7	10	12.50	2.18	14.40
	24	1.88	4.94	6.72
10	10	7.53	2.58	9.92
	24	0.91	3.97	4.84

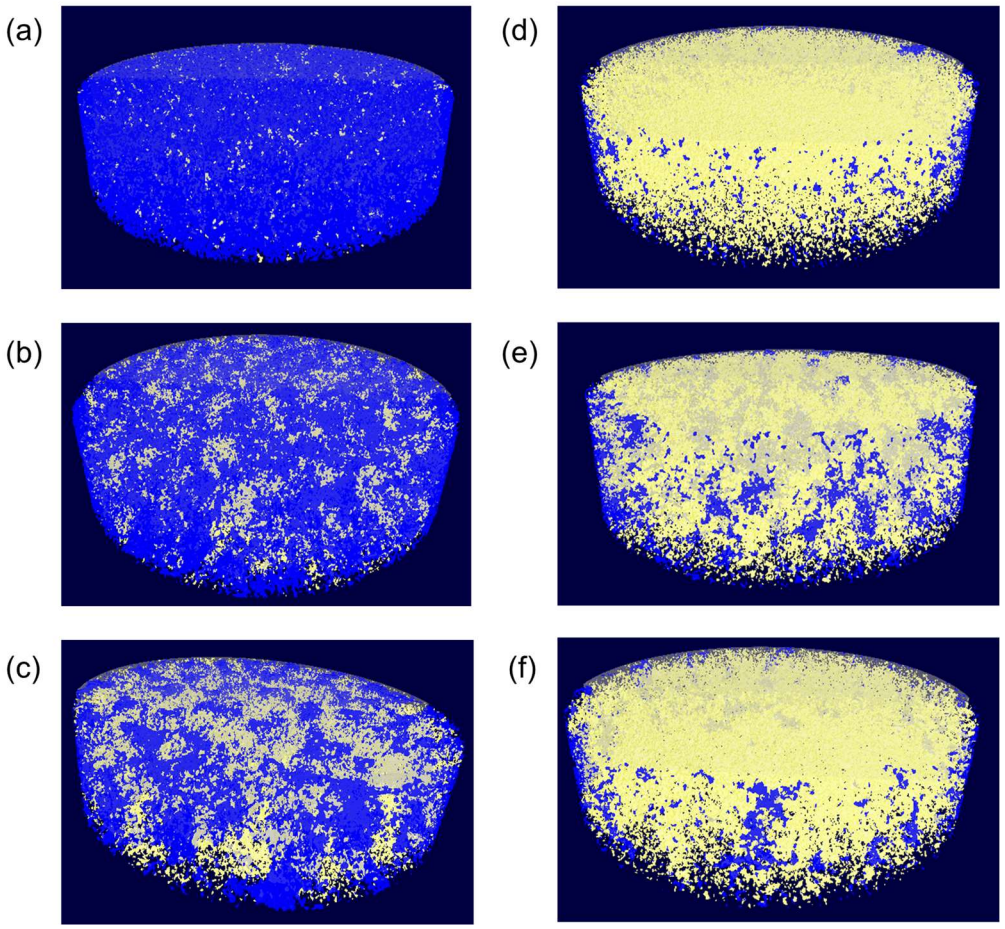

Fig. 4.5. 3D visualization of tablet open and closed pore networks within the volume of interest. Run #13: (a) and (d); Run #7: (b) and (e); Run #10: (c) and (f). Tablets with compression force at 10 kN: (a), (b) and (c); Tablets with compression force at 24 kN: (d), (e) and (f). Distribution was color-coded to differentiate the open pores (blue) from closed pores (yellow).

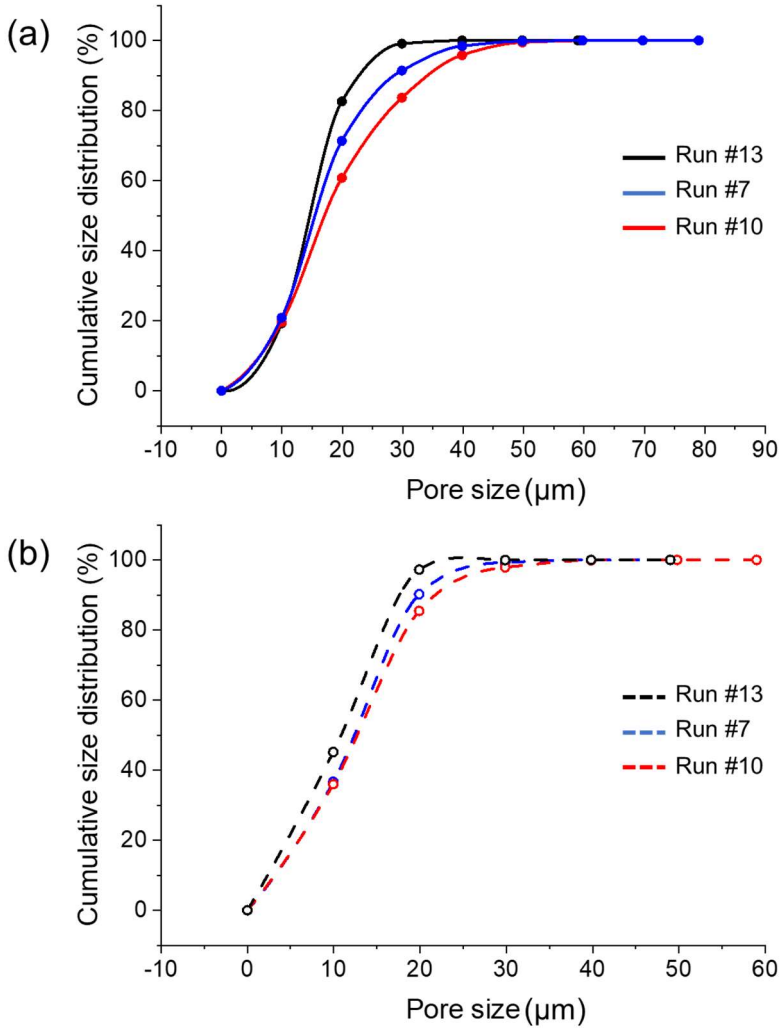

Fig. 4.6. Cumulative pore size distribution of tablets compressed at (a) 10kN and (b) 24 kN.

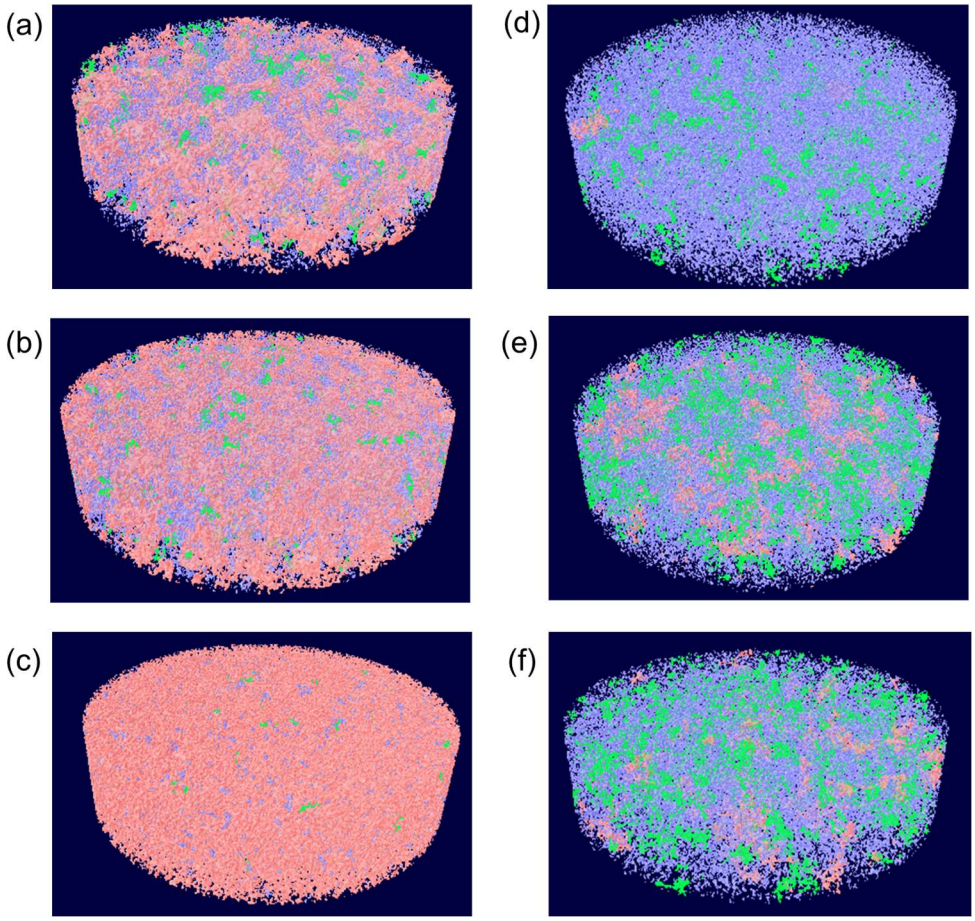

Fig. 4.7. 3D visualization of tablet pore size distribution within the volume of interest. Run #13: (a) and (d); Run #7: (b) and (e); Run #10: (c) and (f). Tablets with compression force at 10 kN: (a), (b) and (c); Tablets with compression force at 24 kN: (d), (e) and (f). The color code represented the pore volume within different size fractions: larger than 10000 voxels (red), between 1000 and 10000 voxels (green) and smaller than 1000 voxels (purple).

Tablet dissolution rate is inextricably interwoven with its physical microstructure (Ansari and Stepanek, 2008; Crean et al., 2010). To understand the process-structure and structure-property relationships, three representative batches of granules (run #7, #10 and #13) were selected and compressed into tablets. Due to distinct processing conditions in

Table 4.3, particles underwent different degrees of deformation and consolidation during granulation. Run #13 produced the most porous granules with a large porosity of 61.9% while run #10 manufactured the most desified granules with a small porosity of 33.7%. One of the DoE center points, run #7, generated granules with an intermediate level of porosity, 46.5%. As shown in Fig. 4.3, tablets compacted from different granules revealed appreciable discrepancies in their morphology. In terms of run #13, both tablet cross-sectional area and surface were relatively amorphous since the weaker granules were fragmented during the compaction process. In contrast, densified granules from run #10 were more resistant to the compression force and were merely subjected to rearrangement and deformation rather than fragmentation. Therefore, distinct boundaries among contiguous granules on both surface and cross section could be easily discovered. Besides, the morphology of tablets from run #7 was deemed to be between run #10 and #13, namely that granules experienced partial fragmentation during tableting. However, it seemd that all granules were inevitably turned into crumbles when the compression force was improved from 10 kN to 24 kN, despite that tablets in run #7 still demonstrated the most homogeneous appearance.

Fig. 4.4 reflected the tablets internal structure with one slice of their 2D binary micro-CT images. The region of interest (ROI) referred to the selected region on a single crossection image. It was apparent that tablets produced with denser granules or higher compression force possessed higher pore volume (more black pixels). The extracted information concerning open and closed pores in volume of interest (VOI) were listed in Table 4.5 and illustrated in Fig. 4.5. In comparison to ROI, the VOI referred to the integration of all ROIs across the selected image levels. In 3D space, closed pores were

defined as a connected assemblage of black voxels thoroughly surrounded by solid (white) voxels whereas open pores were those space situated within or between solid objects but had connections in 3D to the space outside the objects. It could be seen that with the compression force of 10 kN, an overwhelming majority of the pores in run #13 were connected to the outside space (blue color in Fig. 4.5) while more closed pores (yellow color in Fig. 4.5) were detected for run #10. Also, the overall tablet porosity consistently decreased from run #10 to run # 7 and eventually to run #13. It was inferred that denser granules experienced less deformation and more vigorous inter-particle interactions during compation, thereby leading to highly consolidated tablets with larger proportion of closed pores. In terms of 24 kN, nevertheless, the tablet porosity for all three batches declined considerably and almost all pores were encircled by the paritcles. In particular, the cylindrical tablets were surrounded circumferentially by the open pores leaving the closed pores in the inner areas.

The pore size distribution was plotted in Fig. 4.6 and visualized in 3D in Fig. 4.7. It could be discovered that the granule porosity was not only synonymous with the overall tablet porosity including the open/closed pore ratio but engendered different tablet pore size distribtuions. As apltly illustrated in Fig. 4.6 (a), although run #10 had smaller overall porosity compared with run #13, it demonstrated larger pore size in that the stronger granules underwent limited extent of rearrangements during compaction. Again the difference in size distribution became less pronounced as the compression force increased to 24 kN (see Fig. 4.6 (b)), which further corroborated the previous findings that high enough compression force could predominate the tablet morphology and internal structure over granule porosity. Furthermore, Fig. 4.7 showed that significant

amount of pores for run #10 10 kN tablet were colored by red, indicating their size was larger than 10000 voxels. Instead run #13 10 kN tablet exhibited more pores less than 1000 voxels highlighted by the color of purple. At 24 kN, pores of the latter larger than 10000 voxels nearly vanished due to its high compressibility while for the former and run #7 the pores in such a size fraction were still detectable.

4.3.2.2 Real-time monitoring of disintegration and drug release mechanisms

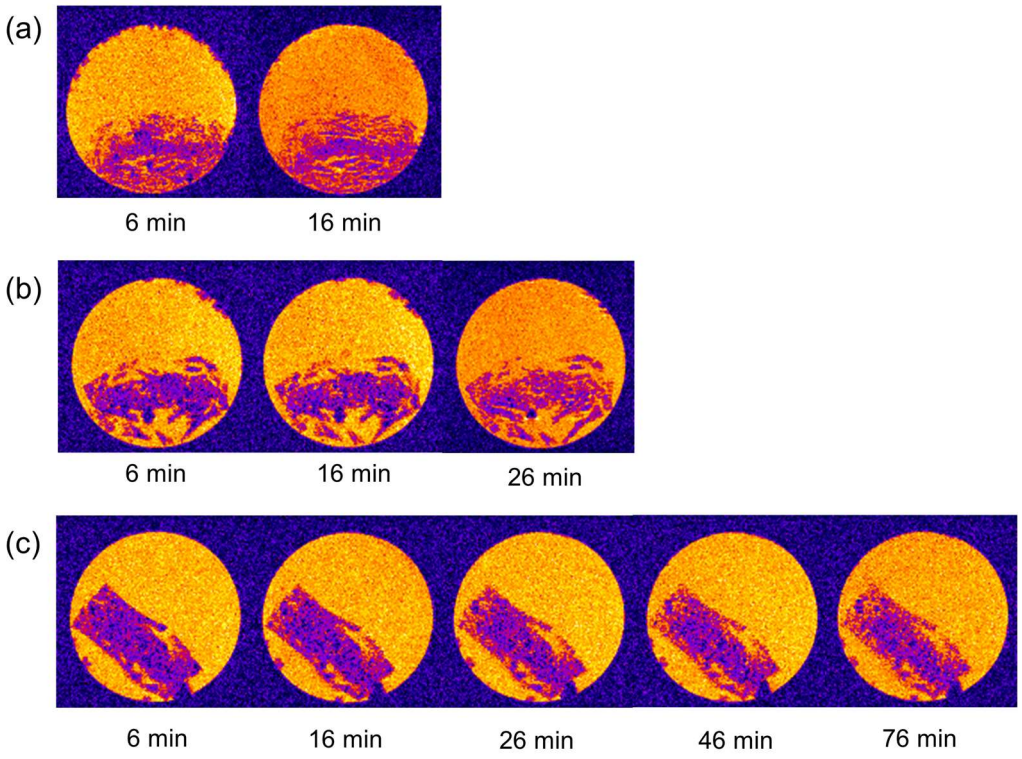

Fig. 4.8. *In situ* real-time observation of disintegration of tablets compressed at 10 kN by MRI. (a) Run #13, (b) Run # 7 and (c) Run # 10. The individual snapshots corresponded to different representative time points of respective MRI movies during dissolution. Colors within the field of view denoted dissolution medium (orange) and tablet (purple).

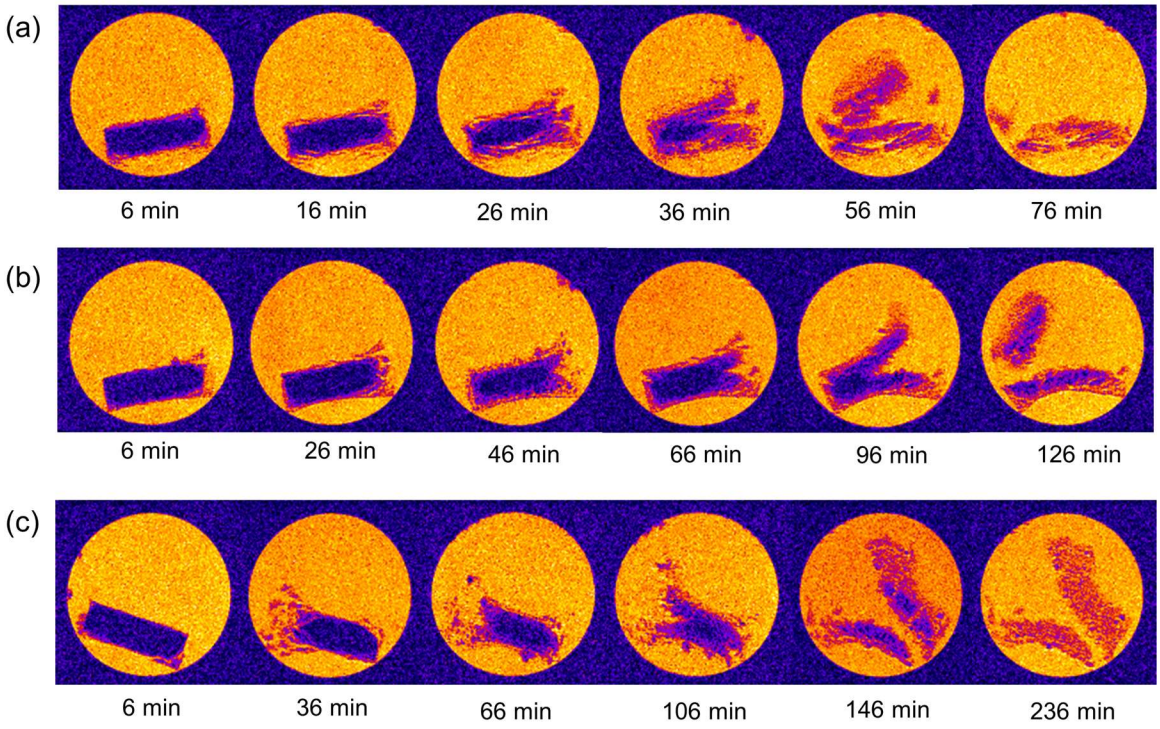

Fig. 4.9. *In situ* real-time observation of disintegration of tablets compressed at 24 kN by MRI. (a) Run #13, (b) Run # 7 and (c) Run # 10. The individual snapshots corresponded to different representative time points of respective MRI movies during dissolution. Colors within the field of view denoted dissolution medium (orange) and tablet (purple).

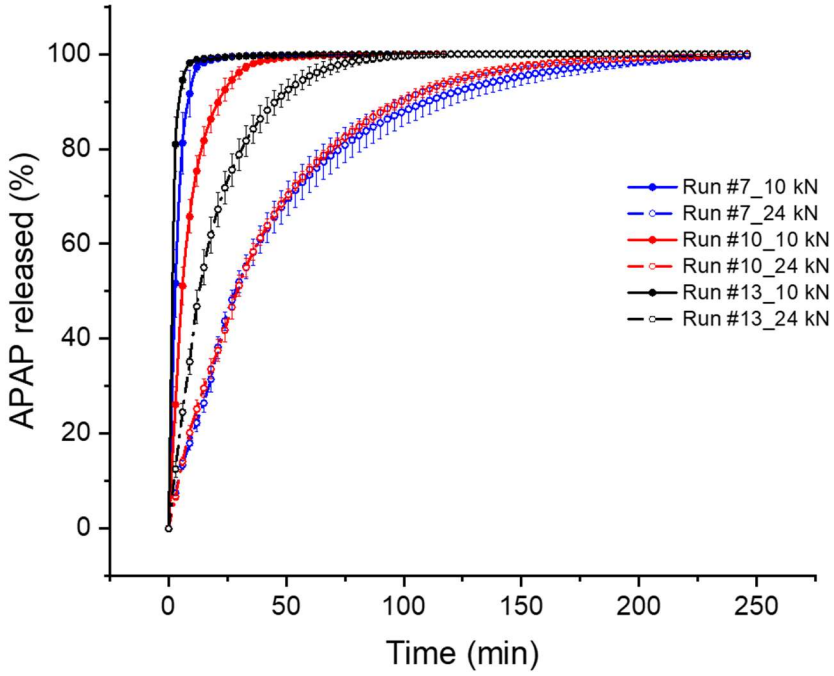

Fig. 4.10. Drug release kinetics of tablets produced at different granulation conditions and compression forces.

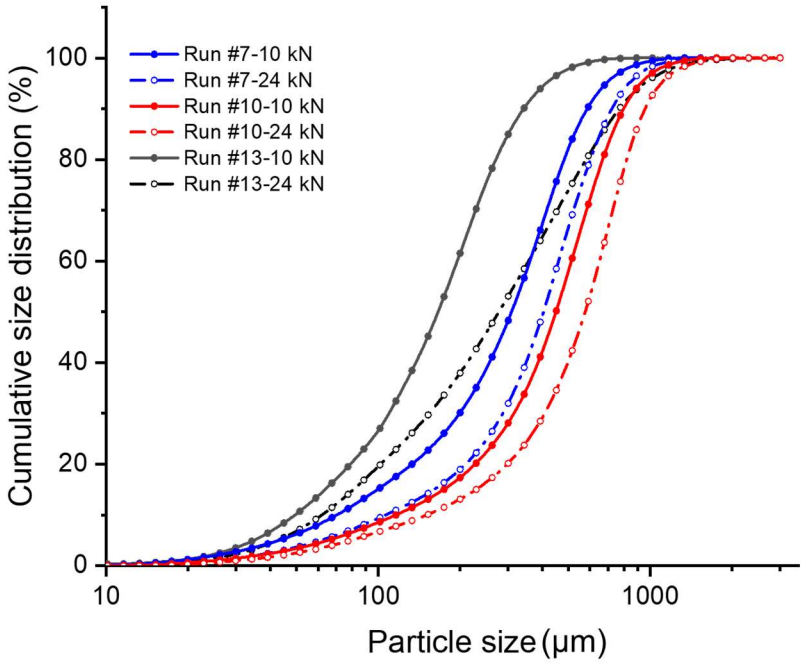

Fig. 4.11. Cumulative particle size distribution after tablet complete disintegration in the dissolution medium.

Table 4.6 Drug release parameters of tablets produced at different premixing, granulation, and compression conditions

Run#	Premixing method	Compression force (kN)	t_{3min} (%)	$t_{90\%}$ (min)	DE_{10min} (%)	DE_{90min} (%)
	Continuous	10	80.97	5.00	77.18	87.43
13	Continuous	24	12.50	45.51	20.08	70.71
	Batch	10	71.15	5.63	73.52	87.09
	Continuous	10	51.67	8.52	62.89	85.87
7	Continuous	24	7.50	110.12	10.82	51.86
	Batch	10	25.43	19.11	41.76	81.55
	Continuous	10	26.11	21.25	39.76	80.87
10	Continuous	24	6.62	98.83	11.33	52.69
	Batch	10	12.66	44.09	25.87	72.78

Fig. 4.8 and Fig. 4.9 depicted the disintegration process of tablets manufactured at 10 and 24 kN, respectively. Specifically, in Fig. 4.8, due to the presence of massive open pores, water rapidly penetrated into the matrix along with the wetting front consistently moving inward until the whole tablet was eventually soaked with dissolution medium, which gave rise to a fast disintegration and erosion process of the tablets from run #13 and #7. The corollary of that was fast drug release kinetics in light of the hydrophilic property of APAP. In contrast, tablet of run #10 remained relatively integral throughout the entire dissolution process by virtue of the closed pores and stronger interparticle bonding after compaction. Therefore, water penetration into the tablet and the ensuing dissolution of drug were relatively slow. In addition, as shown in Fig. 4.9, all tablets exhibited extended disintegration and dissolution behaviors once the compression force enhanced to 24 kN. However, it can be seen that the lamination occurred for all tablets impling the potentil of over compression. The drug release parameters in Table 4.6 and profiles in Fig. 4.10 were in accordance with their respective disintegration and erosion

speed. Particularly, it showed similar dissolution rate in terms of the 24 kN tablets from run #7 and #1, suggesting the undermined implication of granule internal structure.

In addition, the particle size distribution after complete tablet disintegration in Fig. 4.11 further substantiated the aforementationed results. Since original granule size selected for tableting (250-710 μm) was identical for all three batches, the size variation after disintegration embodied the extent of particle resistance to mechanical compression force with porous granules (#13) inclined to be crushed and densified granules (#10) in all likelihood being deformed. It was apparent that particle size steadily increased from run #13 to #7 and to #10, confirming the conclusions elicted from Fig. 4.3. Besides, it was noticeable that size distributions of 24 kN disintegrated tablets shifted to the positive direction of *x*-axis as opposed to those from 10 kN, principally because particles experiencing higher compaction force were still partially combined together even after the tablet disintegration, leading to larger residual aggregates.

4.3.3 Influence of drug agglomerate size distribution on dissolution performance

4.3.3.1 Tablet chemical microstructure

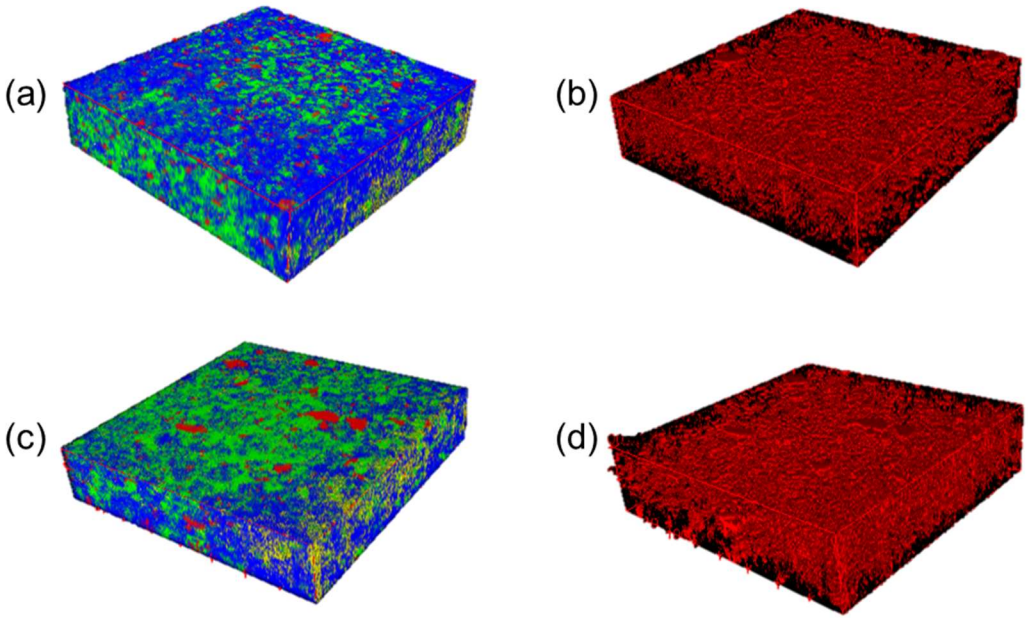

Fig. 4.12. 3D visualization of tablet ingredients distribution. APAP, MCC, Lactose and PVP were color-coded by red, blue, green and yellow, respectively. (a) Multi-component distribution of CM #13. (b) APAP distribution of CM #13. (c) Multi-component distribution of BM #13. (d) APAP distribution of BM #13.

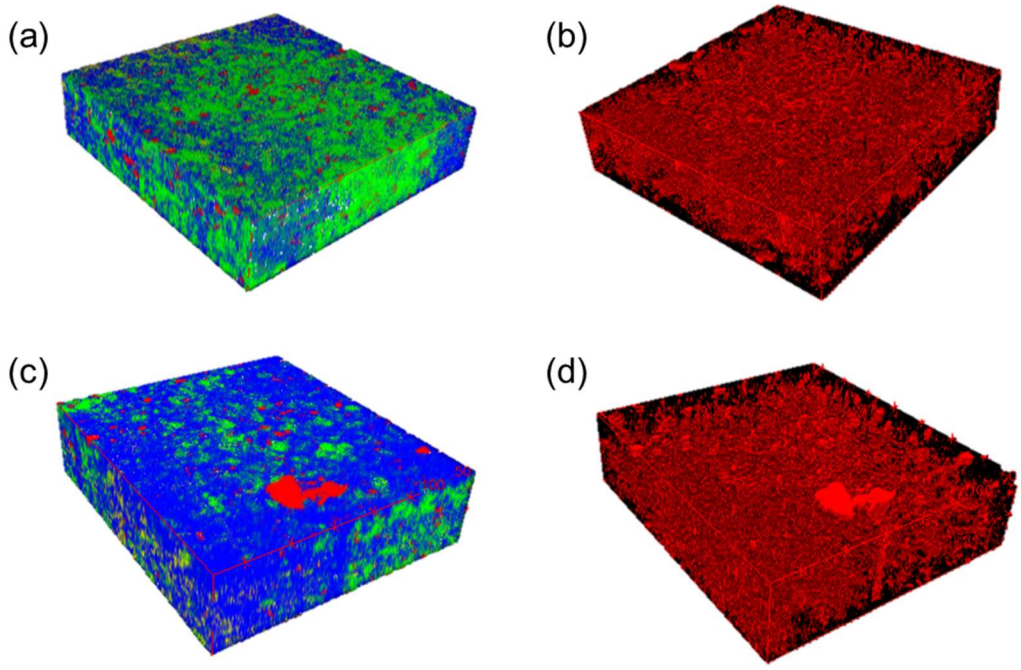

Fig. 4.13. 3D visualization of tablet ingredients distribution. APAP, MCC, Lactose and PVP were color-coded by red, blue, green and yellow, respectively. (a) Multi-component distribution of CM #7. (b) APAP distribution of CM #7. (c) Multi-component distribution of BM #7. (d) APAP distribution of BM #7.

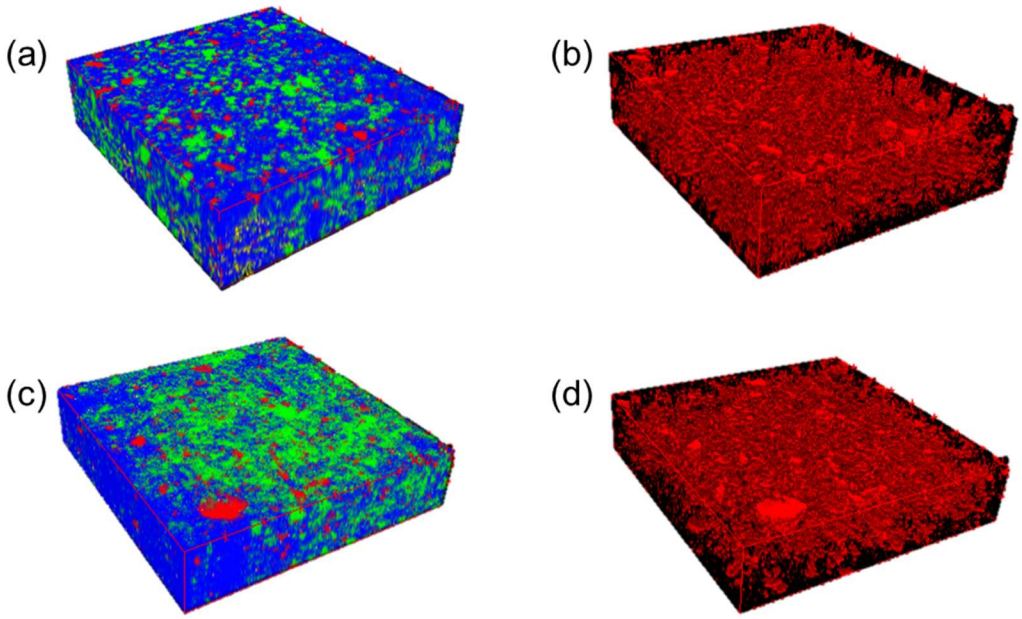

Fig. 4.14. 3D visualization of tablet ingredients distribution. APAP, MCC, Lactose and PVP were color-coded by red, blue, green and yellow, respectively. (a) Multi-component distribution of CM #10. (b) APAP distribution of CM #10. (c) Multi-component distribution of BM #10. (d) APAP distribution of BM #10.

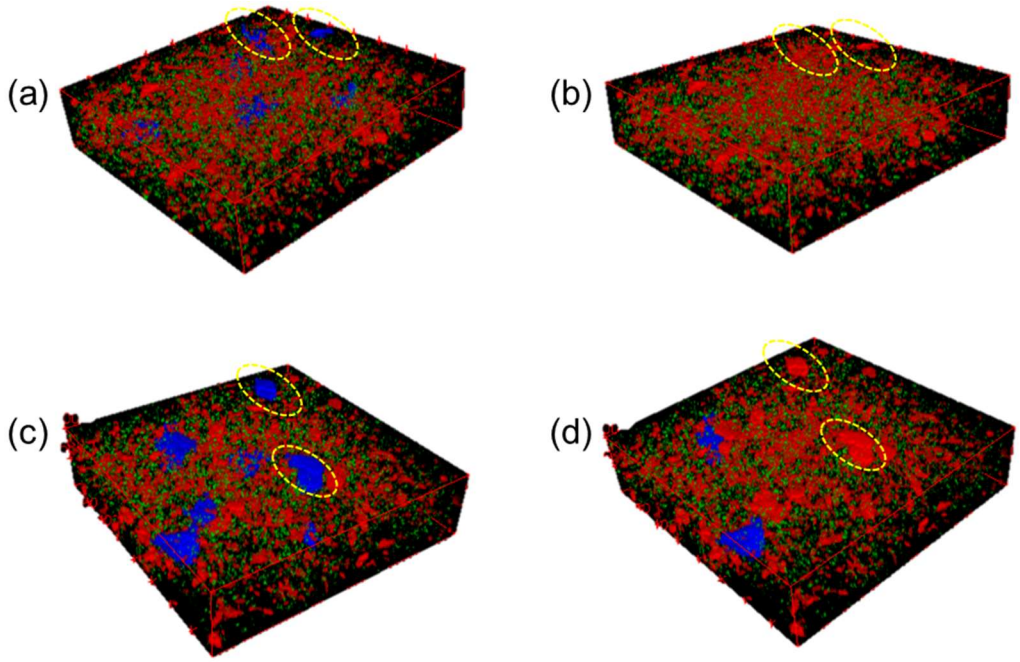

Fig. 4.15. 3D visualization of tablet drug agglomerate size distribution. The color code indicated the agglomerate volume in different size fractions. For (a) CM #13 and (c) BM #13, blue, red and green represented the size larger than 250 µm, between 250 and 50 µm, less than 50 µm, respectively. For (b) CM #13 and (d) BM #13, blue, red and green represented the size larger than 400 µm, between 400 and 50 µm, less than 50 µm, respectively.

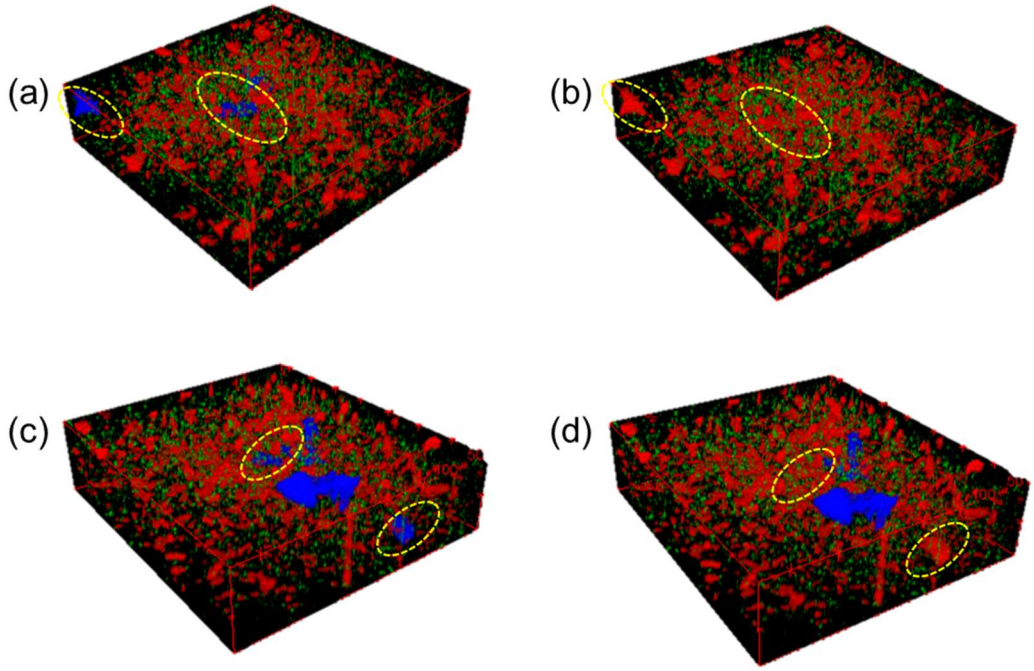

Fig. 4.16. 3D visualization of tablet drug agglomerate size distribution. The color code indicated the agglomerate volume in different size fractions. For (a) CM #7 and (c) BM #7, blue, red and green represented the size larger than 250 µm, between 250 and 50 µm, less than 50 µm, respectively. For (b) CM #7 and (d) BM #7, blue, red and green represented the size larger than 400 µm, between 400 and 50 µm, less than 50 µm, respectively.

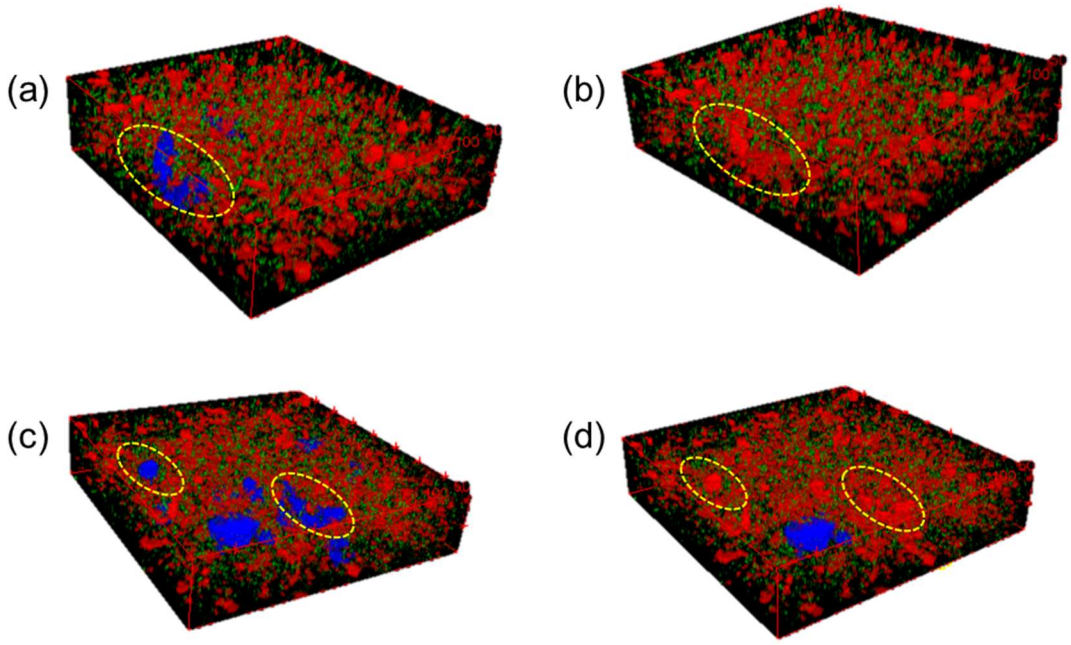

Fig. 4.17. 3D visualization of tablet drug agglomerate size distribution. The color code indicated the agglomerate volume in different size fractions. For (a) CM #10 and (c) BM #10, blue, red and green represented the size larger than 250 µm, between 250 and 50 µm, less than 50 µm, respectively. For (b) CM #10 and (d) BM #10, blue, red and green represented the size larger than 400 µm, between 400 and 50 µm, less than 50 µm, respectively.

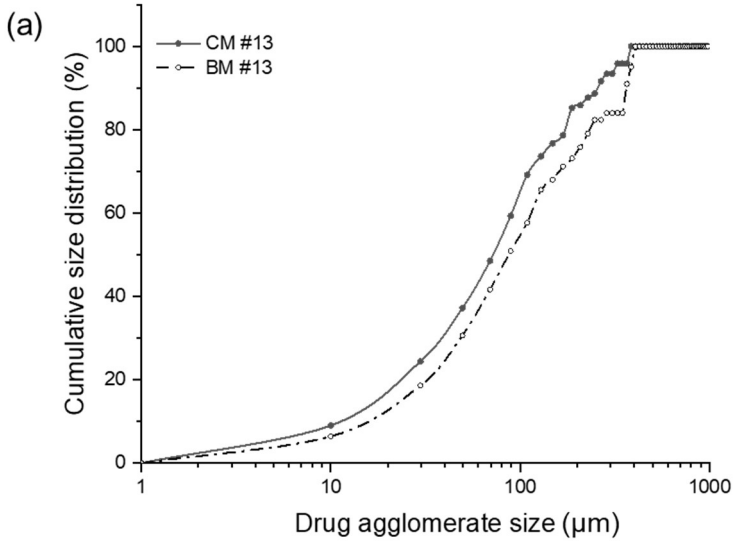
(a)
CM #13
BM #13
Cumulative size distribution (%)
Drug agglomerate size (μm)

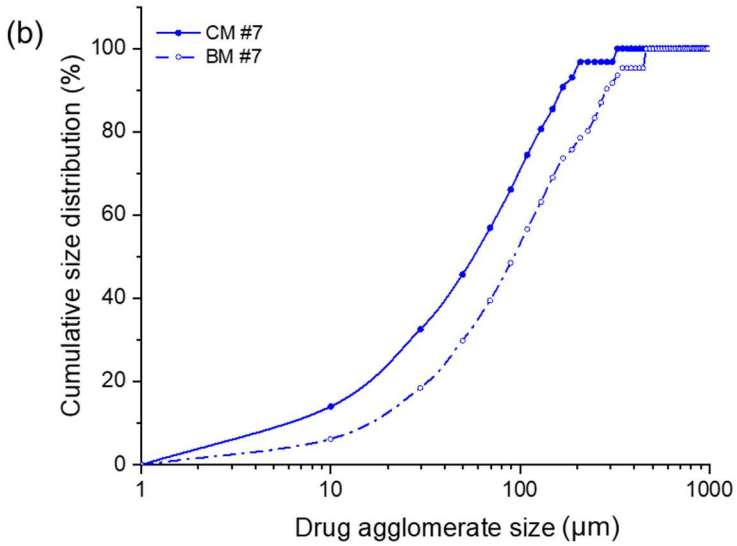
(b)
CM #7
BM #7
Cumulative size distribution (%)
Drug agglomerate size (μm)

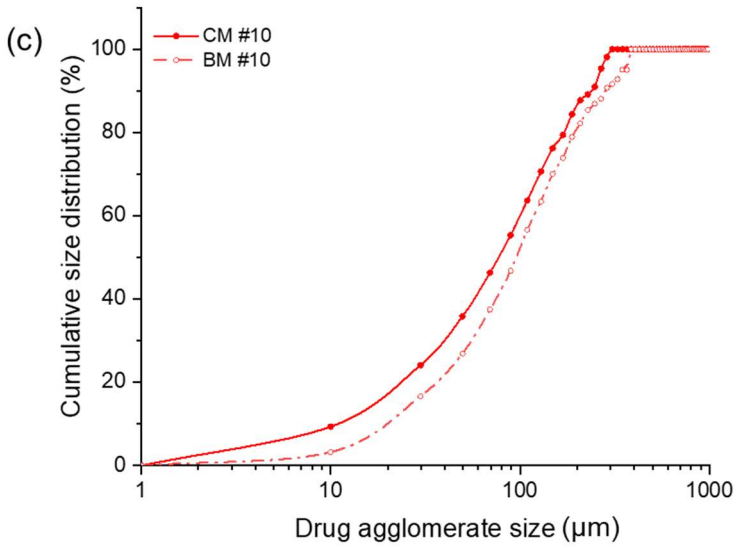
(c)
CM #10
BM #10
Cumulative size distribution (%)
Drug agglomerate size (μm)

Fig. 4.18. Cumulative drug agglomerate size distribution of tablets produced with distinct raw material premixing methods. (a) Run #13. (b) Run #7. (c) Run #10.

Aside from physical microstructure, tablet 3D chemical microstructure was also unveiled by the Raman imaging. Fig. 4.12 (a) and (b) showed the distribution of all ingredients and only APAP in a tablet produced from continuously mixed (CM) blends, respectively, while (c) and (d) conveyed analogous information in a tablet with raw materials premix prepared by batch mixing (BM). Although granulation settings were identical for both scenarios (run #13), stark difference in drug agglomerate size distribution was discovered. Notably continuous convective mixing coupled with delumping by conical mill were able to deliver more efficient micro- (dispersive) and macro- (distributive) mixing where both cohesive drug and excipients were uniformly dispersed and distributied. Specifically, the high-shear mixing associated with conical mill provided intense planar-shear effects for de-agglomeration. The convective mixing accompanied by intermediate-level shear contributed to stretching the interfacial area between ingredients absent from cohesive resistance and distributing them homogeneous throughout the product volume. In contrast, large drug agglomerates remained in the tablet when all ingredients were premixed in the gravity-driven low-shear batch tote blender. Similarly, outcome of Fig. 4.13 and Fig. 4.14 under the respective granultion condition of run #7 and #10 further ascertained the aforementioned inference, i.e, superior blend uniformity and structure at the output of continuous mixer with small scale of segregation and low intensity of segregation.

Furthermore, Fig. 4.15, Fig. 4.16 and Fig. 4.17 specifically focused on APAP rather than all ingredients in the tablets and provided a more straightforward illustration of the

drug agglomerate size distribution. For instance, in Fig. 4.15 (a) and (c), color code identified the APAP spatial distribution in tablets from continuous and batch mixing blends by adopting the first classification of particle/agglomerate size fractions. Green stood for the size smaller than 50 μm; red represented the range from 50 to 250 μm; blue highlighted the particles larger than 250 μm. Fig. 4.15 (b) and (d) provided similar information but utilized the second classification of size fractions that the upper size threshold for visualizing APAP agglomerates increased from 250 to 350 μm. By comparing Fig. 4.15 (a) to (c), more blue domains can be observed in the latter, evidencing more large clumps of drug agglomerates in the BM tablet. Moreover, once the upper size threshold value increased from 250 to 350 μm, all blue domains in CM tablet turned into red (see yellow dash circles in Fig. 4.15 (a) and (b)), indicating the non-existence of agglomerate larger than 350 μm. Nonetheless for BM tablet several APAP domains still remained as blue, i.e., larger than 350 μm, albeit the increase of upper size threshold (see Fig. 4.15 (c) and (d)). The same conclusions can be elicited by examining Fig. 4.16 and Fig. 4.17, irrespective of the granulation parameters. Also, cumulative size distribution in Fig. 4.18 was consistent with the previous findings that the curves of all BM tablets shifted to the positive direction of *x*-axis implying their relatively large size distribution. Therefore, despite that wet granulation accommodated material variability better than direct compression, heterogeneity of chemical structure within tablets was still discovered. Additionally, the degree of heterogenetiy was contingent on whether the dry powders were pre-blended in a batch blender or a continuous blender.

4.3.3.2 Dissolution performance

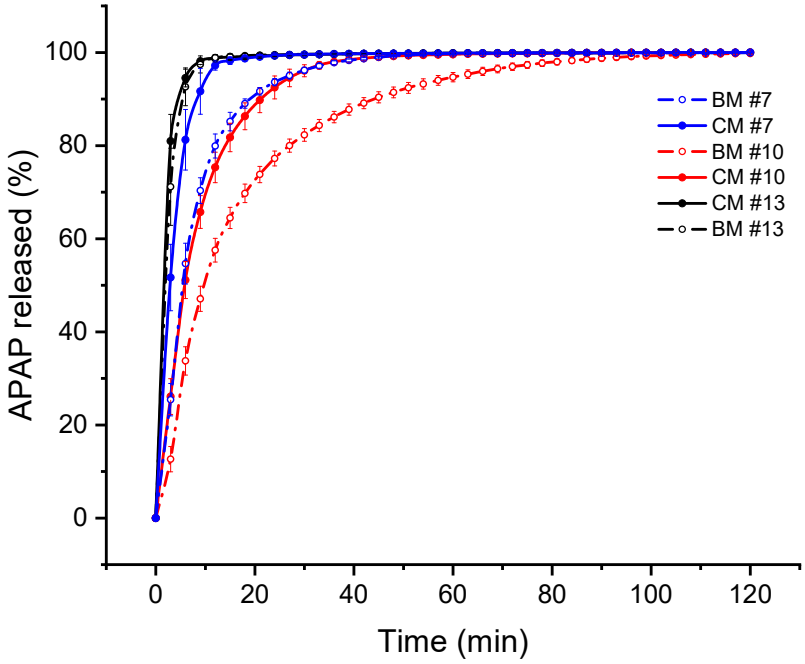

Fig. 4.19. Drug release kinetics of tablets produced with different raw material premixing methods and granulation conditions.

The dissolution profiles in Fig. 4.19 and parameters in Table 4.6 demonstrated remarkable difference regarding the dissolution behavior between CM and BM tablets. According to the student's t-test (not shown), drug agglomerate size had significant influence on the release kinetics. With the identical granulation, tableting and dissolution conditions, tablet physical microstructure in all likelihood were similar to each other. The variation in APAP dissolution rate was thus believed to be stemming from the raw materials pre-mixing stage, namely the discrepancy in drug agglomerate size. It can be seen that all BM tablets displayed slower release rate as opposed to their CM counterparts. In the present study, the grade of APAP used was semi-fine with a median diameter of 29.8 μm. As a result, powder exhibited less desirable flowability and primary particles had a high tendency to form aggregates during mixing where cohesion and

adhesion forces composed of intermolecular forces (van der Waals interactions and hydrogen bonding), electrostatic interactions (contact potential) and capillary forces (liquid bridge between particles and solid bridging due to crystal bonding) had played a pivotal role (Kale et al., 2009). In the following dissolution process, agglomerates with large size or high packing fractions minimized the drug surface exposed to the surrounding medium and was unable to be readily dispersed, thereby resulting in delayed drug release kinetics. By switching to the continuous mixing, breakage of cohesive intra-agglomerate bonds and the concomitant highly dispersed particles could effectively enhance the drug exposure surface area as well as the ensuing dissolution rate.

4.4 Conclusions

In this study, L/S ratio and impeller rotation speed showed predominant effect over powder feeding rate on critical quality attributes of tablets. The process parameters were capable of modulating tablet performance via altering granule properties, primarily size distribution and porosity. Dissolution mechanisms with different granulation conditions were expounded by correlating the tablet physical microstructure to disintegration speed. It was found that higher compression force and denser granules resulted in smaller tablet porosity with more closed pores, which subsequently delayed the matrix erosion and impeded the drug release. The influence of drug agglomerate size on tablet dissolution was also demonstrated by leveraging two distinct raw materials premixing methods. In contrast to low-shear batch mixing, continuous mixing enabled better deagglomeration effect, thus facilitating the release process on account of more dispersed small drug aggregates.

Chapter 5

Continuous high-shear granulation: influence of material properties and binder delivery on critical quality attributes of granules and tablets

5.1 Objectives

This work shed light on the effect of raw material properties and binder delivery methods on the critical quality attributes of granules (size distribution, porosity and drug segregation) and tablets (hardness and drug agglomerate size). Process parameters, such as impeller speed, L/S ratio and throughput, of a continuous high-shear mixer granulator, CoriMix® CM5, were held constant at optimum levels. The objectives were to: (1) investigate the effect of drug hydrophobicity in low-dose formulations; (2) examine the influence of drug primary particle size in low-dose formulations; (3) understand the implications of drug loading by utilizing low-dose, medium-dose and high-dose formulations; (4) assess the impact of binder addition approaches, liquid solution viscosity and surface tension for each studied formulation.

5.2 Materials and methods

5.2.1 Materials

The present study evaluated in total eight different formulations. α-lactose monohydrate (310 NF, Foremost Farms USA, Baraboo, WI) and microcrystalline cellulose (MCC, Avicel® PH101, FMC Biopolymer, Philadelphia, PA) were used as the excipients for each formulation. Caffeine anhydrous (CSPC Innovation Pharmaceutical, Hebei, China), salicylic acid (99+%, ACROS Organics™, Thermo Fisher Scientific, Pittsburgh, PA), ibuprofen 70 (BASF SE, Ludwigshafen, Germany), micronized acetaminophen (APAP, Mallinckrodt Inc, Raleigh, NC), powder acetaminophen

(Mallinckrodt Inc, Raleigh, NC) and dense acetaminophen (Mallinckrodt Inc, Raleigh, NC) were incorporated as model drugs with varying water solubility and primary particle size. Two grades of polyvinylpyrrolidone (PVP, Sigma-Aldrich, Taufkirchen, Germany), K30 and K90, were utilized as binder. The surface tension of selected granulation liquid was altered by the addition of sodium dodecyl sulfate (SDS, Sigma-Aldrich, Taufkirchen, Germany). Specifications of primary particle size and water solubility of model drugs and excipients were listed in Table 5.1.

Table 5.1 Key physical specifications of formulation ingredients

Component	D10 (μm)	D50 (μm)	D90 (μm)	Water solubility, 25 °C (mg/ml)
Caffeine	8.09	31.13	67.71	22
Salicylic acid	5.53	33.94	68.09	2.48
Ibuprofen	9.13	31.96	74.22	0.015
Micronized APAP	5.01	14.49	35.71	19
Powder APAP	10.35	40.20	88.70	19
Dense APAP	28.84	90.65	146.70	19
MCC	22.35	66.79	119.6	Insoluble
Lactose	14.48	71.22	125.3	195

5.2.2 Preparation of binder solutions

For each examined formulation, both dry and wet binder delivery methods were employed. For dry binder addition method, 4% (w/w) PVP K30 was premixed with other ingredients as dry powders. Distilled water as granulation liquid was pumped into the system in dripping mode during granulation process. With respect to wet binder addition method, three different aqueous solutions containing 4% (w/w) PVP K30, 4% (w/w) PVP K90 and 4% (w/w) PVP K30 with 1% (w/w) SDS were prepared accordingly (refer to Table 5.2).

Table 5.2 Binder delivery and composition of granulation aqueous solution

Code of granulation liquid	Binder delivery method	Composition of solutions (% w/w)			
		Solvent	Binding agent		Surfactant
		Distilled water	PVP K30	PVP K90	SDS
L1	Dry	100	-	-	-
L2	Wet	96	4	-	-
L3	Wet	96	-	4	-
L4	Wet	95	4	-	1

5.2.3 Experimental design

A full-factorial design presented in Table 5.3 included eight different formulations accompanied by four granulation liquids for each, which generated thirty-two experiments in total. For each batch code, the letter (e.g. “A”) indicated the formulation while the following number (e.g. “1”) was the number in the code of granulation liquid in Table 5.2. To investigate the effect of drug hydrophobicity in low-dose formulation, batches of “A1-A4”, “B1-B4” and “C1-C4” utilized ibuprofen, salicylic acid, and caffeine as APIs with similar primary particle size but disparate water solubility. To examine the influence of drug primary particle size in low-dose formulation, batches of “D1-D4”, “E1-E4” and “F1-F4” employed micronized, powder and dense APAP as APIs with identical water solubility but distinctive primary particle size (see Table 5.1). To understand the implications of drug loading, batches of “A1-A4”, “G1-G4” and “H1-H4” incorporated ibuprofen with varying percentages to exemplify low-dose, medium-dose and high-dose formulations, respectively.

Table 5.3 The 32-run full-factorial design for continuous high-shear granulation

Batch code	Proportion of formulation component (% w/w)					Granulation liquid	Granulation processing condition		
	Drug		MCC	Lactose	PVP K30		L/S ratio	Throughput (kg/h)	Rotation speed (rpm)
	Type	Loading							
A1	Ibuprofen	8	44	44	4	L1	0.4	15	2000
A2			46	46	-	L2	0.3		
A3					-	L3			
A4					-	L4			
B1	Salicylic Acid	8	44	44	4	L1	0.4		
B2			46	46	-	L2	0.3		
B3					-	L3			
B4					-	L4			
C1	Caffeine	8	44	44	4	L1	0.4		
C2			46	46	-	L2	0.3		
C3					-	L3			
C4					-	L4			
D1	Micronized APAP	8	44	44	4	L1	0.4		
D2			46	46	-	L2	0.3		
D3					-	L3			
D4					-	L4			
E1	Powder APAP	8	44	44	4	L1	0.4		
E2			46	46	-	L2	0.3		
E3					-	L3			
E4					-	L4			
F1	Dense APAP	8	44	44	4	L1	0.4		
F2			46	46	-	L2	0.3		
F3					-	L3			
F4					-	L4			
G1	Ibuprofen	30	33	33	4	L1	0.4		
G2			35	35	-	L2	0.3		
G3					-	L3			
G4					-	L4			
H1	Ibuprofen	80	8	8	4	L1	0.4		
H2			10	10	-	L2	0.3		
H3					-	L3			
H4					-	L4			

5.2.4 Experimental set-up

5.2.4.1 Preparation of raw material blends

The excipients and PVP K30 (only for dry binder addition method) were firstly premixed in a Glatt tumble tote blender (Model TAM 40, Glatt GmbH, Binzen,

Germany) for 30 minutes at 25 RPM, and then transferred into a K-Tron loss-in-weight (LIW) feeder (KT 35, K-Tron Soder, Niederlenz, Switzerland). Another K-Tron LIW feeder (KT 20) was used for dosing API gravimetrically. The drug and excipients were then mixed in a Glatt convective continuous mixer (Model GCG-70) under 260 RPM with a total powder feeding rate of 30 kg/h. A Quadro conical screen mill (Comil®, Model #197S, Quadro Engineering, Ontario, Canada) was integrated into the experimental set-up upstream of the mixer to de-lump agglomerates from incoming powder stream and enhance the micro-mixing behavior with high shear input (see Fig. 5.1 (a)). The mill equipped with a 800 µm round-holed screen was operated at 1420 rpm.

5.2.4.2 Continuous high-shear granulation

Fig. 5.1 illustrated the manufacturing process of granules. The premixed materials were subjected to high-shear granulation in the Lödige CoriMix® CM5 granulator (Gebrüder Lödige Maschinenbau GmbH, Paderborn, Germany). Liquid constituents were pumped tangentially from the top addition port into the product layer through a single phase nozzle in dripping mode. To enable comparable results between different formulations, critical process parameters were held constant at optimum levels, i.e., powder feeding rate of 15 kg/h and impeller rotation speed of 2000 rpm. In particular, L/S ratio was optimized separately with respect to dry and wet binder addition method. The former adopted a liquid content of 0.4 whereas the latter fixed the value at 0.3.

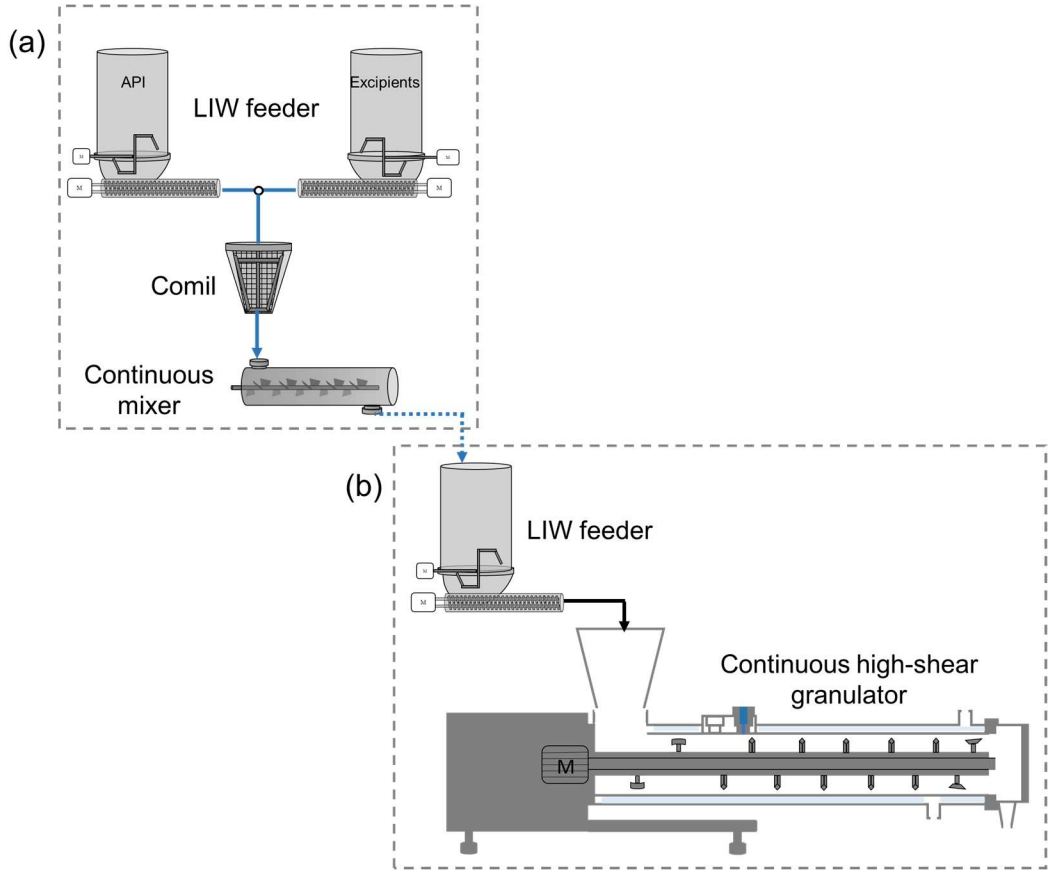

Fig. 5.1. Experimental set-up for granules production. (a) Premixing of raw materials prior to granulation. (b) Continuous high-shear granulation.

5.2.5 Characterization of raw material blends

5.2.5.1 Bulk solids flow properties

The flow properties of raw material blends were measured by a rotational shear cell module associated with the FT4 Powder Rheometer (Freeman Technology, Worcestershire, UK). During testing, powder was firstly filled into a 25 mm/10 ml glass vessel and then subjected to a four-step procedure: conditioning, consolidation, preshearing and shearing. Specifically, conditioning with a helical blade moving downwards and upwards inside the powder bed was used to erase any consolidation history and ensure a homogeneous reproducible state. Prior to preshearing, a vented

piston applied 9 kPa initial consolidation stress on the powder bed followed by the rotation of a shear head inside the bulk materials to achieve a steady-state (preshear point) with a certain normal (σ_p) and shear (τ_p) stresses. Once the preshear point was established, a yield point was obtained by further shearing the sample with a decreased normal stress.

The paired preshear-shear procedure was repeated several times with different normal stresses until a yield locus was acquired. Based on the diagram of shear stress (τ)-normal stress (σ), Mohr circle analysis was deployed for the yield loci to obtain the major principal stress (σ_1) and unconfined yield strength (σ_c), which defined the flow function coefficient (ff_c) in Eq. 5.1. Moreover, the intercept of linear regression of yield loci on the τ-axis was defined as the cohesion (τ_1). The relationship between σ_1, τ_1, angle of internal frinction tan (φ) where φ was the slope of the linearized yield loci and the coordinate of the preshear point (σ_p, τ_p) was described by Eq. 5.2. The relationship between σ_1, σ_c and φ was given by Eq. 5.3.

$$\mathrm{ff_c} = \frac{\sigma_1}{\sigma_c} \tag{5.1}$$

$$\sigma_1 = (1+\sin\varphi)\cdot\left(\frac{\sigma_p + \frac{\tau_1}{\tan\varphi} - \sqrt{A^2\sin^2\varphi - \tau_p^2\cos^2\varphi}}{\cos^2\varphi}\right) - \frac{\tau_1}{\tan\varphi} \tag{5.2}$$

$$\sigma_c = \tau_1 \cdot 2 \cdot \tan\left(45 + \frac{\varphi}{2}\right) \tag{5.3}$$

5.2.5.2 Powder hydrophobicity

To understand the wetting behavior of each feed formulation, droplet penetration tests were performed with different granulating fluids on a static powder bed of raw material blends (see Fig. 5.2). FT4 Powder Rheometer was used to prepare the powder bed with

reproducible conditions. Appropriate amount of premix was subjected to the conditioning procedure in a 50mm/85ml split vessel where a blade traversed up and down several times through the powder bed to eliminate any pre-consolidation history. The conditioned powder bed was then split to generate a level surface for the droplet penetration test. A high-speed camera (GimaGO, NET USA, Highland, IN) was set up and recorded the penetrating process until there was no significant change in light reflection on the powder bed surface when drop penetration was deemed to be complete. The penetration time (t_p) was determined by analyzing the video in ImageJ. The dynamic solid-liquid contact angle (θ_d) calculated from Eq. 5.4 was used to estimate the materials wettability (hydrophobicity).

$$t_p = 1.35 \frac{V_o^{2/3}}{\varepsilon_{eff}^2 R_{eff}} \frac{\mu}{\gamma_{LV} \cos\theta_d} \tag{5.4}$$

where V_o is the droplet volume, ε_{eff} is the effective porosity of powder bed, R_{eff} is the effective pore radius, μ is the liquid viscosity, and γ_{LV} is the liquid-vapor surface tension.

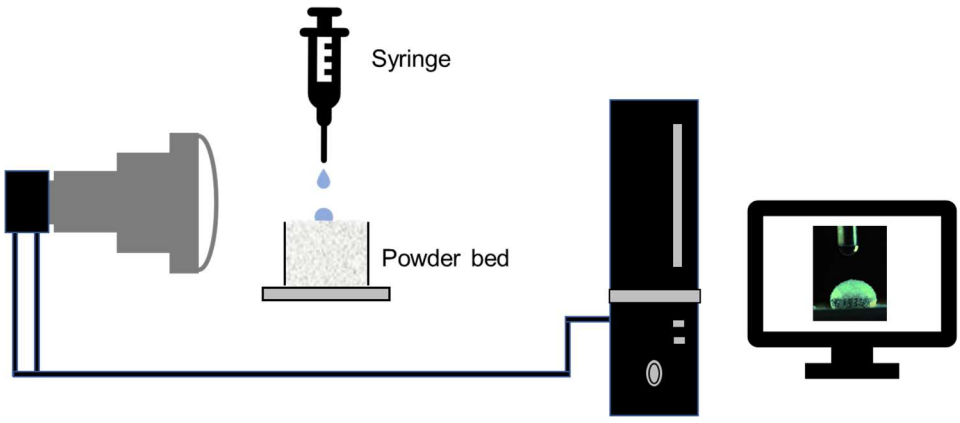

Fig. 5.2. Schematic illustration of the droplet penetration experimental set-up.

5.2.6 Granule characterization

Granules from each experiment were air-dried at ambient conditions until the loss-on-drying moisture content was less than 3%. The dried granules were then subsampled by spinning riffler (Gilson Company, Lewis Center, OH) to ensure unbiased sampling for different characterizations.

5.2.6.1 Particle size distribution

Particle size of raw materials in Table 5.1 was determined by laser diffraction analyzer (Beckman-Coulter Inc., Pasadena, CA). Granule size distribution (GSD) was measured by sieve analysis utilizing a $\sqrt{2}$ series of sieves with screen scale ranging from 38 μm to 4 mm. GSD was plotted as the normalized mass frequency (f_{mi}) shown in Eq. 5.5 versus the midpoint of each size interval on logarithmic scale (Allen and Elsevier, 2003).

$$f_{mi}(\ln x) = \frac{m_i}{\ln(\overline{n_i} / \overline{n_{i-1}})} \tag{5.5}$$

where m_i and $\overline{n_i}$ are the mass fraction and midpoint of size interval i , respectively.

5.2.6.2 Granule porosity

The true density of granules (ρ_t) was measured by a helium pycnometer (AccuPyc II 1340, Micromeritics, Norcross, GA) while the envelope density (ρ_e) was tested by Geopyc 1360 (Micromeritics, Norcross, GA). Granules with a size fraction of 1.0-1.4 mm were placed in a desiccator overnight prior to any densities measurements. The granule porosity (ε_g) was calculated by Eq. 5.6.

$$\varepsilon_g = 1 - \frac{\rho_e}{\rho_t} \tag{5.6}$$

5.2.6.3 Granule drug content uniformity

To examine the drug content uniformity, granules from each formulation in Table 5.3 were firstly sieved into seven different size fractions: less than 63, 63-125, 125-250, 250-500, 500-710, 710-1000 and larger than 1000 μm. 1 g sub-sample from each size fraction was then weighed and incubated in different solvents for 24 hours on a shaking platform without access to light. For granules containing hydrophilic drugs of caffeine and APAP, 10 ml distilled water was used as solvent while for those containing hydrophobic drugs of ibuprofen and salicylic acid, 10 ml methanol was added instead. All solutions were forced through 0.45 μm syringe filters and diluted to an appropriate concentration range if necessary. The UV-Vis absorption of different drugs at respective characteristic wavelength, namely ibuprofen at 264 nm, salicylic acid at 305 nm, caffeine at 273 nm and APAP at 243 nm, was determined by a spectrophotometer (Cary 60, Agilent Technologies, Santa Clara, CA).

The content of active ingredient in granules from each size class was calculated on the basis of calibration models developed for each drug ($R^2 > 0.999$). The extent of drug segregation in different size fractions was depicted by the de-mixing potential (DP) as defined in Eq. 5.7. Typically, DP was employed to quantify the content non-uniformity in order mixture with the assumption that a probability of w was associated with the concentration p in a specific size class. A small DP value signified more homogeneous distribution of drug across all size fractions.

$$\mathrm{DP}(\%) = \frac{100}{\bar{c}} \sqrt{\sum_{i=1}^{n} \frac{w_i}{100} (c_i - \bar{c})^2} \tag{5.7}$$

where $\bar{c}$ was the average concentration of active ingredient; c_i and w_i were the drug concentration and granule weight percent in a particular sieve size range *i*, respectively.

5.2.7 Tablet characterization

The dried granules between 125 to 500 μm from each low-dose formulation were compacted into tablets by a tablet press emulator (Presster™, Metropolitan Computing Corporation, East Hanover, NJ) with an upper compaction force of 10 kN. A round flat-faced punch was used to obtain cylindrical tablets with the diameter of 10 mm. Powder dosing weight was controlled around 350 mg for each tablet.

5.2.7.1 Tensile strength

Tablet thickness was measured by a digimatic digital caliper (Mitutoyo America, Aurora, IL) and radial fracture force was determined in a hardness tester (MultiTest 50, SOTAX, Westborough, MA). Tablet tensile strength was then calculated by the following equation (Fell and Newton, 1970),

$$\sigma_t = \frac{2F}{\pi dh} \tag{5.8}$$

where σ_t was the tablet tensile strength (MPa), F was tablet fracture force (N), d and h were the tablet diameter (mm) and thickness (mm), respectively.

5.2.7.2 Drug agglomerate size distribution

The 3D chemical mapping and structural analysis of drug agglomerates in the tablets with different formulations were investigated by a Raman imaging system (mPAT LAB-Pillerator, H2Optx, San Jose, CA). Layer thickness was defined as 40 microns and in total 20 layers of each tablet were scanned. The field of view was 4×4 mm. Image scan settings were 50 Z steps with 2 microns for each step. The Raman scan settings included

a XY resolution of 10×10 microns and laser current of 160 mA with a exposure time of 10 ms.

5.3 Results and discussion

5.3.1 Influence of drug hydrophobicity in low-dose formulations

5.3.1.1 Flow properties of raw material blends

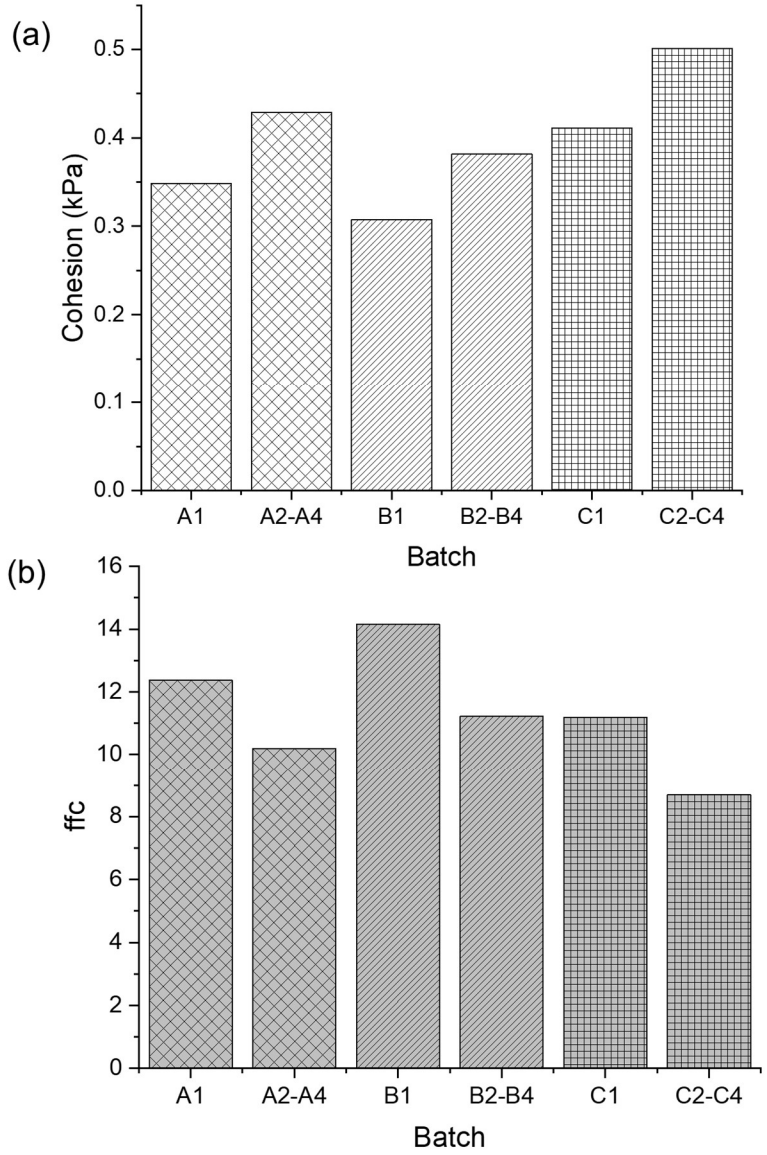

Fig. 5.3. (a) Cohesion and (b) flow function coefficient of low-dose formulation blends with different binder delivery methods and drug hydrophobicity.

Fig. 5.3 showed the cohesion and ff_c of different raw material blends. As mentioned earlier, PVP was premixed with all other ingredients in terms of dry binder addition method. In contrast, only API, MCC and lactose were premixed with repsect to wet binder addition method. Typically, cohesion of powder blends was inversely correlated to their ff_c, namely that better flowability was associated with larger ff_c and lower cohesion. It can be seen from Fig. 5.3 that flow properties of material blends were slightly enhanced with dry binder addition formulation irrespective of the API used. Although only 4 % PVP was added to the formulation, its relatively larger particle size (median diameter above 100 μm) still appreciably contributed to the improvement of powder flow properties.

5.3.1.2 Wettability of raw material blends

Pictures in Fig. 5.4 revealed the wettability of different formulation blends with corresponding granulation liquids. Apparently only some nuances of droplet penetration time can be detected and most of them were less than 1s. For these low-dose formulations, prolonged penetration time was discovered by using the binding solution with higher viscosity and poorly water soluble active ingredient. For instance, C3 demonstrated faster penetration rate compared to A3 and B3, which can be further accelerated by decreasing the solution viscosity. Influence of surface tension in this scenario was negligible given that the wettability of excipients predominated over API in the low-dose blends. Lactose was a water soluble ingredient and MCC has been deemed to be a “molecular sponge” due to its capability to retain and store substantial amount of water.

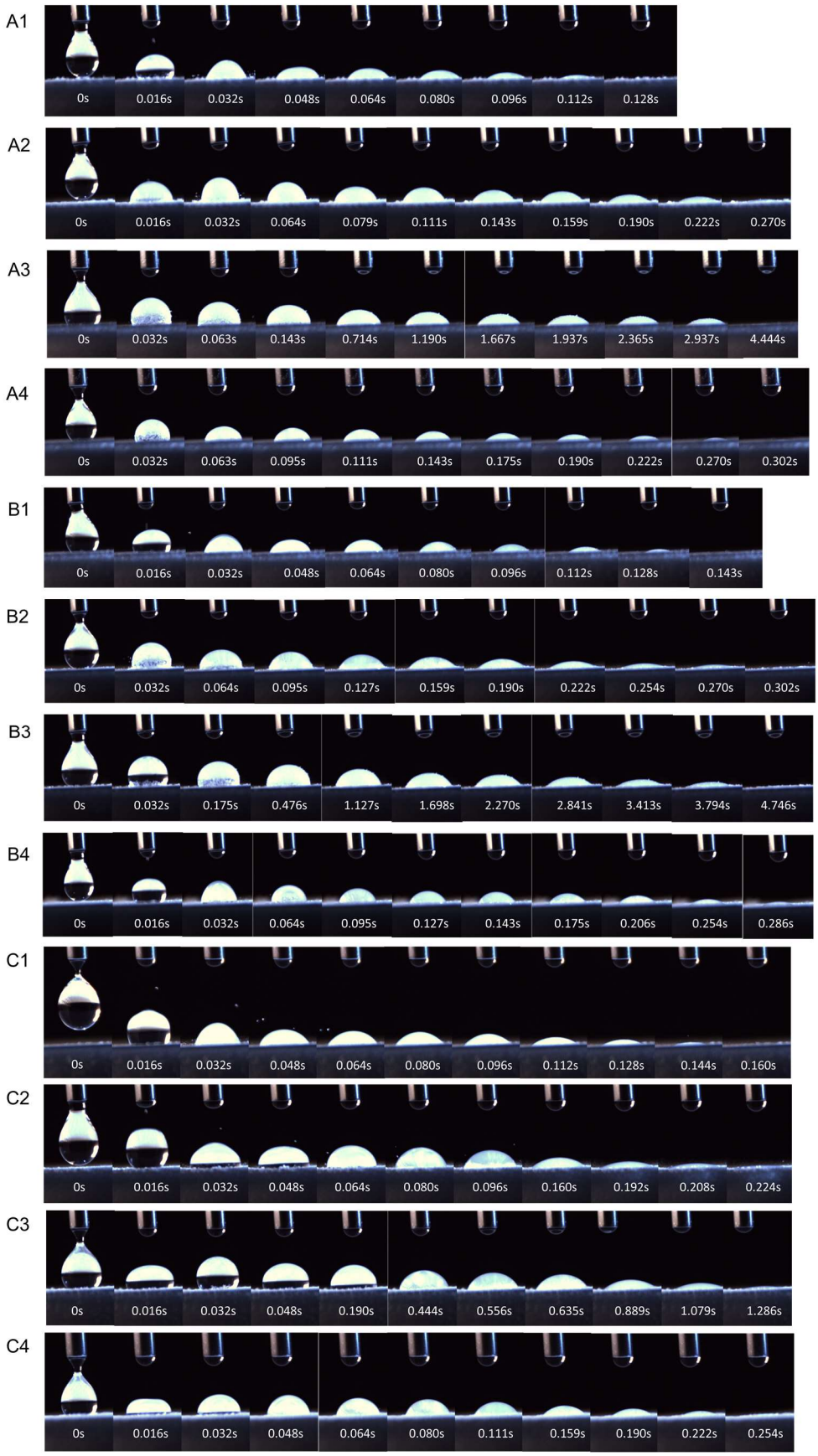
A1
0s 0.016s 0.032s 0.048s 0.064s 0.080s 0.096s 0.112s 0.128s
A2
0s 0.016s 0.032s 0.064s 0.079s 0.111s 0.143s 0.159s 0.190s 0.222s 0.270s
A3
0s 0.032s 0.063s 0.143s 0.714s 1.190s 1.667s 1.937s 2.365s 2.937s 4.444s
A4
0s 0.032s 0.063s 0.095s 0.111s 0.143s 0.175s 0.190s 0.222s 0.270s 0.302s
B1
0s 0.016s 0.032s 0.048s 0.064s 0.080s 0.096s 0.112s 0.128s 0.143s
B2
0s 0.032s 0.064s 0.095s 0.127s 0.159s 0.190s 0.222s 0.254s 0.270s 0.302s
B3
0s 0.032s 0.175s 0.476s 1.127s 1.698s 2.270s 2.841s 3.413s 3.794s 4.746s
B4
0s 0.016s 0.032s 0.064s 0.095s 0.127s 0.143s 0.175s 0.206s 0.254s 0.286s
C1
0s 0.016s 0.032s 0.048s 0.064s 0.080s 0.096s 0.112s 0.128s 0.144s 0.160s
C2
0s 0.016s 0.032s 0.048s 0.064s 0.080s 0.096s 0.160s 0.192s 0.208s 0.224s
C3
0s 0.016s 0.032s 0.048s 0.190s 0.444s 0.556s 0.635s 0.889s 1.079s 1.286s
C4
0s 0.016s 0.032s 0.048s 0.064s 0.080s 0.111s 0.159s 0.190s 0.222s 0.254s

Fig. 5.4. Droplet of binding solutions penetrating into powder bed of low-dose formulation blends with different API hydrophobicity.

5.3.1.3 Granul size distribution

The GSD and sizing metrics (D10, D50 and D90) was illustrated in Fig. 5.5 and Fig. 5.6, respectively. Clearly, a monomodal distribution was obtained by using dry binder addition method and more oversized particles were generated with high viscosity granulation liquid (L3), resulting in a biomodal size distribution with the largest particle sizing metrics. Due to the low viscosity of water, minimum drop overlapping occurred during granulation process, which is conducive to the improvement of liquid redistribution and more homogeneous particle growth. In addition, formulation with caffeine as the active ingredient produced the largest size metrics as opposed to those with ibuprofen and salicylic acid. It was inferred that the intrinsic hydrophilic nature of caffeine may possess higher degree of liquid saturation and was more amenable to paritcle consolidation and coalescence.

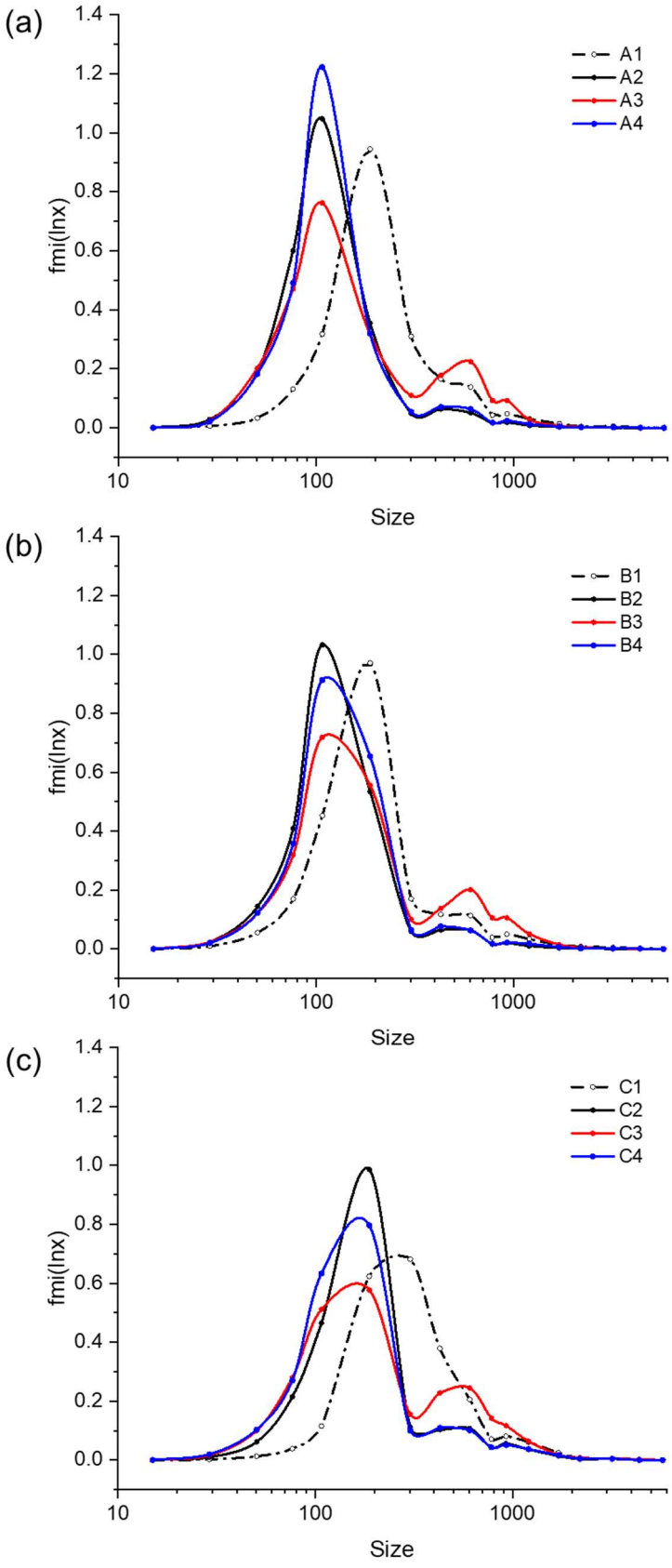
(a)
fmi(lnx)
Size
A1
A2
A3
A4
(b)
fmi(lnx)
Size
B1
B2
B3
B4
(c)
fmi(lnx)
Size
C1
C2
C3
C4

Fig. 5.5. Granule size distribution of low-dose formulations with different drug hydrophobicity. Varying binder delivery methods and solution properties for (a) batch code A (ibuprofen as API), (b) batch code B (salicylic acid as API) and (c) batch code C (caffeine as API).

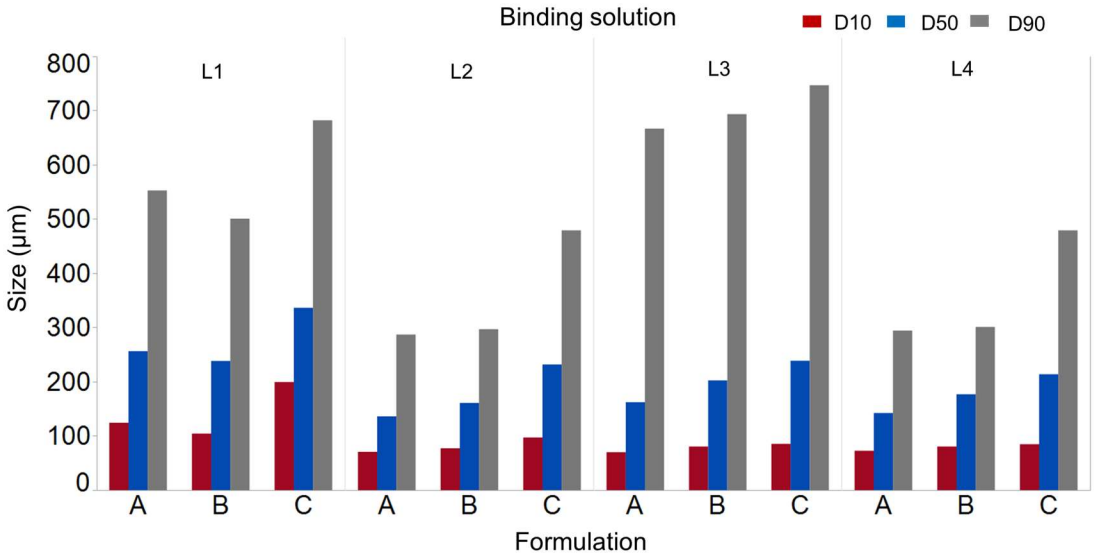

Fig. 5.6. Column plot of granule sizing metrics (D10, D50 and D90) of low-dose formulations with different drug hydrophobicity. Varying binder delivery methods and solution properties (L1, L2, L3 and L4) for (a) batch code A (ibuprofen as API), (b) batch code B (salicylic acid as API) and (c) batch code C (caffeine as API).

5.3.1.4 Porosity

Fig. 5.7 indicated that dry binder delivery method gave rise to the most densified granules whereas solution of PVP K90 generated the most porous granules. Due to the relatively low viscosity of water, granules were subjected to higher extent of deformation during consolidation, thereby leading to granules with smaller voidage. In contrast, particles bound by the viscous PVP K90 solution were more resistant to the collisions and structural modulation. Consequently, pore volume was able to be retained once liquid

evaporated after drying. Furthermore, granule porosity decreased for all formulations by reducing the liquid surface tension.

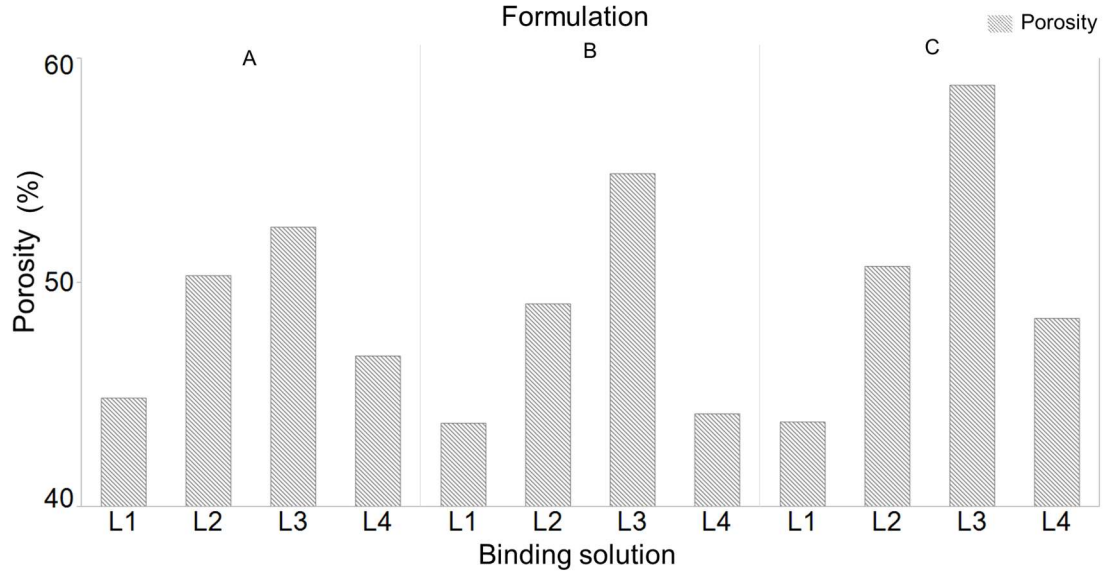

Fig. 5.7. Column plot of granule porosity of low-dose formulations with different drug hydrophobicity. Varying binder delivery methods and solution properties (L1, L2, L3 and L4) for batch code A (ibuprofen as API), batch code B (salicylic acid as API) and batch code C (caffeine as API).

5.3.1.5 Granule drug content uniformity

Fig. 5.8 showed the distribution of active ingredient across the seven size fractions. The drug content in each class as opposed to the overall mean was defined as the percentage drug claim. In terms of formulations with hydrophobic API, it was evident that fine particles (less than 63 μm) and granules in the class of 250-500 μm were super-potent while those in the fraction of 125-250 μm were sub-potent. Besides, the more hydrophobic the API was, the higher extent of super-potency was discovered in the fines. In other words, granules with ibuprofen as the active ingredient demonstrated higher contents in granules less than 63 μm in comparison to those containing salicylic acid.

However, granules with hydrophilic drug, caffeine, as the active ingredient was most sub-potent in the fines and super-potent in the middle size fraction of 125-250 or 250-500 μm. Fig. 5.9 displayed the de-mixing potential for all formulation studied. The results indicated that granules containing caffeine generated the most severe API segregation regardless of the binder delivery method and solution properties.

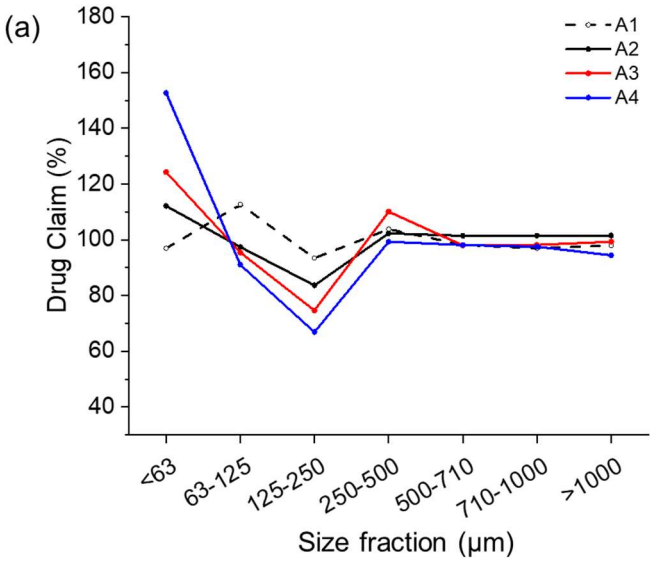
(a)
A1
A2
A3
A4
Drug Claim (%)
180
160
140
120
100
80
60
40
<63
63-125
125-250
250-500
500-710
710-1000
>1000
Size fraction (μm)

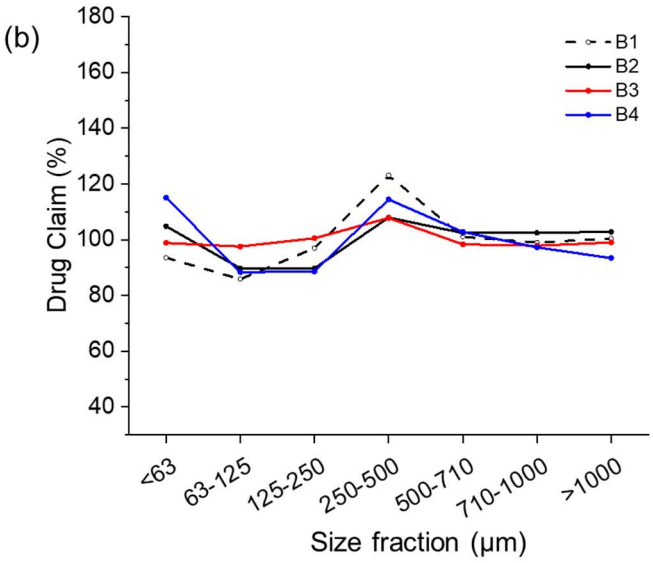
(b)
B1
B2
B3
B4
Drug Claim (%)
180
160
140
120
100
80
60
40
<63
63-125
125-250
250-500
500-710
710-1000
>1000
Size fraction (μm)

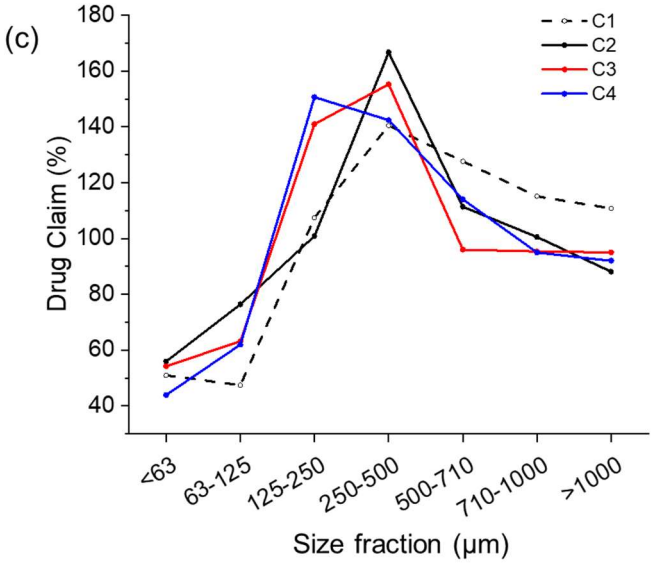
(c)
C1
C2
C3
C4
Drug Claim (%)
180
160
140
120
100
80
60
40
<63
63-125
125-250
250-500
500-710
710-1000
>1000
Size fraction (μm)

Fig. 5.8. Distribution of active ingredient across granule size fractions for low-dose formulations with different drug hydrophobicity. Varying binder delivery methods and solution properties (L1, L2, L3 and L4) for (a) batch code A (ibuprofen as API), (b) batch code B (salicylic acid as API) and (c) batch code C (caffeine as API).

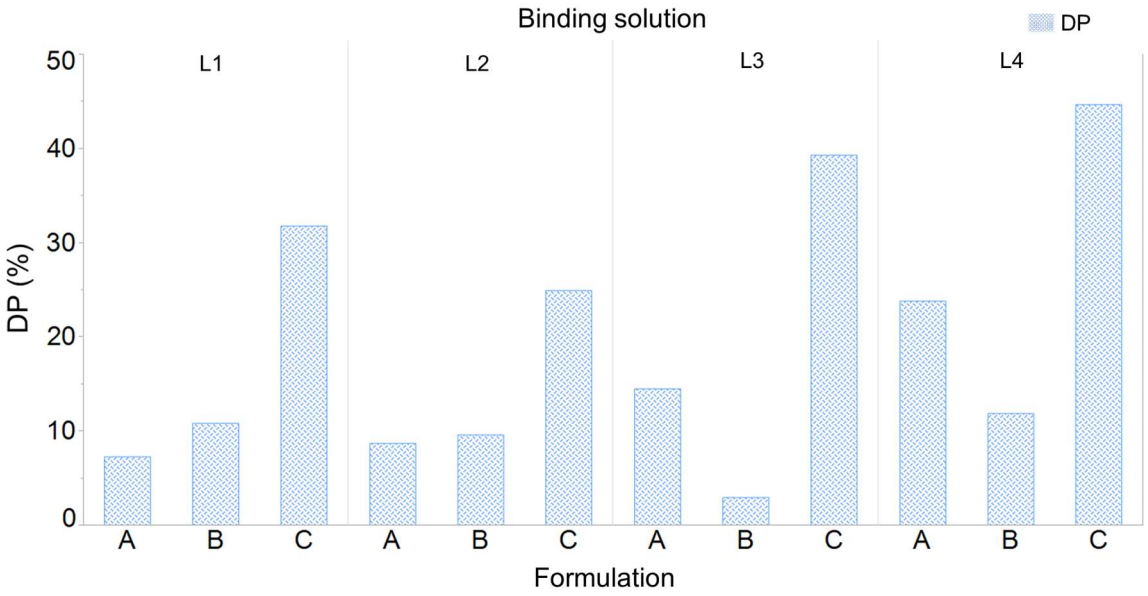

Fig. 5.9. The de-mixing potential for low-dose formulations with different drug hydrophobicity. Varying binder delivery methods and solution properties (L1, L2, L3 and L4) for batch code A (ibuprofen as API), batch code B (salicylic acid as API) and batch code C (caffeine as API).

5.3.1.6 Tablet tensile strength

Fig. 5.10 showed that tablet tensile strength increased in conjunction with the drug water solubility and formulation with ibuprofen demonstrated the smallest tensile strength if the same granulation liquid was adopted. Moreover, dry binder delivery methods L1 produced the most densified granules, which were subjected to less degree of particle rearrangement during compaction. Hence a corollary of that was stronger inter-

particle bonding associated with the highest tensile strength with respect to the identical formulation.

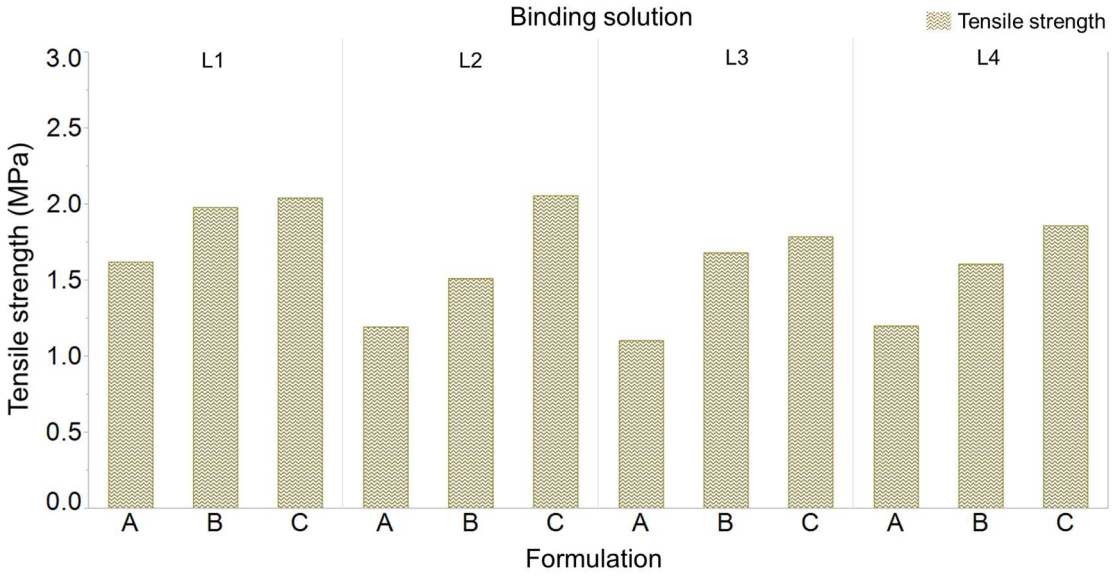

Fig. 5.10. Tablet tensile strength for low-dose formulations with different drug hydrophobicity. Varying binder delivery methods and solution properties (L1, L2, L3 and L4) for batch code A (ibuprofen as API), batch code B (salicylic acid as API) and batch code C (caffeine as API).

5.3.1.7 Tablet drug agglomerate size distribution

The tablet drug agglomerate size distribution was unveiled in Fig. 5.11. The tablets with hydrophobic API demonstrated more homogeneous drug distribution with finer structures. In comparison, tablets with caffeine as the active ingredient reflected larger drug aggregates. Fig. 5.12 further substantiated this conclusion by showing more blue domains in the size fraction above 250 μm. Also, the cumulative size distribution in Fig. 5.13 depicted relatively less dependence on binder delivery methods but pronounced increase of aggregates median diameter as the drug water solubility enhanced.

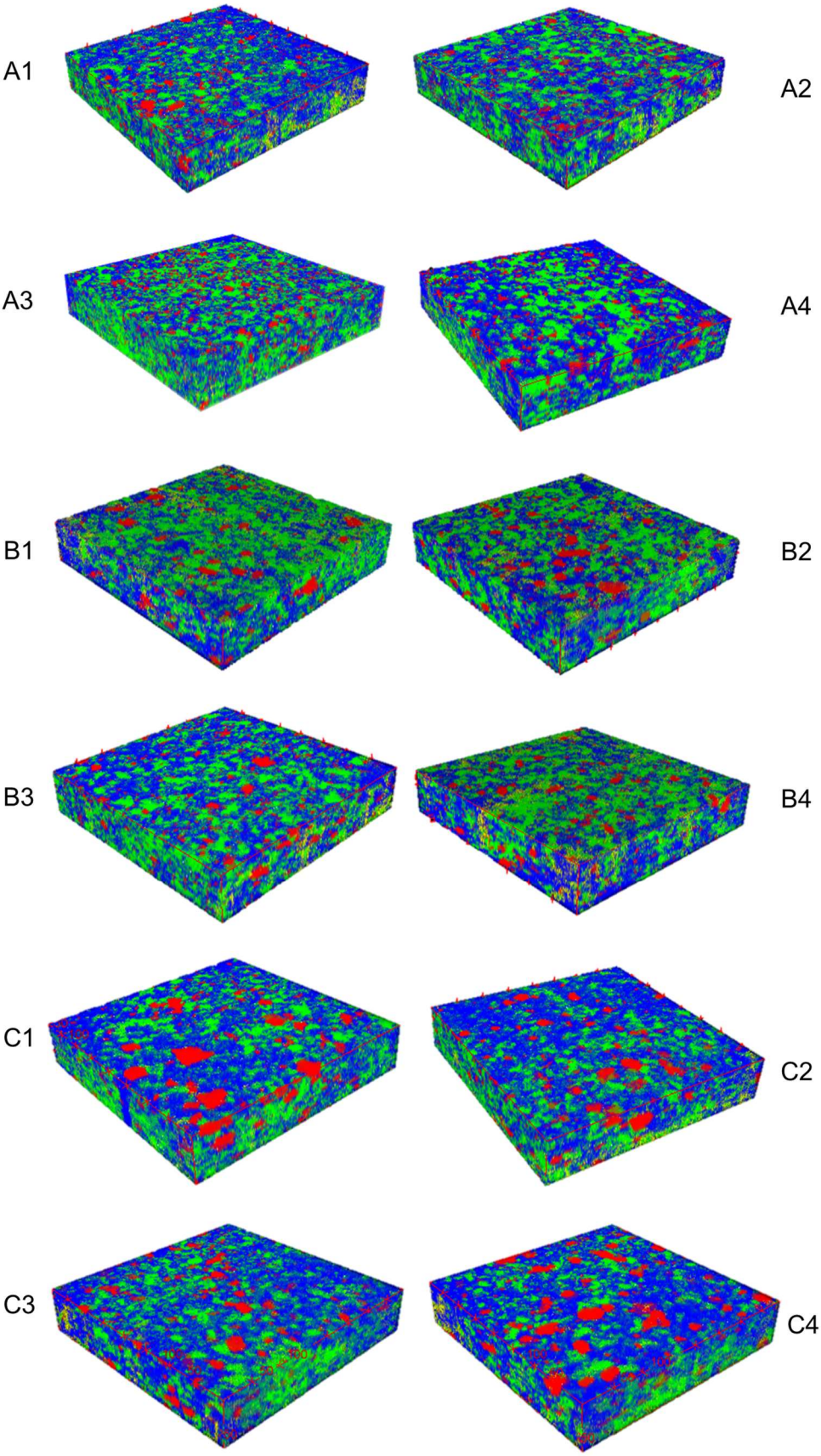
A1
A2
A3
A4
B1
B2
B3
B4
C1
C2
C3
C4

Fig. 5.11. 3D visualization of tablet multi-component distribution for low-dose formulations with different drug hydrophobicity. API, MCC, Lactose and PVP were color-coded by red, blue, green and yellow, respectively.

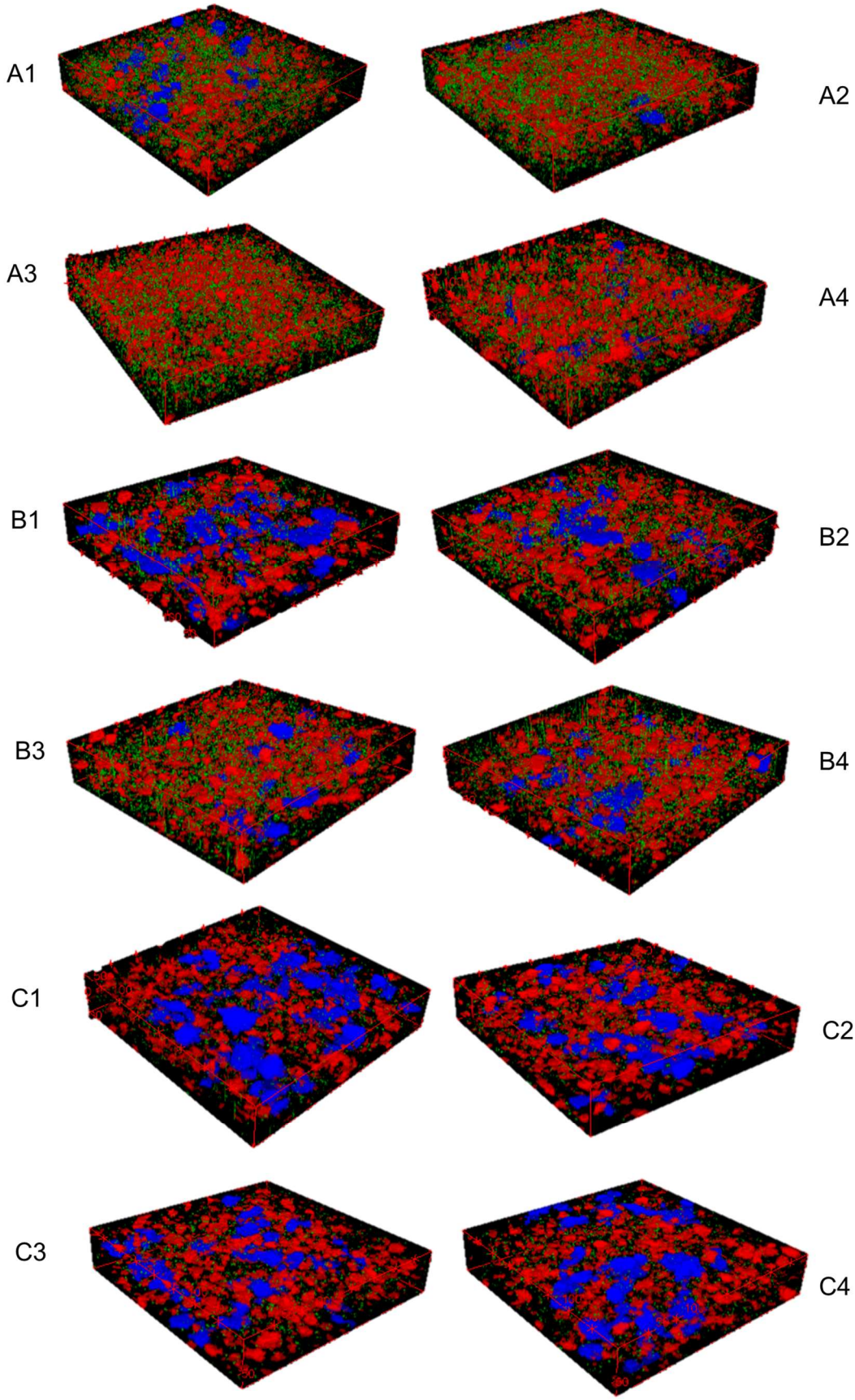
A1
A2
A3
A4
B1
B2
B3
B4
C1
C2
C3
C4

Fig. 5.12. 3D visualization of tablet drug agglomerate size distribution for low-dose formulations with different drug hydrophobicity. The color code indicated the agglomerate volume in different size fractions. Blue, red and green represented the size larger than 250 μm, between 250 and 50 μm, less than 50 μm, respectively.

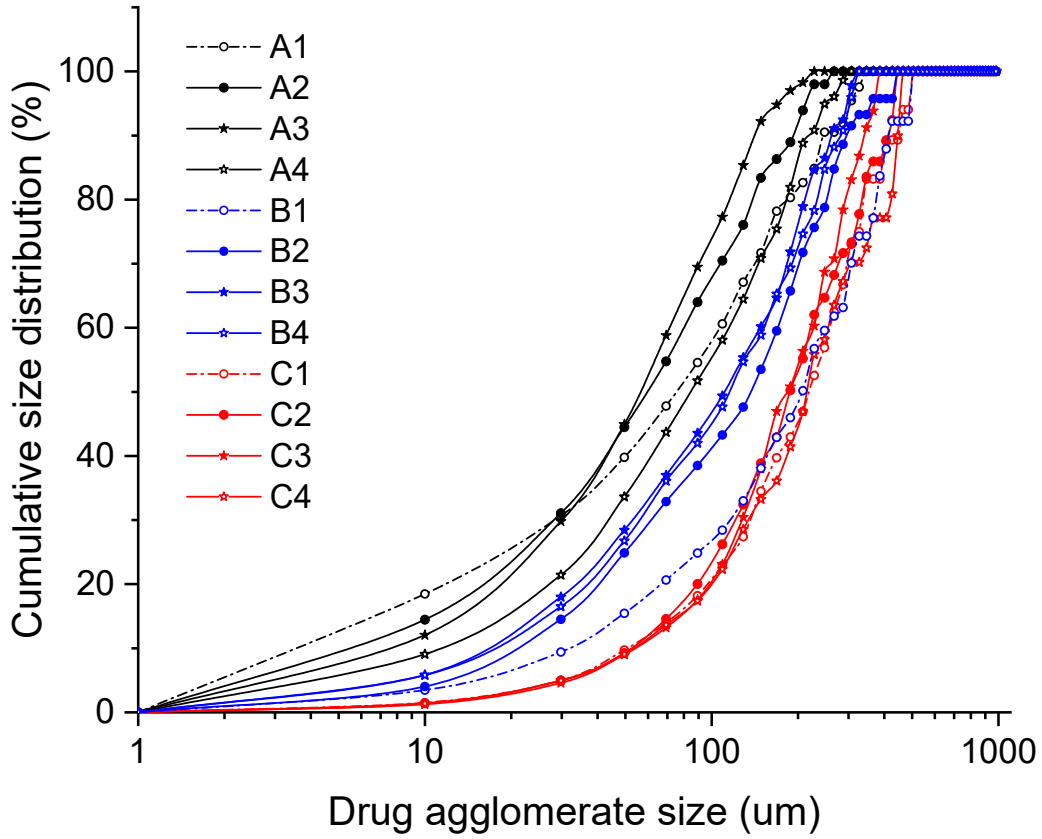

Fig. 5.13. Cumulative drug agglomerate size distribution of tablets produced from low-dose formulations with different drug hydrophobicity

5.3.2 Influence of drug primary particle size in low-dose formulations

5.3.2.1 Flow properties of raw material blends

Fig. 5.14 showed the cohesion and ff_c of raw material blends with varying drug primary particle size. It was apparent that flow properties were ameliorated by increasing the primary particle size of API despite its low dose in the formulation. Specifically, the

premix containing micronized APAP showed the highest cohesion and smallest ff_c, which steadily decreased (cohesion) and increased (ff_c) by incorporating powder APAP and dense APAP as the active ingredient. Besides, PVP with relatively large particle size significantly contributed to the improvement of powder flow properties, which was consistent with the previous results.

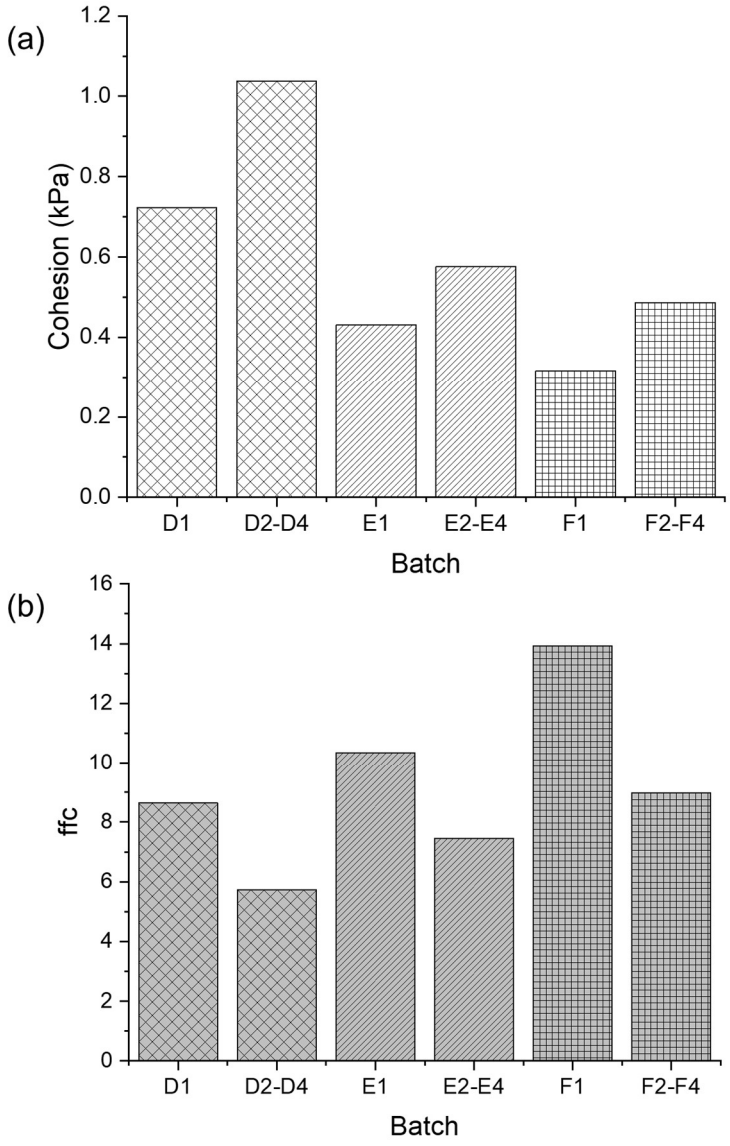

Fig. 5.14. (a) Cohesion and (b) flow function coefficient of low-dose formulation blends with different binder delivery methods and drug primary particle size.

5.3.2.2 Wettability of raw material blends

Fig. 5.15 showed the droplet infiltration time of formulation blends by different granulation liquids. Since the active ingredients utilized in this study were all APAP, very similar wettability was identified between different raw material blends. Moreover, the penetration process was slightly expedited by reducing the solution viscosity.

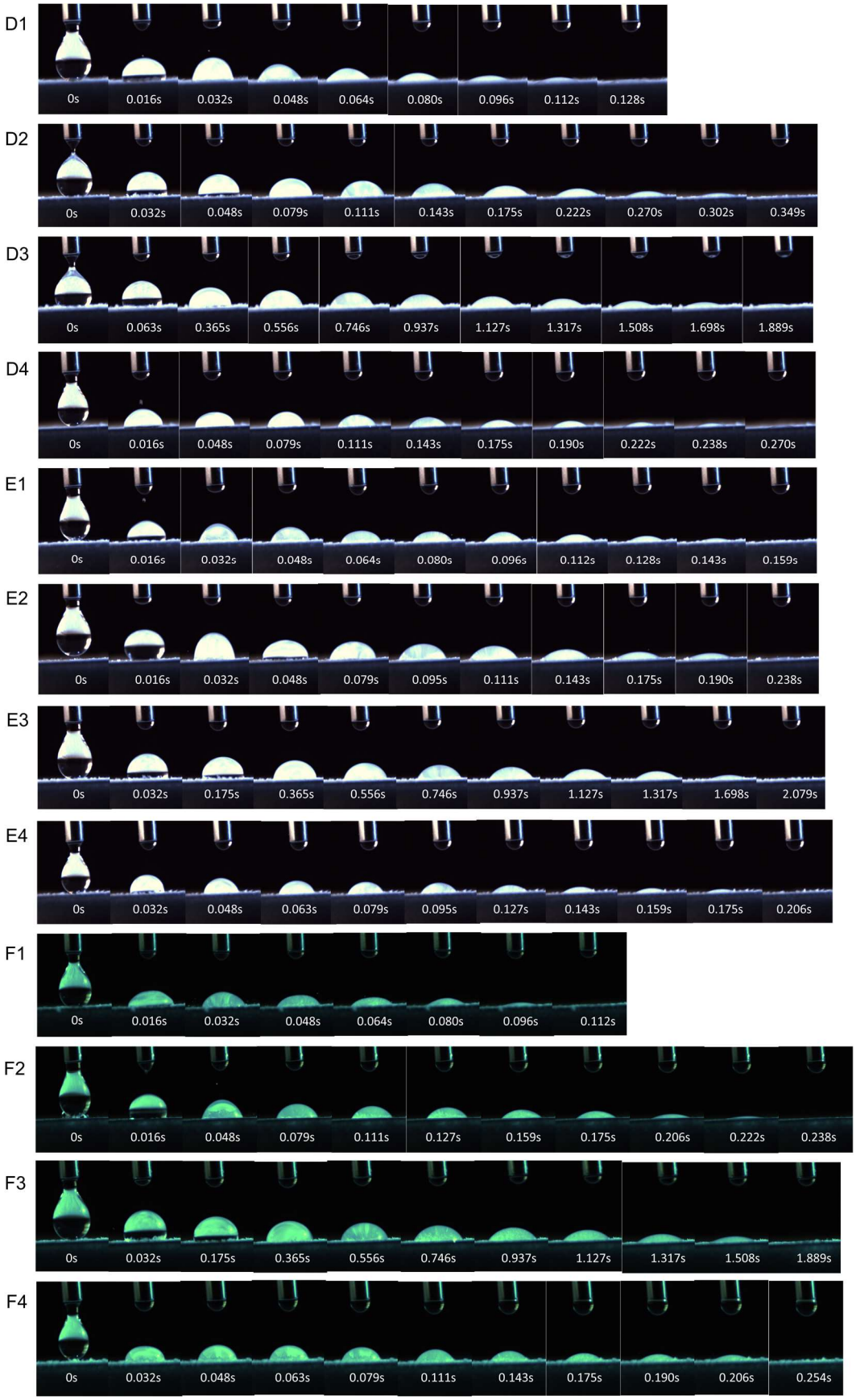
D1
0s 0.016s 0.032s 0.048s 0.064s 0.080s 0.096s 0.112s 0.128s
D2
0s 0.032s 0.048s 0.079s 0.111s 0.143s 0.175s 0.222s 0.270s 0.302s 0.349s
D3
0s 0.063s 0.365s 0.556s 0.746s 0.937s 1.127s 1.317s 1.508s 1.698s 1.889s
D4
0s 0.016s 0.048s 0.079s 0.111s 0.143s 0.175s 0.190s 0.222s 0.238s 0.270s
E1
0s 0.016s 0.032s 0.048s 0.064s 0.080s 0.096s 0.112s 0.128s 0.143s 0.159s
E2
0s 0.016s 0.032s 0.048s 0.079s 0.095s 0.111s 0.143s 0.175s 0.190s 0.238s
E3
0s 0.032s 0.175s 0.365s 0.556s 0.746s 0.937s 1.127s 1.317s 1.698s 2.079s
E4
0s 0.032s 0.048s 0.063s 0.079s 0.095s 0.127s 0.143s 0.159s 0.175s 0.206s
F1
0s 0.016s 0.032s 0.048s 0.064s 0.080s 0.096s 0.112s
F2
0s 0.016s 0.048s 0.079s 0.111s 0.127s 0.159s 0.175s 0.206s 0.222s 0.238s
F3
0s 0.032s 0.175s 0.365s 0.556s 0.746s 0.937s 1.127s 1.317s 1.508s 1.889s
F4
0s 0.032s 0.048s 0.063s 0.079s 0.111s 0.143s 0.175s 0.190s 0.206s 0.254s

Fig. 5.15. Droplet of binding solutions penetrating into powder bed of low-dose formulation blends with different drug primary particle size.

5.3.2.3 Granul size distribution

The GSD and sizing metrics (D10, D50 and D90) was illustrated in Fig. 5.16 and Fig. 5.17, respectively. Monomodal distributions were discovered for all formulations by leveraging dry binder addition method. In contrast, more oversized particles were generated after increasing the viscosity of granulation liquids, engendering in a biomodal size distribution. Overall, formulation with different active ingredients produced comparable size metrics.

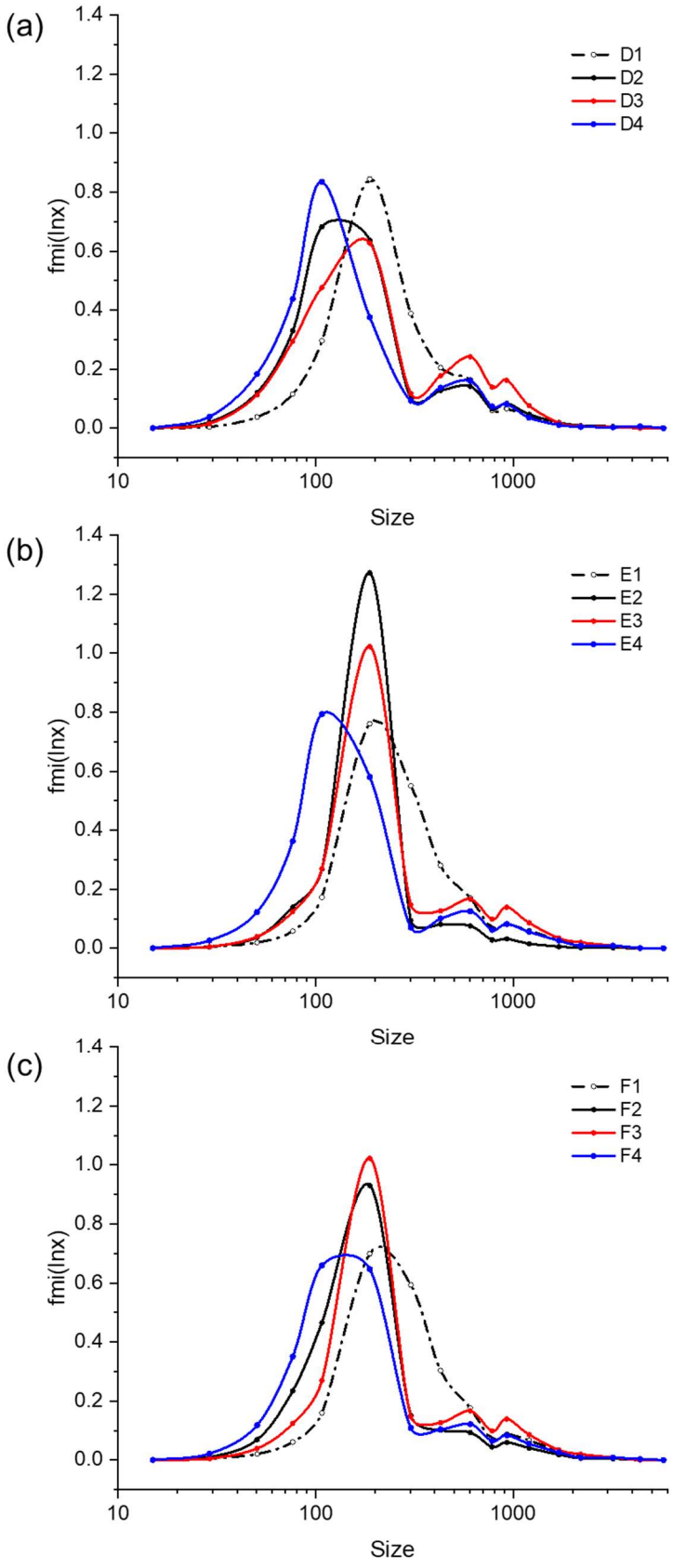
(a)
D1
D2
D3
D4
fmi(lnx)
Size
(b)
E1
E2
E3
E4
fmi(lnx)
Size
(c)
F1
F2
F3
F4
fmi(lnx)
Size

Fig. 5.16. Granule size distribution of low-dose formulations with different drug primary particle size. Varying binder delivery methods and solution properties for (a) batch code D (micronized APAP as API), (b) batch code E (powder APAP as API) and (c) batch code F (dense APAP as API).

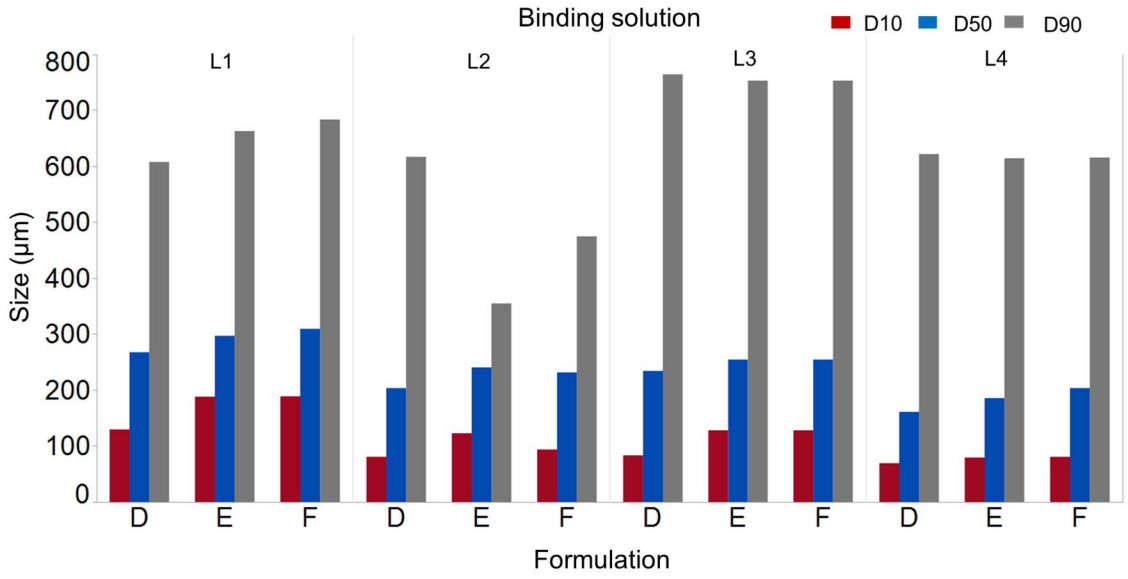

Fig. 5.17. Column plot of granule sizing metrics (D10, D50 and D90) of low-dose formulations with different primary particle size. Varying binder delivery methods and solution properties (L1, L2, L3 and L4) for batch code D (micronized APAP as API), batch code E (powder APAP as API) and batch code F (dense APAP as API).

5.3.2.4 Porosity

Fig. 5.18 indicated that dry binder delivery method again produced the most densified granules whereas binding liquid containing PVP K90 generated the most porous granules. Due to the relatively low viscosity of water, granules were subjected to higher extent of deformation during consolidation, thereby leading to granules with smaller voidage.

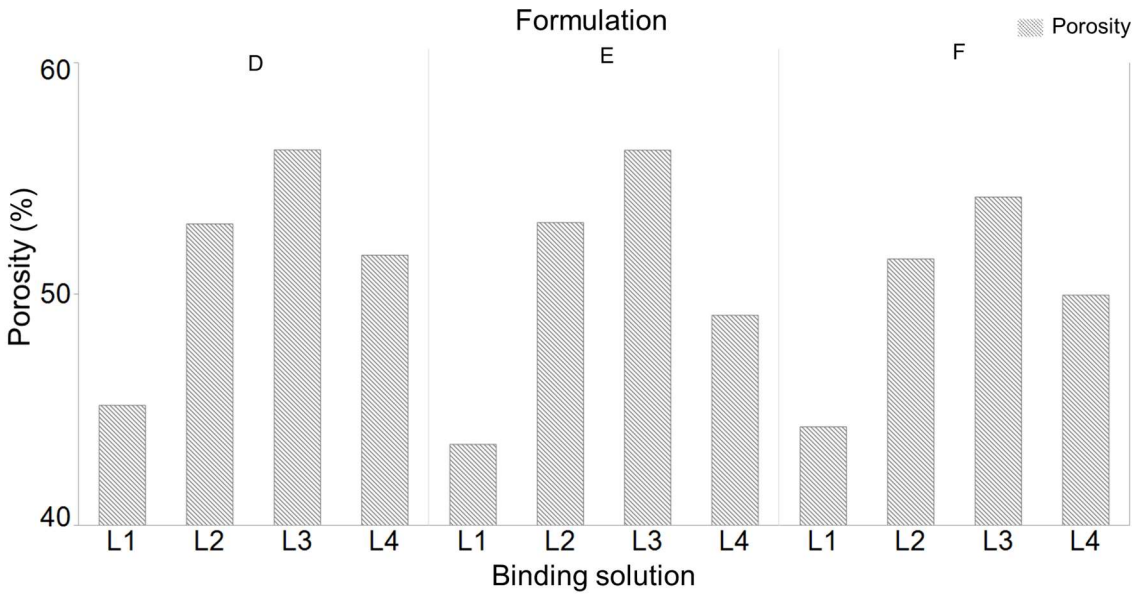

Fig. 5.18. Column plot of granule porosity of low-dose formulations with different drug primary particle size. Varying binder delivery methods and solution properties (L1, L2, L3 and L4) for batch code D (micronized APAP as API), batch code E (powder APAP as API) and batch code F (dense APAP as API).

5.3.2.5 Granule drug content uniformity

Fig. 5.19 showed the distribution of active ingredient across all size fractions. In terms of formulations adopting micronized APAP and wet binder delivery methods, it was clear that fine particles (less than 63 μm) and granules in the class of 250-500 μm were super-potent while those in the fraction of 125-250 μm were sub-potent. Besides, the drug content in the fines consistently declined as the API primary particle size increased. In other words, granules with micronized APAP as the active ingredient demonstrated higher contents in granules less than 63 μm in comparison to those containing powder or dense APAP. Particularly, granules with dense APAP as the active ingredient was most sub-potent in the fines and super-potent in the middle size fraction of 250-500 μm. Fig. 5.20 displayed the de-mixing potential for all formulation studied. The results indicated

that granules containing powder APAP demonstrated the least degree of API segregation regardless of the binder delivery method and solution properties.

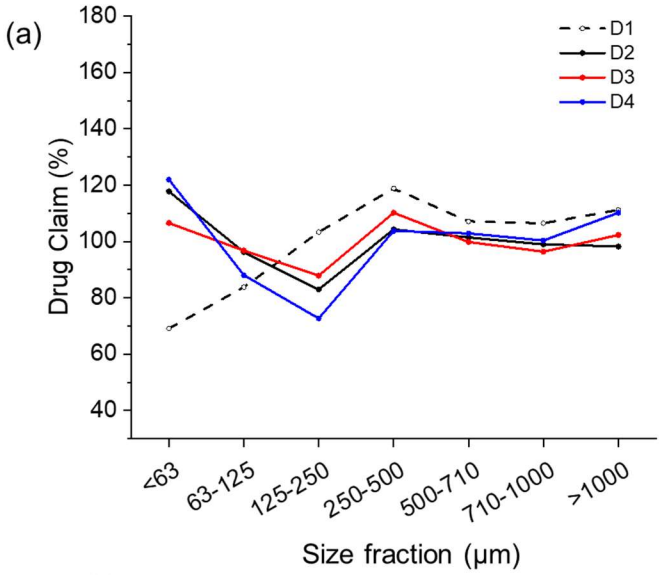
(a)
D1
D2
D3
D4
Drug Claim (%)
180
160
140
120
100
80
60
40
<63
63-125
125-250
250-500
500-710
710-1000
>1000
Size fraction (μm)

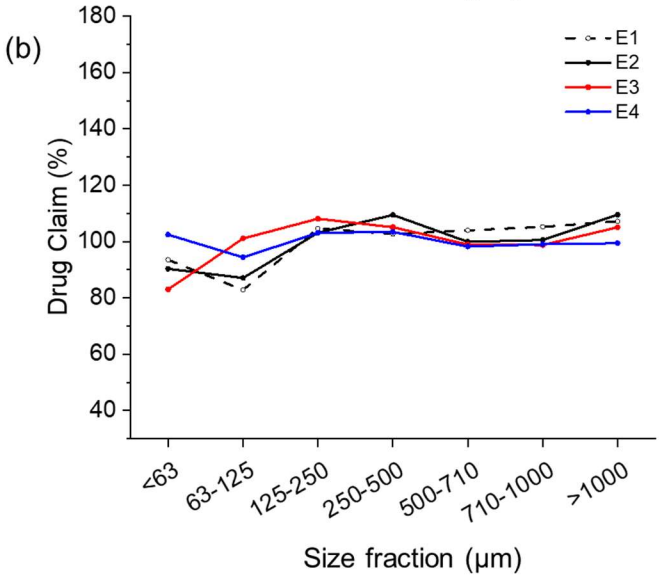
(b)
E1
E2
E3
E4
Drug Claim (%)
180
160
140
120
100
80
60
40
<63
63-125
125-250
250-500
500-710
710-1000
>1000
Size fraction (μm)

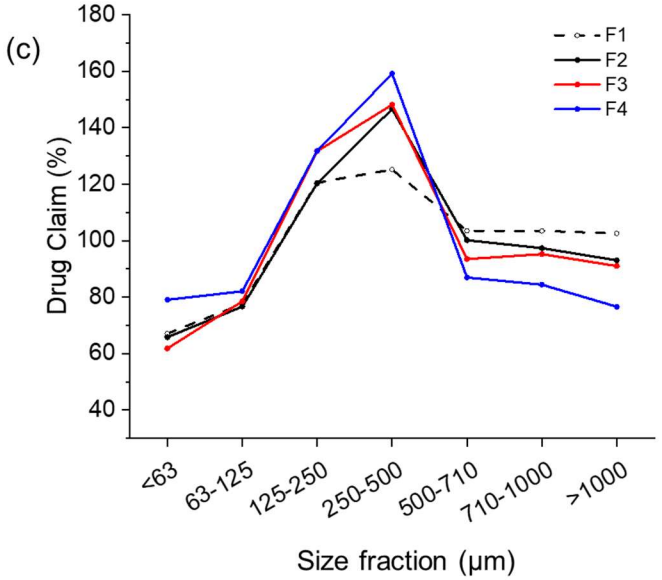
(c)
F1
F2
F3
F4
Drug Claim (%)
180
160
140
120
100
80
60
40
<63
63-125
125-250
250-500
500-710
710-1000
>1000
Size fraction (μm)

Fig. 5.19. Distribution of active ingredient across granule size fractions for low-dose formulations with different drug primary particle size. Varying binder delivery methods and solution properties (L1, L2, L3 and L4) for (a) batch code D (micronized APAP as API), (b) batch code E (powder APAP as API) and (c) batch code F (dense APAP as API).

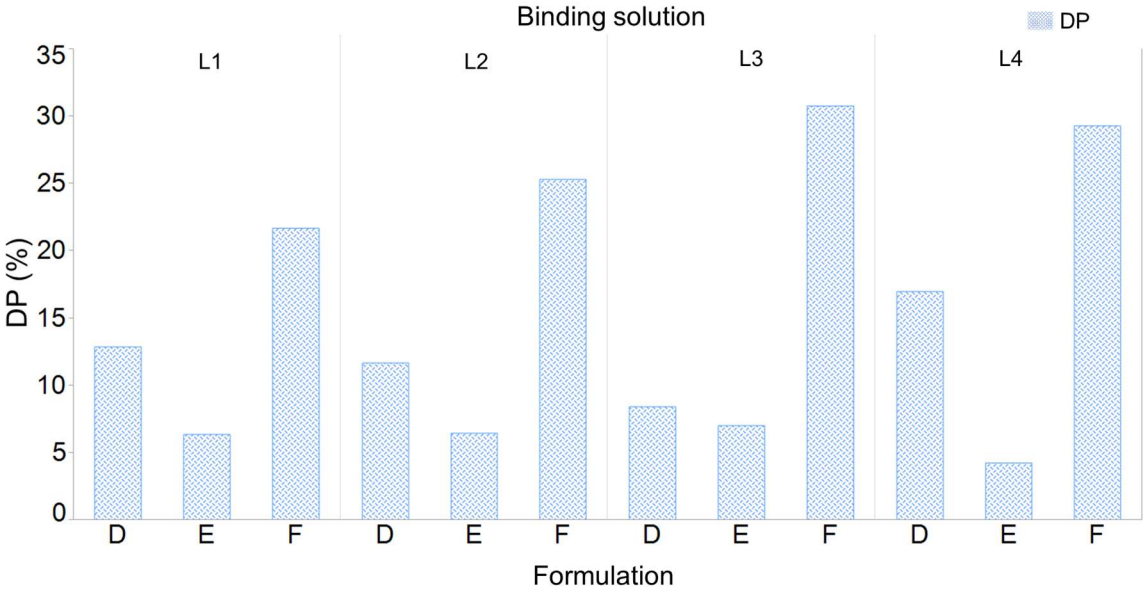

Fig. 5.20. The de-mixing potential for low-dose formulations with different drug primary particle size. Varying binder delivery methods and solution properties (L1, L2, L3 and L4) for batch code D (micronized APAP as API), batch code E (powder APAP as API) and batch code F (dense APAP as API).

5.3.2.6 Tablet tensile strength

Fig. 5.21 illustrated that tensile strength of tablets from formulation with micronized APAP approximated to that from the formulation with powder or dense APAP. In particular, the tensile strength showed a tendency to decrease as the surface tension of granulation liquid was reduced.

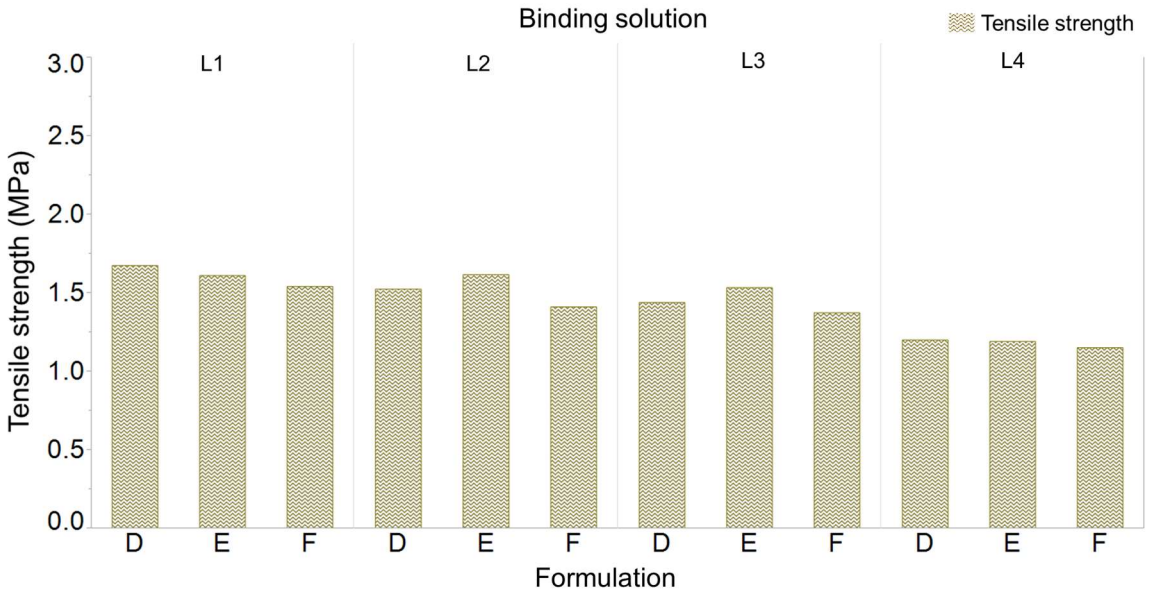

Fig. 5.21. Tablet tensile strength for low-dose formulations with different drug primary particle size. Varying binder delivery methods and solution properties (L1, L2, L3 and L4) for batch code D (micronized APAP as API), batch code E (powder APAP as API) and batch code F (dense APAP as API).

5.3.2.7 Tablet drug agglomerate size distribution

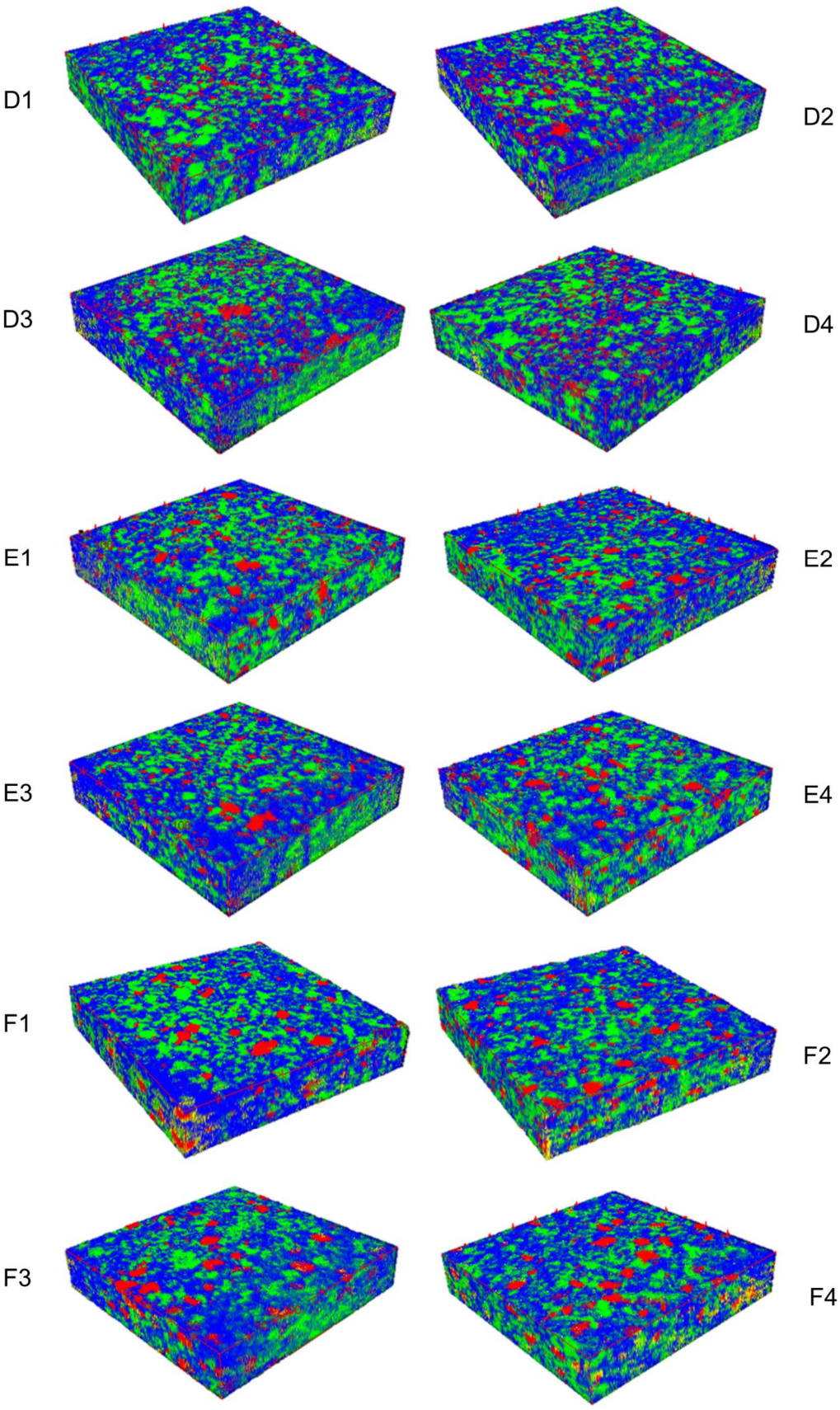
D1
D2
D3
D4
E1
E2
E3
E4
F1
F2
F3
F4

Fig. 5.22. 3D visualization of tablet multi-component distribution for low-dose formulations with different drug primary particle size. API, MCC, Lactose and PVP were color-coded by red, blue, green and yellow, respectively.

The tablet drug agglomerate size distribution was unveiled in Fig. 5.22. Although micronized APAP was more cohesive and inclined to form agglomerates, tablets demonstrated more homogeneous drug distribution with finer structures. In comparison, tablets with dense APAP as the active ingredient reflected larger drug aggregates. Fig. 5.23 further substantiated this conclusion by showing more blue domains in the size fraction above 250 μm. Consequently, it was believed that the high level of shear stress during granulation overcame the inter-particle cohesiveness and effectively de-agglomerated the drug aggregates enabling the dominant influence of primary particle size on the volume of drug domain. Also, the cumulative size distribution in Fig. 5.24 depicted relatively less dependence on binder delivery methods but pronounced increase of aggregates median diameter as the drug primary particle size enhanced.

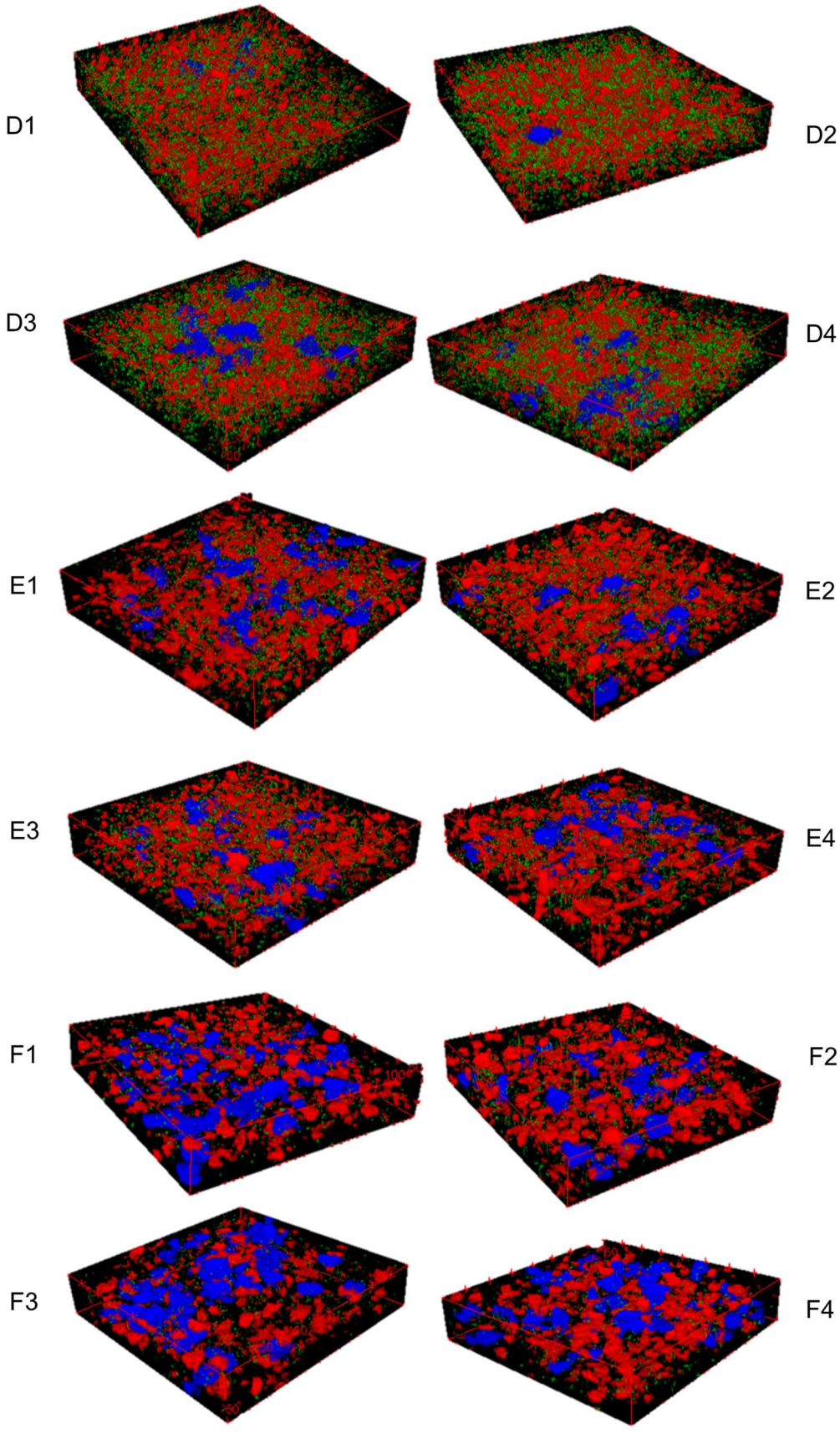
D1
D2
D3
D4
E1
E2
E3
E4
F1
F2
F3
F4

Fig. 5.23. 3D visualization of tablet drug agglomerate size distribution for low-dose formulations with different drug primary particle size. The color code indicated the agglomerate volume in different size fractions. Blue, red and green represented the size larger than 250 μm, between 250 and 50 μm, less than 50 μm, respectively.

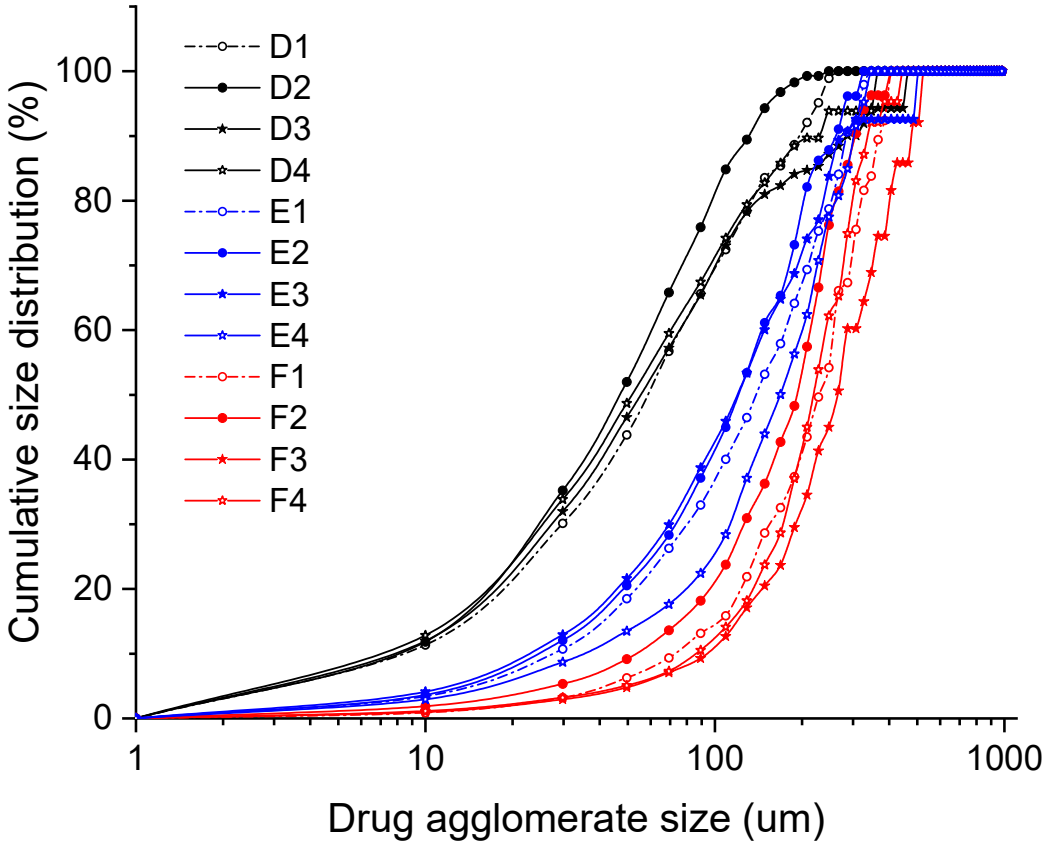

Fig. 5.24. Cumulative drug agglomerate size distribution of tablets produced from low-dose formulations with different drug primary particle size.

5.3.3 Influence of drug loading in formulation

5.3.3.1 Flow properties of raw material blends

As shown in Fig. 5.25, powder flow properties were considerably compromised after increasing the drug loading primarily because of the relatively small particle size and thus

high cohesiveness of ibuprofen. The effect of including PVP in the formulation on reducing cohesion and enhancing ff_c was less influential with respect to the medium-dose and high-dose formulations.

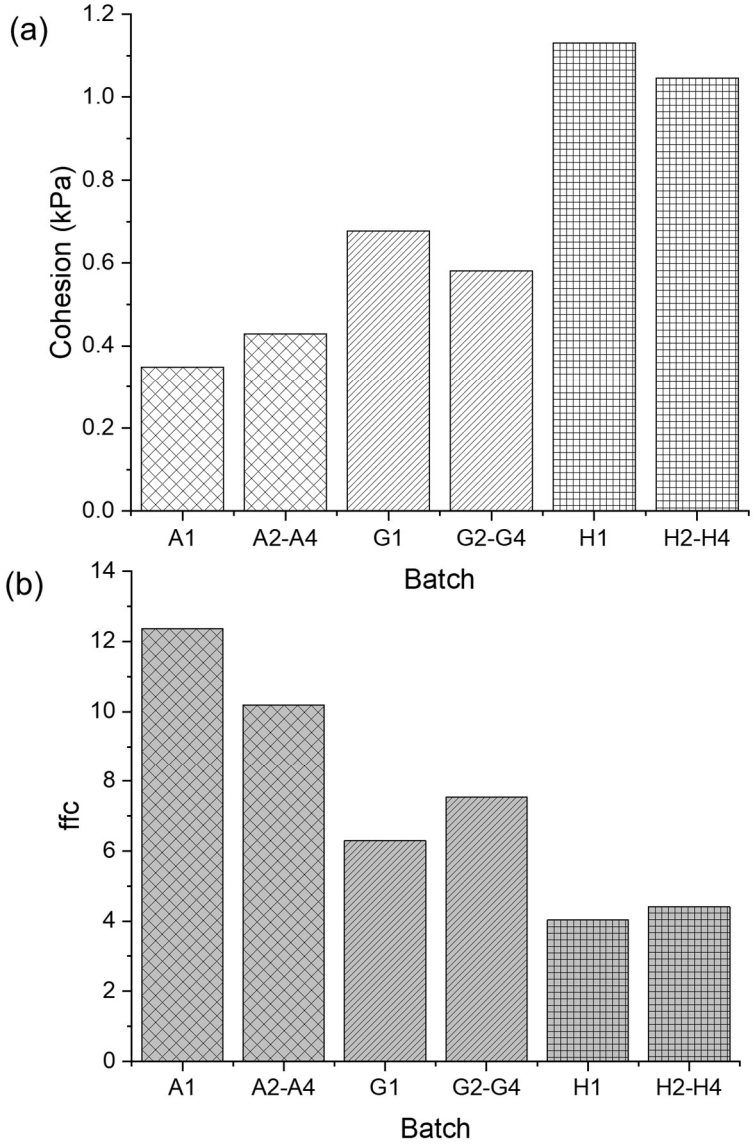

Fig. 5.25. (a) Cohesion and (b) flow function coefficient of formulation blends with different ibuprofen loadings and binder delivery methods.

5.3.3.2 Wettability of raw material blends

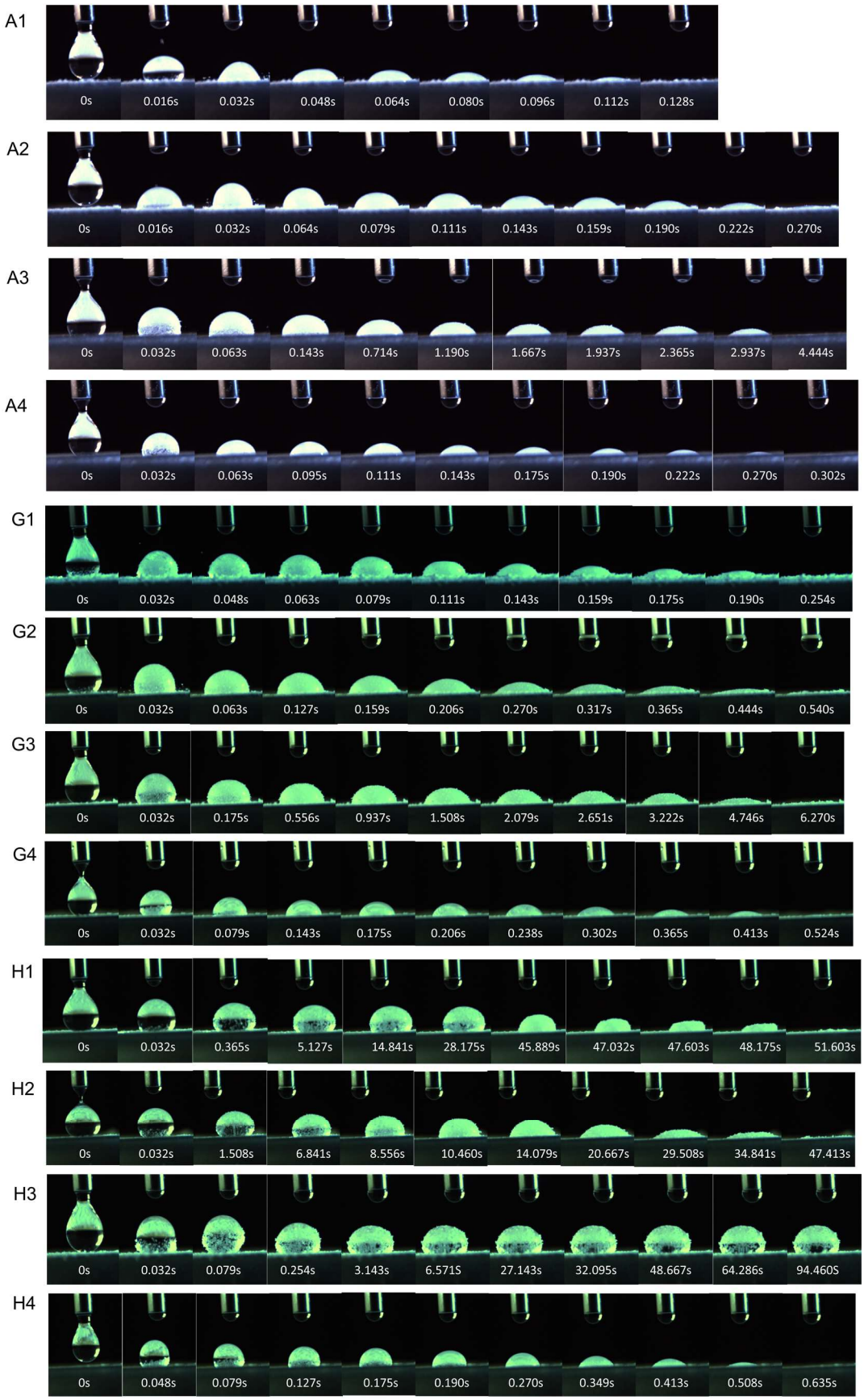
A1
0s 0.016s 0.032s 0.048s 0.064s 0.080s 0.096s 0.112s 0.128s
A2
0s 0.016s 0.032s 0.064s 0.079s 0.111s 0.143s 0.159s 0.190s 0.222s 0.270s
A3
0s 0.032s 0.063s 0.143s 0.714s 1.190s 1.667s 1.937s 2.365s 2.937s 4.444s
A4
0s 0.032s 0.063s 0.095s 0.111s 0.143s 0.175s 0.190s 0.222s 0.270s 0.302s
G1
0s 0.032s 0.048s 0.063s 0.079s 0.111s 0.143s 0.159s 0.175s 0.190s 0.254s
G2
0s 0.032s 0.063s 0.127s 0.159s 0.206s 0.270s 0.317s 0.365s 0.444s 0.540s
G3
0s 0.032s 0.175s 0.556s 0.937s 1.508s 2.079s 2.651s 3.222s 4.746s 6.270s
G4
0s 0.032s 0.079s 0.143s 0.175s 0.206s 0.238s 0.302s 0.365s 0.413s 0.524s
H1
0s 0.032s 0.365s 5.127s 14.841s 28.175s 45.889s 47.032s 47.603s 48.175s 51.603s
H2
0s 0.032s 1.508s 6.841s 8.556s 10.460s 14.079s 20.667s 29.508s 34.841s 47.413s
H3
0s 0.032s 0.079s 0.254s 3.143s 6.571S 27.143s 32.095s 48.667s 64.286s 94.460S
H4
0s 0.048s 0.079s 0.127s 0.175s 0.190s 0.270s 0.349s 0.413s 0.508s 0.635s

Fig. 5.26. Droplet of binding solutions penetrating into powder bed of formulation blends with different ibuprofen loadings.

Droplet penetration time in Fig. 5.26 demonstrated stark difference in formulations with different drug loadings. The high-dose blends, especially H3, showed the longest penetration process with dropet remaining on the powder bed surface after 90 s.

5.3.3.3 Granul size distribution

The GSD in Fig. 5.27 for medium-dose and high-dose formulations displayed multimodal distributions principally due to the poor wettability of material blends. In particular, the majority of granules from formulation H1 were above 1 mm and highly densified and hence less desirable for downstream processing such as tabletting. In Fig. 5.28, formulations with dry binder delivery method showed relatively large sizing metrics in contrast to those using wet binding solutions. This was mainly attributed to the higher L/S ratio (0.4) and ensuing degree of liquid saturation promoting the granule growth.

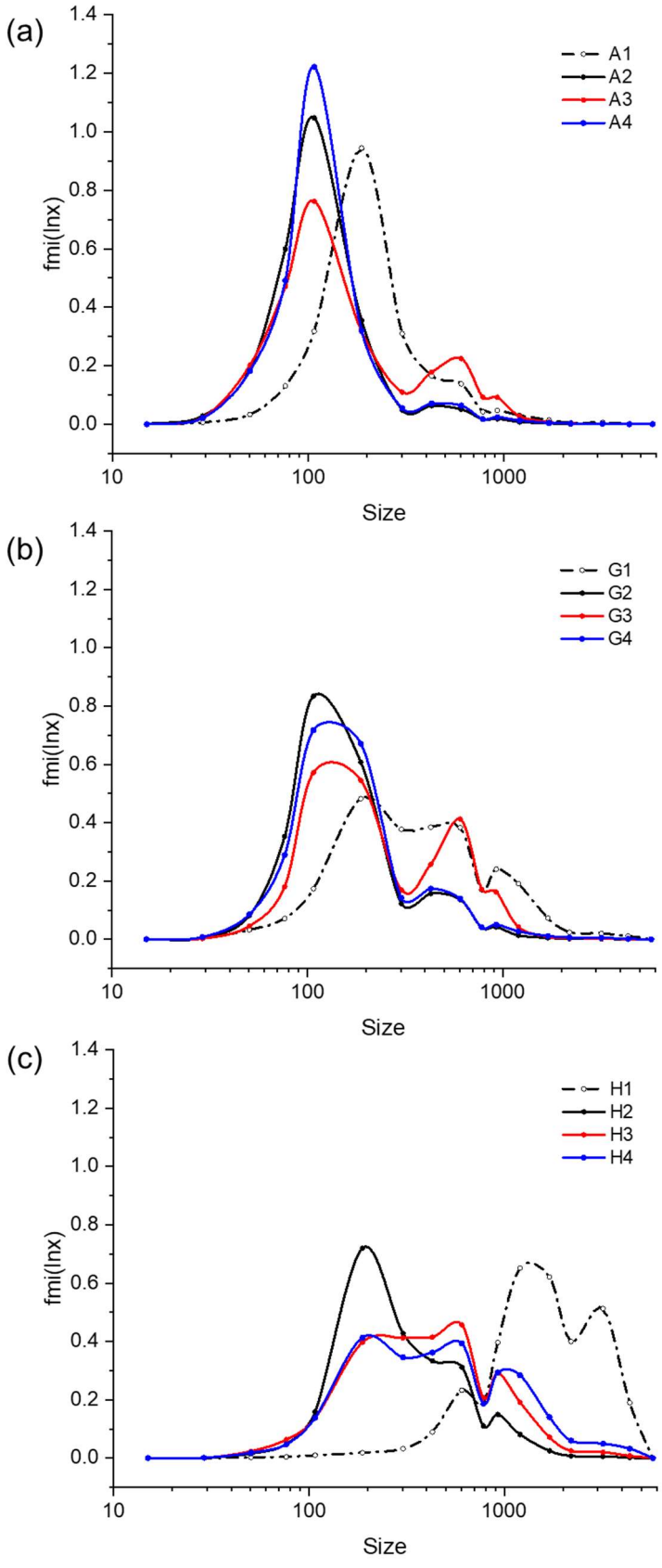
(a)
A1
A2
A3
A4
fmi(lnx)
Size
(b)
G1
G2
G3
G4
fmi(lnx)
Size
(c)
H1
H2
H3
H4
fmi(lnx)
Size

Fig. 5.27. Granule size distribution of formulations with different ibuprofen loadings. Varying binder delivery methods and solution properties for (a) batch code A (low-dose), (b) batch code G (medium-dose) and (c) batch code H (high-dose).

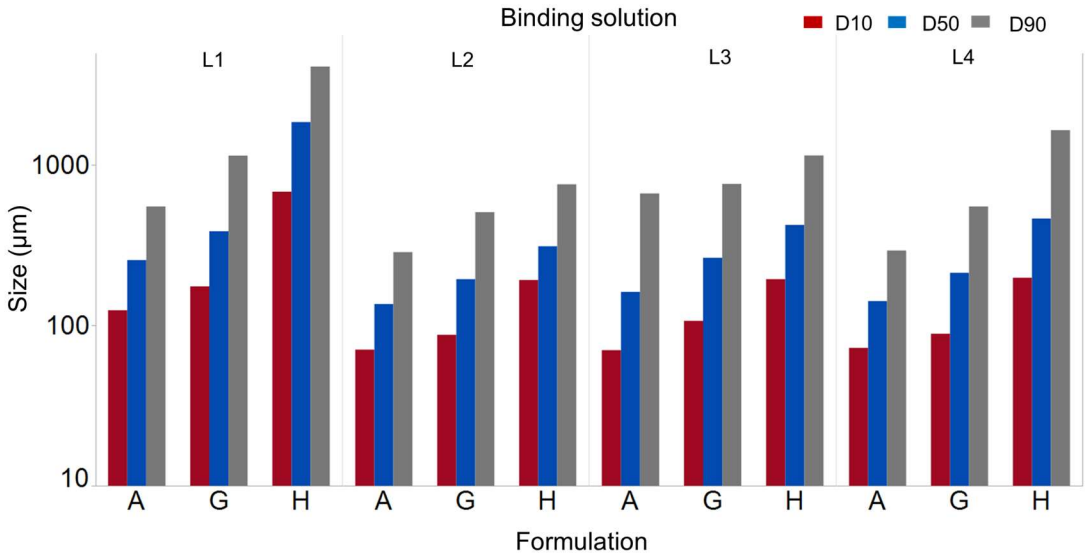

Fig. 5.28. Column plot of granule sizing metrics (D10, D50 and D90) of formulations with different ibuprofen loadings. Varying binder delivery methods and solution properties (L1, L2, L3 and L4) for batch code A (low-dose), (b) batch code G (medium-dose) and (c) batch code H (high-dose).

5.3.3.4 Porosity

Fig. 5.29 indicated that dry binder delivery method again produced the most densified granules whereas binding liquid containing PVP K90 generated the most porous granules. Due to the relatively low viscosity of water, granules were subjected to higher extent of deformation during consolidation, thereby leading to granules with smaller voidage. Besides, with the same binder delivery method, granule porosity decreased as drug loading increased in the formulation.

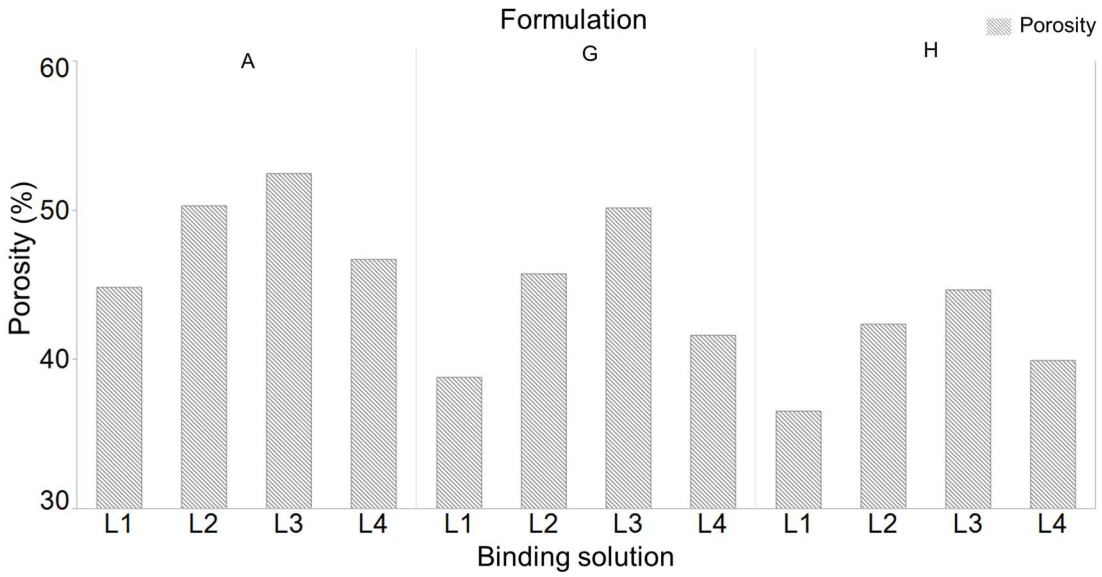

Fig. 5.29. Column plot of granule porosity of formulations with different ibuprofen loadings. Varying binder delivery methods and solution properties (L1, L2, L3 and L4) for batch code A (low-dose), (b) batch code G (medium-dose) and (c) batch code H (high-dose).

5.3.3.5 Granule drug content uniformity

Fig. 5.30 and Fig. 5.31 indicated that the drug segregation was minimum for medium-dose and high-dose granules. Due to the low binding capability after surface tension reduction, low-dose granules with L4 as the binder delivery method revealed the highest de-mixing potential.

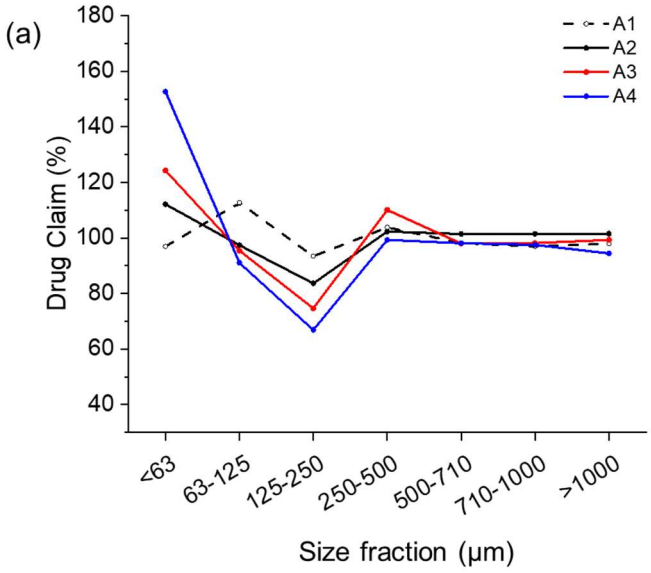
(a)
A1
A2
A3
A4
Drug Claim (%)
180
160
140
120
100
80
60
40
<63
63-125
125-250
250-500
500-710
710-1000
>1000
Size fraction (μm)

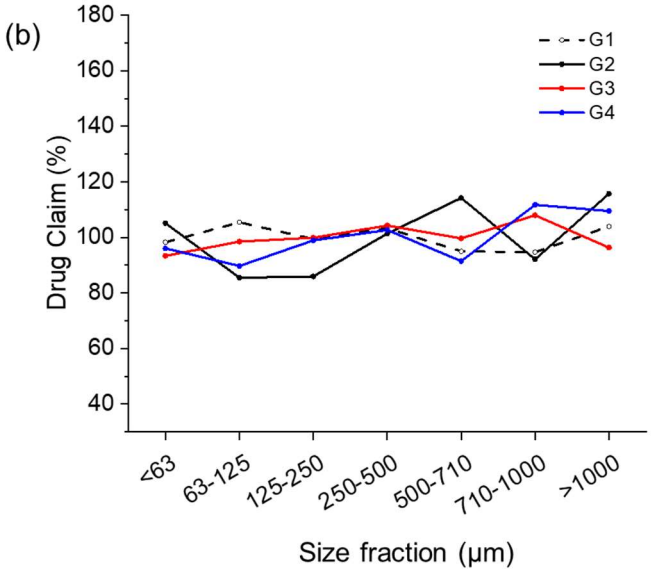
(b)
G1
G2
G3
G4
Drug Claim (%)
180
160
140
120
100
80
60
40
<63
63-125
125-250
250-500
500-710
710-1000
>1000
Size fraction (μm)

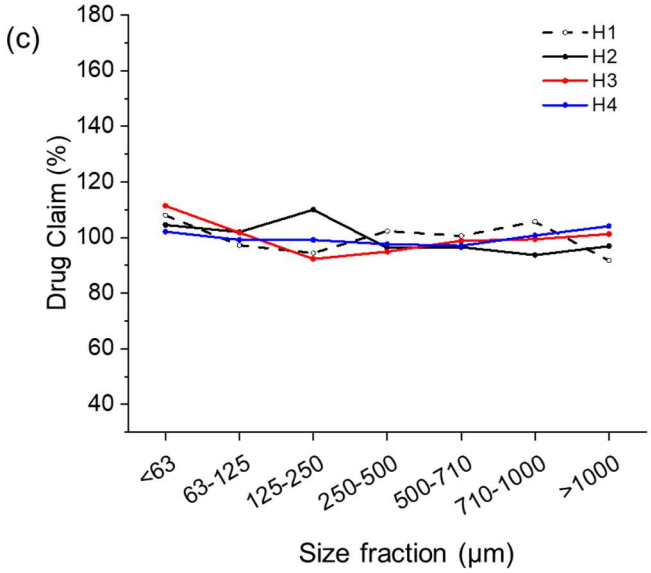
(c)
H1
H2
H3
H4
Drug Claim (%)
180
160
140
120
100
80
60
40
<63
63-125
125-250
250-500
500-710
710-1000
>1000
Size fraction (μm)

Fig. 5.30. Distribution of active ingredient across granule size fractions for formulations with different ibuprofen loadings. Varying binder delivery methods and solution properties (L1, L2, L3 and L4) for batch code A (low-dose), (b) batch code G (medium-dose) and (c) batch code H (high-dose).

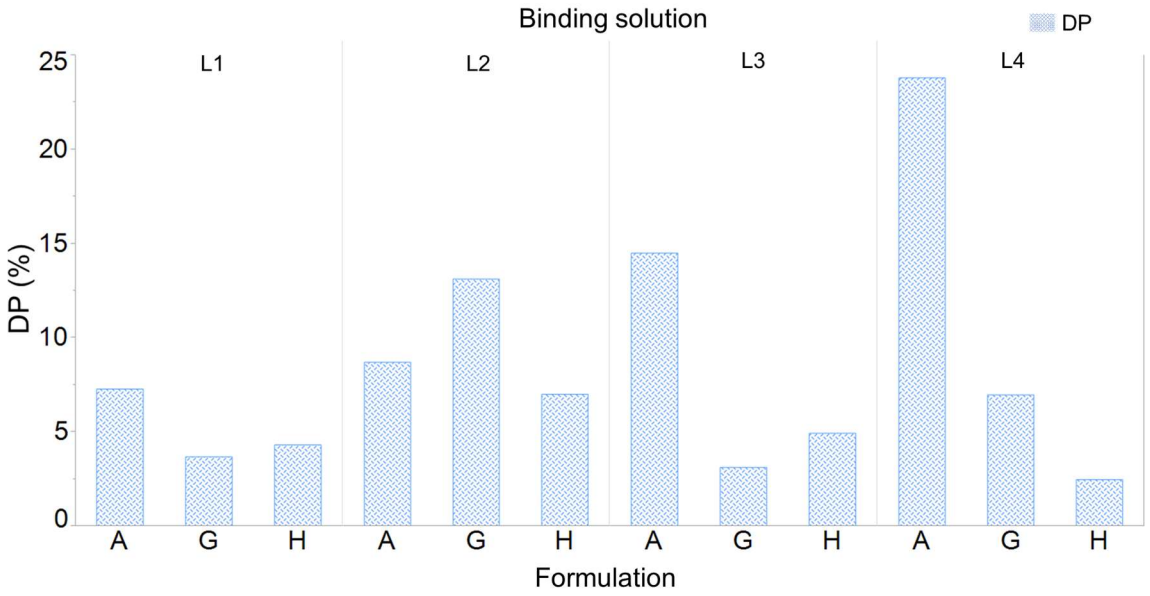

Fig. 5.31. The de-mixing potential for formulations with different ibuprofen loadings. Varying binder delivery methods and solution properties (L1, L2, L3 and L4) for batch code A (low-dose), (b) batch code G (medium-dose) and (c) batch code H (high-dose).

5.4 Conclusions

The present study investigated the effect of formulation and binder delivery method on critical quality attributes of granules and tablets. Low-dose formulations showed similar flow properties and wettability irrespective of the penetration liquids. Also, binder delivery method had more significant effect on granule size distribution compared to the variation of active ingredients. Higher viscosity binder tended to form oversize particles due to the inability of being uniformly redistributed within a very short residence time. The dry binder delivery method produced more densified granules on account of the high

degree of deformation and consolidation during granultion. In contrast, the active ingredient in different formulations demonstrated more dominant effect on drug agglomerate size distribution. APIs with poor water solubility or smaller primary particle size displayed a tendency to form smaller aggregates in the tablets with enhanced distributive and dispersive mixing ensuring uniform and finer distribution structure. The drug segregation extent was primarily controlled by drug loading where the high-dose formulation revealed the lowest de-mixing potential.

Chapter 6

Towards better design and understanding of continuous wet granulation process. Part I: investigation of twin-screw granulator by employing sequential experimentation strategy

6.1 Objectives

Considering a scenario of commercial manufacturing, formulation in all likelihood has already been predetermined as part of the registered process. In order to ensure product quality and safety, the priority, ipso facto, is to design a flexible and robust manufacturing process. This emphasizes the needs to leverage DoE, an essential element of QbD, rather than the best-guess or one-factor-at-a-time approaches, to full comprehend the complex correlation between critical process and equipment factors and critical quality attributes, which after optimization can assist in establishing the design space for the end-product (Yu, 2008). However, in the absence of prior knowledge and experience to a new system or process, there is an abundance of variables, levels and range available to the investigator. According to *Pareto principle*, approximately 80% of the events stem from 20% of the possible causes (Montgomery, 2013). In this context, different experimental strategies can either stimulate technical knowledge or preclude progress by wasting valuable time and resources. The philosophy employed in this study is called sequential experimentation strategy based on an evolutionary adaptation of successive experimental phases where concrete knowledge of the system gathered from previous phases will provide insightful guidance for planning the subsequent experiments (Flores and Norbury, 1991). By implementing such a continual refinement process, it can

systemically and efficiently advance the system understanding from initial conjecture and hypothesis to an eventual optimized state with quantitative description.

Currently, very few studies shed lights on leveraging sequential design strategy towards better design and understanding of continuous wet granulation process. The present work aims to (1) commence with screening experimental design to accommodate numerous candidate factors of potential importance and identify those significantly affecting response variables, (2) comprehensively investigate the relationship between CPPs and CQAs of granules and tablets by implementing response surface methodology, and (3) locate the optimum operational regions and propose design space based on the defined target product quality profiles.

6.2 Material and methods

6.2.1 Materials

A low-dose formulation used in this study was composed of 8% (w/w) caffeine anhydrous (CSPC Innovation Pharmaceutical Co., Ltd., Hebei, China) as the model drug and 44% (w/w) α-lactose monohydrate (310 NF, Foremost Farms USA, Baraboo, WI) and 44% (w/w) microcrystalline cellulose (MCC, Avicel® PH101, FMC Biopolymer, Philadelphia, PA) as the excipients. Moreover, 4% (w/w) polyvinylpyrrolidone (PVP K30, Fisher Scientific, Pittsburgh, PA) was added as a dry binder to the powder mixture. Distilled water was used as granulation liquid. Several key specifications of each ingredient and premix were shown in Table 6.1.

Table 6.1 Materials specifications and physical properties

Component	D10 (μm)	D50 (μm)	D90 (μm)	Bulk density (g/ml)	Tapped density (g/ml)	Hausner Ratio
Caffeine	9.01	33.85	83.16	-	-	-
MCC	25.16	63.97	112.9	-	-	-
Lactose	15.26	67.32	114.4	-	-	-
Premix	15.32	55.82	98.85	0.469	0.641	1.365

6.2.2 Raw materials premixing

All the ingredients were firstly passed through a No. 35 mesh sieve (500 μm) for deagglomeration and then premixed in the ResonantAcoustic® Mixer (LabRAM™, Resodyn Acoustic Mixer, Inc., Butte, MT) for 3 minutes with mixing intensity (acceleration value) of 45 g's. A twin-screw loss-in-weight microfeeder (MT12, Coperion K-Tron, Inc., Sewell, NJ) equipped with coarse concave screws was used to feed premix into the twin-screw granulator. At 100% motor speed, the feeding capacity (feed factor) is 1.4 kg/h.

6.2.3 Twin-screw granulation

Thermo Scientific™ Pharma 11 co-rotating parallel TSG (Thermo Fisher Scientific, Karlsruhe, Germany) was used for the granules production (Fig. 6.1 (a)). It features a screw diameter of 11mm, processing length of length to diameter (L/D) ratio 40:1, max. screw speed of 1000rpm and throughput from 20 g/h to 2.5 kg/h. Fig. 6.1 (b) showed one of the screw configurations investigated in the screening experiments, which was further adopted and fixed in the subsequent response surface design. From left to right, it consisted of eleven standard conveying elements (CE) with helix pitch of 1 L/D, one 1 L/D distributive feed screw (DFS), nineteen 1 L/D CEs, five 0.25 L/D kneading elements (KE), four 1 L/D CEs, two long pitch 2 L/D CEs (*l*CE) and one short pitch 0.5 L/D CE (*s*CE), which can be referred to as "11CE-1DFS-19CE-5KE-4CE-2*l*CE-1*s*CE".

CE mainly functions to transport materials between different zones whiling imparting low mechanical energy. In contrast, KE has very limited conveying capacity but subjects liquid/powder mixture to vigorous shearing force for dispersive mixing and agglomerate size reduction. The staggering angle between two contiguous KEs dictates the magnitude and direction of generated drag flow. DFS can exponentially increase materials interfacial area, thereby promoting content uniformity by distributive mixing where the extensional and folding chaotic flows homogeneously distribute ingredients devoid of cohesive resistance throughout the product volume. Fig. 6.1 (c) illustrated that powder and liquid were delivered into the barrel through the 1st and 2nd zones, respectively. Kneading blocks were arranged in the 3rd zone following liquid addition port and DFS, if configured, was in the 7th zone. In addition, the main feed zone 1 is permanently cooled while temperature of the remaining zones is controllable.

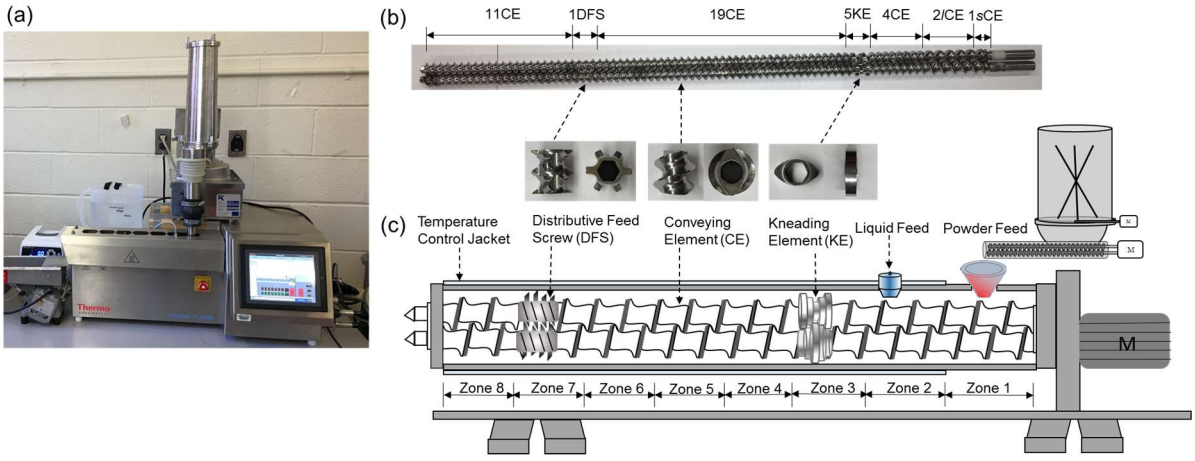

Fig. 6.1. (a) Thermo Scientific™ Pharma 11 twin-screw granulator, (b) configuration of screws, and (c) schematics of granulator functioning principles.

6.2.4 Experimental design and model regression methodologies

6.2.4.1 Screening design

Table 6.2 shows the candidate factors of potential importance in the screening stage. Each independent continuous variable: screw speed (x_1), barrel temperature (x_2), liquid to solid (L/S) ratio (x_3) and throughput (x_4) and discrete numeric variable: KE staggering angle (x_5) and number (x_6), were investigated at three different levels. Particularly, the rotational direction of KE staggering angle was considered to be in the reverse direction because their outer lobes rotated in the opposite direction as opposed to the flights of conveying screws. KE number of 5 or 9 was configured as one block whereas that of 14 was separated by one standard CE into two blocks (7 in each). The two levels of categorical variable indicate the inclusion of DFS (x_7) in the screw configuration (w/) or that it was replaced with a standard CE (w/o). Besides, one of the most important granule attributes: size distribution (D10, D50, D90 and span) and one crucial mechanical parameter for materials processability: torque, were used as the responses for screening.

Table 6.2 Independent variables with specified levels and responses in the screening design

Independent variable			Level			Response
Continuous	Discrete numeric	Categorical	Low	Intermediate	High	
Screw speed (rpm)			200	500	800	Granule size distribution (D10, D50, D90 and span); Torque
Barrel temperature (°C)			25	35	45	
L/S ratio			0.35	0.45	0.55	
Throughput (kg/h)			0.4	0.8	1.2	
	KE staggering angle (°)		30	60	90	
	KE number		5	9	14	
		DFS	w/ or w/o			

Typically, standard classical designs such as are factorials and fractional factorials are orthogonal designs whose information matrices are diagonal matrices. Due to the practical constraints in this study, however, an irregularly shaped domain of interest was constructed by mixed-level quantitative and qualitative factors. It is thus more advisable to adopt flexible optimal design for estimating main effects and two-factor interactions. Among several popular design optimality criteria, D-optimal is deemed to be the most appropriate for designs in the screening situation (García et al., 2005). As postulated in Eq. 6.1, a multiple linear regression model describes the relationship between responses and independent variables.

$$\boldsymbol{y} = \mathbf{X}\boldsymbol{\beta} + \boldsymbol{\varepsilon} \tag{6.1}$$

where $\boldsymbol{y}$, $\mathbf{X}$, $\boldsymbol{\beta}$ and $\boldsymbol{\varepsilon}$ denote $(n \times 1)$ vector of observations, $(n \times p)$ model matrix, $(p \times 1)$ vector of regression coefficients and $(n \times 1)$ vector of random errors, respectively. The estimation of $\boldsymbol{\beta}$ by least-squares fitting, $\hat{\boldsymbol{\beta}}$, measures the influence of corresponding factors on the responses:

$$\hat{\boldsymbol{\beta}} = (\boldsymbol{X}^{\mathrm{T}}\boldsymbol{X})^{-1}\boldsymbol{X}^{\mathrm{T}}\boldsymbol{y} \tag{6.2}$$

where $\boldsymbol{X}^{\mathrm{T}}\boldsymbol{X}$ and $(\boldsymbol{X}^{\mathrm{T}}\boldsymbol{X})^{-1}$ are called information matrix and dispersion matrix, respectively. Eq. 6.2 reveals the correlation between quality of estimated coefficients and experimental design because it is directly controlled by the properties of dispersion matrix or model matrix that is further determined by the design matrix. The joint confidence region for $\hat{\boldsymbol{\beta}}$ is represented by hyperellipsoids and can be obtained by Eq. 6.3:

$$(\beta - \hat{\beta})^{\mathrm{T}} (\boldsymbol{X}^{\mathrm{T}} \boldsymbol{X})(\beta - \hat{\beta}) \leq p s^2 F_{[\alpha,(p,\gamma)]} \tag{6.3}$$

where p, s^2 and $F_{\alpha,(p,\gamma)}$ are number of coefficients in the model, estimate of the error variance and the critical F-values with (p,γ) degrees of freedom at the significance level α, respectively. It can have different volumes, shapes and orientations corresponding to different quality of estimated coefficients, which is, in turn, also dictated by the design matrix. The D-optimal design fulfills such a criterion by proper selection of runs as maximizing the determinant of information matrix $\left|(\boldsymbol{X}^T \boldsymbol{X})\right|$, thereby minimizing the volume of joint confidence region and the overall estimation variance of model regression coefficients (Brown, 2009).

In this study, a 40-run D-optimal design (see Table 6.3) with the D-efficiency of 85.09% was generated by JMP® statistical software (SAS Institute Inc., Cary, NC). Relationship between responses (y) and independent variables (x) were approximated by the second-order interaction models as follows, Eq. 6.4:

$$y = \beta_0 + \sum_{i=1}^{k} \beta_i x_i + \sum_{i<j} \sum \beta_{ij} x_i x_j + \varepsilon \tag{6.4}$$

The target is to precisely estimate model coefficients for factors screening. Besides, RunOrder in Table 6.3 is the randomized run order to conduct experiments while StdOrder is the standard order sorted according to screw configuration. Note that all experimental run numbers mentioned in the following sections refer to the StdOrder.

Table 6.3 The 40-run D-optimal design for four 3-level continuous factors, two 3-level discrete numeric factors and one 2-level categorical factor

StdOrder	RunOrder	x_1	x_2	x_3	x_4	x_5	x_6	x_7
1	1	800	45	0.35	0.4	90	14	w/
2	14	200	25	0.55	0.4	90	14	w/
3	32	800	45	0.55	1.2	90	14	w/
4	38	200	45	0.35	1.2	90	14	w/
5	4	800	25	0.35	0.4	90	14	w/o
6	24	200	25	0.35	1.2	90	14	w/o
7	26	200	45	0.55	0.4	90	14	w/o
8	35	800	25	0.55	1.2	90	14	w/o
9	9	500	35	0.45	0.8	60	9	w/o
10	2	200	45	0.55	1.2	30	14	w/o
11	13	200	45	0.35	0.4	30	14	w/o
12	21	800	45	0.55	0.4	30	14	w/o
13	27	200	25	0.55	0.4	30	14	w/o
14	37	800	45	0.35	1.2	30	14	w/o
15	7	200	45	0.55	0.4	30	14	w/
16	23	200	25	0.55	1.2	30	14	w/
17	28	800	25	0.35	1.2	30	14	w/
18	39	800	25	0.55	0.4	30	14	w/
19	40	200	25	0.35	0.4	30	14	w/
20	17	500	35	0.45	0.8	60	9	w/
21	3	200	45	0.55	0.4	30	5	w/o
22	6	800	45	0.35	0.4	30	5	w/o
23	15	800	25	0.35	1.2	30	5	w/o
24	16	800	45	0.55	1.2	30	5	w/o
25	31	200	45	0.35	1.2	30	5	w/o
26	10	800	25	0.55	1.2	30	5	w/
27	12	800	45	0.35	1.2	30	5	w/
28	30	800	25	0.35	0.4	30	5	w/
29	33	200	25	0.35	1.2	30	5	w/
30	34	200	25	0.55	0.4	30	5	w/
31	25	500	35	0.45	0.8	60	9	w/o
32	5	200	45	0.35	0.4	90	5	w/
33	8	200	45	0.55	1.2	90	5	w/
34	19	800	45	0.55	0.4	90	5	w/
35	18	800	25	0.35	1.2	90	5	w/
36	20	200	25	0.55	1.2	90	5	w/o
37	22	800	25	0.55	0.4	90	5	w/o
38	29	800	45	0.35	1.2	90	5	w/o
39	11	200	25	0.35	0.4	90	5	w/o
40	36	500	35	0.45	0.8	60	9	w/

6.2.4.2 Response surface design

By deploying response surface methodology, an empirical model with satisfactory adequacy was developed to reliably estimate the experimental variability and precisely predict responses over the design space. Concretely, three critical factors identified from the screening stage (barrel temperature, L/S ratio and throughput) were further investigated at three different levels (see Table 6.4). Comprehensive characterizations were performed to examine the influence of independent variables exerted on the critical quality attributes of granules (size distribution, shape, porosity, densities, flowability and processability) and tablets (hardness and dissolution). As shown in Table 6.5, a 30-run 3^3 factorial design augmented with 3 center points was generated by the JMP® software. Process optimization was based on the second-order quadratic models, Eq. 6.5, that accounts for the curvature in different x_i directions:

$$y = \beta_0 + \sum_{i=1}^{k} \beta_i x_i + \sum_{i=1}^{k} \beta_{ii} x_i^2 + \sum_{i<j} \sum \beta_{ij} x_i x_j + \varepsilon \tag{6.5}$$

Table 6.4 3-level independent variables and responses in the response surface design

Independent variable	Level			Response	
	Low	Intermediate	High	Granules	Tablets
Barrel temperature (°C)	25	35	45	Granules size distribution (D10, D50, D90, Span); Shape (Eccentricity); Porosity; Bulk density; Tapped density; Flowability (Hausner ratio); Torque	Tensile strength; Porosity; *In-vitro* dissolution
L/S ratio	0.35	0.45	0.55		
Throughput (kg/h)	0.4	0.8	1.2		

Table 6.5 The 30-run response surface design for three 3-level continuous factors

StdOrder	RunOrder	x_2	x_3	x_4
1	13	25	0.35	0.4
2	15	25	0.35	0.8
3	9	25	0.35	1.2
4	8	25	0.45	0.4
5	2	25	0.45	0.8
6	26	25	0.45	1.2
7	28	25	0.55	0.4
8	6	25	0.55	0.8
9	18	25	0.55	1.2
10	10	35	0.35	0.4
11	14	35	0.35	0.8
12	21	35	0.35	1.2
13	12	35	0.45	0.4
14	17	35	0.45	0.8
15	29	35	0.45	0.8
16	4	35	0.45	0.8
17	25	35	0.45	0.8
18	30	35	0.45	1.2
19	27	35	0.55	0.4
20	19	35	0.55	0.8
21	16	35	0.55	1.2
22	23	45	0.35	0.4
23	24	45	0.35	0.8
24	20	45	0.35	1.2
25	11	45	0.45	0.4
26	3	45	0.45	0.8
27	1	45	0.45	1.2
28	5	45	0.55	0.4
29	7	45	0.55	0.8
30	22	45	0.55	1.2

6.2.4.3 Stepwise least squares regression

Optimal variables selection in the final regression model necessitates striking a balance between parsimony (fewer regressors if possible) and accuracy (more regressors if requisite). For both screening and response surface designs, forward stepwise regression was employed to select a subset of terms that are the most influential. By starting with a null model that has no predictors but only one intercept, the JMP® software successively adding or removing regressor variables until the stopping rule, Akaike information

criterion with a correction for finite sample sizes (AICc) or Bayesian Information Criterion (BIC), is satisfied (Bendel and Afifi, 1977). The finalized model minimizes AICc or BIC as defined by Eq. 6.6 and 6.7, which rewards goodness of fit (maximum likelihood function) but simultaneously penalizes increasing model terms to discourage overfitting.

$$\text{AICc} = -2LogL(\beta) + 2p + 2p(p+1)/(q-p-1) \tag{6.6}$$

$$\text{BIC} = -2LogL(\beta) + p\ln(q) \tag{6.7}$$

where $L(\beta)$, p and q represent the likelihood function, number of estimated coefficients in the model and number of observation in the data set, respectively.

6.2.5 Granule characterization

Granules from each experiment were air-dried at ambient conditions until the loss-on-drying moisture content was less than 3%. The dried granules were then subsampled by spinning riffler (Gilson Company Inc., Lewis Center, OH) to ensure unbiased sampling for different characterizations.

6.2.5.1 Particle size distribution

The particle size of raw materials and premix listed in Table 6.1 were determined by laser diffraction analyzer (Beckman-Coulter Inc., Pasadena, CA). Granule size distribution (GSD) was measured by sieve analysis utilizing a $\sqrt{2}$ series of sieves with screen scale ranging from 38 μm to 4 mm. GSD was plotted as the normalized mass frequency (f_{mi}) shown in Eq. 6.8 versus the midpoint of each size interval on logarithmic scale (Allen and Elsevier, 2003).

$$f_{mi}(\ln x) = \frac{m_i}{\ln(\overline{n_i} / \overline{n_{i-1}})} \tag{6.8}$$

where m_i and $\overline{n_i}$ are the mass fraction and midpoint of size interval i, respectively.

6.2.5.2 Granule porosity

The true density of granules (ρ_t) was measured by a helium pycnometer (AccuPyc II 1340, Micromeritics, Norcross, GA) while the envelope density (ρ_e) was tested by Geopyc 1360 (Micromeritics, Norcross, GA). Granules with a size fraction of 1.0-1.4 mm were placed in a desiccator overnight prior to any densities measurements. The granule porosity (ε_g) was calculated by Eq. 6.9.

$$\varepsilon_g = 1 - \frac{\rho_e}{\rho_t} \tag{6.9}$$

6.2.5.3 Bulk and tapped densities

The bulk densities of granules (ρ_B) and raw materials premix were measured by FT4 powder rheometer (Freeman Technology, Wayne, PA). Tapped density (ρ_T) was measured via an automated tapped density analyzer (Quantachrome Instruments, Boynton Beach, FL) associated with a 250 ml graduated cylinder. Hausner ratio (HR) defined by Eq. 6.10 was used to describe the flowability of granules.

$$\mathrm{HR} = \frac{\rho_T}{\rho_B} \tag{6.10}$$

6.2.6 Tablet characterization

Granules between 125 to 500 μm were compacted into tablets by a tablet press emulator (Presster™, Metropolitan Computing Corporation, East Hanover, NJ) with an upper compaction force of 10 kN. It emulated the Fette Compacting 1200i tablet press (24 station). A round flat-faced punch was used to obtain cylindrical tablets with 10 mm diameter (d). Powder dosing weight was controlled around 350 mg for each tablet.

6.2.6.1 Tensile strength

Tablet thickness (h) was measured by a digimatic digital caliper (Mitutoyo America, Aurora, IL) and radial fracture force (F) was determined in a hardness tester (MultiTest 50, SOTAX, Westborough, MA). Tablet tensile strength (σ_t) was then calculated by Eq. 6.11 (Fell and Newton, 1970).

$$\sigma_t = \frac{2F}{\pi dh} \tag{6.11}$$

6.2.6.2 Tablet porosity

With the apparent density (ρ_o) given by tablet weight and volume, tablet porosity (ε_t) can be obtained with a similar equation as granule porosity:

$$\varepsilon_t = 1 - \frac{\rho_o}{\rho_t} \tag{6.12}$$

6.2.6.3 In vitro Dissolution

Six tablets from each batch were dissolved in 900 ml phosphate buffer solution at pH 7.4 and 37.3 °C (USP <711>). The dissolution apparatus (708-DS, Agilent Technologies, Santa Clara, CA) coupled with a UV/Vis spectrophotometer were utilized to measure caffeine absorbance at the wavelength of 273 nm. Drug concentration at each time point was then derived from a standard UV calibration curve with the linear correlation (R^2 = 0.9998) from 0.01 to 0.32 g/L. Parameters $t_{3\,\mathrm{min}}$, $t_{90\%}$ and dissolution efficiency ($DE_{10\,\mathrm{min}}$) were used to characterize and compare the drug release profiles. $t_{3\,\mathrm{min}}$ and $t_{90\%}$ correspond to the percentage of drug dissolved after 3 min and the time necessary to release 90% of the drug, respectively. $DE_{10\,\mathrm{min}}$ defined in Eq. 6.13 is the area under the

dissolution curve up to 10 min dissolution as a percentage of the area of the rectangle described 100% dissolution at the same time (Costa and Sousa Lobo, 2001).

$$\mathrm{DE}_{10\ \mathrm{min}}\ (\%) = \frac{\int_0^t k \cdot dt}{k_{100} \cdot t} \cdot 100 \tag{6.13}$$

where k is the drug percent dissolved at time t.

6.3 Results and discussion

6.3.1 Screening design

6.3.1.1 Model reduction based on stepwise regression

Statistical analysis for the screening experiments in Table 6.3 excluded run #10 and #16, primarily due to the inability to produce granules under these processing conditions. The highest level of throughput, L/S ratio and KE number coupled with the lowest level of screw speed resulted in excessive materials hold-up volumes and shear force in the granulator. Torque, therefore, exceeded the equipment upper limit rendering materials unprocessable.

The full second-order interaction model for D10, one of the screening responses specified in Table 6.2, comprised twenty-nine terms in total including intercept, seven main effects and twenty-one interaction effects. The stepwise fit history of D10 in Fig. 6.2 demonstrated the change of AICc and BIC criterion values as the number of regressors increased in the model. It also exemplified the generation of a more efficient *reduced model* that tackles the trade-off between goodness of fit and simplicity. Eq. 6.14 showed the finalized seven-parameter model consisting of one intercept and six influential independent variables satisfying the criterion to minimize AICc. The terms included an interaction effect KE number*KE staggering angle and all main effects

except for barrel temperature and DFS. A slightly different model composed of intercept and five regressors was obtained by adopting minimum BIC stopping rule due to its larger penalty term in the definition (not shown). Table 6.6 summarized the independent variables in each reduced model of screening responses. The regression statistics, adjusted R^2 and prediction R^2, signified satisfactory model performance. It can be seen that DFS was the sole marginal factor compared with the remaining main effects significantly contributing to either GSD or torque.

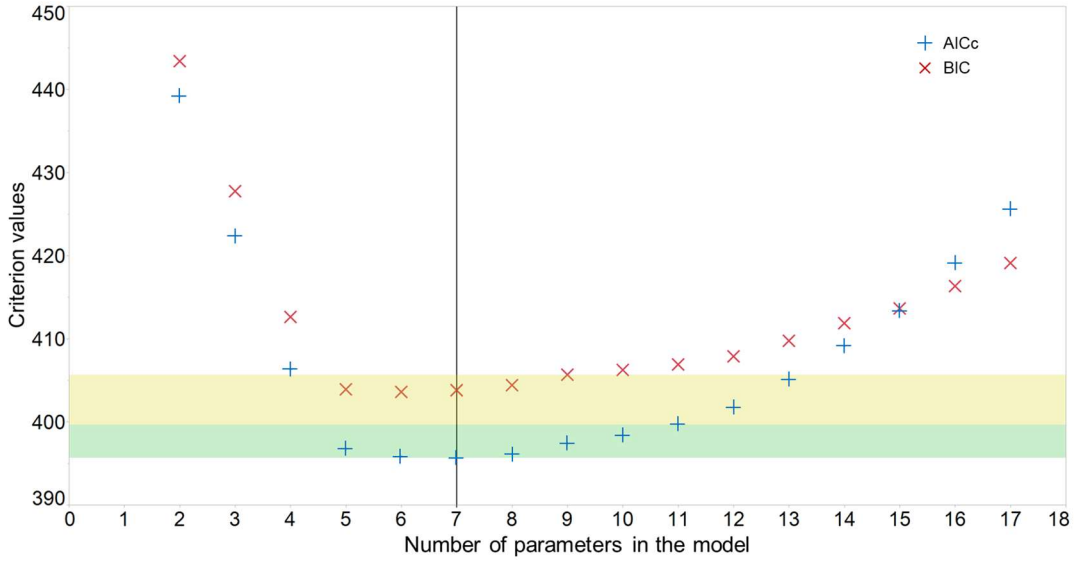

Fig. 6.2. Plot of criterion values (+: AICc and ×: BIC) versus parameter numbers in the stepwise regression model of D10. Black solid line indicates the minimum AICc value (Min_{AICc}) obtained with seven parameters. Shaded green and yellow zone are defined by the range [Min_{AICc}, Min_{AICc}+4] and (Min_{AICc}+4, Min_{AICc}+10], respectively.

$$\widehat{D10} = 245.77 + 59.85 \cdot \left(\frac{(x_1 - 500)}{300}\right) + 48.47 \cdot \left(\frac{(x_3 - 0.45)}{0.1}\right) + 11.62 \cdot \left(\frac{(x_4 - 0.8)}{0.4}\right)$$
$$- 25.97 \cdot \left(\frac{(x_5 - 60)}{30}\right) + 39.33 \cdot \left(\frac{(x_6 - 9.5)}{4.5}\right) - 14.18 \cdot \left(\frac{(x_5 - 60)}{30}\right)\left(\frac{(x_6 - 9.5)}{4.5}\right)$$

(6.14)

Table 6.6 t-statistic of independent variables and regression statistics of screening reduced interaction models

Regressor	Screening response				
	D10 (μm)	D50 (μm)	D90 (μm)	Span	Torque (N·m)
x_1	9.22	5.98	-1.68	-11.75	-10.99
x_2					-2.18
x_3	7.46	5.03	-3.32	-9.69	-16.54
x_4	1.71	2.15	-0.57		11.11
x_5	-4.04	-6.43	-2.36	2.24	-5.50
x_6	6.06	7.43	2.34	-3.26	13.50
x_7					
x_1*x_3		2.62	4.41	3.31	
x_1*x_4		2.86	2.87		-6.41
x_1*x_6					-8.82
x_3*x_4		2.47			-4.29
x_3*x_5		2.93	2.36	-2.66	
x_3*x_6				3.56	-6.42
x_4*x_5			2.52		4.13
x_4*x_6			-4.01		
x_5*x_6	-2.18	-3.35		3.29	2.28
Regression Statistics					
Adj R-Sq	0.83	0.84	0.65	0.88	0.96
Pred R-Sq	0.81	0.81	0.55	0.84	0.94

6.3.1.2 Variable selection for response surface design

To enable a convenient and reliable control over quality attributes during manufacturing process, screw configuration was decided to be optimized and fixed for the response surface design, leaving only the CPPs adjustable. Contour plot in Fig. 6.3 (a) was based on the reduced model of D10, illustrating the influence of KE number and staggering angle. The increase in KE number and decrease in offset angle could maximize D10 suggesting that granule growth and coalescence predominated over breakage. The addition of KE accentuated the vigorous smearing mechanisms and prolonged the consolidation and coalescence events while more wet agglomerates from

upstream sections progressively accumulated in the kneading blocks (El Hagrasy and Litster, 2013). Fines reduction in this case was improved largely due to the increased surface area of granule fragments available for dry fines layering.

Staggering angle dictated the gap volume between the tips of each pair of KE. Smaller advance angle such as 30° kneading block configuration was associated with longer divergence in the middle channel and thus subjected the materials to less frequent KE intersection. The kneading discs with neutral 90° configuration, in contrast, kept alternating between barrel wall and the middle channel to chop off or squeeze the agglomerates through rotating tips, thereby engendering more breakage. Similar trends were observed for D50 and D90 (not shown). However, the highest level of KE number in conjunction with lowest level of offset angle generated the smallest span (narrowest size distribution) primarily by virtue of the balance between promoted granule growth and breakage of over-granulated particles (not shown).

Furthermore, the effect of KE number and staggering angle on torque as shown in Fig. 6.3 (b) bore some resemblance to that on D10. The highest torque was generated with 14 kneading discs mainly in that the largest amount of materials was processed in the kneading section. In addition, unlike the neutral 90° configuration providing a certain passage for materials to move forward, 30° reverse configuration smeared those wet agglomerates against barrel wall with resultant shear-elongation, which could also contribute to the torque increase and compromise materials processability to some extent.

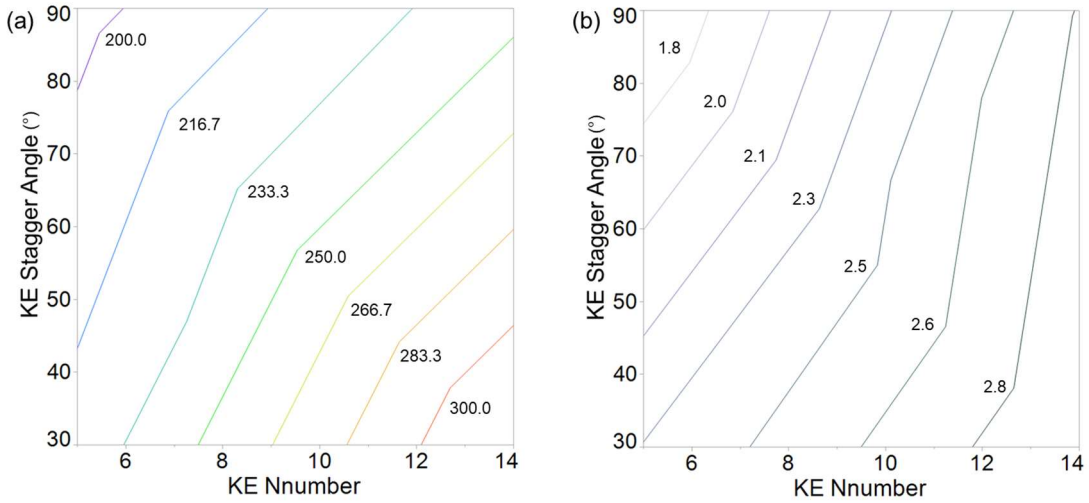

Fig. 6.3. Contour plots of (a) D10 and (b) Torque in terms of KE staggering angle versus KE number. The rest of independent variables are fixed at intermediate levels.

Based on the specified limits of predefined quality target values of each response (see Table 6.7, overlaid contour plots in Fig. 6.4 showed the history of exploratory trials to determine the optimum settings or ranges of these critical factors for response surface design. For instance, the green and blue areas in Fig. 6.4 (a) indicated the conditions giving rising to granules span above 2 and D10 below 180 μm, respectively. Analogously, the red area in Fig. 6.4 (b) embodied the produced D90 larger than 1050 μm. The unshaded portion (white area) was deemed to be the design space where L/S ratio and throughput can be adjusted arbitrarily and ensure a satisfactory process without transcending the boundaries. The significant influence of these two process parameters may also be exploited for a capable control loop conducive to real-time adjustment at different levels. By examining a series of operation conditions, the target in screening stage is thus to maximize the "sweet spot" and enable greater sensitivity and amenability of granulation process with respect to diverse quality specifications. Compared to Fig. 6.4 (d) that has the whole entire operation window as "sweet spot", Fig. 6.4 (a), (b) and (c)

demonstrated separately the necessity for a screw speed beyond 500 rpm, smaller KE staggering angle and less kneading discs in the screw configuration so as to ameliorate the fines reduction (D10), produce granules with monomodal size distribution (span), enhance materials processability (torque) and obviate the over-granulated particles or lumps undesirable for tableting (D50 and D90).

On the basis of aforementioned analysis, three critical process parameters, throughput, L/S ratio and barrel temperature were selected for further investigation in the response surface design as specified in Table 6.4. All other independent variables were held constant at their optimum levels: screw speed at 700 rpm, KE staggering angle at 60°, KE number at 5 and DFS in the screw configuration.

Table 6.7 Responses with specified quality target values in the screening design

Quality target value	Response				
	D10 (μm)	D50 (μm)	D90 (μm)	Span	Torque (N·m)
Low limit	180	-	-	-	-
High limit	-	600	1050	2	3

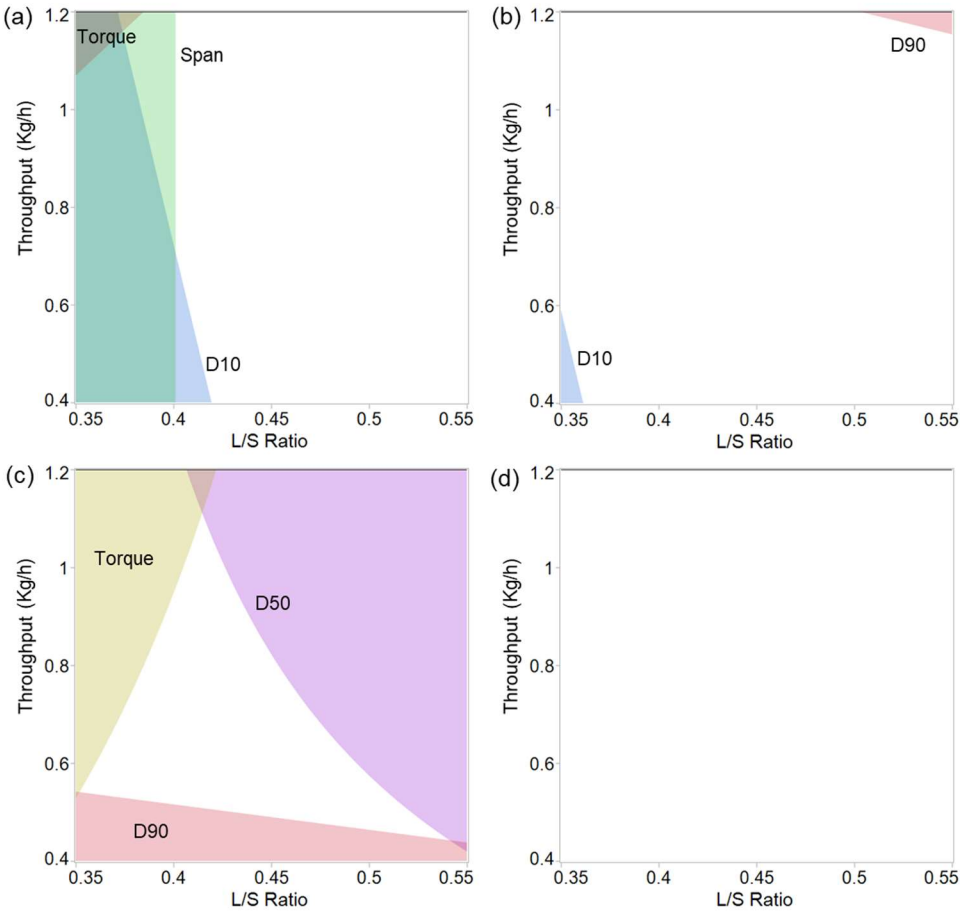

Fig. 6.4. Design space in terms of throughput and L/S ratio with barrel temperature at 45°C and DFS in the screw configuration. Plots are based on the overlay of screening response contours. (a) Screw speed at 500 rpm, KE staggering angle at 60° and KE number at 5; (b) screw speed at 700 rpm, KE staggering angle at 90° and KE number at 5; (c) screw speed at 700 rpm, KE staggering angle at 60° and KE number at 14 and (d) screw speed at 700 rpm, KE staggering angle at 60° and KE number at 5.

6.3.2 Response surface design

6.3.2.1 Model reduction and adequacy checking

Table 6.8 exemplified the analysis of variance (ANOVA) results for the full second-order quadratic model of D10. It showed that the "model" source of variability was subdivided into several components. All three main effects with *P*-values well below 0.05

had significant influence on D10 whereas the barrel temperature-throughput interaction *F* ratio has a *P*-value of 0.0739, indicating some interaction between these factors. The residual sum of squares was partitioned into a *pure error* component arising from the replication of the center points and a *lack of fit* component comprising the sums of squares for higher degree of interaction and polynomial terms excluded in the model. The *P*-value of 0.5759 signified no strong evidence of *lack of fit*, namely that the statistic F_0 follows $F_{0.05,\,22,\,3}$ distribution, confirming the linearity of regression function.

A reduced model of D10 was further developed predicated on stepwise regression. After removing some nonsignificant terms from the full model, the adjusted R^2 (0.87) and prediction R^2 (0.84) both increased compared to those in Table 6.8, enabling the final model function more effectively as a predictor of new data. Table 6.9 summarized the independent variables in different response surface reduced quadratic models regrading critical granule and tablet attributes. The regression statistics (Adj R-Sq and Pred R-Sq) of most models are indicative of satisfactory performance that more than 80 percent of variability were expected to be explained in terms of fitting measured data as well as predictive ability in new experiments. However, it was noticeable that the adjusted R^2 of bulk density (0.70), tapped density (0.41) and Hausner ratio (0.45) were relatively small, implying more residual variability remained unexplained in the current experiment. Their respective prediction R^2 were 0.64, 0.33 and 0.25, which were not unreasonable, considering the amount of data variability accounted for in the model. Typically, aside from granulation processing conditions, granule densities and flowability can also be affected by some nuisance factors whose implication might be considerable yet difficult to control, such as particle morphology, materials moisture content or relative humidity

during measurement. Therefore, it is not surprising that statistics of ρ_B, ρ_T and HR were inferior to that of other responses.

Table 6.8 ANOVA for D10 with response surface full quadratic model

Source	Sum of Squares	Degree of Freedom	Mean Square	*F* Value	Prob > *F*
Model	20881.052	9	2320.12	20.064	<0.0001*
x_2	5587.769	1	5587.769	48.322	<0.0001*
x_3	12739.579	1	12739.579	110.165	<0.0001*
x_4	1875.837	1	1875.837	16.222	0.0007*
x_2*x_3	9.423	1	9.423	0.0815	0.7782
x_2*x_4	411.425	1	411.425	3.558	0.0739
x_3*x_4	13.768	1	13.768	0.119	0.7337
x_2^2	235.691	1	235.691	2.038	0.1688
x_3^2	0.271	1	0.271	0.0023	0.9618
x_4^2	8.076	1	8.076	0.0698	0.7943
Residual	2312.713	20	115.64		
Lack of Fit	1970.841	17	115.932	1.0173	0.5759
Pure Error	341.872	3	113.957		
Cor Total	23193.765	29			

Adj R-Sq: 0.86, Pred R-Sq: 0.78. *statistical significance at α=0.05.

Table 6.9 t-statistic of independent variables and regression statistics of response surface reduced quadratic model

Regressor	Response													
	D10	D50	D90	Span	ε_g	ρ_B	ρ_T	HR	Torque	σ_t	ε_t	t_{3min}	$t_{90\%}$	DE_{10min}
x_2	7.36	6.14		-4.39	-1.97			-0.98	-5.26	-12.24	4.74	2.31		
x_3	11.11	8.41	-12.06	-14.97	-14.53	7.64	4.61	-2.59	-19.42	-8.11	-3.41	-10.5	16.21	-11.42
x_4	4.26	7.73	7.36		5.33	2.04		-3.22	6.89	-2.68				
x_2*x_3		3.06			5.04			2.73						
x_2*x_4	-2.00													
x_3*x_4			-2.43		-4.04									
x_2^2		-2.56		2.27	-4.31									
x_3^2		2.90				2.70				-2.09			-3.43	
x_4^2			-1.75					1.84						
Regression Statistics														
Adj R-Sq	0.87	0.86	0.88	0.89	0.91	0.70	0.41	0.45	0.94	0.88	0.53	0.80	0.90	0.82
Pred R-Sq	0.84	0.81	0.86	0.88	0.88	0.64	0.33	0.25	0.93	0.85	0.46	0.77	0.89	0.80

In addition, certain assumptions on the errors such as normality and independence should be satisfied by utilizing ANOVA for testing the hypothesis of no difference in

treatment means. The residuals between an estimate of the corresponding observation are expected to be structureless with no obvious patterns, provided that the model is adequate (Montgomery, 2013). A normal probability plot constructed in Fig. 6.5 (a) showed that distribution of D10 residuals approximately resembled a straight line and thus was not grossly nonnormal. Moderate departures from normality was reflected by the tendency inclined to bend upward slightly on the right side and downwards on the left side. However, it was generally of little concern under such a scenario given that the fixed effects ANOVA was considered to be robust to the normality assumption. Notice that the residual at the bottom left corner in Fig. 6.5 (a) deviated more severely than others, which deserved further careful investigation before interpreting it as an outlier. After standardizing this residual by error mean square, a value of 2.72 (less than 3) ruled out the possibility that its presence may distort the ANOVA results. Furthermore, the random scattered patterns of D10 residuals versus fitted values in Fig. 6.5 (b) did not discover any abnormalities, confirming that the errors with constant variance and mean centered at zero were independently distributed without correlating to any other variable or predicted response. Model adequacy checking of the remaining responses did not reveal any violation of the underlying assumptions either (not shown).

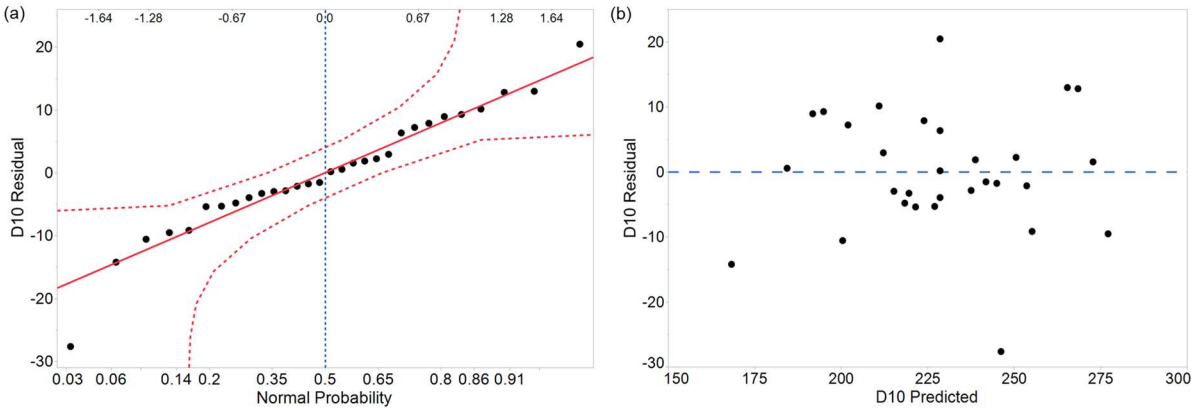

Fig. 6.5. Plots of model adequacy checking. (a) Normal probability plot of residuals. Red solid line, red dash lines and blue dash line denote diagonal reference line, 95% Lilliefors confidence bounds and 50th percentile reference line, respectively. Top *x*-axis shows normal quantile scale while bottom shows probability scale. (b) Plot of D10 residuals versus fitted values. Blue dash line represents the mean of residuals.

6.3.2.2 The effect of CPPs on granule CQAs

6.3.2.2.1 Granule size distribution

The selected contour plots in Fig. 6.6 manifested the interaction between different critical factors and their effects on D10, D50, D90 and span. The enhancement of L/S ratio, throughput or barrel temperature could effectively facilitate granule growth, as aptly illustrated by the increase of D10 from 154.1 to 281.3 μm and D50 from 374.8 to 547.8 μm. The elevation of barrel temperature led to more dramatic increment of D10 when materials feeding rate diminished (Fig. 6.6 (a)) and analogously of D50 with the addition of more granulation liquid (Fig. 6.6 (b)). With respect to D90, it ranged from 738.6 to 1155.9 μm in the response surface design. The influence of barrel temperature on eliminating over-granulated particles was marginal whilst that of throughput was more significantly pronounced at lower L/S ratios compared to the scenarios when liquid content was above 0.5 (Fig. 6.6 (c)). Besides, the size distribution consistently narrowed (smaller span values) along with rising granulation temperature and water addition amount (Fig. 6.6 (d)). As shown in Fig. 6.7, GSD from selected batches were compared using one-factor-at-a-time approach to visualize the effect of L/S ratio and barrel temperature. These two critical parameters were altered individually and successively over their scope in the DoE while all other operational variables were held constant at the

intermediate levels. It was evident that granules produced at higher liquid content tended to display a more monomodal size distribution with median diameter around 500 μm, in contrast to those from 0.35 L/S ratio where broader multimodal distribution with more fines and oversized lumps were generated (Fig. 6.7 (a)). In addition, Fig. 6.7 (b) corroborated the curvature effect concerning barrel temperature observed in Fig. 6d and in the reduced quadratic model of span in Table 6.9. As L/S ratio increased from 0.35 to 0.45, the granulation performance was firstly improved with more desirable particle size and size distribution, yet slightly deteriorated into a condition comparable to Run #5 with further increase of L/S ratio from 0.45 to 0.55.

In the current study, water addition amount was demonstrated to be a very influential factor in the granulation process. It dominated the degree of liquid saturation of granules essential for coalescence relied on mechanical mixing and shear forces during consolidation process. Sub-saturated and deformable particles could be easily combined into larger particles during collision owing to the free liquid in contact zone and reduced induction period (Liu et al., 2000). The newly generated wet surfaces after shear-elongation and breakage of granules also played a pivotal role in picking up the surrounding fines through layering, thereby effectively increasing D10 and narrowing the size distribution. Furthermore, varying degree of barrel filling could ensue from the alternation of throughput that a higher value resulted in more materials hold-up volume accompanied by constricted packing of primary particles. The surface velocity of powder bed as a result decreased to trigger less granule breakage with promoted plug flow behavior, which was eventually reflected by the enlarged size and porosity (Dhenge et al., 2013a). Given the low residence time for TSG, increasing barrel temperature caused

faster solubility rate of ingredients, especially binder PVP, in the granulation liquid, boosting the particle coalescence and steady growth with more effectively functioned binder solution.

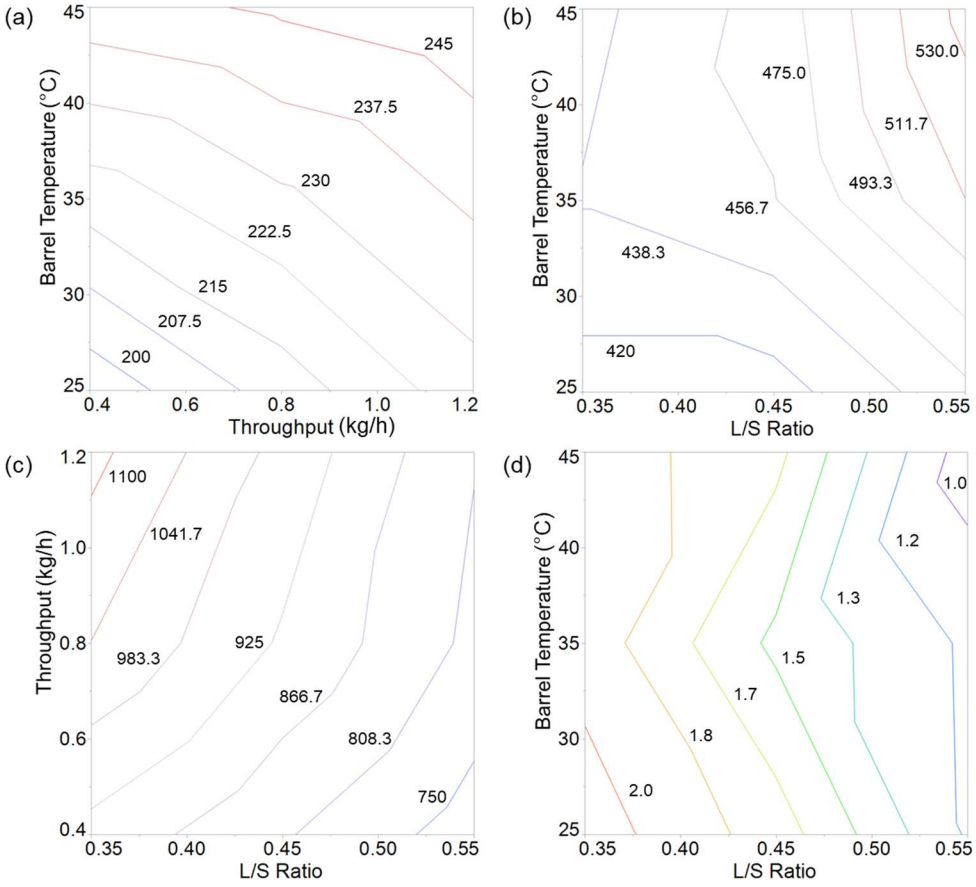

Fig. 6.6. Contour plots of (a) D10, (b) D50, (c) D90 and (d) span. The third variable for each plot was fixed at intermediate level.

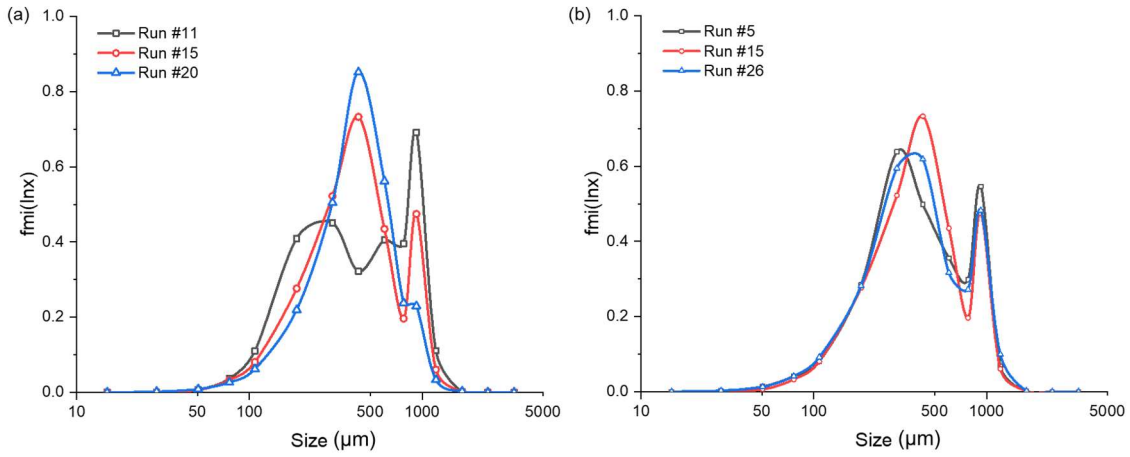

Fig. 6.7. Granule size distribution of selected runs in Table 6.5. (a) Varying L/S ratio with barrel temperature and throughput fixed at intermediate levels (Run #11: 0.35 L/S ratio; Run #15: 0.45 L/S ratio; Run #20: 0.55 L/S ratio). (b) Varying barrel temperature with L/S ratio and throughput fixed at intermediate levels (Run #5: 25 °C; Run #15: 35 °C; Run #26: 45 °C).

6.3.2.2.2 Porosity

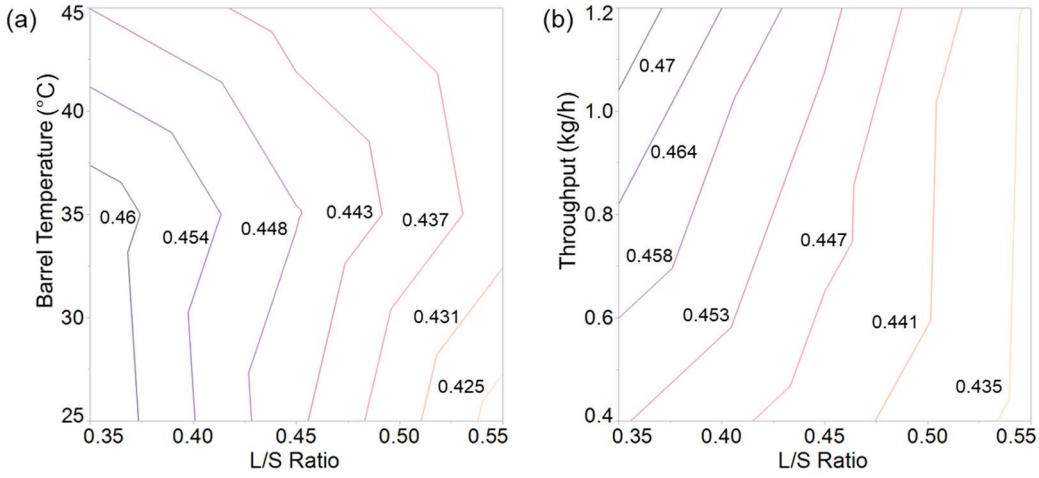

Fig. 6.8. Contour plots of porosity. (a) Barrel temperature versus L/S ratio. (b) Throughput versus L/S ratio. The third variable for each plot was fixed at intermediate level.

With regard to porosity, the *P*-value revealed that barrel temperature was a nonsignificant parameter. However, stepwise regression for porosity suggested the inclusion of all three main effects in the model (refer to Table 6.9), largely due to the quadratic curvature it induced and the interaction effect with L/S ratio. Removing barrel temperature from the model would have resulted in the violation of hierarchical principle, namely that higher order terms in the model, such as barrel temperature*barrel temperature or barrel temperature*L/S ratio, entailed the inclusion of all its lower order terms as well.

The ANOVA results reflected that L/S ratio was of paramount importance as opposed to the other two factors. As depicted in Fig. 6.8, granule porosity was more susceptible to the change of L/S ratio at low levels of barrel temperature and high levels of throughput. In essence the low-viscosity liquid binder (water in this case) could also function as a lubricant during granulation process to mitigate inter-particle frictions and thus bolster the consolidation and concomitant effect on reducing granule voidage. Therefore, it was obvious that more densified granules with smaller porosity was associated with increasing L/S ratio on account of abated dynamic strength and enhanced deformability (Iveson et al., 2001). Moreover, powder feed rate controlled the degree of channel filling that a high fill ratio exerted more throughput force on the powder bed. Fig. 6.8 (b) showed that granules porosity increased up to 0.47 along with the increasing powder feed rate from 0.4 to 1.2 kg/h, especially when water addition was low. The larger porosity could be principally ascribed to the shortened residence time stemmed from high upstream throughput force, which conveyed materials out of granulator faster and subjected particles to less compaction and interaction.

6.3.2.2.3 Granule density and flowability

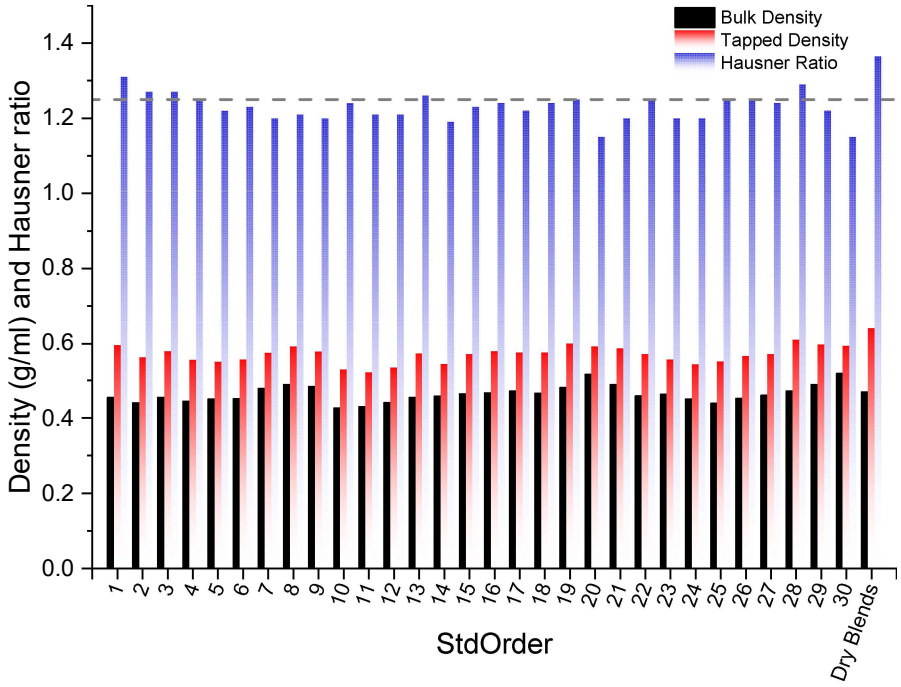

Fig. 6.9. Bar plots of granule bulk density, tapped density and Hausner ratio versus standard run order in the response surface design. Grey dash line represents the fair flow level when Hausner ratio equals to 1.25. Properties of raw materials mixture was listed as a control group.

Fig. 6.9 exhibited the variation of granule bulk density, tapped density and flowability (Hausner ratio) alongside the standard run order in response surface design in Table 6.5. Overall, bulk and tapped densities increased with increasing L/S ratio irrespective of the throughput level, despite that the increase was more prominent from L/S ratio 0.45 to 0.55 (e.g., black bar of StdOrder 4 to 6 versus 7 to 9) while the subtle nuance was more challenging to discern from 0.35 to 0.45 (e.g., black bar of StdOrder 1 to 3 versus 4 to 6). Notice that StdOrder 1 to 9, 10 to 21 and 22 to 30 were operated at the barrel temperature of 25, 35 and 45 °C, respectively. However, little difference could be detected concerning

bulk and tapped densities under different temperatures when other two parameters were held constant, confirming its negligible effect indicated by the reduced quadratic models in Table 6.9. Typically, smaller Hausner ratio signifies superior flowability and efficiency of particle packing. In comparison with raw material blends, granule bulk densities displayed very limited degree of increase partly due to the high particle porosity whereas enhancement of flow properties was in evidence for the majority of runs whose Hausner ratio were beneath the fair flow level of 1.25.

In the present study, particle size and shape interplayed and both contributed to the granular flow behavior. The enlarged size reduced particle contact surface areas in a confined space, which was associated with inter-particle cohesive forces with repercussions on bulk flowability. It also enabled minimal air to be entrapped in the powder bed, rendering the granules less compressible with high stiffness and thus more resistant to normal stress. Particle shape on the other hand may impede the flow in the light of irregular morphology and rough surface formed when agglomerates underwent the shear-elongation functioning mechanism of KEs (Ridgway and Rupp, 1969).

6.3.2.3 The effect of CPPs on processability

It can be seen from Table 6.9 that only three main effects were included in the reduced model of torque, i.e., no interaction effect or quadratic effect was significant. Fig. 6.10 illustrated the extent to which throughput and L/S ratio affected materials processability. Torque values consistently descended as more granulation liquid was injected into the system while a converse trend was discovered when the degree of channel filling escalated. Increasing the throughput brought about heavier conveying loads of materials on the screws, which enforced more mechanical energy on rotation at predefined speed

and subjected powder mass to more intensive compaction force (Koster and Thommes, 2010). The decreasing trend of torque could be mainly ascribed to the water lubrication effect at higher L/S ratios, alleviating the resistance to screw compression as well as materials friction against barrel wall and screw elements. Moreover, the ANOVA results revealed that processability was inevitably compromised when barrel temperature declined from 45 to 25 °C (not shown). This could be explained by the fact that more thermal energy accelerated the dissolution of PVP in the granulation liquid and facilitated the rotation with lower binder viscosity, hence compensating for the amount of mechanical energy consumed towards conveying and shearing of materials.

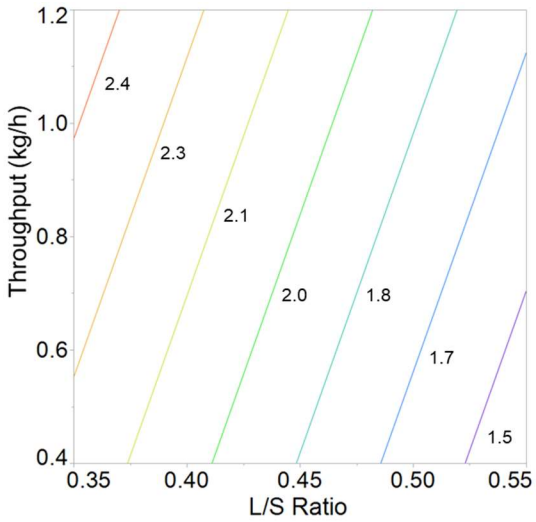

Fig. 6.10. Contour plot of torque with respect to throughput versus L/S ratio. The third variable was fixed at intermediate level.

6.3.2.4 The effect of CPPs on tablet CQAs

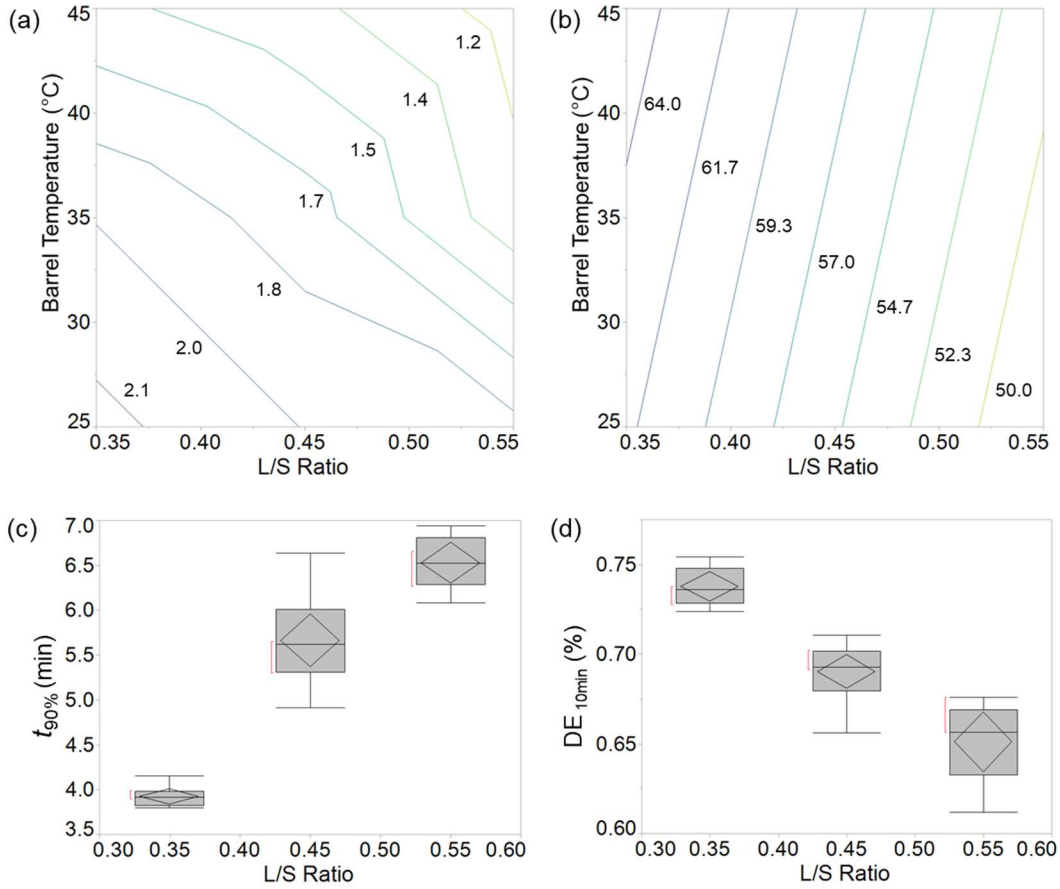

Fig. 6.11. Contour plot of (a) tensile strength (MPa) and (b) $t_{3\,\mathrm{min}}$ (%) with respect to barrel temperature versus L/S ratio. The third variable was fixed at intermediate level. Outlier box plot of (c) $t_{90\%}$ (min) and (d) DE_{10min} (%) versus L/S ratio. The confidence diamond indicates the mean and the upper and lower 95% of the mean. Red bracket outside the box identifies the densest 50% of the observations.

The ANOVA results identified L/S ratio as the most predominant parameter over the other two factors regarding tablet CQAs. It can be seen in Table 6.9 that stepwise regression included L/S ratio for all the five reduced models of tablet attributes. As illustrated in Fig. 6.11 (a), more fragile tablets with lower tensile strength were produced with increasing L/S ratio and barrel temperature. In terms of dissolution performance,

Fig. 6.11 (b) revealed that drug release rate was slightly accelerated with raised barrel temperature but evidently slackened by utilizing high L/S ratio granules for tablet compaction. It was observed that up to approximately 64% of caffeine could be dissolved within the first three minutes at 0.35 L/S ratio whereas this value declined to 50% if 0.55 L/S ratio was adopted. The results from Fig. 6.11 (c) and (d) further substantiated such a conclusion elicited from Fig. 6.11 (b), viz. the positive correlation between drug dissolution rate and L/S ratio during granulation process. It took less than four minutes to dissolve 90% of caffeine associated with the highest dissolution efficiency of 75%. In contrast, the aforementioned time was prolonged by almost three minutes and the DE_{10min} diminished by roughly 10% once L/S ratio increased to 0.55. Overall, the dissolution profiles are indicative of immediate release characteristic for all tablets from different granulation processing conditions in the 30-run response surface design.

In general, both the tableting process such as compression force or die geometry and the attributes of intermediates granules controlled the properties of final drug product. It was found that the tablet porosity was marginally predicated on the original intragranular porosity and the granule shape yet decreased considerably as the applied pressure increased during tableting (Johansson and Alderborn, 2001). Therefore, it is not surprising that the regression statistics of tablet porosity in Table 6.9 was less desirable. In addition, similar trend can be disclosed in terms of the effect of L/S ratio on tablet tensile strength and granule voidage. The extent of granule deformation during tableting regulated the evolution of tablet microstructure with respect to intergranular pore size and contact areas. Particles experiencing higher degree of densification during granulation (less porous) could undermine the establishment of intergranular bonding and

compactability eventually resulting in smaller tablet strength. Moreover, lower tablet tensile strength was typically accompanied by faster disintegration during dissolution, which may in turn accelerate the drug release rate. However, in the present study, it seemed that granule porosity predominated the dissolution over tablet tensile strength and disintegration time, namely that tablets compacted from more consolidated granules with increasing L/S ratio displayed slower release of active ingredient notwithstanding the weakened mechanical properties. It was thus postulated that the dissolution mechanism in this scenario was drug diffusion through intragranular structure (diffusion-controlled) rather than tablet disintegration (erosion-controlled). Denser granules were featured with more closed pores and slower water ingress speed and hence delayed the drug diffusion and dissolution rate.

6.4 Conclusions

This study demonstrated the implementation of sequential experimental strategy towards better design and understanding of twin-screw wet granulation process. In the screening stage, D-optimal design was leveraged to examine a broad spectrum of process and screw configuration variables. Based on the stepwise regression, reduced second-order interaction model developed for each screening response was used for exploring the design space. In light of the predefined quality target values, screw speed (700 rpm), KE staggering angle (60°), KE number (5) and DFS (w/) were held constant at optimum levels that maximize the design space while barrel temperature, throughput and L/S ratio were selected for further investigation in the following stage.

In the response surface design, comprehensive characterization studies were carried out to delve into the correlation between CPPs and CQAs of granule and tablet. Second-

order quadratic models were developed with satisfactory model adequacy and regression statistics (adjusted and prediction R^2). L/S ratio was identified as the most predominating factor followed by throughput and barrel temperature. Less water addition brought about granules with broader size distribution, porous internal structure and deteriorated flowability and tablets with stronger tensile strength but accelerated drug release. Throughput and barrel temperature mainly impacted on the CQAs through alternation of materials barrel filling degree and ingredient solubility and interaction with distinct thermal energy input, respectively. As a continuation of the present work, Part II will focus on the implementation of complementary process analytical technologies enabling real-time release testing of granule and tablet CQAs during continuous pharmaceutical manufacturing process.

Chapter 7

Towards better design and understanding of continuous wet granulation process. Part II: implementing complementary in-line process analytical techniques in twin-screw granulation

7.1 Objectives

It is notable that different PATs owing to radically distinct functioning mechanisms may inevitably exhibit strengths and weaknesses towards monitoring different properties. Despite the aforementioned PAT studies on TSG introduced in Chapter 1, very little research has been initiated to extract comprehensive information with regard to critical quality attributes of granules. The present study aims for a better design and understanding of TSG process by effectively leveraging several complementary in-line analytical tools: (1) Eyecon^{TM} 3D imaging for real-time monitoring granule size and shape, (2) NIR spectroscopy for quantitively predicting granule physical attributes (size, porosity, bulk/tapped densities and flowability), and (3) Raman spectroscopy for evaluating granule drug content uniformity.

7.2 Materials and methods

7.2.1 Materials

As listed in Table 7.1, the formulation used in this study contained low-dose caffeine anhydrous (CSPC Innovation Pharmaceutical Co., Ltd., Hebei, China) as a model drug and equal weight percentage of α-lactose monohydrate (310 NF, Foremost Farms USA, Baraboo, WI) and microcrystalline cellulose (MCC, Avicel® PH101, FMC Biopolymer, Philadelphia, PA) as the excipients. Besides, dry binder addition method was adopted by premixing polyvinylpyrrolidone (PVP K30, Fisher Scientific, Pittsburgh, PA) with all

other ingredients. Distilled water was used as the binding liquid and dripped into the granulator through a peristaltic pump. Several key specifications regarding raw materials and premix were shown in Table 7.1.

Table 7.1 Formulation specifications and key material physical properties

Component	Percentage (% w/w)	D10 (μm)	D50 (μm)	D90 (μm)	Bulk density (g/ml)	Tapped density (g/ml)	Hausner Ratio
Caffeine	8	8.77	32.58	81.69	-	-	-
MCC	44	25.88	67.26	117.27	-	-	-
Lactose	44	13.32	76.85	158.14	-	-	-
PVP	4	-	-	-	-	-	-
Premix	-	16.32	61.89	108.48	0.462	0.637	1.379

7.2.2 Preparation of premix

To enable better blends homogeneity, a No. 35 mesh sieve (500 μm) was used to remove oversized agglomerates in each ingredient prior to the mixing in a ResonantAcoustic® Mixer (LabRAM™, Resodyn Acoustic Mixer, Butte, MT) set for 3 minutes and intensity (acceleration value) of 45 g's. The premix was then fed into the granulation system by a twin-screw loss-in-weight microfeeder (MT12, Coperion K-Tron, Sewell, NJ) configured with coarse concave screws. The feeding capacity (feed factor) was calibrated to be 1.37 kg/h at 100% motor speed.

7.2.3 Experimental set-up

Fig. 7.1 (a) showed the Thermo Scientific™ Pharma 11 co-rotating parallel twin-screw granulator (Thermo Fisher Scientific, Karlsruhe, Germany) used for manufacturing granules. Several signature characteristics include screw diameter 11mm, highest barrel temperature 280 °C, processing length to diameter (L/D) ratio 40:1, maximum screw speed 1000rpm, and throughput from 20 g/h to 2.5 kg/h. Screw configuration as depicted in Fig. 7.1 (b) was optimized in the previous study and held constant for all the current

experiments. It comprised eleven standard conveying elements (CE) with helix pitch of 1 L/D, one 1 L/D distributive feed screw (DFS), nineteen 1 L/D CEs, five 0.25 L/D kneading elements (KE) arranged in 60° staggering angle, four 1 L/D CEs, two long pitch 2 L/D CEs (*l*CE) and one short pitch 0.5 L/D CE (*s*CE). In particular, different types of screws were designed for distinct functionalities during the granulation process. CE primarily conveyed the materials forward, albeit the associated low mechanical shear input. KE had very limited transport capacity across different zones yet enforced intimate mixing of liquid and powder mixture via vigorous shear-elongation and breakage. DFS effectively promoted the liquid redistribution and layering by creating more intense distributive flows. A more detailed schematic description of granulator functioning principles can be found in earlier work.

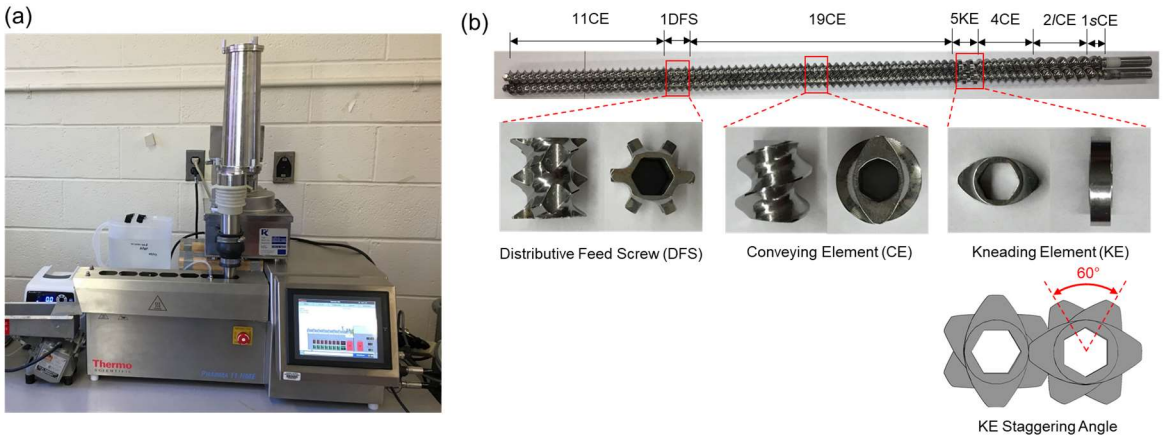

Fig. 7.1. (a) Thermo Scientific™ Pharma 11 twin-screw granulator and (b) screw configuration with enlarged DFS, CE and KE. The offset angle between two contiguous KEs was 60°.

Fig. 7.2 illustrated the experimental set-up for integrating PATs in the TSG process. It can be seen that premixed materials were delivered into the granulator barrel through the 1st zone immediately followed by the addition of binding liquid at the 2nd zone. Besides,

kneading blocks were located in the 3rd zone next to the nozzle position while DFS was in the downstream 7th zone. During each experiment, the produced granules were continuously funneled onto a conveyor platform and carried forward through the sampling interface of in-line analytical tools (Eyecon™, NIR and Raman) mounted over the belt, thus avoiding any potential fouling of measurement window or probe. When Eyecon™ was implemented, the speed of conveyor belt was optimized at 10 fpm to ensure a well-spread monolayer of granules. For the other two spectroscopic techniques, by contrast, a lower speed of 2 fpm was utilized to generate a granule stacking thickness of approximately 1 cm, thereby preventing the potential interference of transmission onto the belt made from polyvinyl chloride.

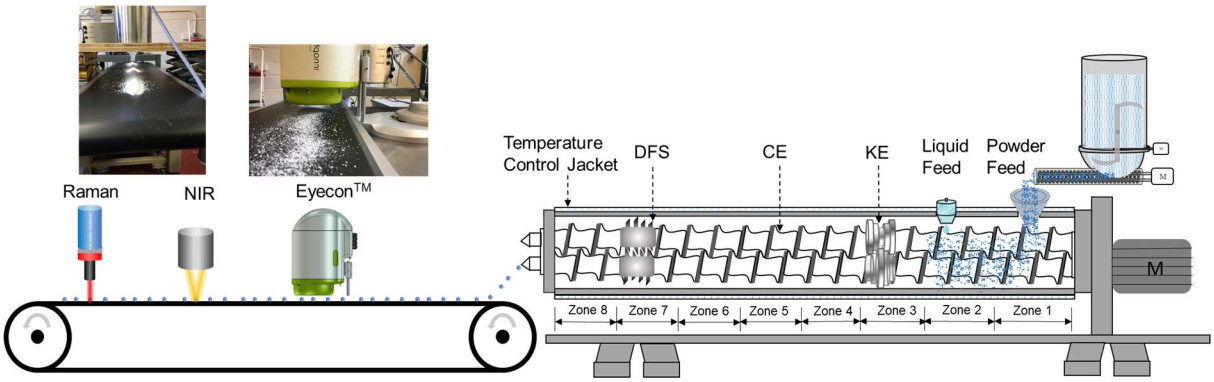

Fig. 7.2. Schematic of experimental set-up for implementation of in-line PATs in TSG.

7.2.4 Design of experiments

The response surface design previously employed in Chapter 6 was further adopted in the present study, namely that each critical process parameter (barrel temperature, liquid to solid ratio and throughput) was investigated at three different levels (see Table 7.2). Also, comprehensive characterizations were conducted to obtain the critical quality attributes of granules (size distribution, porosity, bulk density, tapped density and flowability) at different operation conditions. As displayed in Table 7.3, the JMP®

statistical software (SAS Institute, Cary, NC) generated a 30-run 3^3 factorial design augmented with 3 center points that was performed for each integrated analytical technique. Moreover, RunOrder in Table 7.3 is the randomized run order for carrying out the actual experiments while StdOrder is the standard order sorted according to barrel temperature and L/S ratio for more convenient results comparison and graph plotting. Note that all experimental run numbers mentioned in the following sections refer to the StdOrder.

Table 7.2 CPPs and granule CQAs investigated in the response surface design

CPP	Level			Granule CQAs
	Low	Intermediate	High	
Barrel temperature (°C)	25	35	45	Granules size distribution (D10, D50, D90, Span); Porosity; Bulk density; Tapped density; Flowability (Hausner ratio)
L/S ratio	0.35	0.45	0.55	
Throughput (kg/h)	0.4	0.8	1.2	

Table 7.3 The 30-run response surface design for three 3-level CPPs

StdOrder	RunOrder	Barrel temperature	L/S ratio	Throughput
1	13	25	0.35	0.4
2	15	25	0.35	0.8
3	9	25	0.35	1.2
4	8	25	0.45	0.4
5	2	25	0.45	0.8
6	26	25	0.45	1.2
7	28	25	0.55	0.4
8	6	25	0.55	0.8
9	18	25	0.55	1.2
10	10	35	0.35	0.4
11	14	35	0.35	0.8
12	21	35	0.35	1.2
13	12	35	0.45	0.4
14	17	35	0.45	0.8
15	29	35	0.45	0.8
16	4	35	0.45	0.8
17	25	35	0.45	0.8
18	30	35	0.45	1.2
19	27	35	0.55	0.4
20	19	35	0.55	0.8
21	16	35	0.55	1.2
22	23	45	0.35	0.4
23	24	45	0.35	0.8
24	20	45	0.35	1.2
25	11	45	0.45	0.4
26	3	45	0.45	0.8
27	1	45	0.45	1.2
28	5	45	0.55	0.4
29	7	45	0.55	0.8
30	22	45	0.55	1.2

7.2.5 Granule characterization

Granules from each experiment were air-dried at ambient conditions until the loss-on-drying moisture content was less than 3%. The dried granules were then subsampled by spinning riffler (Gilson Company Inc., Lewis Center, OH) to ensure unbiased sampling for different characterizations.

7.2.5.1 Particle size distribution

The particle size of raw materials and premix listed in Table 7.1 were determined by laser diffraction analyzer (Beckman-Coulter Inc., Pasadena, CA). Granule size distribution (GSD) was measured by sieve analysis utilizing a $\sqrt{2}$ series of sieves with screen scale ranging from 38 μm to 4 mm. GSD was plotted as the normalized mass frequency (f_{mi}) shown in Eq. 7.1 versus the midpoint of each size interval on logarithmic scale (Allen and Elsevier, 2003).

$$f_{mi}(\ln x) = \frac{m_i}{\ln(\overline{n_i} / \overline{n_{i-1}})} \tag{7.1}$$

where m_i and $\overline{n_i}$ are the mass fraction and midpoint of size interval i , respectively.

7.2.5.2 Granule porosity

The true density of granules (ρ_t) was measured by a helium pycnometer (AccuPyc II 1340, Micromeritics, Norcross, GA) while the envelope density (ρ_e) was tested by Geopyc 1360 (Micromeritics, Norcross, GA). Granules with a size fraction of 1.0-1.4 mm were placed in a desiccator overnight prior to any densities measurements. The granule porosity (ε_g) was calculated by Eq. 7.2.

$$\varepsilon_g = 1 - \frac{\rho_e}{\rho_t} \tag{7.2}$$

7.2.5.3 Bulk and tapped densities

The bulk densities of granules (ρ_B) and raw materials premix were measured by FT4 powder rheometer (Freeman Technology, Wayne, PA). Tapped density (ρ_T) was measured via an automated tapped density analyzer (Quantachrome Instruments, Boynton

Beach, FL) associated with a 250 ml graduated cylinder. Hausner ratio (HR) defined by Eq. 7.3 was used to describe the flowability of granules.

$$\mathrm{HR} = \frac{\rho_T}{\rho_B} \tag{7.3}$$

7.2.6 Implementation of PATs in TSG

7.2.6.1 Eyecon™ 3D imaging system

Eyecon™ (Innopharma Laboratories, Dublin, Ireland) is a 3D particle characterizer providing size, shape and surface morphology information in-line and in real-time. It is equipped with a charge-coupled device camera encircled by red, green and blue LEDs that pulses flash light every microsecond to capture the image of passing granules in a fixed viewpoint. In order to derive the particle three-dimensional (3D) features, illumination direction from different sources is arranged according to the principle of photometric stereo. After transforming the image intensities contingent on different light-emitting diode (LED) illuminants and particle surface orientation, the light reflection models were developed to recover a representation of Monge patch or surface height map at points corresponding to each pixel, followed by acquisition of a detailed topological description of particles. Once the particle edges are fully detected, its size is estimated from a 3D-projected two-dimensional (2D) image where an iterative optimization takes place to find the equivalent diameter of the best fitting ellipse.

For materials with moving speed less than 10 m/s, Eyecon™ is capable of detecting the particle size variation of ±1 μm within the range of 50 to 3000 μm and recording images every 2 seconds. Moreover, this direct measurement system does not entail any material-based calibration prior to granulation experiments. As shown in Eq. 7.4, the average particle size (D) was calculated by maximum and minimum Martin's diameters

(D_{max} and D_{min}) of the ellipse. Eccentricity as defined in Eq. 7.5 and its relative standard deviation (RSD) was to characterize the particle shape. The larger value (closer to 1) of eccentricity is indicative of more spherical ellipse or particle. In terms of size distribution, the theoretical particle mass (M) was used and equated to the product of particle volume and density (ρ). Since density was assumed to be identical for all particles, Eq. 7.6 showed that M was directly proportional to D^3.

Key configuration settings of the analysis software Eyepass^{TM} were kept constant in this study and included integration time (60 s), maximum detection diameter (3000 μm), false agglomeration filter (0.02), edge contrast threshold (25) and analysis block size (501 pixels).

$$D = \frac{D_{max} + D_{min}}{2} \tag{7.4}$$

$$\text{Eccentricity} = \sqrt{1 - (\frac{D_{min}}{D_{max}})^2} \tag{7.5}$$

$$M = \frac{\pi \cdot D^3 \cdot \rho}{6} \tag{7.6}$$

7.2.6.2 NIR spectroscopy

In the current study, as granules moved through the sampling area, NIR spectra were consecutively collected in diffuse reflectance mode using MATRIX-F FT-NIR spectrometer collected by OPUS 7.2 software (Bruker Optics, Billerica, MA). The NIR probe (emission head) contains two light sources illuminating the sampling spot of 10 mm in diameter. Irradiated granules are thick enough (on the scale of centimeter) to effectively hinder the transmission of NIR beam. A total of 60 spectra were obtained for each DoE run. Each spectrum was the average of 32 scans and resolution of 8 cm^{-1}. The

total acquisition time was approximately 7 seconds for each spectrum. Posteriorly, in conjunction with the granule physical properties acquired in section 2.5 (Y variables), 20 spectra (X variables) were selected for construction of calibration models while another 10 spectra (X variables) served as test set for model validation. The SIMCA 14.1 software (Umetrics AB, Umeå, Sweden) was deployed for partial least squares (PLS) regression. Previous report indicated that physical properties such as bulk density was associated with the baseline offset variations of NIR spectra. Data pretreatment of 1st derivative was applied in selected NIR spectral range (wavenumber 4500 to 9000 cm^{-1}) prior to PLS fitting with mean centering as scaling. The derivative was calculated by Savitzky-Golay algorithm with a 25-point segment size and a second-order polynomial.

The calibration models were assessed based on the prediction of independently collected data (test set). The main figure of merit in test set validation is the root mean square error of prediction (RMSEP) as defined in Eq. 7.7. In addition, due to the varying order of magnitude and units regrading different granule properties such as D90 and bulk density, it was more convenient to adopt relative standard error of prediction (RSEP%) (Eq. 7.8) to normalize the square of residuals by the square of reference values, rendering the predictive abilities of different calibration models more comparable. Also, standard deviation (SD) and relative standard deviation (RSD) were utilized to evaluate the model precision with respect to the 10 repeated test set samples (Román-Ospino et al., 2016).

$$\text{RMSEP} = \sqrt{\sum_{i=1}^{n} \frac{(\hat{y}_{i,pred} - y_{i,ref})^2}{n}} \tag{7.7}$$

$$\text{RSEP}(\%) = \sqrt{\frac{\sum_{i=1}^{n} (\hat{y}_{i,pred} - y_{i,ref})^2}{\sum_{i=1}^{n} (y_{i,ref})^2}} \times 100 \tag{7.8}$$

7.2.6.3 Raman spectroscopy

During granulation process, the Kaiser PhAT System^{TM} analyzer (Kaiser Optical Systems, Ann Arbor, MI) was used to acquire the spectra of continuously produced granules. Samples were illuminated by a 400 mW Invictus NIR diode laser at the wavelength of 785 nm. The instrument was operated in reflectance mode where the PhAT probe was mounted 120 mm above the conveyor belt for collecting Raman photons. The nominal beam diameter at focal position was 6 mm and laser exposure time was 2.5 seconds. An acquisition time of 6 seconds provided sufficient Raman intensity and signal-to-noise ratio. For each DoE run, a total of 120 consecutive spectra in the range of 150 to 1900 cm^{-1} were obtained with the resolution of 1 cm^{-1}. Also, a dark spectrum was collected prior to each experiment and was automatically subtracted from the raw spectra.

In order to quantitatively predict the granule drug content, a calibration model was developed based on the premix of raw materials with seven known concentrations of anhydrous caffeine (4.4, 5.6, 6.8, 8, 9.2, 10.4, 11.6 %w/w). The identical experimental set-up and Raman system settings were utilized for acquiring the total 120 spectra of dry blends. In particular, 50 spectra were selected for construction of calibration models whilst another 25 spectra served as test set for model validation. Standard normal variate (SNV) as pretreatment method was applied on the spectral data to correct for multiplicative variations followed by 2nd derivative to correct the baseline offset and slopes difference as well as improve the resolution of overlapped spectral features. The figures of merit RMSEP and RSEP were used to examine the model validity based on the selected spectral range of 440-460, 545-565, 615-635, 735-755, 1590-1610 and 1690-

1710 cm^{-1}. PLS regression method was then applied on the pretreated spectra for determination of caffeine amount in granules.

Aa a reference method, UV-Vis spectroscopy was employed to validate the predicted caffeine concentration in the granules. Samples collected from each DoE condition during the steady state were air-dried at ambient conditions until the loss-on-drying moisture content was less than 3%. A quantity of 1 g dried granules was dissolved in 10 mL distilled water for 12 h followed by a dilution of 40 times and measurement of caffeine absorbance at the wavelength of 273 nm. Drug concentration was then derived from a standard UV-Vis calibration curve with the linear correlation (R^2 = 0.9998) from 0.01 to 0.32 g/L.

7.3 Results and discussion

7.3.1 Eyecon™ 3D imaging system

7.3.1.1 Influence of L/S ratio on granule size and shape

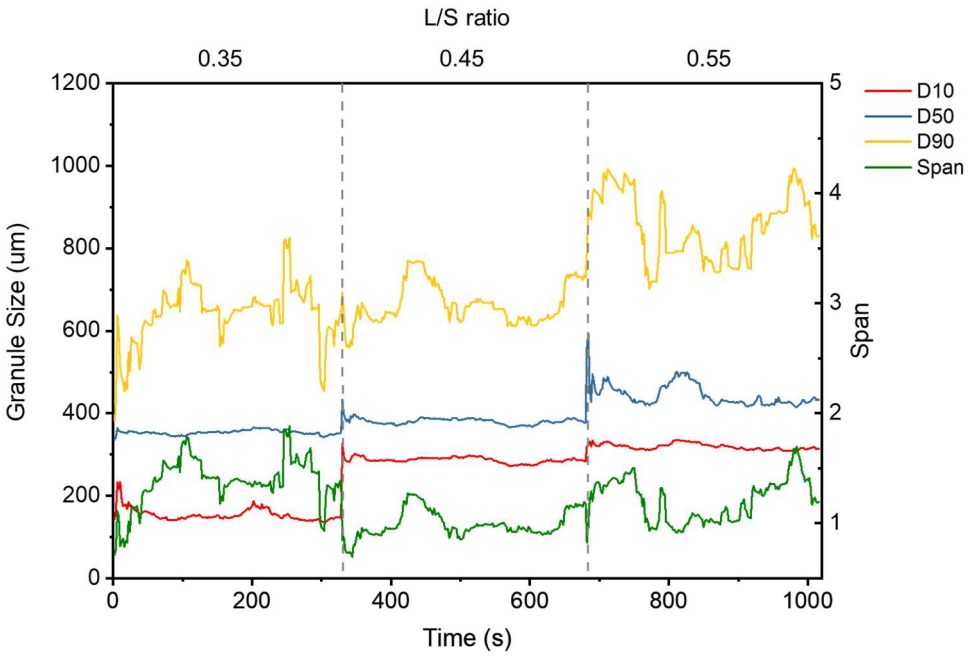

Fig. 7.3. Variation of GSD metrics (D10, D50, D90 and Span) versus time at different L/S ratios. The top *x*-axis indicated L/S ratio of 0.35, 0.45 and 0.55 separated by two grey dash lines, corresponding to the DoE StdOrder 10, 13 and 19, respectively. Throughput and barrel temperature were held constant at 0.4 kg/h and 35 °C, respectively.

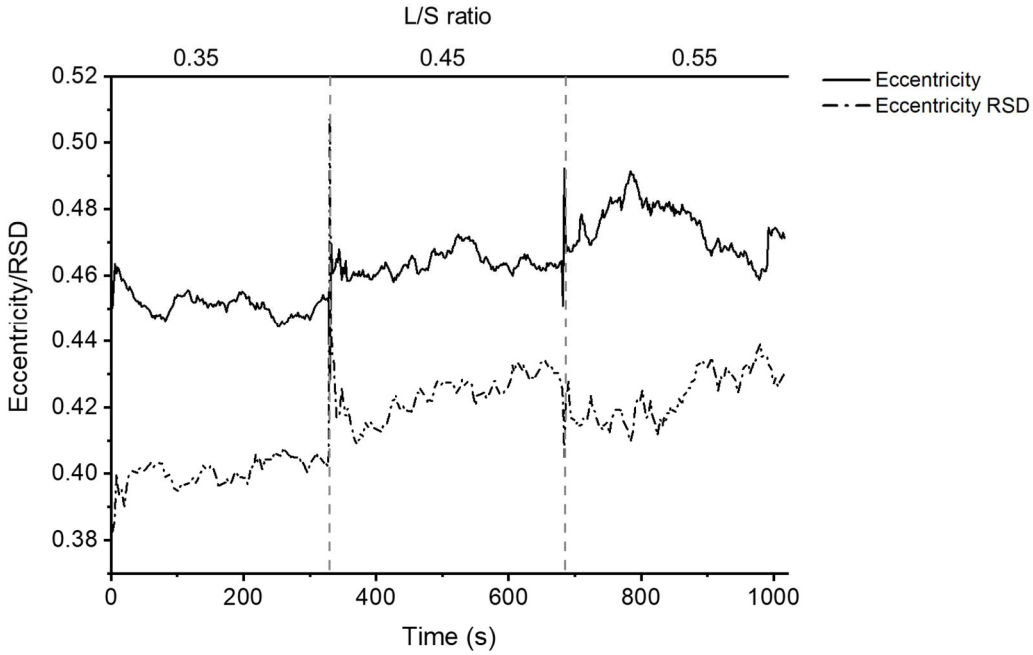

Fig. 7.4. Variation of particle shape metrics (eccentricity and its RSD) versus time at different L/S ratios. The top *x*-axis indicated L/S ratio of 0.35, 0.45 and 0.55 separated by two grey dash lines, corresponding to the DoE StdOrder 10, 13 and 19, respectively. Throughput and barrel temperature were held constant at 0.4 kg/h and 35 °C, respectively.

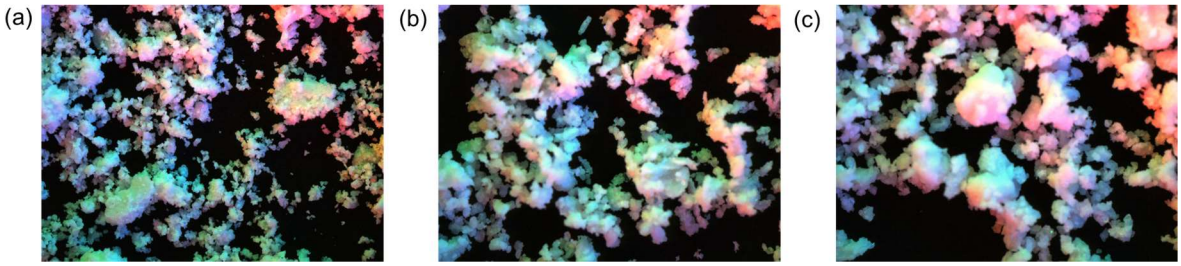

Fig. 7.5. Representative Eyecon^{TM} images captured at L/S ratios of (a) 0.35, (b) 0.45 and (c) 0.55 corresponding to the DoE StdOrder 10, 13 and 19, respectively.

Fig. 7.3 shows the GSD metrics (D10, D50, D90 and span) as a function of time that were estimated from the captured images. StdOrder 10, 13 and 19 were selected as representative batches to illustrate the influence of L/S ratio with the other two variables of throughput and barrel temperature held constant. Overall, it can be observed that granule size consistently increased and span slightly decreased as more binding liquid was added in the system. This trend was in accordance with the conclusions elicited from previous studies that higher degree of liquid saturation can effectively promote the particle consolidation and coalescence and prolong the steady growth of granules. Fine particles were combined onto larger aggregates with wet surfaces through layering, thus narrowing the size distribution. In particular, D10 and D50 demonstrated distinct step change in conjunction with the variation of L/S ratio whereas D90 and span embodied more dramatic fluctuation. Since D90 was in the numerator in calculating span, it was not surprising to observe that span followed analogous trend as opposed to D90.

Similarly, Fig. 7.4 illustrated the variation of particle shape parameter, eccentricity, as granulation process evolved to higher L/S ratios. It can be discerned that average eccentricity increased with increasing L/S ratio. According to the definition of eccentricity in Eq. 7.5, larger values were synonymous with less irregularly shaped particles on account of the closer values between D_{min} and D_{max}. Particles with the presence of more granulation liquid were inclined to undergo more significant deformation, resulting in less protuberated angularities on the surface, i.e. more spherical granules. In addition, this particle shape metric fluctuated more severely as indicated by

the increasing RSD values from L/S ratio 0.35 to 0.55, partly due to the declining particle count associated with the formation of more liquid bridges among particles. The representative images in Fig. 7.5 displayed distinct increment of particle size and decrease of particle number along with increasing water content in the granulator.

By converting the number distribution into volume or mass distribution, the image analysis algorithm of the device imparted heavier leverage to larger particles as the percentile value increased from D10 to D90 showing greater variability. In this study, the overall diminished number of larger particles made a difference during the transformation of size calculation. Also, larger agglomerates were believed to be underrepresented in Eyecon^{TM} in comparison to finer particles primarily owing to the higher likelihood of particle overlapping or being partially identified in the field of view. Consequently, larger particles were prone to demonstrate substantial influence associated with higher measurement variability during size determination. By virtue of its stability and sensitivity, D10, an indicator of level of fines, was hence deemed to be a more suitable parameter compared to D90 that should be employed in monitoring and control of size enlargement process.

7.3.1.2 Sensitivity of Eyecon™ to process perturbation

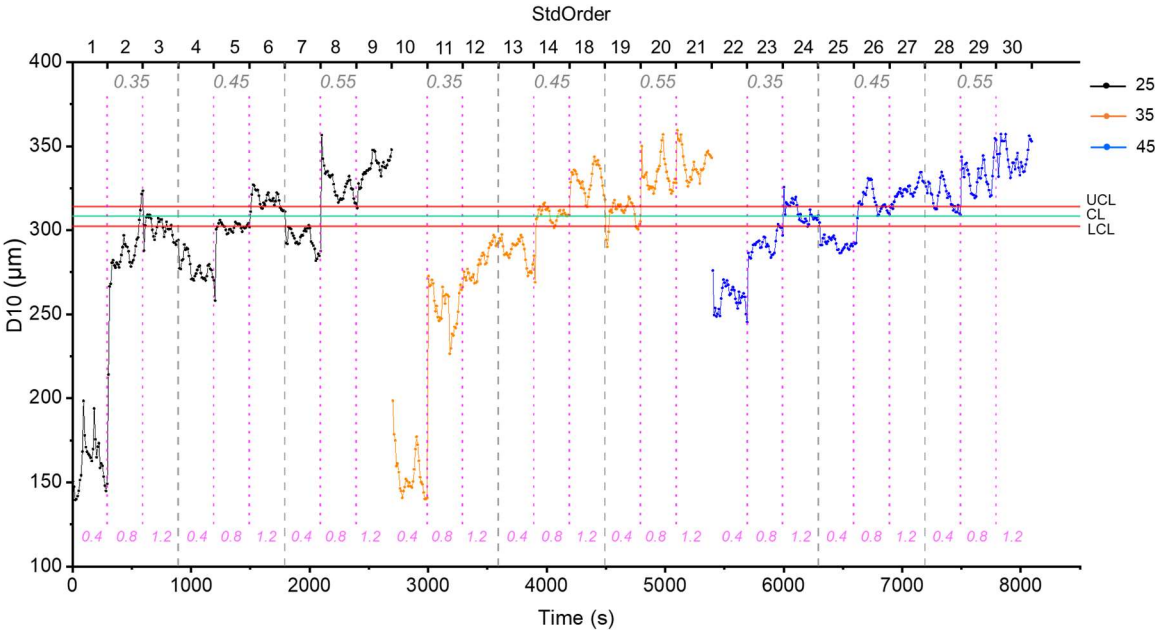

Fig. 7.6. $\bar{X}$ control chart for D10 versus StdOrder (top *x*-axis) and time (bottom *x*-axis) in the entire 30-run DoE. Upper and lower red solid lines represented the UCL and LCL of StdOrder 14, respectively. Green solid line represented the CL of StdOrder 14. Consecutive D10 values at different barrel temperatures was connected with a straight line (black: 25 °C, orange: 35 °C and blue: 45 °C). Connected D10 values at different L/S ratios (0.35, 0.45 and 0.55) in each barrel temperature zone were separated by grey dash lines. Connected D10 values at different throughput (0.4, 0.8 and 1.2 kg/h) in each L/S ratio zone were separated by pink dot lines.

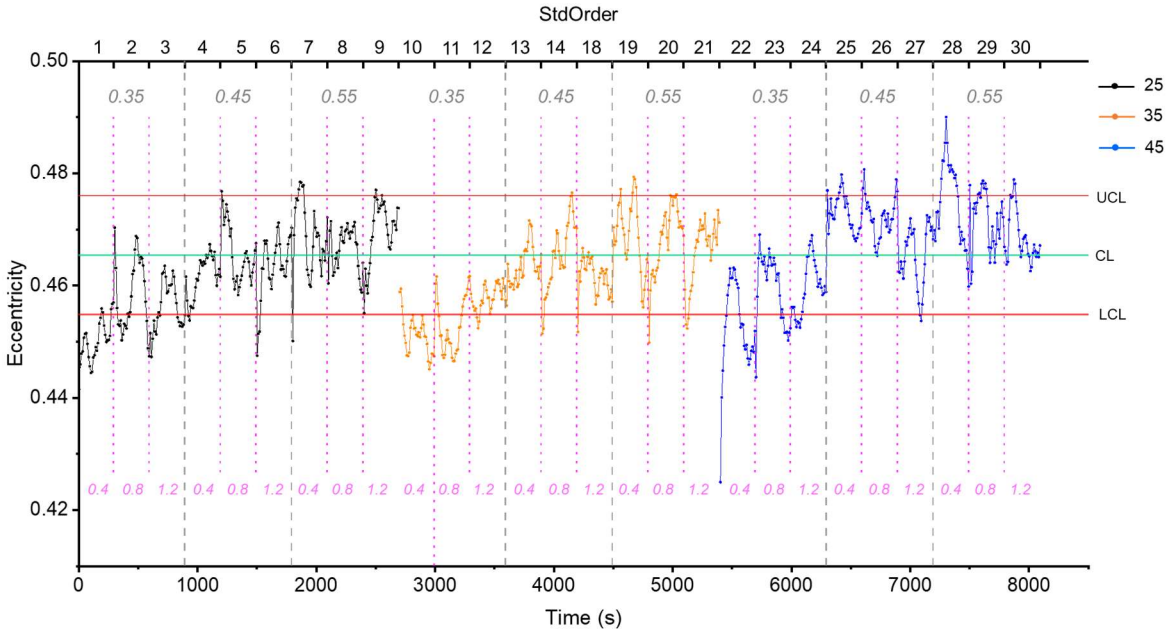

Fig. 7.7. $\bar{X}$ control chart for eccentricity versus StdOrder (top *x*-axis) and time (bottom *x*-axis) in the entire 30-run DoE. Upper and lower red solid lines represented the UCL and LCL of StdOrder 14, respectively. Green solid line represented the CL of StdOrder 14. Consecutive eccentricity values at different barrel temperatures was connected with a straight line (black: 25 °C, orange: 35 °C and blue: 45 °C). Connected eccentricity values at different L/S ratios (0.35, 0.45 and 0.55) in each barrel temperature zone were separated by grey dash lines. Connected eccentricity values at different throughput (0.4, 0.8 and 1.2 kg/h) in each L/S ratio zone were separated by pink dot lines.

Control chart is a valuable tool to not only identify the presence of special-cause variation and monitor process robustness but bring the quality attribute back within the control limits. When a process is stable, consistent and in statistical control over time, it exhibits common cause variation intrinsic to the process, otherwise some undesirable states such as threshold state, state of chaos or brink of chaos may occur. As illustrated in Fig. 7.6, process profile captured by Eyecon^{TM} camera was established by plotting the

D10 values of 27 DoE runs in a time series. The top *x*-axis showed that only one of the four replicated center points, StdOrder 14, was included whereas the remaining three runs, StdOrder 15, 16 and 17 were excluded from the graph. The vertical pink dot lines or grey dash lines depicted the onset of step change in either throughput or L/S ratio. Furthermore, sensitivity of the imaging system towards unexcepted perturbations or set point changes during manufacturing process was evaluated according to the D10 signature changes throughout the DoE. The ultimate target is to explore the potential of deploying this sensor for prospective process control.

As a result, quantitative assessment of the process state was enabled by constructing the mean chart ($\overline{X}$) of D10 in the DoE center point operation condition (StdOrder 14), which provided a more practical avenue for controlling the process. Three essential elements of the control chart, upper control limit (UCL), centerline (CL) and lower control limit (LCL), for D10 of StdOrder 14 were determined by Eq. 7.9, 7.10 and 7.11 respectively and exhibited in Fig. 7.6. The limits were obtained according to the overall mean and standard deviation of extracted D10 values. The subgroup size in UCL and LCL equations was set to 5. It can be interpreted that the data output from most other processing conditions were significantly different from that of the StdOrder 14 since those values were beyond the tight control limits. These scenarios would be considered as out of control state, provided that center point was the predefined target operation condition. Furthermore, control chart for eccentricity was developed in Fig. 7.7 as a contrast to D10. Apparently, the larger magnitude of fluctuation embedded in the eccentricity output data impeded its implementation as quality attribute for process monitoring and control. The majority of eccentricity values fall within the control limits

set for StdOrder 14, albeit the different operation conditions for other runs. Therefore, it was inevitably confronted with high risks of utilizing eccentricity for process monitoring where the process may considerably deviate from the set point due to the disruption or interference from unknown factors without being detected.

$$\text{UCL} = \hat{\mu}_{\text{Y}} + 3\frac{\hat{\sigma}_{\text{Y}}}{\sqrt{n}} \tag{7.9}$$

$$\text{CL} = \hat{\mu}_{\text{Y}} \tag{7.10}$$

$$\text{UCL} = \hat{\mu}_{\text{Y}} - 3\frac{\hat{\sigma}_{\text{Y}}}{\sqrt{n}} \tag{7.11}$$

7.3.2 NIR spectroscopy

The most prominent absorption bands in the NIR region (780-2500 nm) is dominated by overlapping overtones and combinations of fundamental vibrations of functional groups involving hydrogen atom, e.g. C-H, N-H, and O-H. In comparison with the complete absorption or specular reflection occurred in mid-IR, the low absorptivity of NIR permits deeper sample penetration depth and direct analysis in either transmittance or reflectance mode. It has long been recognized that NIR reflectance exhibits cross-sensitivity. An NIR beam incident on the granules propagates diffusively along with absorption in the layer until the remaining attenuated light is backscattered towards the entry surface. The diffuse reflectance provides a representative spectrum that contains both chemical and physical material information stemming from the concurrent absorption and scattering effects. Hence it is sensitive to the particulate nature (particle size, shape, packing density, surface morphology and texture) that can affect the path length light travels and penetration of radiation into the sample (Rosas et al., 2012).

7.3.2.1 Evaluation of calibration set based on cross-validation

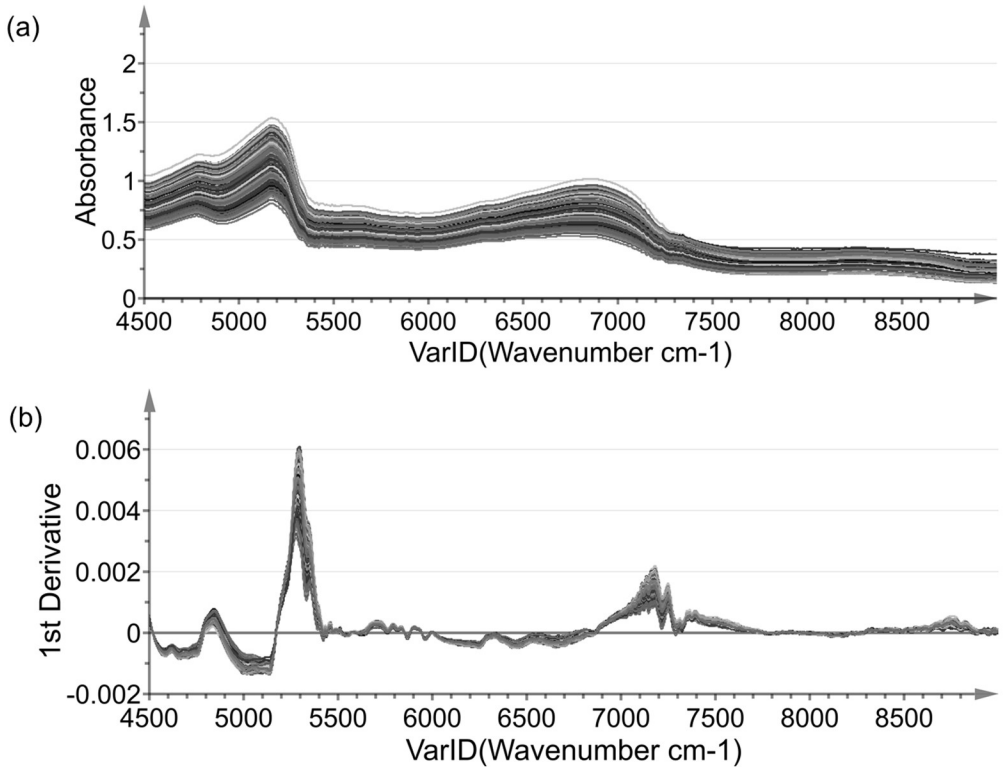

Fig. 7.8. NIR calibration spectra of selected range (wavenumber 4500-9000 cm^{-1}). (a) raw spectra, (b) spectra after 1st derivative pretreatment.

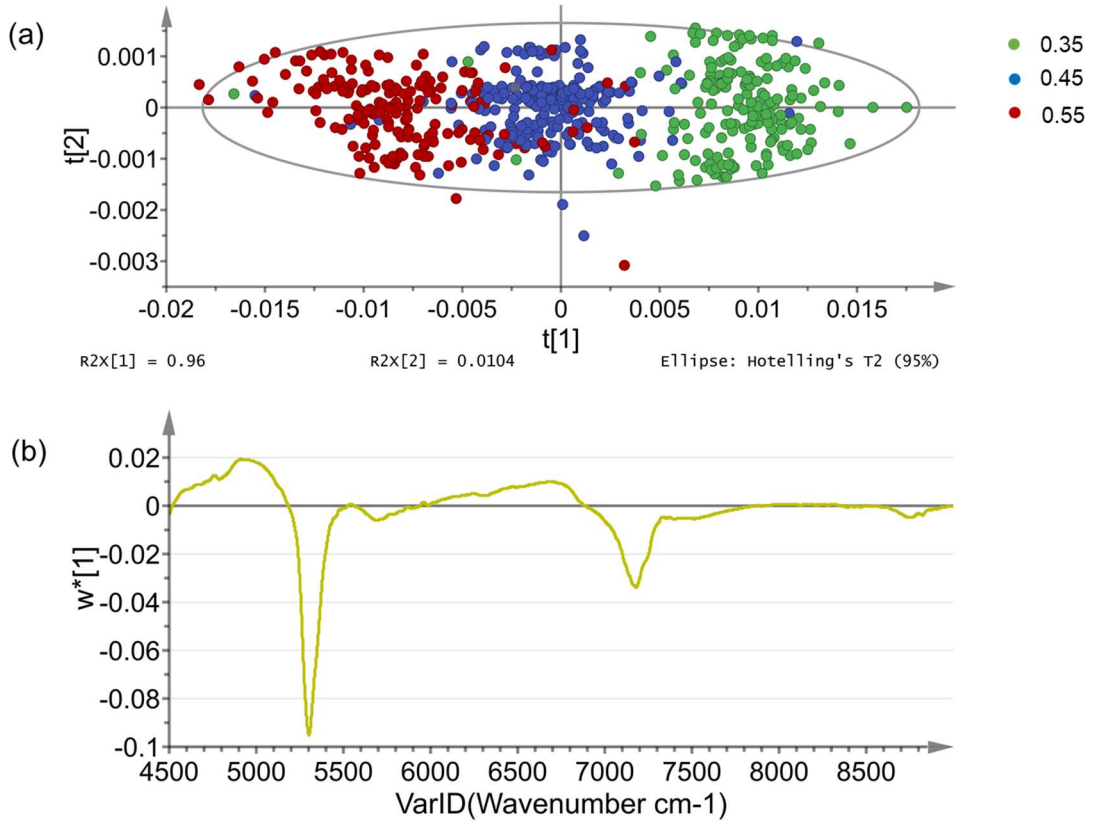

Fig. 7.9. (a) PLS scores scatter plot of calibration set X-data based on 1st derivative from 4500-9000 cm^{-1}. Progression of the first component from left to right was colored by L/S ratio. (b) Line plot of the first X-weight vector, $w^*[1]$, of the PLS model.

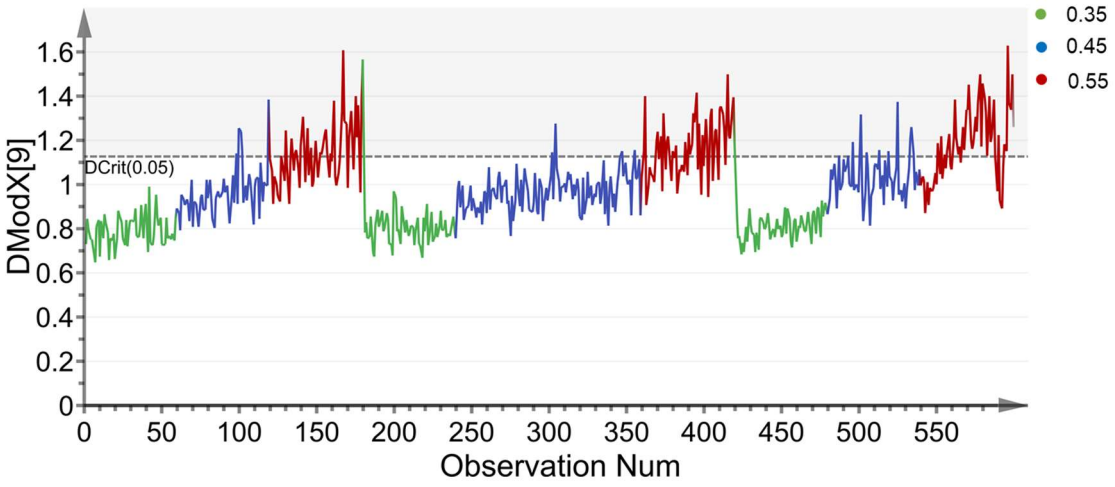

Fig. 7.10. Plot of DModX versus observation number in the X-data of calibration set after using nine PLS factors. Color coding indicated the variation of observation residuals at different L/S ratios. Dcrit denoted the critical value of DModX and was calculated from the *F*-distribution at 95% confidence level.

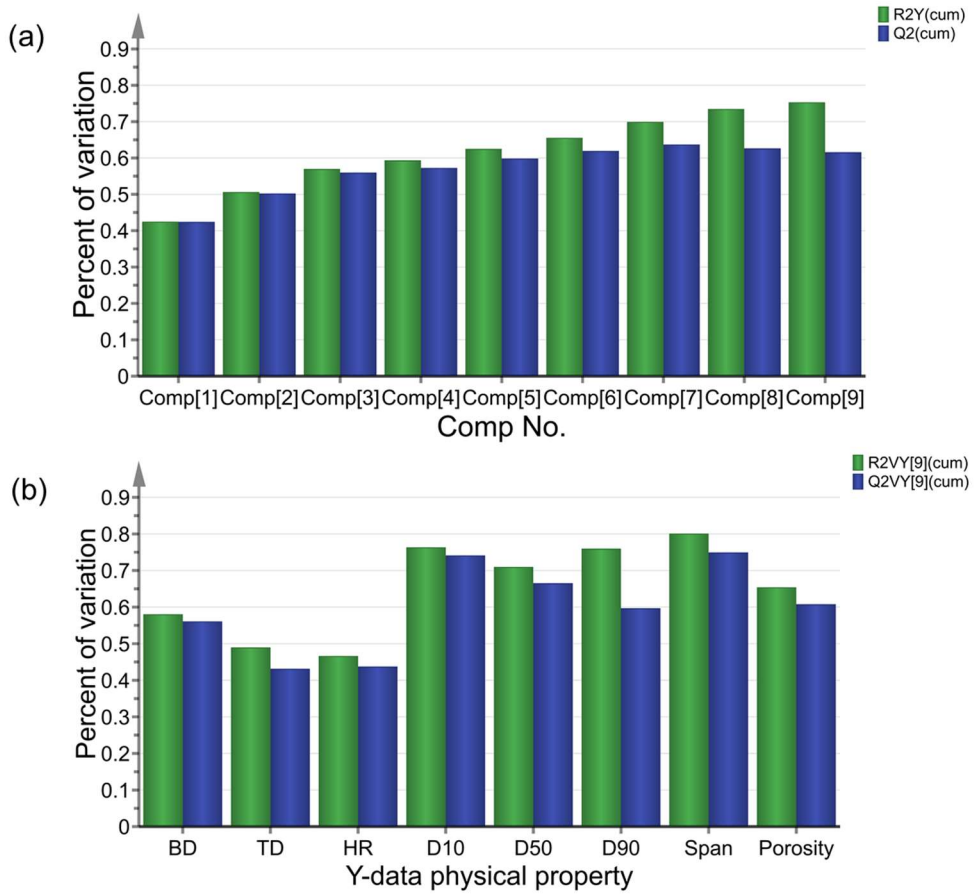

Fig. 7.11. (a) PLS model summary of fit plot. R2Y (sum) indicated the overall cumulative percent of variation in the calibration set Y-data explained by the model as the increase of principal component. Q2 indicated the cumulative percent of variation in the calibration set Y-data predicted by the model according to cross validation. (b) PLS Y-data overview plot. R2VY depicted the goodness of fit of individual response in the calibration set after nine PLS components. Q2VY depicted goodness of prediction of individual response in the calibration set after nine PLS components.

Fig. 7.8 showed the raw NIR spectra of the 600 observations including 30 DoE runs and 20 spectra for each. The variation of granule physical properties such as size, morphology and packing density contributed to the additive, multiplicative and wavelength-dependent effects. Pretreatment of 1st derivative was applied on the raw spectra to eliminate the additive baseline shifts. The PLS scores scatter plot in Fig. 7.9 (a) indicated that the first principle component explained 96 percent variance while the second factor only accounted for 0.0104 percent in the X-data. The color-based clustering in the horizonal direction evidently illustrated that levels of water addition dominated the first factor, as aptly corroborated by the weight line plot in Fig. 7.9 (b) suggesting the considerable water absorbance around 5300 and 7100 cm^{-1} because of -OH combination and first overtone, respectively. Our previous study indicated that L/S ratio predominated over throughput and barrel temperature in terms of granule physical properties. The water addition amount had profound implications on particle consolidation and coalescence and was interwoven with primary granule attributes like size distribution and porosity, which could further impact on the secondary properties such as flowability, compactability, drug release rate, etc.

Notwithstanding the overlapped observations in the vertical direction, it could still be discerned that point swarm was separated according to the degree of powder feed rates, to which the second factor ought to be attributed (not shown). Moreover, Fig. 7.9 (a) revealed no strong outliers or subgroups in the X-data so it is appropriate to fit a single PLS calibration model to the entire data set. The moderate outliers in the X-data were identified by the residuals of each observation, namely the *distance to the model in X-space* (DModX), where the maximum tolerable distance (Dcrit) for the dataset was

calculated. Typically, observations with DModX values larger than the Dcrit are deemed to be moderate outliers and those displayed a DModX twice as large as Dcrit were indicative of more serious outliers. It can be observed in Fig. 7.10 that the residuals increased with more granulation liquid addition and the majority of residuals beyond the Dcrit was those X-data acquired at 0.55 L/S ratio.

Fig. 7.11 (a) showed that according to cross-validation, nine PLS components are significant in modeling and prediction of Y-data responses. The total percentage of variation explained was 75.3 percent with the first factor accounting for 42.5 percent. Although the addition of last three components slightly enhance the goodness of fit, they made very little difference in improving the model predictive ability. Therefore, the model complexity should be situated between 4 and 6 PLS components. In Fig. 7.11 (b), it can be seen that most responses exhibited satisfactory Q2VY larger than 0.5 as opposed to the less well modeled tapped density and Hausner ratio whose Q2VY were slightly below 0.5. In general, except for the granulation processing conditions, bulk and tapped densities were also susceptible to some nuisance factors, such as ambient conditions, graduated cylinder type, materials charging during test, etc., whose influence might be significant yet challenging to control. Therefore, an appreciable proportion of variation within the measured data of bulk and tapped densities could be ascribed to the noise rather than the CPPs. Similarly, it is not surprising that Hausner ratio, a dependent variable of tapped density, demonstrated relatively low prediction accuracy. Nevertheless, the overall picture showed a strong, quantitative relationship between the factors and responses.

7.3.2.2 Model validation by test set

The calibration model was subsequently applied to the test set observations. In accordance with Fig. 7.9 (a), the scores scatter plot in Fig. 7.12 demonstrated analogous homogeneous patterns as well as the paramount importance of L/S ratio in modulating the granule physical properties. It can be seen that almost all the validation set observations fell within the tolerance ellipse based on the training set. No strong outliers were detected and only several moderate outliers were observed at the highest level of L/S ratio (not shown). As a result, the calibration set observations were representative of the test set samples and the PLS model constructed could be employed for prediction of test set responses. The plots in Fig. 7.13 depicted the relationship between actual and predicted values for each physical property in the external validation set. Different PLS factors might be applied for different responses, e.g. 4 factors for D90, 6 factors for porosity and 5 factors for the remaining granule attributes. The visual assessment of model fit reflecting variation due to random effects was satisfactory.

Table 7.4 and 7.5 listed the figures of merit of the PLS model for each response in the 30-run responses surface design. Overall, the model exhibited excellent predictive capacity for different CQAs at varying granulation conditions with low prediction errors (high accuracy with RSEPs less than 5%) and standard deviation of repeatability studies (high precision with RSD less than 5%). Only several span values at high L/S ratio settings were suffered from relatively large prediction residuals with regard to the reference values and data dispersion within the replicates.

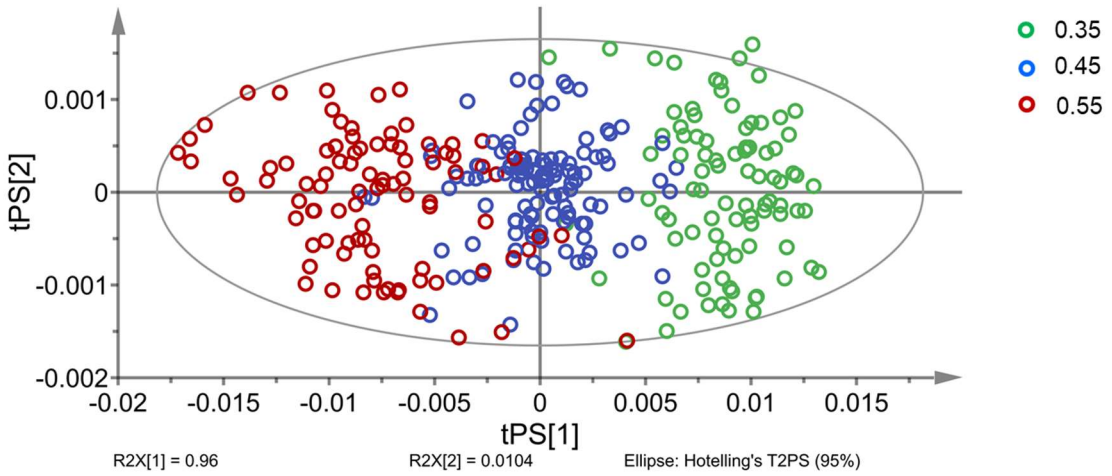

Fig. 7.12. Scatter plot of the predicted score vectors of the test set. Progression of the first component from left to right was colored by L/S ratio.

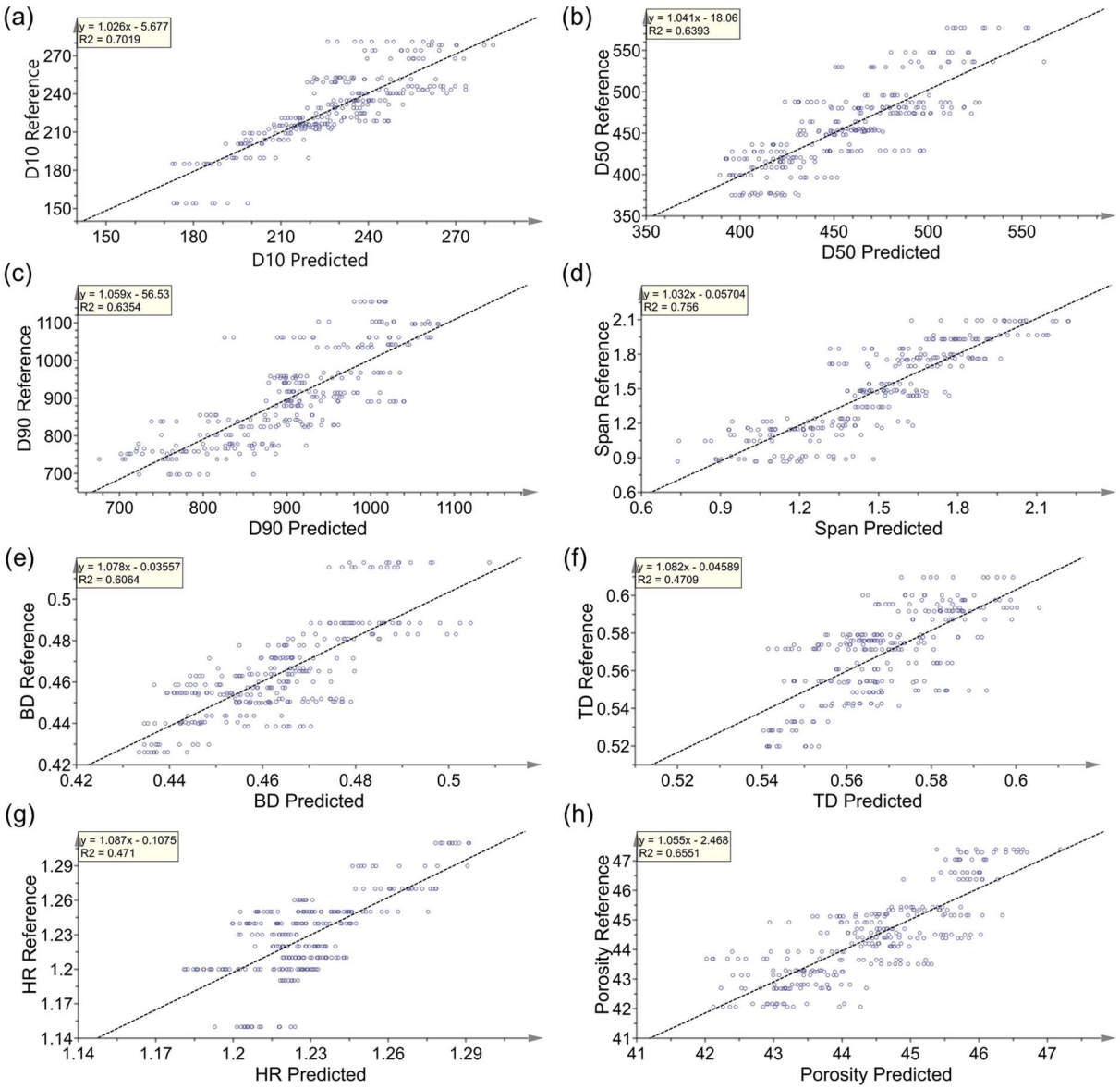

Fig. 7.13. Prediction of granule physical properties versus reference values in the test set with different PLS factors. (a) D10 (five factors); (b) D50 (five factors); (c) D90 (four factors); (d) span (five factors); (e) bulk density (BD) (five factors); (f) tapped density (TD) (five factors); (g) Hausner ratio (HR) (five factors); (h) porosity (six factors).

Table 7.4 Figures of merit (RMSEP and RSEP) of the calibration models based on test set validation for granule CQAs of the 30-run response surface design

StdOrder	D10		D50		D90		Span		Bulk Density		Tapped Density		Hausner ratio		Porosity	
	RMSEP	**RSEP(%)**	RMSEP	**RSEP(%)**	RMSEP	**RSEP(%)**	RMSEP	**RSEP(%)**	RMSEP	**RSEP(%)**	RMSEP	**RSEP(%)**	RMSEP	**RSEP(%)**	RMSEP	**RSEP(%)**
1	29.39	**19.08**	37.60	**10.03**	119.04	**13.36**	0.14	**7.15**	0.0102	**2.23**	0.0236	**3.97**	0.026	**1.96**	0.69	**1.52**
2	6.41	**3.47**	19.73	**4.71**	38.41	**3.62**	0.09	**4.27**	0.0046	**1.05**	0.0053	**0.94**	0.010	**0.77**	1.15	**2.43**
3	13.40	**7.06**	18.75	**4.30**	103.40	**9.38**	0.24	**11.50**	0.0102	**2.23**	0.0154	**2.66**	0.010	**0.77**	1.17	**2.47**
4	6.54	**3.20**	38.47	**10.21**	55.93	**6.63**	0.10	**6.14**	0.0111	**2.49**	0.0121	**2.19**	0.022	**1.77**	0.97	**2.22**
5	6.75	**3.05**	10.37	**2.47**	55.91	**5.83**	0.14	**8.17**	0.0090	**2.01**	0.0172	**3.15**	0.010	**0.79**	0.60	**1.36**
6	8.83	**3.98**	12.92	**2.85**	169.35	**15.97**	0.36	**19.31**	0.0204	**4.52**	0.0112	**2.02**	0.015	**1.26**	1.05	**2.33**
7	5.69	**2.63**	11.94	**2.92**	89.54	**12.83**	0.24	**20.46**	0.0136	**2.85**	0.0058	**1.01**	0.019	**1.62**	1.05	**2.49**
8	6.53	**2.78**	8.94	**1.96**	23.76	**3.14**	0.05	**4.64**	0.0101	**2.06**	0.0085	**1.44**	0.022	**1.82**	0.55	**1.28**
9	15.94	**6.34**	21.88	**4.55**	63.87	**7.63**	0.21	**17.62**	0.0108	**2.23**	0.0105	**1.81**	0.019	**1.62**	1.15	**2.72**
10	4.57	**2.28**	4.80	**1.20**	44.70	**4.94**	0.12	**6.73**	0.0115	**2.69**	0.0154	**2.92**	0.022	**1.79**	0.40	**0.89**
11	6.74	**3.22**	17.85	**4.18**	64.99	**6.28**	0.12	**6.32**	0.0114	**2.64**	0.0264	**5.08**	0.022	**1.82**	0.83	**1.77**
12	4.07	**1.89**	52.67	**10.79**	152.98	**13.23**	0.13	**6.58**	0.0073	**1.65**	0.0165	**3.10**	0.022	**1.82**	1.24	**2.64**
13	7.81	**3.66**	11.86	**2.86**	59.08	**7.17**	0.14	**9.27**	0.0036	**0.80**	0.0175	**3.06**	0.033	**2.64**	1.14	**2.53**
14	22.29	**8.95**	9.31	**2.08**	38.50	**4.09**	0.05	**3.13**	0.0043	**0.94**	0.0205	**3.78**	0.031	**2.64**	0.29	**0.66**
15	5.68	**2.48**	17.03	**3.67**	14.31	**1.56**	0.07	**4.87**	0.0037	**0.79**	0.0065	**1.14**	0.015	**1.26**	0.36	**0.82**
16	11.16	**4.97**	12.94	**2.86**	28.42	**3.18**	0.09	**6.00**	0.0064	**1.38**	0.0154	**2.66**	0.022	**1.79**	0.62	**1.38**
17	3.30	**1.40**	20.99	**4.37**	30.39	**3.45**	0.14	**10.19**	0.0078	**1.66**	0.0107	**1.86**	0.010	**0.79**	0.23	**0.51**
18	13.90	**5.77**	25.80	**5.44**	103.91	**12.55**	0.14	**11.03**	0.0067	**1.44**	0.0107	**1.86**	0.022	**1.79**	0.36	**0.78**
19	17.59	**7.23**	17.27	**3.64**	47.40	**6.42**	0.16	**15.47**	0.0076	**1.58**	0.0246	**4.09**	0.022	**1.77**	1.18	**2.70**
20	16.91	**6.87**	22.12	**4.54**	32.27	**4.02**	0.11	**9.95**	0.0332	**6.43**	0.0117	**1.97**	0.060	**5.17**	0.79	**1.86**
21	12.76	**4.59**	51.40	**8.91**	71.55	**9.19**	0.23	**27.09**	0.0101	**2.06**	0.0072	**1.22**	0.019	**1.62**	0.66	**1.50**
22	7.97	**3.75**	41.06	**10.35**	58.93	**6.44**	0.08	**4.58**	0.0141	**3.07**	0.0235	**4.12**	0.022	**1.77**	1.43	**3.29**
23	6.16	**2.85**	24.79	**5.79**	34.65	**3.32**	0.17	**8.83**	0.0128	**2.77**	0.0112	**2.02**	0.019	**1.62**	1.03	**2.32**
24	9.05	**3.91**	17.55	**3.65**	41.83	**3.81**	0.13	**7.38**	0.0131	**2.92**	0.0185	**3.41**	0.019	**1.62**	0.70	**1.52**
25	7.44	**3.10**	13.36	**2.95**	64.81	**8.45**	0.17	**14.33**	0.0258	**5.88**	0.0328	**5.97**	0.022	**1.77**	0.23	**0.53**
26	21.04	**9.63**	54.62	**12.74**	44.82	**4.70**	0.31	**17.86**	0.0191	**4.22**	0.0153	**2.71**	0.022	**1.77**	0.49	**1.09**
27	22.46	**8.88**	18.03	**3.64**	40.17	**4.15**	0.20	**13.69**	0.0072	**1.56**	0.0065	**1.14**	0.022	**1.79**	1.10	**2.48**
28	39.03	**13.88**	59.22	**11.17**	70.17	**9.33**	0.31	**35.02**	0.0101	**2.14**	0.0239	**3.93**	0.032	**2.50**	0.85	**1.98**
29	24.72	**9.01**	46.22	**8.44**	92.72	**11.97**	0.32	**35.22**	0.0101	**2.06**	0.0110	**1.84**	0.010	**0.79**	0.47	**1.09**
30	16.37	**6.12**	25.14	**4.69**	52.23	**6.11**	0.18	**16.59**	0.0284	**5.48**	0.0070	**1.18**	0.060	**5.17**	0.55	**1.28**

Table 7.5 Figures of merit (SD and RSD) of the calibration models based on test set validation for granule CQAs of the 30-run response surface design

StdOrder	D10		D50		D90		Span		Bulk Density		Tapped Density		Hausner ratio		Porosity	
	SD	**RSD(%)**	SD	**RSD(%)**	SD	**RSD(%)**	SD	**RSD(%)**	SD	**RSD(%)**	SD	**RSD(%)**	SD	**RSD(%)**	SD	**RSD(%)**
1	8.41	**4.61**	12.59	**3.07**	39.43	**3.93**	0.14	**7.01**	0.0058	**1.31**	0.0062	**1.08**	0.0043	**0.34**	0.56	**1.23**
2	5.42	**2.99**	8.11	**2.02**	29.77	**2.88**	0.09	**4.50**	0.0046	**1.04**	0.0048	**0.85**	0.0091	**0.72**	0.36	**0.78**
3	8.54	**4.26**	14.77	**3.49**	37.67	**3.74**	0.13	**6.76**	0.0058	**1.31**	0.0054	**0.96**	0.0091	**0.72**	0.52	**1.12**
4	6.00	**2.89**	8.23	**1.98**	31.73	**3.56**	0.10	**6.22**	0.0057	**1.26**	0.0051	**0.91**	0.0155	**1.26**	0.41	**0.91**
5	3.72	**1.73**	6.26	**1.46**	15.02	**1.66**	0.05	**3.12**	0.0026	**0.56**	0.0024	**0.42**	0.0078	**0.64**	0.20	**0.45**
6	7.21	**3.17**	13.54	**2.98**	36.91	**4.13**	0.12	**7.69**	0.0065	**1.38**	0.0101	**1.80**	0.0069	**0.57**	0.53	**1.20**
7	5.60	**2.57**	8.15	**1.95**	35.76	**4.58**	0.11	**7.77**	0.0046	**0.98**	0.0052	**0.90**	0.0172	**1.42**	0.37	**0.86**
8	2.81	**1.17**	5.63	**1.22**	23.35	**3.05**	0.05	**4.54**	0.0086	**1.78**	0.0027	**0.46**	0.0075	**0.61**	0.30	**0.70**
9	13.19	**5.46**	23.06	**4.79**	62.18	**7.65**	0.22	**17.61**	0.0107	**2.21**	0.0110	**1.90**	0.0172	**1.42**	0.72	**1.68**
10	3.73	**1.88**	4.68	**1.18**	17.96	**1.90**	0.06	**3.12**	0.0029	**0.67**	0.0025	**0.46**	0.0146	**1.19**	0.31	**0.69**
11	5.83	**2.84**	8.79	**2.13**	21.74	**2.23**	0.09	**4.65**	0.0048	**1.10**	0.0049	**0.90**	0.0075	**0.61**	0.19	**0.42**
12	4.26	**1.99**	9.24	**2.12**	13.12	**1.31**	0.04	**2.27**	0.0040	**0.90**	0.0031	**0.56**	0.0075	**0.61**	0.21	**0.46**
13	6.14	**2.81**	7.79	**1.83**	28.58	**3.26**	0.10	**6.44**	0.0038	**0.85**	0.0049	**0.88**	0.0019	**0.16**	0.34	**0.77**
14	4.55	**2.00**	9.27	**2.08**	12.81	**1.42**	0.05	**3.19**	0.0026	**0.57**	0.0034	**0.60**	0.0022	**0.18**	0.24	**0.53**
15	5.98	**2.61**	11.36	**2.52**	12.75	**1.40**	0.07	**4.33**	0.0033	**0.72**	0.0056	**0.99**	0.0069	**0.57**	0.20	**0.45**
16	6.72	**2.87**	11.16	**2.43**	23.77	**2.61**	0.09	**6.31**	0.0061	**1.31**	0.0054	**0.96**	0.0146	**1.19**	0.37	**0.83**
17	3.42	**1.46**	6.40	**1.39**	11.66	**1.28**	0.04	**2.93**	0.0026	**0.56**	0.0035	**0.61**	0.0078	**0.64**	0.21	**0.47**
18	6.44	**2.54**	12.82	**2.58**	24.02	**2.58**	0.08	**6.20**	0.0038	**0.81**	0.0035	**0.61**	0.0146	**1.19**	0.29	**0.65**
19	9.36	**3.62**	14.58	**3.01**	47.79	**6.35**	0.17	**16.49**	0.0066	**1.38**	0.0084	**1.46**	0.0155	**1.26**	0.53	**1.25**
20	6.90	**2.64**	13.52	**2.68**	29.74	**3.64**	0.10	**9.37**	0.0049	**1.02**	0.0058	**1.00**	0.0076	**0.63**	0.34	**0.77**
21	7.81	**2.91**	15.67	**2.97**	46.39	**5.56**	0.14	**13.67**	0.0086	**1.78**	0.0072	**1.23**	0.0172	**1.42**	0.53	**1.21**
22	6.16	**2.83**	10.93	**2.50**	19.35	**1.99**	0.07	**4.32**	0.0047	**1.05**	0.0042	**0.77**	0.0155	**1.26**	0.30	**0.67**
23	3.75	**1.69**	6.50	**1.44**	24.30	**2.39**	0.07	**3.74**	0.0045	**1.00**	0.0101	**1.80**	0.0172	**1.42**	0.43	**0.94**
24	8.79	**3.73**	15.86	**3.24**	17.82	**1.68**	0.10	**6.05**	0.0078	**1.69**	0.0069	**1.23**	0.0172	**1.42**	0.40	**0.87**
25	7.36	**3.10**	9.00	**1.94**	50.18	**6.19**	0.15	**12.14**	0.0048	**1.04**	0.0069	**1.19**	0.0155	**1.26**	0.22	**0.50**
26	9.89	**4.16**	15.91	**3.31**	34.99	**3.79**	0.14	**9.93**	0.0071	**1.52**	0.0071	**1.23**	0.0155	**1.26**	0.45	**1.01**
27	6.14	**2.65**	9.79	**2.04**	28.79	**2.89**	0.09	**5.84**	0.0042	**0.90**	0.0056	**0.99**	0.0146	**1.19**	0.42	**0.92**
28	12.25	**5.02**	18.91	**3.99**	71.14	**9.22**	0.22	**19.94**	0.0087	**1.86**	0.0091	**1.56**	0.0152	**1.21**	0.64	**1.48**
29	8.02	**3.20**	13.68	**2.72**	42.50	**4.95**	0.13	**10.88**	0.0086	**1.78**	0.0065	**1.10**	0.0078	**0.64**	0.27	**0.61**
30	10.97	**4.30**	20.19	**3.88**	55.01	**6.42**	0.17	**14.84**	0.0085	**1.73**	0.0074	**1.25**	0.0076	**0.63**	0.57	**1.33**

7.3.3 Raman spectroscopy

Unlike the NIR detectable transition that necessitates molecule dipole moment change during vibration, Raman active transition is associated with a change in polarizability of the molecule upon excitation. The granulation process in this work involves the addition of water to induce particle coalescence and growth. Raman instead of NIR spectroscopy was selected for quantitively monitoring the variation of drug concentration at different TSG conditions. One advantageous aspect with Raman is that the effect of particle physical variation is not as prominent as NIR. Also, water is characteristic of intense absorption bands with NIR due to the fundamental O-H stretching vibrations accompanied by considerable dipole moment change, which may unfavorably interfere

with the detection of drug absorption in the same spectrum (Nagy et al., 2017). In contrast, for the strong polar bond of O-H in water, small distance change of charges will marginally influence the polarization, generating extremely weak Stokes Raman scattering. Once irradiated with monochromatic laser light, the relatively symmetric molecular structure of caffeine demonstrates strong distortion of electron cloud and hence Raman signals. Besides, with Raman spectroscopy, the inelastically scattered photons engendered by the interaction between incident light and vibrational illuminated molecule can reveal the vibrational energy levels of a molecule, thereby enabling chemical identification and structure elucidation (Harting and Kleinebudde, 2018). Consequently, the sharp and well-resolved bands not only provide information about drug concentration but the potential transition of polymorph form from anhydrous caffeine to monohydrate caffeine.

7.3.3.1 Development of calibration model with raw materials premix

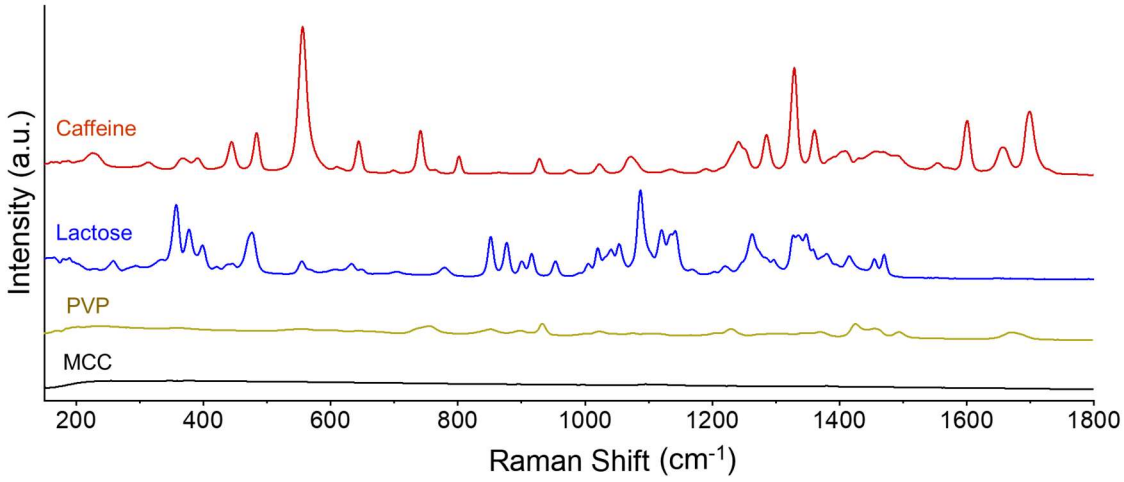

Fig. 7.14. Reference Raman spectra of the raw materials. Intensity is in arbitrary unit. Spectra are normalized and shifted to facilitate visual comparison of the peak locations.

Fig. 7.14 compared the Raman spectra of pure ingredients in the formulation. MCC exhibited low peak intensity and few peaks principally due to the fluorescence. In Fig. 7.15 (a), the raw Raman spectra of dry blends demonstrated evident ascending baseline and fluorescence effect. Pretreatment methods of SNV and 2nd derivative were applied to correct the baseline shift and spurious data generated by laser intensity fluctuations, eliminate the fluorescence broad band signal and amplify the Raman signal (see Fig. 7.15 (b)). In comparison to Fig. 7.14, distinct peaks in the spectral range of 440-460, 545-565, 615-635, 735-755, 1590-1610 and 1690-1710 cm^{-1} could be attributed to caffeine, thus being selected to construct the PLS calibration model.

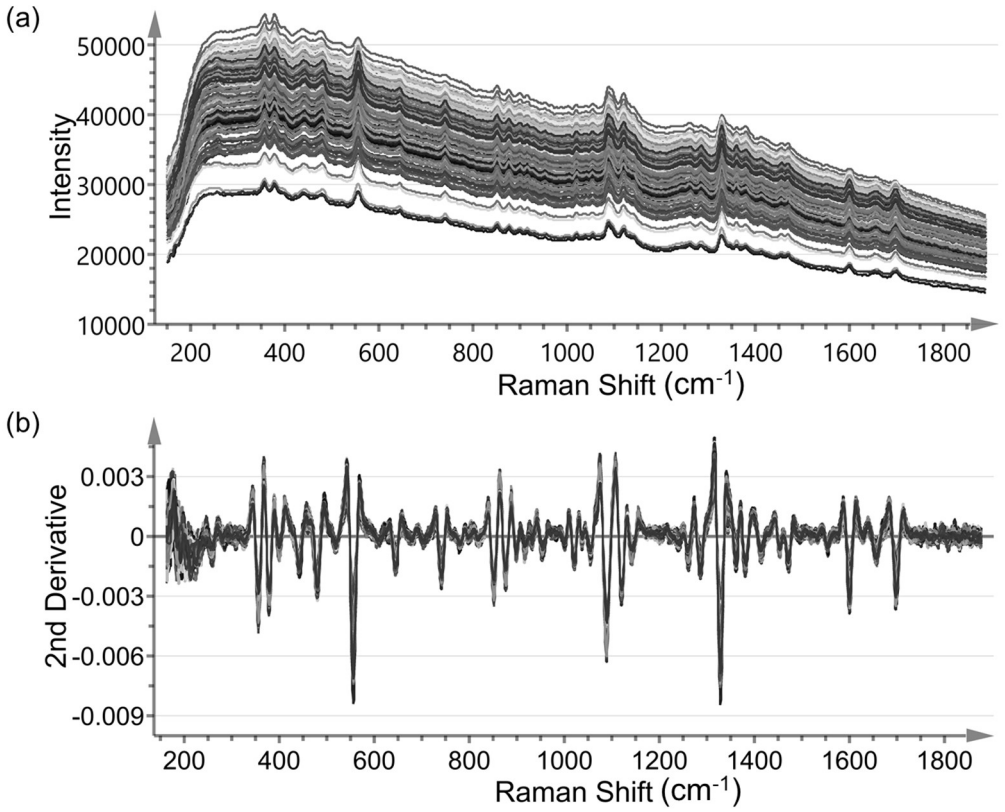

Fig. 7.15. Raman spectra of dry blends calibration set. (a) raw spectra, (b) spectra after pretreatments of SNV followed by 2st derivative.

Cross-validation suggested two PLS components in modeling and prediction of Y-data responses. The scores scatter plot in Fig. 7.16 indicated that the first principle component captured 93 percent spectral variation while only 1.68 percent stemmed from the second factor in the X-data. The color-based clustering in the horizonal direction clearly illustrated that varying caffeine concentrations in different raw material dry blends dominated the first factor. Meanwhile, the total percentage of variation explained in Y-data was 90.6 percent with the first factor accounting for 81.7 percent. The cumulative cross-validated variation in the Y-data was 90.3 percent.

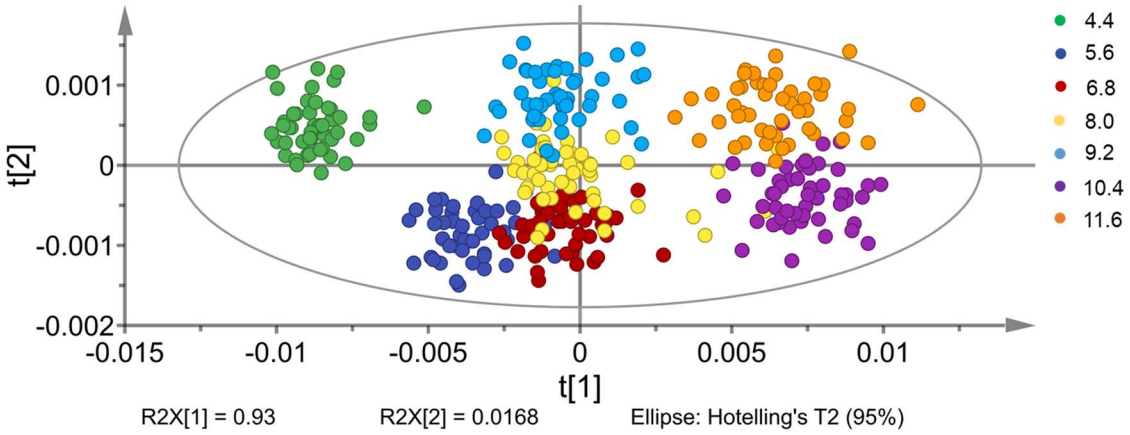

Fig. 7.16. PLS scores scatter plot of calibration set X-data after preprocessing. Color coding was based on the drug concentration (% w/w) in different dry blends.

7.3.3.2 Model validation by test set of raw materials premix

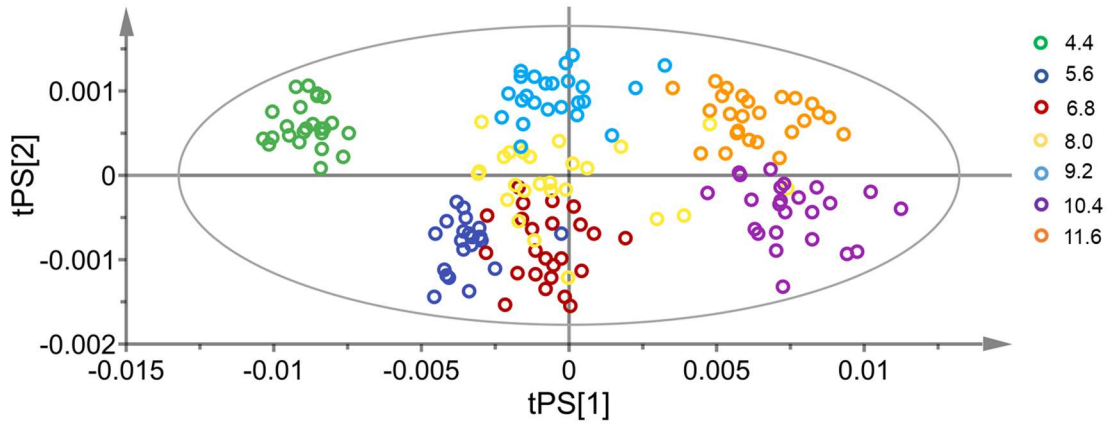

Fig. 7.17. Scatter plot of the predicted score vectors of the validation set. Progression of the first component from left to right was colored according to the predicted drug concentration (% w/w).

The calibration model was subsequently validated by the test set observations. The scores scatter plot in Fig. 7.17 demonstrated analogous homogeneous patterns as well as the predominant first factor owing to difference in caffeine concentration. It can be seen that all the validation set observations fell within the tolerance ellipse based on the training set. No strong outliers were detected and the majority of moderate outliers arose from the predicted concentration of 6.8, 8 and 9.2 percent (not shown). Consequently, the calibration set observations were representative of the test set samples and the PLS model constructed could be employed for prediction of test set caffeine content. The plots in Fig. 7.18 depicted the relationship between actual and predicted response in the external validation set after two PLS factors. The visual assessment of model fit (0.905) was satisfactory.

Table 7.6 listed the figures of merit of the PLS model for different test set drug concentrations. Overall, the model exhibited inadequate predictive capacity with

relatively high prediction errors (the highest RSEP of 16.48%) and standard deviation of repeatability studies (the highest RSD of 13.44%). One of the reasons might be attributed to the inhomogeneity of raw materials premix.

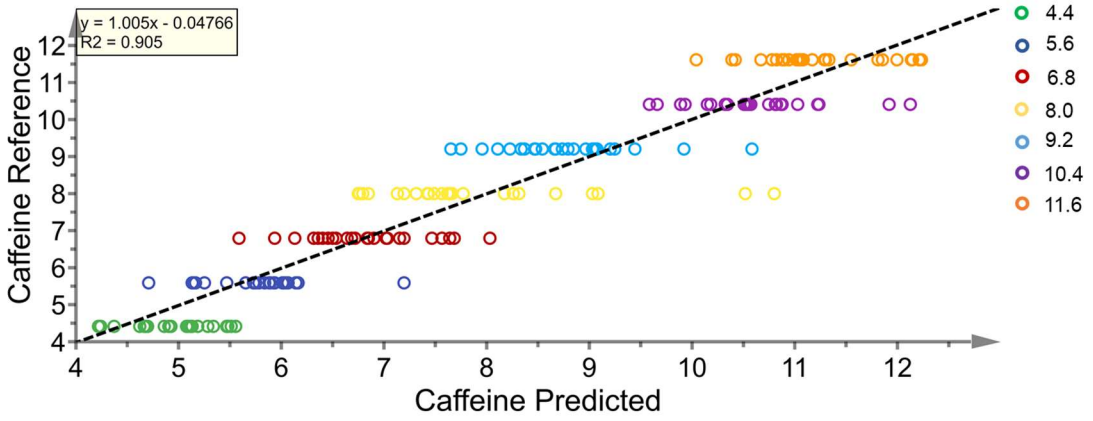

Fig. 7.18. Predicted caffeine concentration (% w/w) versus reference values in the validation set with two PLS factors.

Table 7.6 Figures of merit of the calibration model based on test set validation for caffeine content

Premix reference drug content (% w/w)	SD	RSD(%)	RMSEP	RSEP(%)
4.4	0.4046	8.08	0.7254	16.48
5.6	0.4909	8.47	0.5173	9.23
6.8	0.5891	8.64	0.5770	8.48
8	1.0523	13.44	1.0469	13.08
9.2	0.9335	10.45	0.9532	10.36
10.4	0.5566	5.28	0.5586	5.37
11.6	0.6538	5.82	0.7425	6.40

7.3.3.3 Prediction of granules drug content during TSG

Fig. 7.19 showed the raw spectra of granules that bore high degree of resemblance to the dry blends spectra in the calibration set (refer to Fig. 7.15 (a)). The individuals control chart in Fig. 7.20 displayed the granule drug content during TSG process that are monitored in-line and over time. This plot revealed that the granulation process was

within control, despite that the average of predicted caffeine concentration was slightly above the theoretical value in the formulation.

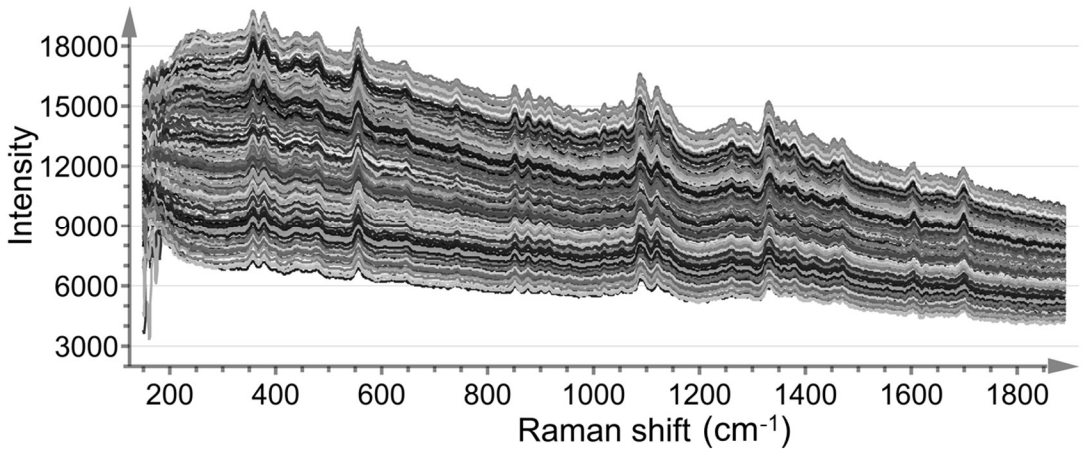

Fig. 7.19. Raw Raman spectra of granules in the prediction set.

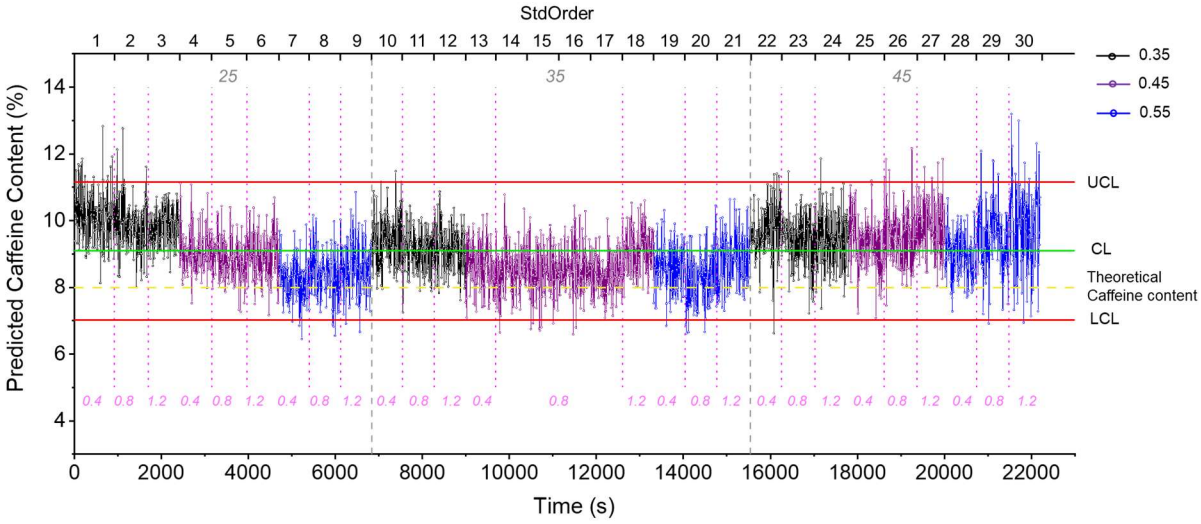

Fig. 7.20. Individuals control chart for predicted caffeine concentration in time series (bottom *x*-axis) and StdOrder (top *x*-axis) of the entire 30-run DoE. Upper and lower red solid lines represented the UCL and LCL while green solid line represents the CL, which were calculated on the basis of all predicted values. The yellow dash line depicted the theoretical caffeine concentration (8% w/w) in the formulation. Consecutive prediction values were connected with a straight line where black, purple, and blue line represented

0.35, 0.45 and 0.55 L/S ratio, respectively. Connected prediction values at different barrel temperatures (25, 35 and 45 °C) were separated by grey dash lines. Connected prediction values at different throughput (0.4, 0.8 and 1.2 kg/h) in each barrel temperature zone were separated by pink dot lines.

7.3.3.4 Validation of predicted drug concentration in granules

The drug content in granules was measured by UV-Vis spectroscopy. Table 7.7 listed the model figures of merit based on the reference value from each DoE condition. The average RSD in terms of the 30-run response surface design was 7.86% whereas the average RSEP was 17.79%.

Table 7.7 Figures of merit of the calibration model validated by granule prediction set for caffeine concentration

StdOrder	Granule reference drug content (% w/w)	SD	RSD(%)	RMSEP	RSEP(%)
1	8.09	0.7581	7.47	2.1974	27.17
2	8.02	0.7464	7.56	1.9976	24.90
3	8.00	0.5363	5.47	1.8747	23.43
4	7.84	0.6169	6.79	1.3962	17.82
5	7.66	0.6070	6.86	1.3339	17.41
6	7.83	0.6804	7.60	1.3075	16.69
7	7.90	0.6044	7.32	0.6954	8.80
8	8.11	0.6809	8.10	0.7404	9.13
9	7.70	0.7410	8.61	1.1679	15.17
10	8.02	0.7504	7.95	1.6002	19.95
11	7.81	0.5940	6.53	1.4232	18.23
12	7.73	0.6553	7.15	1.5703	20.31
13	8.14	0.6869	7.94	0.8529	10.48
14	7.69	0.6578	7.70	1.0811	14.06
15	8.21	0.7129	8.43	0.7502	9.13
16	7.96	0.6713	7.84	0.9004	11.31
17	7.71	0.5810	6.98	0.8492	11.02
18	7.76	0.6486	7.13	1.4899	19.20
19	7.82	0.6572	7.62	1.0341	13.23
20	7.73	0.7045	8.56	0.8606	11.14
21	7.64	0.7378	8.34	1.4076	18.42
22	8.16	0.7458	7.73	1.6622	20.37
23	8.03	0.7401	7.84	1.5821	19.69
24	8.08	0.7843	8.28	1.5953	19.74
25	7.96	0.7537	8.11	1.5364	19.31
26	8.00	0.8038	8.46	1.7004	21.25
27	7.87	0.7964	8.12	2.0997	26.69
28	7.93	0.6733	7.53	1.2203	15.39
29	7.81	0.8919	9.42	1.8854	24.15
30	7.78	1.2060	12.30	2.3489	30.17

7.4 Conclusions

This study demonstrated the feasibility of implementing three complementary PAT tools for in-line analysis of continuously produced granules. Eyecon^{TM} was capable of capturing the particle size and shape variation at different granulation processing conditions. PLS model based on NIR spectra demonstrated strong predictive ability

towards critical granule physical attributes. Raman spectroscopy was leveraged to monitor the drug content and revealed that more caffeine was dissolved as L/S ratio increased to higher levels.

Chapter 8

Conclusions and future perspectives

8.1 Summary

This dissertation was geared towards enhancing process understanding and facilitating the paradigm transformation from conventional batch manufacturing processes to more futuristic and advantageous continuous processes. Different commerically available continuous granulators were comprehensively investigated by employing pharmaceutical quality by design methodologies.

Specific aim I including Chapter 2, 3 and 6 of this dissertation mainly focused on exploring the relationships between CPPs and CQAs of different commercial continuous twin-screw and high-shear granulators with different scales by leveraging DoE, multivariate data analysis and fundamental granulation regime maps.

Chapter 2 examined the Glatt GCG70 continuous high-shear mixer granulator that has received much less attention: a tubular mixer equipped with an axially placed shaft. The effect of process and design variables on GSD were investigated based on the drop penetration tests, nucleation regime map and aided by statistical tools. The findings can be summarized as follows.

- Granule size distribution can be controlled by manipulating process variables, with the most desirable median diameter (200-300 μm) obtained at L/S ratio 0.3 and rotation speed either 275 or 660 rpm.
- Design parameters showed less considerable impact on liquid redistribution and granule growth.

- A broad size distribution and ungranulated fines were observed even for the relatively optimum operation conditions.
- Binder delivery can be ameliorated in the future studies. Liquid solution should be sprayed through an atomizing nozzle to reduce the droplet size, decrease the penetration time and shift the granulation to drop controlled regime.
- Design of mixing tools can be improved by utilizing sharper blades, which increases the level of shear input and eliminates the over-granulated particles more efficiently.

Chapter 3 conducted statistical analysis of the Lödige CM5 continuous high-shear mixer granulator and Thermo EuroLab 16mm twin-screw granulator. The comparison studies between these two granulators were conducive to transferring manufacturing technologies tailored for different products. Knowledge gap between important process parameters and critical granule attributes was bridged by deploying QbD methodologies. The design space of each granulator was identified on the basis of desirable specifications. Moreover, the discrepancies in granulator performance were expounded via delving into the underlying granulation mechanisms. The elicited conclusions were summarized as follows.

- As continuous granulators, both Lödige and TSG generated granules with controllable attributes within a very short residence time.
- Lödige produced granules with a smaller size variance and finer internal structure after the “real” high shear granulation process, leading to a wider design space and higher flexibility in terms of tight specifications.
- TSG with such a particular screw configuration provided a granulation environment with intermediate shear level.

- Granules from TSG exhibited multimodal distributions, especially at low liquid addition level, and subtler difference of physical microstructure.
- The ungranulated materials were always present, suggesting the suboptimal liquid dispersion and micro-mixing efficiency of liquid and powder.
- The strong influence of rotation speed and L/S ratio on Lödige offered potential for a capable control loop to make real time adjustments through manipulating process parameters.
- While TSG illustrated narrower design space, it demonstrated robustness towards process variation, which was critical for maintaining product quality against unexpected changes or noise factors during the manufacturing process.
- Granulation mechanisms explored on the basis of nucleation and growth regime maps revealed that for most cases liquid binder was uniformly distributed with fast droplet penetration into the powder bed and that granule consolidation and coalescence mainly took place in the nucleation, steady growth and rapid growth regimes.

Chapter 6 shed light on leveraging sequential experimentation strategy towards better design and understanding of continuous wet granulation process. Investigation of the Thermo Pharma 11mm twin-screw granulator commenced with screening experimental design to accommodate numerous candidate factors of potential importance and identified those significantly affecting response variables. Following that, comprehensive studies were performed to explore the relationship between CPPs and CQAs of granules and tablets by implementing response surface methodology. The design space was eventually proposed after locating the optimum operational regions based on the defined target product quality profiles. The findings were summarized as follows.

- In the screening stage, D-optimal design was leveraged to examine a broad spectrum of process and screw configuration variables.
- Based on the predefined quality target values, screw speed (700 rpm), KE staggering angle (60°), KE number (5) and DFS (w/) were held constant at optimum levels that maximize the design space while barrel temperature, throughput and L/S ratio were selected for further investigation in the following stage.
- In the response surface design, comprehensive characterization studies were carried out to delve into the correlation between CPPs and CQAs of granule and tablet.
- L/S ratio was identified as the most predominating factor followed by throughput and barrel temperature.
- Less water addition brought about granules with broader size distribution, porous internal structure and deteriorated flowability and tablets with stronger tensile strength but accelerated drug release.
- Throughput and barrel temperature mainly impacted on the CQAs through alternation of materials barrel filling degree and ingredient solubility and interaction with distinct thermal energy input, respectively.

Specific aim II as presented in Chapter 4 primarily focused on the implications of varying processing conditions in continuous high-shear granulation for modulating tablet properties. The relationship among input process parameters, intermediate granule properties and final drug product tablet attributes was unraveled by utilizing multivariate data analysis. Furthermore, diverse imaging techniques were employed to elucidate the underlying dissolution mechanisms accompanied by distinct tablet physical

microstructures as well as the influence of tablet drug agglomerate size distribution (chemical microstructure) on release kinetics. The findings were summarized as follows.

- L/S ratio and impeller rotation speed showed predominant effect over powder feeding rate on critical quality attributes of tablets.
- The process parameters were capable of modulating tablet performance via altering granule properties, primarily size distribution and porosity.
- The longer residence time of materials underwent inside the granulator, the following concomitant results were obtain: larger particle size, smaller porosity, better flowability, more spherical particles, higher tablet tensile strength and slower drug release kinetics.
- Higher compression force and denser granules resulted in smaller tablet porosity with more closed pores, which subsequently delayed the matrix erosion and impeded the drug release.
- With a higher percentage of open pore, water infiltrated rapidly into tablet and fast disintegration process and drug release kinetics were induced.
- For tablets with non-homogeneous chemical microstructure, i.e., poor distributive and dispersive mixing associated with more large API agglomerates, the reduced contacting area between drug particles and dissolution medium postponed the release rate.
- In contrast to low-shear batch mixing, continuous mixing enabled better deagglomeration effect, thus facilitating the release process on account of more dispersed small drug aggregates.

Specific aim III as elaborated in Chapter 5 concentrated on understanding the influence of raw material properties and binder delivery method on criticacl quality attributes in continuous high-shear granulation process. This study revealed the effect of drug hydrophobicity and primary particle size in low-dose formulations. Besides, the influence of drug loading was investigated by utilizing low-dose, medium-dose and high-dose formulations. In addition, the impact of binder addition approaches, liquid solution viscosity and surface tension were assessed for each studied formulation. The findings were summarized as follows.

- Low-dose formulations showed similar flow properties and wettability irrespective of the penetration liquids.
- Binder delivery method had more significant effect on granule size distribution compared to the variation of active ingredients.
- Higher viscosity binder tended to form oversize particles due to the inability of being uniformly redistributed within a very short residence time.
- The dry binder delivery method produced more densified granules on account of the high degree of deformation and consolidation during granulation.
- The active ingredient in different formulations demonstrated more dominant effect on drug agglomerate size distribution.
- APIs with poor water solubility or smaller primary particle size displayed a tendency to form smaller aggregates in the tablets with enhanced distributive and dispersive mixing ensuring uniform and finer distribution structure.
- The drug segregation extent was primarily controlled by drug loading where the high-dose formulation revealed the lowest de-mixing potential.

Specific aim IV as discussed in Chapter 7 explored the feability of deploying complementary in-line analytical tools to enable real-time release testing. Eyecon^{TM} direct imaging was integrated for real-time granule size and shape assessment. Near-infrared (NIR) spectroscopy was implemented to predict granule physical attributes (size, porosity, bulk density, tapped density and flowability). Raman spectroscopy was used for in-line evaluation of granule drug content uniformity. The results were concluded as follows.

- Eyecon^{TM} exhibited capability of real-time monitoring of particle size and shape variation at different granulation conditions.
- Granule size consistently increased, and span slightly decreased as more binding liquid was added in the system.
- D10 and D50 demonstrated distinct step change in conjunction with the variation of L/S ratio whereas D90 and span embodied more dramatic fluctuation.
- By virtue of the stability and sensitivity of D10, it was deemed to be a more suitable parameter compared to D90 that should be employed in monitoring and control of size enlargement process.
- PLS models based on NIR spectra demonstrated strong predictive ability (precision and accuracy) towards critical granule physical attributes.
- The developed in-line Raman spectroscopic method for continuous API quantification exhibited a satisfactory predictive performance but can be further optimized in the future studies.
- The real-time monitoring of drug content during twin-screw granulation revealed that more caffeine was dissolved as L/S ratio increased to higher levels.

8.2 Recommendations for future work

Chapter 5 had extensively examined the effect of raw materials and binding solution properties. For future study, liquid-solid contact angle, viscosity and surface tension of different liquids can be evaluated and used for PLS model development to quantitatively correlate the material flow properties, hydrophobicity with granule and tablet characteristics. Such a relationship in conjunction with the understanding of critical process parameters will be valuable for constructing a regime map for twin-screw granulator (TSG). The currently developed regime maps as described in this dissertation are primarily for wet granulation carried out by high-shear mixer granulators (HSG) or fluidized bed granulators (FBG). Granulation in these reactors is driven by the underlying rate processes such as wetting and nucleation, coalescence and consolidation, and breakage and attrition. A major difference between HSG or FBG and TSG is that the former is a closed batch system where the aforementationed granulation mechanisms can occur simultaneously and are difficult to be separated from each other. In contrast, TSG is an open-end continuous system with process steady state. Those rate processes are physically separable and can take place consecutively along the length of screws in the barrel.

Binders are considered as one of the crucial excipients for a successful wet granulation formulation, which creates structural mixture of all the ingredients by cohesive network. This dissertation primarily utilized an inert synthetic polymer PVP as the binder. Future study may consider comparing the PVP to other binding agents such as cellulose-based polymers (e.g. HPMC) and natural polymers (e.g. starch). Different categories of binders with the identical concentration can generate granules and tablets with distinct crushing

strength. The addition of excessive binder in formulation or the use of highly viscous binding solution generally produce tablets with large tensile strength that do not disintegrate readily, thus, impeding drug release. On the other hand, a low binder concentration will lead to fragile granules and large amount of undesirable fines. In addition, studies in this dissertation principally adopted regular lactose and MCC Avicel® PH101 as the excipients. Future work should also assess the performance of different grades of lactose and MCC to rationalize the seleciton of excipients.

The granulation liquid was injected exclusively through dripping mode in this dissertation. For TSG, the space in the barrel is confined and there is very limited free volume available for distributive mixing of liquid and solids. Future work can explore some other wetting methods like spraying and foam delivery to improve the efficiency of liquid redistribution. In particular, form delivery has been recognized as a robust technique enabling homogeneous spread of liquid over relatively large material surface area without oversaturating the initially contacted powder bed. This is more critical for the scenarios where low screw speed and high throughput engender a high degree of barrel filling level as well as a low powder surface velocity.

Granulation of hydrophobic powders is very common in pharmaceutical industry. Previous investigation on batch granulation processes confirmed the possibility of modulating the granule properties by forming a “liquid marble”. Nucleation can be triggered by spreading the sub-micron particles over the sessile droplet, which subsequently form a hollow internal structure following liquid evaporation. This technique enables simultaneous control of granule size and structure, handle a high loading of hydrophobic active ingredient and improved flow and compression

characteristics. The formulation with 80% ibuprofen studied in Chapter 5 can be further evaluated for the possibility of forming liquid marbles in continuous high-shear granulation. X-ray imaging can be leveraged to visualize the core structure of granules produced at different processing consitions and binding liquids.

In addition, the Lödige CM5 granulator can be coupled with the drying system Glatt GPCG 2-GF 5 that is available at C-SOPS. In this first stage, a screening design can be deployed to assess a wide range of variables of potential importance such as the throughput, L/S ratio, impeller speed, drying temperature, air velocity and several dryer design parameters that control the intermediate hold-up volume. Residence time distribution for each operation condition should be carefully evaluated since it is critical for understanding the drying dynamics and the concomitant implications for granule properties. Certain granulation conditions can produce fragile granules with low mechanical strength. Eyecon^{TM} as a result can be integrated both before and after the dryer to examine discrepancy in size change after drying. NIR spectroscopy can be used for monitoring granule physical attributes as well as the residual moisture content after drying. Raman spectroscopy can be implemented to monitor drug content uniformity and solid-state transformation after granulation and drying. This investigation may enable a successful technology transfer of a commercially available product from a batch fluidized bed granulation and drying process to a modular continuous high-shear granulation and fluidized bed drying process.

Another topic to be considered in the future studies is called moisture-activated dry granulation (MADG). This is a simple, economical and noval granulation process that necessitates a small amount of water to activate the granule formation without the

subsequent drying step. The stepwise addition and mixing of different formulation ingredients enables the attachment of drug to excipients as well as the absorption and redistribution of liquid constituents, thus generating homogeneous, free-flowing and compactible granular particles. Twin-screw granulator is ideal for this technology by virtue of its flexibility of adjusting liquid and powder feed locations to accommodate different needs. In the agglomeration stage, a nonabsorbent, easy-to-wet ingredient such as lactose monohydrate can be used as the filler. Low L/S ratio should be adopted to spary water onto the powder mixture to moisten the binder and induce the agglomeration. In the following moisture-distribution and absorption stage, moisture absorbents like microcrystalline cellulose or silicon dioxide are added to dry the agglomerates by redistributing the absorbed liquid within the mixture.

Reference

Abdelhamid, D.S., Zhang, Y., Lewis, D.R., Moghe, P.V., Welsh, W.J., Uhrich, K.E., 2015. Tartaric acid-based amphiphilic macromolecules with ether linkages exhibit enhanced repression of oxidized low density lipoprotein uptake. Biomaterials 53, 32-39.
Adams, M.J., Mullier, M.A., Seville, J.P.K., 1994. Agglomerate strength measurement using a uniaxial confined compression test. Powder Technol 78, 5-13.
Allen, T., 2003. Powder Sampling and Particle Size Determination, First ed. . Elsevier, B.V., Amsterdam, The Netherlands.
Allen, T., Elsevier, 2003. Powder sampling and particle size determination, Amsterdam; Elsevier.
Ansari, M.A., Stepanek, F., 2008. The effect of granule microstructure on dissolution rate. Powder Technol 181, 104-114.
Ax, K., Feise, H., Sochon, R., Hounslow, M., Salman, A., 2008. Influence of liquid binder dispersion on agglomeration in an intensive mixer. Powder Technol 179, 190-194.
Badawy, S.I.F., Narang, A.S., LaMarche, K., Subramanian, G., Varia, S.A., 2012. Mechanistic basis for the effects of process parameters on quality attributes in high shear wet granulation. Int J Pharmaceut 439, 324-333.
Beer, P., Wilson, D., Huang, Z.Y., De Matas, M., 2014. Transfer from High-Shear Batch to Continuous Twin Screw Wet Granulation: A Case Study in Understanding the Relationship Between Process Parameters and Product Quality Attributes. J Pharm Sci-Us 103, 3075-3082.
Bendel, R.B., Afifi, A.A., 1977. Comparison of Stopping Rules in Forward "Stepwise" Regression. Journal of the American Statistical Association 72, 46-53.
Brown, S.D., 2009. Comprehensive chemometrics : chemical and biochemical data analysis. Elsevier, Amsterdam.
Chablani, L., Taylor, M.K., Mehrotra, A., Rameas, P., Stagner, W.C., 2011. Inline Real-Time Near-Infrared Granule Moisture Measurements of a Continuous Granulation–Drying–Milling Process. Aaps Pharmscitech 12, 1050-1055.
Chan, E.L., Reynolds, G.K., Gururajan, B., Salman, A.D., Hounslow, M.J., 2012. Blade-Granule Bed Stress in a Cylindrical High-Shear Granulator: Variability Studies. Chem Eng Technol 35, 1435-1447.
Costa, P., Sousa Lobo, J.M., 2001. Modeling and comparison of dissolution profiles. Eur J Pharm Sci 13, 123-133.
Crean, B., Parker, A., Roux, D.L., Perkins, M., Luk, S.Y., Banks, S.R., Melia, C.D., Roberts, C.J., 2010. Elucidation of the internal physical and chemical microstructure of pharmaceutical granules using X-ray micro-computed tomography, Raman microscopy and infrared spectroscopy. Eur J Pharm Biopharm 76, 498-506.
De Beer, T., Burggraeve, A., Fonteyne, M., Saerens, L., Remon, J.P., Vervaet, C., 2011. Near infrared and Raman spectroscopy for the in-process monitoring of pharmaceutical production processes. Int J Pharmaceut 417, 32-47.
de Villiers, M.M., 1996. Influence of agglomeration of cohesive particles on the dissolution behaviour of furosemide powder. Int J Pharmaceut 136, 175-179.
Dhenge, R.M., Cartwright, J.J., Doughty, D.G., Hounslow, M.J., Salman, A.D., 2011. Twin screw wet granulation: Effect of powder feed rate. Advanced Powder Technology 22, 162-166.
Dhenge, R.M., Cartwright, J.J., Hounslow, M.J., Salman, A.D., 2012. Twin screw wet granulation: Effects of properties of granulation liquid. Powder Technol 229, 126-136.
Dhenge, R.M., Fyles, R.S., Cartwright, J.J., Doughty, D.G., Hounslow, M.J., Salman, A.D., 2010. Twin screw wet granulation: Granule properties. Chem Eng J 164, 322-329.
Dhenge, R.M., Washino, K., Cartwright, J.J., Hounslow, M.J., Salman, A.D., 2013a. Twin screw granulation using conveying screws: Effects of viscosity of granulation liquids and flow of powders. Powder Technol 238, 77-90.

Dhenge, R.M., Washino, K., Cartwright, J.J., Hounslow, M.J., Salman, A.D., 2013b. Twin screw granulation using conveying screws: Effects of viscosity of granulation liquids and flow of powders. Powder Technol 238, 77-90.
Djuric, D., Kleinebudde, P., 2008. Impact of Screw Elements on Continuous Granulation With a Twin-Screw Extruder. J Pharm Sci-Us 97, 4934-4942.
Djuric, D., Kleinebudde, P., 2010. Continuous granulation with a twin-screw extruder: Impact of material throughput. Pharm Dev Technol 15, 518-525.
Djuric, D., Van Melkebeke, B., Kleinebudde, P., Remon, J.P., Vervaet, C., 2009. Comparison of two twin-screw extruders for continuous granulation. Eur J Pharm Biopharm 71, 155-160.
El Hagrasy, A.S., Cruise, P., Jones, I., Litster, J.D., 2013a. In-line Size Monitoring of a Twin Screw Granulation Process Using High-Speed Imaging. J Pharm Innov 8, 90-98.
El Hagrasy, A.S., Hennenkamp, J.R., Burke, M.D., Cartwright, J.J., Litster, J.D., 2013b. Twin screw wet granulation: Influence of formulation parameters on granule properties and growth behavior. Powder Technol 238, 108-115.
El Hagrasy, A.S., Hennenkamp, J.R., Burke, M.D., Cartwright, J.J., Litster, J.D., 2013c. Twin screw wet granulation: Influence of formulation parameters on granule properties and growth behavior. Powder Technol 238, 108-115.
El Hagrasy, A.S., Litster, J.D., 2013. Granulation rate processes in the kneading elements of a twin screw granulator. Aiche J 59, 4100-4115.
Fell, J.T., Newton, J.M., 1970. Determination of tablet strength by the diametral-compression test. J Pharm Sci-Us 59, 688-691.
Flores, G.E., Norbury, D.H., 1991. A sequential experimentation strategy and response surface methodologies for process optimization, [1991 Proceedings] IEEE/SEMI Advanced Semiconductor Manufacturing Conference and Workshop, pp. 165-174.
Fonteyne, M., Correia, A., De Plecker, S., Vercruysse, J., Ilic, I., Zhou, Q., Vervaet, C., Remon, J.P., Onofre, F., Bulone, V., De Beer, T., 2015a. Impact of microcrystalline cellulose material attributes: A case study on continuous twin screw granulation. Int J Pharmaceut 478, 705-717.
Fonteyne, M., Soares, S., Vercruysse, J., Peeters, E., Burggraeve, A., Vervaet, C., Remon, J.P., Sandler, N., De Beer, T., 2012. Prediction of quality attributes of continuously produced granules using complementary pat tools. Eur J Pharm Biopharm 82, 429-436.
Fonteyne, M., Vercruysse, J., De Leersnyder, F., Van Snick, B., Vervaet, C., Remon, J.P., De Beer, T., 2015b. Process Analytical Technology for continuous manufacturing of solid-dosage forms. TrAC Trends in Analytical Chemistry 67, 159-166.
Fonteyne, M., Vercruysse, J., Diaz, D.C., Gildemyn, D., Vervaet, C., Remon, J.P., De Beer, T., 2013. Real-time assessment of critical quality attributes of a continuous granulation process. Pharm Dev Technol 18, 85-97.
Gamlen, M.J., Eardley, C., 1986. Continuous Extrusion Using a Raker Perkins MP50 (Multipurpose) Extruder. Drug Dev Ind Pharm 12, 1701-1713.
García, I., Sarabia, L., Cruz Ortiz, M., Aldama, J.M., 2005. Usefulness of D-optimal designs and multicriteria optimization in laborious analytical procedures: Application to the extraction of quinolones from eggs. Journal of Chromatography A 1085, 190-198.
Hansuld, E.M., Briens, L., 2014. A review of monitoring methods for pharmaceutical wet granulation. Int J Pharmaceut 472, 192-201.
Hapgood, K.P., Litster, J.D., Biggs, S.R., Howes, T., 2002. Drop penetration into porous powder beds. J Colloid Interf Sci 253, 353-366.
Hapgood, K.P., Litster, J.D., Smith, R., 2003. Nucleation regime map for liquid bound granules. Aiche J 49, 350-361.
Harting, J., Kleinebudde, P., 2018. Development of an in-line Raman spectroscopic method for continuous API quantification during twin-screw wet granulation. Eur J Pharm Biopharm 125, 169-181.

Iveson, S.M., Litster, J.D., 1998a. Fundamental studies of granule consolidation part 2: Quantifying the effects of particle and binder properties. Powder Technol 99, 243-250.
Iveson, S.M., Litster, J.D., 1998b. Growth regime map for liquid-bound granules. Aiche J 44, 1510-1518.
Iveson, S.M., Litster, J.D., 1998c. Liquid-bound granule impact deformation and coefficient of restitution. Powder Technol 99, 234-242.
Iveson, S.M., Litster, J.D., Ennis, B.J., 1996. Fundamental studies of granule consolidation Part 1: Effects of binder content and binder viscosity. Powder Technol 88, 15-20.
Iveson, S.M., Litster, J.D., Hapgood, K., Ennis, B.J., 2001. Nucleation, growth and breakage phenomena in agitated wet granulation processes: a review. Powder Technol 117, 3-39.
Iveson, S.M., Neil, P.W., 2004. Brittle to plastic transition in the dynamic mechanical behavior of partially saturated granular materials. J Appl Mech-T Asme 71, 470-475.
Järvinen, M.A., Paavola, M., Poutiainen, S., Itkonen, P., Pasanen, V., Uljas, K., Leiviskä, K., Juuti, M., Ketolainen, J., Järvinen, K., 2015. Comparison of a continuous ring layer wet granulation process with batch high shear and fluidized bed granulation processes. Powder Technol 275, 113-120.
Johansson, B., Alderborn, G., 2001. The effect of shape and porosity on the compression behaviour and tablet forming ability of granular materials formed from microcrystalline cellulose. Eur J Pharm Biopharm 52, 347-357.
Kale, K., Hapgood, K., Stewart, P., 2009. Drug agglomeration and dissolution – What is the influence of powder mixing? Eur J Pharm Biopharm 72, 156-164.
Kayrak-Talay, D., Dale, S., Wassgren, C., Litster, J., 2013. Quality by design for wet granulation in pharmaceutical processing: Assessing models for a priori design and scaling. Powder Technol 240, 7-18.
Kayrak-Talay, D., Litster, J.D., 2011. A priori performance prediction in pharmaceutical wet granulation: Testing the applicability of the nucleation regime map to a formulation with a broad size distribution and dry binder addition. Int J Pharmaceut 418, 254-264.
Keleb, E.I., Vermeire, A., Vervaet, C., Remon, J.P., 2002. Continuous twin screw extrusion for the wet granulation of lactose. Int J Pharmaceut 239, 69-80.
Koster, M., Thommes, M., 2010. In-line dynamic torque measurement in twin-screw extrusion process. Chem Eng J 164, 371-375.
Kumar, A., Alakarjula, M., Vanhoorne, V., Toiviainen, M., De Leersnyder, F., Vercruysse, J., Juuti, M., Ketolainen, J., Vervaet, C., Remon, J.P., Gernaey, K.V., De Beer, T., Nopens, I., 2015. Linking granulation performance with residence time and granulation liquid distributions in twin-screw granulation: An experimental investigation. Eur J Pharm Sci.
Kumar, A., Vercruysse, J., Toiviainen, M., Panouillot, P.E., Juuti, M., Vanhoorne, V., Vervaet, C., Remon, J.P., Gernaey, K.V., De Beer, T., Nopens, I., 2014. Mixing and transport during pharmaceutical twin-screw wet granulation: Experimental analysis via chemical imaging. Eur J Pharm Biopharm 87, 279-289.
Kumar, V., Taylor, M.K., Mehrotra, A., Stagner, W.C., 2013. Real-Time Particle Size Analysis Using Focused Beam Reflectance Measurement as a Process Analytical Technology Tool for a Continuous Granulation–Drying–Milling Process. Aaps Pharmscitech 14, 523-530.
Laske, S., Paudel, A., Scheibelhofer, O., Sacher, S., Hoermann, T., Khinast, J., Kelly, A., Rantannen, J., Korhonen, O., Stauffer, F., De Leersnyder, F., De Beer, T., Mantanus, J., Chavez, P.-F., Thoorens, B., Ghiotti, P., Schubert, M., Tajarobi, P., Haeffler, G., Lakio, S., Fransson, M., Sparen, A., Abrahmsen-Alami, S., Folestad, S., Funke, A., Backx, I., Kavsek, B., Kjell, F., Michaelis, M., Page, T., Palmer, J., Schaepman, A., Sekulic, S., Hammond, S., Braun, B., Colegrove, B., 2017. A Review of PAT Strategies in Secondary Solid Oral Dosage Manufacturing of Small Molecules. J Pharm Sci-Us 106, 667-712.

Lee, S., O'Connor, T., Yang, X., Cruz, C., Chatterjee, S., Madurawe, R., Moore, C.V., Yu, L., Woodcock, J., 2015. Modernizing Pharmaceutical Manufacturing: from Batch to Continuous Production. J Pharm Innov, 1-9.

Li, H., Thompson, M.R., O'Donnell, K.P., 2014. Understanding wet granulation in the kneading block of twin screw extruders. Chem Eng Sci 113, 11-21.

Litster, J.D., Hapgood, K.P., Michaels, J.N., Sims, A., Roberts, M., Kameneni, S.K., 2002. Scale-up of mixer granulators for effective liquid distribution. Powder Technol 124, 272-280.

Litster, J.D., Hapgood, K.P., Michaels, J.N., Sims, A., Roberts, M., Kameneni, S.K., Hsu, T., 2001. Liquid distribution in wet granulation: dimensionless spray flux. Powder Technol 114, 32-39.

Liu, L.X., Litster, J.D., Iveson, S.M., Ennis, B.J., 2000. Coalescence of deformable granules in wet granulation processes. Aiche J 46, 529-539.

Luypaert, J., Massart, D.L., Vander Heyden, Y., 2007. Near-infrared spectroscopy applications in pharmaceutical analysis. Talanta 72, 865-883.

Maniruzzaman, M., Ross, S.A., Dey, T., Nair, A., Snowden, M.J., Douroumis, D., 2017. A quality by design (QbD) twin—screw extrusion wet granulation approach for processing water insoluble drugs. Int J Pharmaceut.

Meng, W., Kotamarthy, L., Panikar, S., Sen, M., Pradhan, S., Marc, M., Litster, J.D., Muzzio, F.J., Ramachandran, R., 2016. Statistical analysis and comparison of a continuous high shear granulator with a twin screw granulator: Effect of process parameters on critical granule attributes and granulation mechanisms. Int J Pharmaceut 513, 357-375.

Meng, W., Oka, S., Liu, X., Omer, T., Ramachandran, R., Muzzio, F.J., 2017. Effects of Process and Design Parameters on Granule Size Distribution in a Continuous High Shear Granulation Process. J Pharm Innov.

Montgomery, D.C., 2013. Design and analysis of experiments. John Wiley & Sons, New York.

Nagy, B., Farkas, A., Gyürkés, M., Komaromy-Hiller, S., Démuth, B., Szabó, B., Nusser, D., Borbás, E., Marosi, G., Nagy, Z.K., 2017. In-line Raman spectroscopic monitoring and feedback control of a continuous twin-screw pharmaceutical powder blending and tableting process. Int J Pharmaceut 530, 21-29.

Ohno, I., Hasegawa, S., Yada, S., Kusai, A., Moribe, K., Yamamoto, K., 2007. Importance of evaluating the consolidation of granules manufactured by high shear mixer. Int J Pharmaceut 338, 79-86.

Pandey, P., Tao, J., Chaudhury, A., Ramachandran, R., Gao, J.Z., Bindra, D.S., 2013. A combined experimental and modeling approach to study the effects of high-shear wet granulation process parameters on granule characteristics. Pharm Dev Technol 18, 210-224.

Pathare, P.B., Bas, N., Fitzpatrick, J.J., Cronin, K., Byrne, E.P., 2011. Effect of high shear granulation process parameters on the production of granola cereal aggregates. Biosystems Engineering 110, 473-481.

Plank, R., Diehl, B., Grinstead, H., Zega, J., 2003. Quantifying liquid coverage and powder flux in high-shear granulators. Powder Technol 134, 223-234.

Punčochová, K., Ewing, A.V., Gajdošová, M., Sarvašová, N., Kazarian, S.G., Beránek, J., Štěpánek, F., 2015. Identifying the mechanisms of drug release from amorphous solid dispersions using MRI and ATR-FTIR spectroscopic imaging. Int J Pharmaceut 483, 256-267.

Ridgway, K., Rupp, R., 1969. The effect of particle shape on powder properties. Journal of Pharmacy and Pharmacology 21, 30S-39S.

Ritala, M., Holm, P., Schaefer, T., Kristensen, H.G., 1988. Influence of Liquid Bonding Strength on Power-Consumption during Granulation in a High Shear Mixer. Drug Dev Ind Pharm 14, 1041-1060.

Román-Ospino, A.D., Singh, R., Ierapetritou, M., Ramachandran, R., Méndez, R., Ortega-Zuñiga, C., Muzzio, F.J., Romañach, R.J., 2016. Near infrared spectroscopic calibration models for real time monitoring of powder density. Int J Pharmaceut 512, 61-74.

Rosas, J.G., Blanco, M., González, J.M., Alcalà, M., 2012. Real-time determination of critical quality attributes using near-infrared spectroscopy: A contribution for Process Analytical Technology (PAT). Talanta 97, 163-170.
Saleh, K., Vialatte, L., Guigon, P., 2005. Wet granulation in a batch high shear mixer. Chem Eng Sci 60, 3763-3775.
Sayin, R., El Hagrasy, A.S., Litster, J.D., 2015a. Distributive mixing elements: Towards improved granule attributes from a twin screw granulation process. Chem Eng Sci 125, 165-175.
Sayin, R., El Hagrasy, A.S., Litster, J.D., 2015b. Distributive mixing elements: Towards improved granule attributes from a twin screw granulation process. Chem Eng Sci 125, 165-175.
Sayin, R., Martinez-Marcos, L., Osorio, J.G., Cruise, P., Jones, I., Halbert, G.W., Lamprou, D.A., Litster, J.D., 2015c. Investigation of an 11mm diameter twin screw granulator: Screw element performance and in-line monitoring via image analysis. Int J Pharmaceut 496, 24-32.
Schaafsma, S.H., Vonk, P., Kossen, N.W.F., 2000. Fluid bed agglomeration with a narrow droplet size distribution. Int J Pharmaceut 193, 175-187.
Seem, T.C., Rowson, N.A., Ingram, A., Huang, Z., Yu, S., de Matas, M., Gabbott, I., Reynolds, G.K., 2015. Twin screw granulation — A literature review. Powder Technol 276, 89-102.
Smirani-Khayati, N., Falk, V., Bardin-Monnier, N., Marchal-Heussler, L., 2009. Binder liquid distribution during granulation process and its relationship to granule size distribution. Powder Technol 195, 105-112.
Tardos, G.I., Khan, M.I., Mort, P.R., 1997. Critical parameters and limiting conditions in binder granulation of fine powders. Powder Technol 94, 245-258.
Teżyk, M., Milanowski, B., Ernst, A., Lulek, J., 2016. Recent progress in continuous and semi-continuous processing of solid oral dosage forms: a review. Drug Dev Ind Pharm 42, 1195-1214.
Vercruysse, J., 2015. Use of a continuous twin screw granulation and drying system during formulation development and process optimization. Eur J Pharm Biopharm 89, 239-247.
Vercruysse, J., Toiviainen, M., Fonteyne, M., Helkimo, N., Ketolainen, J., Juuti, M., Delaet, U., Van Assche, I., Remon, J.P., Vervaet, C., De Beer, T., 2014. Visualization and understanding of the granulation liquid mixing and distribution during continuous twin screw granulation using NIR chemical imaging. Eur J Pharm Biopharm 86, 383-392.
Vervaet, C., Remon, J.P., 2005. Continuous granulation in the pharmaceutical industry. Chem Eng Sci 60, 3949-3957.
Wang, S.L., Ye, G.H., Heng, P.W.S., Ma, M.X., 2008. Investigation of high shear wet granulation processes using different parameters and formulations. Chem Pharm Bull 56, 22-27.
Yu, L.X., 2008. Pharmaceutical Quality by Design: Product and Process Development, Understanding, and Control. Pharm Res 25, 781-791.
Yu, L.X., Amidon, G., Khan, M.A., Hoag, S.W., Polli, J., Raju, G.K., Woodcock, J., 2014. Understanding Pharmaceutical Quality by Design. The AAPS Journal 16, 771-783.
Zhang, Y., Chan, J.W., Moretti, A., Uhrich, K.E., 2015. Designing polymers with sugar-based advantages for bioactive delivery applications. Journal of Controlled Release 219, 355-368.
Zhang, Y., Feng, J., McManus, S.A., Lu, H.D., Ristroph, K.D., Cho, E.J., Dobrijevic, E.L., Chan, H.-K., Prud'homme, R.K., 2017. Design and Solidification of Fast-Releasing Clofazimine Nanoparticles for Treatment of Cryptosporidiosis. Molecular Pharmaceutics 14, 3480-3488.
Zhang, Y., Li, Q., Welsh, W.J., Moghe, P.V., Uhrich, K.E., 2016a. Micellar and structural stability of nanoscale amphiphilic polymers: Implications for anti-atherosclerotic bioactivity. Biomaterials 84, 230-240.
Zhang, Y., Mintzer, E., Uhrich, K.E., 2016b. Synthesis and characterization of PEGylated bolaamphiphiles with enhanced retention in liposomes. J Colloid Interf Sci 482, 19-26.